PHYSIK-DEPARTMENT

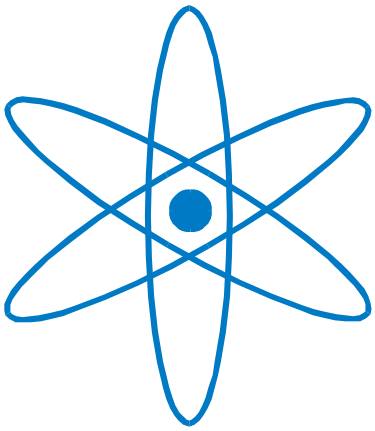

Supramolecular Engineering of Regular and Disordered Networks on Metal Surfaces

Dissertation

von

Matthias Marschall

TECHNISCHE UNIVERSITÄT

MÜNCHEN

TECHNISCHE UNIVERSITÄT MÜNCHEN

Lehrstuhl E20 -
Molekulare Nanowissenschaften & Chemische
Physik von Grenzflächen

Supramolecular Engineering of Regular and Disordered Networks on Metal Surfaces

Matthias Günter Marschall

Vollständiger Abdruck der von der Fakultät für Physik der Technischen Universität München zur Erlangung des akademischen Grades eines Doktors der Naturwissenschaften genehmigten Dissertaion.

Vorsitzender: Univ.-Prof. Dr. Harald Friedrich

Prüfer der Dissertation:

1. Univ.-Prof. Dr. Johannes Barth
2. Priv.-Doz. Dr. Markus Lackinger,
Ludwig-Maximilians-Universität München

Die Promotion wurde am 30.06.2011 bei der Technischen Universität München eingereicht und durch die Fakultät für Physik am 13.07.2011 angenommen.

Acknowledgement

In den Vergangenen Jahren wurde ich während meiner Promotion im Lehrstuhl von Prof. Johannes Barth, dem ich für diese Möglichkeit sehr zu Dankbar bin, von vielen Leuten mit Rat und Tat unterstützt. Schon bei meiner Ankunft in München wurde ich herzlich willkommen geheißen und wurde schnell integriert. Besonders unterstütz hat mich während der gesamten Laufzeit Dr. Joachim Reichert der mir nicht nur als Mentor sondern auch als Freund zur Seite stand. Dabei fanden wir stets die richtigen Lösungen um speziell nach dem Umzug des Equipments von Vancouver nach München wieder Experimente durchführen zu können.
Große Unterstützung habe ich ebenfalls erfahren durch Dr. Florian Klappenberger während gemeinsamer Messungen am Synchrotron in BESSY-II Berlin. Ebenfalls für gute und produktive Zusammenarbeit dankbar bin ich Dr. Willi Auwärter und Knud Seufert, die Zeit und Nerven für mein Projekt opferten.
Für ihre Unterstützung möchte ich mich auch bedanken bei den Menschen des Lehrstuhls E20 die stets mit Rat und Tat zur Stelle waren, Dr. Peter Feulner, Dr. Hartmut Schlichting, Karl Eberle, Max Glanz, Karl Kölbl, Reinhold Schneider und insbesondere der guten Seele des Lehrstuhls Kamila Wilson.
Dankbar bin ich ebenfalls den Doktoranden um mich herum, die stets für einen gelungenen Mittelweg zwischen Arbeit und Spaß gesorgt haben und so ein sehr angenehmes Arbeitsklima erzeugt haben.
Auch meiner Familie möchte ich einen großen Dank aussprechen, dass sie egal bei welchen Entscheidungen immer zu mir gestanden hat, mich unterstützt und an mich geglaubt hat.
Besonders Dankbar bin ich meiner Freundin Serena Ghironi für ihre Liebe, Zuwendung und Antrieb, welcher mich auch in schwierigen Zeiten wieder aufgebaut und voran gebracht hat.

Abstract

The engineering and predetermination of supramolecular structures by molecular self-assembly to create functional surfaces is a very challenging task. To study the constitutive molecule-molecule and molecule-substrate interaction the scanning tunneling microscopy with its possibility to image objects on the single atom and molecular level is the appropriate tool.
In this work two carbonitrile functionalized oligophenyl molecules have been investigated on the Ag(111) and Cu(111) surface by means of scanning tunneling microscopy, X-ray photoelectron spectroscopy and near-edge absorption fine structure spectroscopy at temperatures between 6 and 300 K. The difference between the molecules is the position of the functional moieties. For the first molecule both substituents are symmetric in *meta* position on the terminating phenyl ring and for the second molecule the substituents are asymmetric in *para* and *meta* position on the terminating phenyl ring, respectively. On the surface the molecules isomerises into a *cis* and two *trans* species (the first molecule) and two *trans* species (the second molecule).
The first molecule exhibits on the Ag(111) surface organic 1D molecular ribbons and highly ordered molecular islands featuring a commensurate fit with the sample surface. On Cu(111) similar molecular structures could be resolved as well. However with increasing molecular coverage the molecular orientation and hence the resolved pattern changes from a molecule adsorbed almost coplanar with its phenyl rings on the surface to an almost perpendicular orientation. Subsequent cobalt evaporation on top of the molecular pattern leads to a fully reticulated 2D random metal-organic network defined by distinct three- and fourfold nodal motifs. The random network could serve as a model system for 2D glassy networks.
The second molecule forms two different supramolecular networks: a dense packed and a porous. Both exhibit a commensurable fit with the surface. By additional cobalt evaporation a room temperature stable metal-organic random network constructed of three- and fourfold nodal motifs could be created.

Contents

List of Figures

List of Tables

Chapter 1

Introduction

The ability to achieve the strongest and the most advanced materials has been the foundation of powerful kingdoms, states and in recent days companies. Where in the past a sword of iron gave benefit compared to a bronze one, nowadays structural control on the materials is the essential key to push the strength and hardness to the limit or access new dimensions of miniaturization. The implementation of nanoscale structures and building blocks promises novel functionalities and applications not just for the bulk structure. The control to structure surfaces in a well-ordered manner is of special interest. Miniaturization of structures on surfaces is desired for the electronic industry and for chemists in order to provide advanced catalytic and gas sensing platforms [1], to prevent corrosion [2], to minimize friction and keep the surface clean. Two different approaches could be utilized to structure surfaces in a controlled manner. The first way is used in principle from ancient times; to remove material with diverse tools from the bulk in order to shape a predetermined design. This approach is called top-down approach. State of the art semiconductor industry employs the top-down approach, where small structures are constructed from large entities. However, it is predicted to reach certain physical limits in near future. The realization of structures in the range of 25 nm is still very complex and costly and will unlikely reach the ultimate limit of miniaturization.

The second way is to manipulate atomic and molecular building blocks to self-assemble the desired structure from scratch. Developing new pathways to control single atoms or molecular building blocks from the atomic to the macroscopic scale to manufacture faultless products is the ultimate goal of the so called bottom up approach [3]. Alignment phenomena of adsorbed molecules are often an interplay between thermodynamic and growth kinetics driven by the minimization of the free energy and lead surprisingly often homogeneous structures [4]. The self-assembly of small building blocks is one Ansatz of the so called bottom-up approach [3]. The

guide for self-assembly is nature which reaches ultimate perfection in combining complex molecules and at the same time provides an enormous range of functionalities. Exploiting this nature given structural design unexpected possibilities to tailor novel materials became accessible. To handle molecular self-assembly at surfaces, a detailed knowledge about substrate-adsorbate and adsorbate-adsorbate interaction is indispensable.

The investigation of the assembled structures as well as of the building blocks is a key task, which became accessible with Binnig and Rohrer's invention of the scanning probe microscope [5]. The scanning probe technique and especially the scanning tunneling microscope (STM) changed the view into the nanoscale, due to its real space imaging capability [6] and its versatility for different environments. Based on this approach it was possible to study single molecules on an atomistic level [7] and the manipulation of single atoms and molecules could be demonstrated [8]. Crommie et. al. were able to build a quantum corral out of 48 Fe atoms and observed the embedded eigenstates exemplifying quantum mechanical effects [9]. Also molecules can interact with the electrons of the so called electron surface gas resulting in standing wave pattern [10] which can be utilized to control the arrangement of single metal adatoms [11]. It became feasible to structure the surface on an atomic scale [9], synthesize [12] and dissociate molecules [13–15] and establish distinct covalent bonds [16]. With the implementation of ferromagnetic probes it became possible to observe magnetic domains [17,18] and with increasing sensitivity even the spin orientation of single atoms can be resolved [19]. Despite its manipulation ability the STM is not a tool to structure surfaces on a large scale due to the limited manipulation steps per time, but for fundamental research it is a useful tool to create nanoscale structures [20, 21]. All these experiments aim to gain a better understanding of adsorbed molecules, interaction between molecular and atomistic adsorbates and interactions of the adsorbates with surfaces. Especially to comprehend the dynamic process of adsorbate-adsorbate interaction, which is the major ingredient for self-assembly, a variable temperature, fast scanning tunneling microscope is the instrument of choice.

The physical properties of the investigated structures change dramatically by reducing the particle size, for example due to an enhanced surface to volume ratio. Nanoparticles of Fe_2O_3 i. e. oxidize strongly exhibiting pyrophoric character. The comprehension of these properties at the nanoscale is essential to structure surfaces and to engineer highly organized systems [22]. Such control and selective design of nanostructured devices is of special interest for the semiconductor and data storage industry which aims to increase the density of functional units and to miniaturize

materials. Nanostructuring of surfaces to implement even smaller entities for data storage or transistor application is one major goal. The functionalization of surfaces for catalytic or sensor applications opens up an enormous playground as well. Most catalytic processes take place at elevated temperature. To employ self-assembled molecular networks coordination strategies are just a first step towards a high temperature stable molecular pattern exhibiting distinct reaction centers to trigger the desired reaction. To achieve high temperature stability metal coordination bonds or even covalent interaction in the self-assembled molecular networks can be employed.

1.1 Concepts of Supramolecular Engineering

Until now lithography and micro imprinting techniques [23] are the instruments of choice to create microscopic structures. The density of transistors increases steadily and chasing Moore's law, formulated in the 60′s. Nowadays industrial standards reached 25 nm inter-structural distance [24] utilizing ultra violet light sources for the lithography process [25]. Electron beam lithography is also a method with high spatial resolution at reasonable costs but the focused electron beam is limited to repairing and research duties. To advance to the next level of miniaturization in semiconductor structures, X-ray sources have to be implemented which require sophisticated and costly techniques for short wave optics, a vacuum environment, a beam source and so on, which are not yet available on large scale.
Many advances have been made to engineer nanostructures at surfaces from atoms and molecules [3] like Lego™ bricks due to interdisciplinary efforts and methods of chemistry, physics and biology. The introduction to this versatile and interesting field and the basic conceptual models and ideas will be focus of this chapter.

Not just in recent years considerable effort has been made to understanding the interaction of molecular building blocks which form promising structures. Furthermore one should take into account that "*molecules do not act if they do not bind*" which means that for a molecular interaction there is a need for receptors as Paul Ehrlich introduced in his concept of the receptor [26]. To tailor molecular network formations selective bond formation is the major key. Emil Fischer in 1894 presented in his Nobel price awarded "*lock and key*" concept the idea of the steric fit. The steric fit implies the geometrical complementarity of the interacting species which is the basis of molecular recognition. After identification the species have to remain in a stable configuration which requires affinity and interaction. In the late 19th

century Alfred Werner introduced the idea of coordination, founding the basis of metallo-supramolecular chemistry [27].
In recent years these concepts gained more interest since novel experimental methods such as nuclear magnetic resonance (NMR) spectroscopy and scanning probe techniques allow to analyze the structure and the properties of molecular networks arising from coordination interaction. Coordination chemistry is based on the principles of non-covalent interaction, molecules assemble spontaneously into extended poly-molecular arrays presenting a well defined microscopic organization. The interactions offer different properties especially in terms of strength and directionality as well as bond distances and angles. In a real system repulsive forces i.e. from adjoining molecular components, the solvent, the substrate and other factors influence the binding situation as well. In comparison to covalent bond motives the intermolecular forces are thermally less stable but reversible and thus more flexible. The flexibility of the system is one of the main advantages of supramolecular engineering and may result in self-correction of defective features. The process is driven by the minimization of the systems minimal free energy. Self-correction in this context means the reconfiguration and reversibility of non-covalent bond motives. The intermolecular non-covalent bonds are based on distinct selection rules so called molecular recognition [28]. Molecular recognition is "*binding with purpose*" and implies the storage and the read out of molecular information. By the directed identification of the single building blocks the coordination partner can influence the electrical, optical and conformational properties. This scheme is an essential factor to build up structures from atomic and molecular units with a selective functionality. The receptors are characterized by a distinct size, shape, dimensionality and their electronic properties. The interacting species have to fit like key and lock. Non-covalent interactions are weak compared to covalent bindings. Typically hydrogen bond formations have 0.1 to 5 kcal/Mol, whereas covalent bonds comprise 40 to 100 kcal/Mol. Thus for non-covalent bonds it can be important to have a rather large contact area where multiple bond sites can be established.

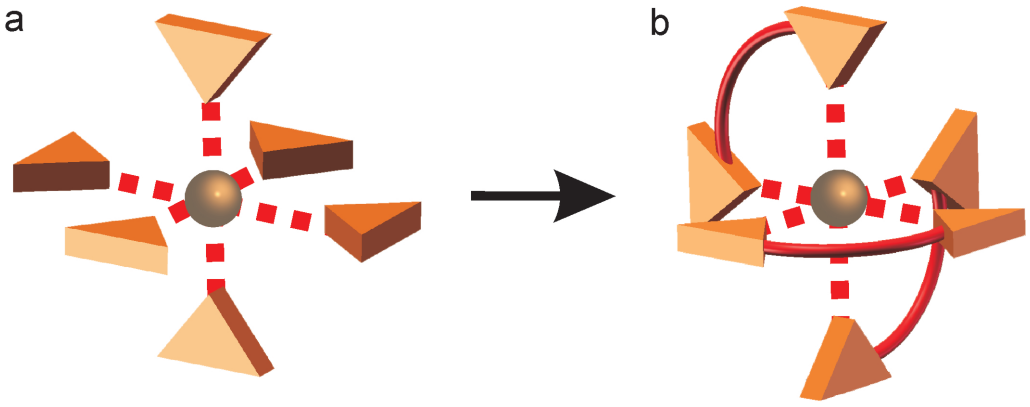

Figure 1.1: Model of chelat reaction. **(a)** Central Ni atom surrounded by six ammonium receptors (triangles). **(b)** Formation of covalent bonds between two receptors by bidentate ligands (red tubes). The chemical reaction equation displays the reaction presented in the schematic model.

Depending on the number of possible binding sites on the molecule, monotopic and multitopic receptors can be distinguished. Monotopic receptors provide a single binding site whereas multitopic receptors provide two and more binding sites [29, 30]. In the simplest case a single atom is surrounded by receptors, e. g. a metal cation surrounded by six ammonia ligands. Figure 1.1 *a* displays this situation for a central Ni ion surrounded by ammonia. The selective coordination of alkali cations has become the base of supramolecular chemistry [31]. If two ammonia groups are connected via covalent bonds forming ethylendiamine the residual three ethylendiamine entities posses still six coordination sites to the Ni center. Even if both components rely on the same number of coordination motives the latter is 10^8 times more stable than the first. The model of this formation is displayed in figure 1.1 *b*. The corresponding equation of the chemical reaction is displayed beneath the models. The reason for the enhancement of the stability is called chelate effect, derived from the Greek word *chely*, denoting a lobster claw. "*The whole is greater than the sum of its parts*" finds a suitable expression here. The enhanced stability and the reduced total free energy (ΔG°) is a result of the combination of entropic (ΔS°) and enthalpic (ΔH°) factors.

$$\Delta G^\circ = \Delta H^\circ - T\Delta S^\circ \tag{1.1}$$

For example in solution the reaction would increase the entropy by releasing more components into solution (four species before and seven after) and therewith increasing the systems degree of freedom. Furthermore the receptors with a multitopic bond site are harder to remove since the second coordination site is stabilizing

the complex.
Especially in biological systems the presence of one species can increases the receptor's affinity for a second species. This effect is called positive cooperativity. For example the presence of one O_2 molecule to one of the four myoglobine units in hemoglobin increases the reactivity of the other three myoglobines to O_2 molecules. The reverse effect would be called negative cooperativity.
The presented fundamental requirements for the design of supramolecular building blocks are just an extract of the rules which need to be taken into consideration while designing artificial molecular building blocks for supramolecular engineering. On surfaces, where all our experiments have been accomplished, it is essential to provide a reasonably sized contact area in order to interact with adjacent molecules as well as geometrical and site complementarity to permit adsorption. The transport of the building blocks is an essential aspect. Diffusion on the surface is thermally activated and shall be deemed to be a random hopping process of the building blocks. Herein the diffusivity D describes the mean square distance traveled by an adsorbate per time unit which typically follows an Arrhenius law [32]. Hence at a certain temperature the transport of the building blocks to a defined position is limited. The availability of building blocks is further subject to the evaporation rate F. The distance a building block has to travel on the surface until getting in contact to the next adsorbate or cluster is thus determined by the ratio D/F. If the diffusion is faster than the evaporation rate (large D/F ratio) the system can grow close to equilibrium conditions. The adsorbate migrates about the sample surface finding the minimum energy configuration. However with a large deposition rate (small D/F ratio) the pattern formation is dominated by the migration kinetics which can lead to metastable structures [3].

Functionalisation and structuring of surfaces at the nanoscale is the focus of this work. The bottom up approach where molecular and atomic components fabricate the desired structures is the fundamental principle. The formation is driven by the competition between kinetics and thermodynamics included in the idea of self-processes. For self-processes we have to distinguish between systems that underlie certain kinetic limitations and systems in thermodynamic equilibrium. In this project we rely on systems close to thermodynamic equilibrium which we call self assembled systems. Hence the spontaneous formation of molecular and atomic building blocks, so called tectons [33], resulting in discrete non-covalent bond layers under equilibrium conditions is called supramolecular self-assembly [3, 30, 31, 34]. The key to fabricate supramolecular self-assembled structures is the understanding and the control of non-covalent connections between the tectons while bringing

them together in one aggregate. During the tailoring of molecular building blocks one should consider, that the energy values gained by the self-assembly formation are in the order of 2 to 20 $kcal/nm^2$ [35]. For covalent reaction entropy normally is of secondary importance, but for the low interaction energies prevailing in non-covalent bindings the loss of translation entropy, which can be estimated by a rule of thumb for millimolar concentration to approximately -TΔ S= +5.5 kcal/Mol, can not be neglected [34]. Supramolecular self-assembly should not be distinguished with templating. This involves organic or inorganic, temporary or permanent "*helper*" species guiding the assembly. Templating can be involved in self-assembly but is then considered as initial step, whereas the entire self-assembling process comprises several steps.

Nature offers the best examples for perfect self-assemblies, with self-healing properties. The well known tobacco mosaic virus (TMV) is an astonishing example [36]. Its rod like structure is formed by a central strand ribonucleic acid (RNA) 6400 bases long. Onto this backbone a coat protein self-assembles consisting of 2130 proteins each consistent of 158 amino acids and together they form a perfect helical structure. Even more remarkable is the fact that, if the virus gets fragmented into its components and mixed under physiological conditions, the virus reassembles into a non distinguishable copy of the original.

1.1.1 Supramolecular Self-assembly Mediated by Hydrogen Bonding

The arrangement of tectons mediated by hydrogen bonds has been explored widely in the field of liquid crystals, in solution and in solid state [37–40]. Also on surfaces hydrogen mediated networks have been extensively studied yielding numerous impressive publications over the last decade. The crucial point in designing such a network is the choice of the molecular shape and the positioning of hydrogen-bonding donor and acceptor groups. The arrangement of a 1 dimensional (1D) array for example requires just two bonding sites preferably positioned on the ends of a chain like molecule. By recognition the components now can form 1D string networks. Terephthalic acid (TPA, see figure 1.2 *a*) with its two carboxylic acid groups substituted on a phenyl ring is the ideal example. Linear dicarboxylic acids are found in the bulk [41, 42]. The carboxylic groups act as donor and acceptor at the same time. Together they form 1D hydrogen-bridge mediated chains. An atomistic model of the resulting formation is presented in figure 1.2 *b* wherein the hydrogen bridge is marked with red dotted lines. Also porphyrin molecules with sub-

stituted cyanophenyl (bis(cyanophenyl)-bis(di-tertiarybutylphenyl) BCTBPP porphyrin) groups in *trans* position (figure 1.2 *c*) assemble in well ordered 1D ribbons on the reconstructed Au(111) surface [20, 43]. The carbonitrile groups of the porphyrin molecule exhibit a high electronegativity and mediate an interaction with the hydrogens of the adjacent molecule. Figure 1.2 *d* presents an atomistic model of the resulting formation. By selective bond formation a chain structure was formed. Every N in the CN group is connected to two hydrogens of the adjacent molecule. The orientation of the molecules to another is influenced by long-range dipole-dipole interaction where hydrogen-binding interactions further stabilize the formation.
The binding can be programmed by the positioning of the donor and acceptor groups, limiting the possible bond formations and forcing the self-assembled system into the desired direction. Nevertheless steric repulsion and other factors have to be considered during structure formation as well. For 2- and even 3-dimensional arrays the molecular pattern becomes more difficult. For a 2D network formation chain motifs are not sufficient and bifurcation motives are required as well. A bifurcation relys on more complex structural schemes, which require 3 or more binding sites. Theobald and co-workers [44] utilized two complementary molecules constructing a 2D hydrogen bridge mediated network. The first, perylene tetra-carboxylic di-imide (PTCDI) is a rod like molecule exhibiting binding sites on each end (see figure 1.2 *e*). The second molecule they implemented is the melamine (see figure 1.2 *f*), which on a surface provides three binding sites comprising an angle of 120°. The triangular shape of melamine together with the PTCDI as connection bar in between can form an extended supramolecular honeycomb network [44]. An atomistic model of the resolved network formation is depicted in figure 1.2 *g*. The binding motive between the two molecules is marked with the red dotted lines. In contrast to the examples presented earlier now two different molecules form a hydrogen bridge with one nitrogen and two oxygen atoms on each binding site. Here Fischers [45] key and lock principle can be nicely seen, since the two molecules just fit in a predetermined way. The formed hexagonal network with nanopores could serve as host for guest molecules. All three model systems have multitopic bond sites to stabilize the resulting structure.
But not just by an increased number of binding sites 2D networks can be formed. Recent publications on linear oligophenyls show that chain motives can exhibit bifurcation motives as well by the formation of supramolecular macrocycles assembled in nodes. Utilizing olygophenyls functionalized with carbonitrile groups in *para* position, on the outer ends of the rod pointing away from the molecular backbone, different complex nodal motives could be found resulting in a porous 2D network [46, 47].

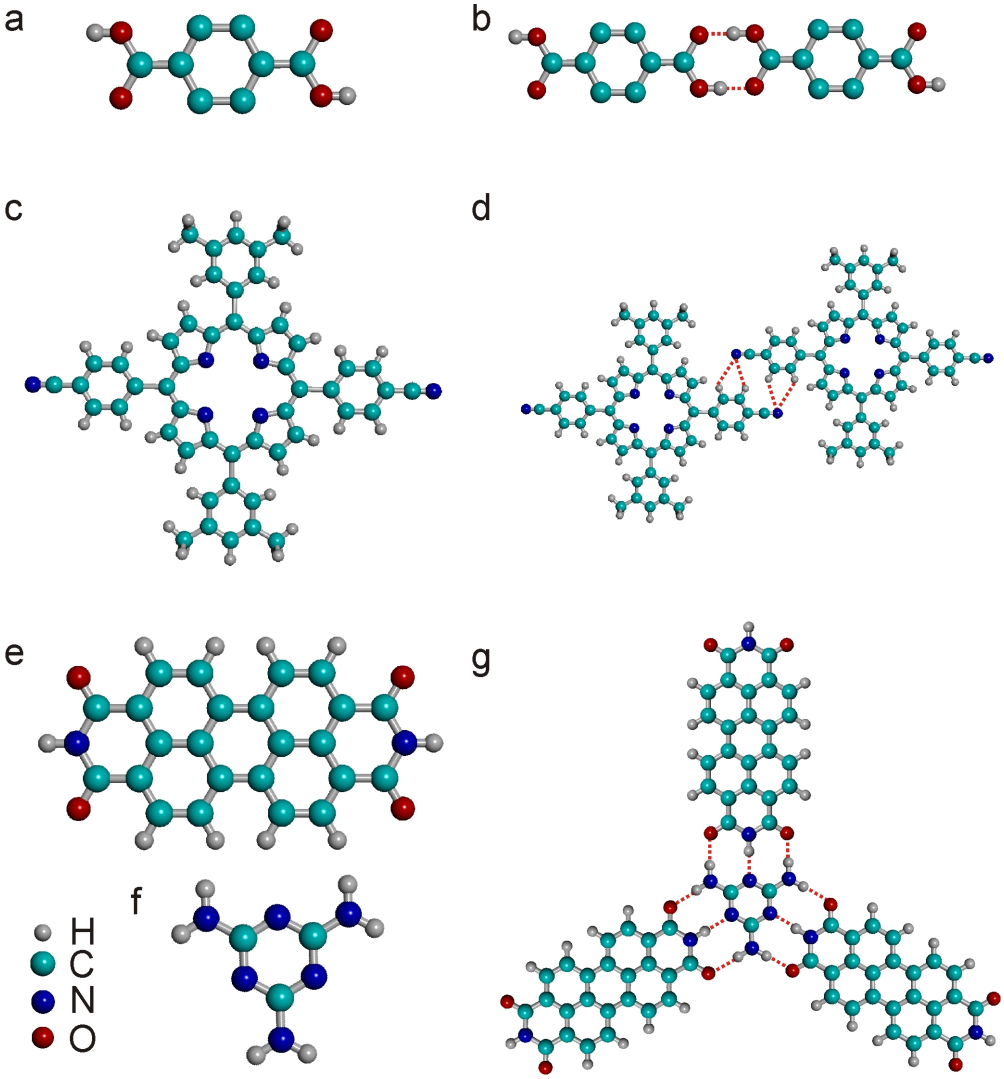

Figure 1.2: Atomistic models of four different molecules in combination with a possible resulting hydrogen mediated structure. **(a)** Terephthalic acid (TPA) forming a **(b)** hydrogen bridge mediated structure by the carboxylic acid. **(c)** Atomistic model of bis(cyanophenyl)-*trans*-bis(di-tertiarybutylphenyl) porphyrin (trans-BCTBPP) porphyrin **(d)** connected to an adjacent molecule mediated by functional CN groups. **(e)** Perylene tetra-carboxylic di-imide (PTCDI) and **(f)** melamine forming a **(g)** supramolecular network using the lock and key principle.

1.1.2 Supramolecular Self-assembly on Surfaces Mediated by Metal Coordination

Most of the hydrogen mediated networks exhibit no room temperature stability. Nevertheless, supramolecular chemistry does not exclusively rely on hydrogen bridge formation. The strongest non-covalent coordination motive is the metal ligand formation. Strategies of metal coordination are well known in solution chemistry. In

principle we distinguish between a metal center and a tecton coordinating to the metal center. The metal complexes feature similar binding affinity in all directions exhibiting a spherical recognition scheme before coordinating to any tecton. Depending on the character of the tecton capsules or polymeric structures can be predetermined (see figure 1.3 *a,b*). The binding of a guest species into a cavity will yield an inclusion complex a so called cryptate [48, 49]. The central complex increases the stability of the surrounding host and produces various new structures and routes for selective structure formation. In 1987 the Nobel Prize was given to Donald J. Cam, Jean-Marie Lehn and Charles J. Pederson for their work opening the field of supramolecular chemistry.

With the specific design of protected metal complexes like the Ru(II) complex $[Ru([9]ane\text{-}S3)Cl2(DMSO)]^{2+}$ in combination with ligand species like $4,4'-$bipyridile cuboidale molecules have been self-assembled in 1998 by J. Thomas and co-workers with a variable 3D cavity size protecting an enclosed molecule. Figure 1.3 *c* depicts a model of the structure formation [50].

To design molecular layers at surfaces the incorporation of metal complexes was an important step as well. Now structures can be stabilized by the co-deposition of transition metals and novel functionalities can be approached. Carbonitrile and pyridine groups were found to form stable structures. i.e. a porphyrin molecule with two substituted phen-1,4-diyl-ethynyl-pyridyl groups can form 1D molecular networks after Co co-deposition. Besides 1D structures, metal coordination strategies are well suited for network formation in 2D due to the multiple divergent binding possibilities. Stepanow and co-workers implemented dicarboxylic oligophenyls with varying backbone length and co-deposited Fe atoms on the Cu(100) surface [51]. The self-assembled patterns exhibit long range order with rectangular cavities. The size of the cavities is tunable by varying the molecular backbone length. Another example for the variation of the cavity size was published by U. Schlickum and co-workers. The underlying structure is an oligophenyl with substituted carbonitrile groups on the outer phenylring in *para* position. On Ag(111) extended honeycomb lattices have been found after Co co-evaporation featuring a cavity size up to 29 nm^2 [52]. Metal coordinated chain formations are highly stable but can be manipulated with the tip of a scanning tunneling microscope (i.e. see section 3.5.1).

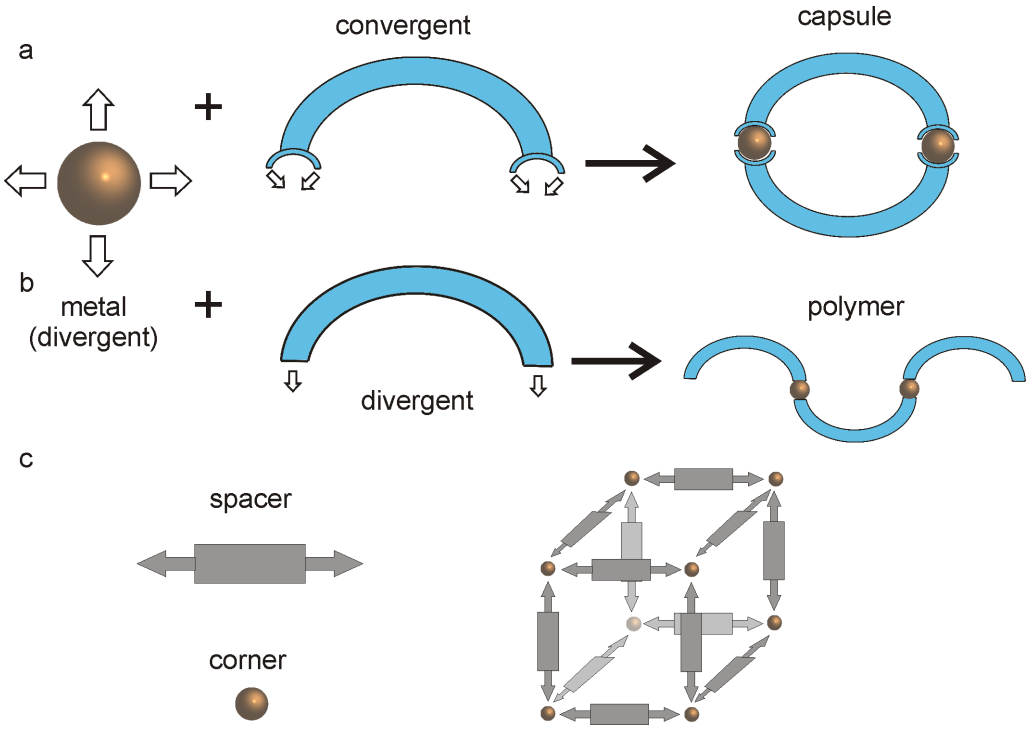

Figure 1.3: Conceptual models for metal coordination. **(a)** Capsul formation from a divergent metal center combined with a convergent ligand. **(b)** Polymer formation based on a divergent metal center and a divergent ligand. **(c)** Formation of a cuboidale molecule based on spacer and corner building blocks.

A promising route for novel self-assembly strategies on surfaces could be based on the allosteric effect. Herein an effector induces changes of the conformation of a tecton and changes its reactivity. Such a tecton could be for example a metal-adatom or metal-complex positioned in a defined position on the surface. Another pathway could be the utilization of metal centers in phthalocyanine or porphyrin molecules. Evaporated molecules can coordinate with this metal complex and open a new bond site induced by the coordination. In biology allosteric functions regulate the activity of enzymes [53–57]. These pathways exhibiting positive cooperativity could also be utilized for a stepwise growth into the third dimension. First promising steps of self-assembled structures into the third dimension have been reported previously by Liu et. al. [58] and Ecija [59].

1.2 Chirality

While selecting appropriate molecular building blocks for supramolecular self-assembly another important factor has to be taken into account, the chirality of the employed species. The most basic example for chirality is right in front of us, our left and right hand. They are mirror-symmetric counterparts but not superimpos-

able. An object is called chiral when it is not superimposable with its mirror image by rotation. The assembly of achiral building blocks on surfaces can result in the formation of chiral molecules or chiral structures. Recently a Kagomé lattice build from achiral molecules have been described by Schlickum et. al. [46]. Here two mirror symmetric assemblies could be resolved.
For numerous reactions the formation of one of two enantimers would be preferred (chiral discrimination). Therefore a chiral surface has to be implemented in the reaction process. This process could have a large influence on the assembly of optical active chiral patterns [60]. Some chiral molecules are optically active and rotate the plane of linearly polarized light while the light is passing through the molecule.
Molecules which have no chirality in the gas phase can form different isomers upon surface confinement. These molecules are referred as prochiral molecules. For many different systems it was discovered that chiral or prochiral molecules segregate into homochiral structures on the surface [46, 47, 61–64]. The extended homochiral molecular networks rely on hydrogen-bridge formation, Van der Waals and dipole-dipole interaction exhibiting a high regularity [65, 66]. Scanning tunneling microscopy has been employed with big success to study chirality of single adsorbed molecules [67–70] and to provide evidence about enantiopure networks [61, 71]. The identification of the chirality especially for pharmaceutical application is of fundamental relevance [66, 72].

1.3 Linear Oligophenyl Molecules

The group of poly-*para*-phenyl molecules attracted high attention in recent years due to their interesting physical properties. Solids and thin films made from this class of molecules show a wide bandgap of 3−3.5 eV [73]. Due to the wide band gap the molecule is a perfect candidate for light emitting devices [74]. Especially the hexaphenyl was found to feature promising characteristics [73, 75, 76] such as blue photoluminescence with a high hole mobility. Gundlach and co-workers employed *p*-hexaphenyl as active layer in organic thin film transistors. Even polarized electroluminescence could be produced by the growth of oriented thin films of *p*-hexaphenyl [77]. The blue light could be converted to red and green in combination with appropriate dye layers acting as a filter, providing a RGB light source [78].
The performance of the self-assembled layer strongly depends on the degree of order in the system [79]. The emission of polarized light requires the molecules to be oriented in parallel in the active layer. To steer the orientation of the layer is one of the crucial tasks for the self-assembly process. The azimuthal orientation e.g. could

be predetermined by rubbing the precursor layer linearly over the sample [73] or by epitaxial growth on anisotropic substrates [80–82].

To employ self-assembly strategies and to enhance the interaction of the molecules, functional carbonitrile (CN) groups have been substituted in *para* position. The CN groups are well known to mediate interactions to hydrogen atoms of adjecant molecules and to form metal organic complexes [83]. In several applications such as conductive organic crystals [84] and thin films [85] or in metal-organic magnets [86,87] CN groups play major roles. They are also exploited in 2D supramolecular structures i.e. in substituted porphyrin molecules on Au(111) [20].

In recent years linear oligophenyls with substituted CN groups have been self-assembled by hydrogen mediated [46, 47, 88] or metal organic [52, 89, 90] structure formation and studied by means of scanning tunneling microscopy, photoelectron spectroscopy (XPS) and near edge X-ray absorption fine structure (NEXAFS) spectroscopy. The backbone has been varied from three phenyl rings up to six. Different molecular patterns could be found depending on the molecular coverage, the backbone length and temperature. In a submonolayer all of them are commensurate with the surface. Starting with three phenyl rings (pNC-pPh$_3$-pCN) in the molecular backbone on the Ag(111) surface the molecules exhibit a chevron like pattern extended homogeneously over wide areas (see figure 1.4 *a*). One molecule in the image is displayed as a bright rod and we found just two orientations forming the chevron-like pattern. With increasing chain length things become more complicated. The pNC-pPh$_4$-pCN molecule for example self-assembles in a rhombic structure, again extended without any mismatch over large areas (see figure 1.4 *a*). Remarkably the nodal formation of the CN groups evokes a chiral pattern formed by an achiral molecule. By increasing the chain length to five phenyl rings the resolved structure becomes more complex forming a Kagomé like pattern with different chirality (see figure 1.4 *a*) [91]. None of these hydrogen-bond mediated patterns is stable at room temperature (RT). At RT only dense packed island can be found with molecules positioned parallel with their molecular backbone to each other.

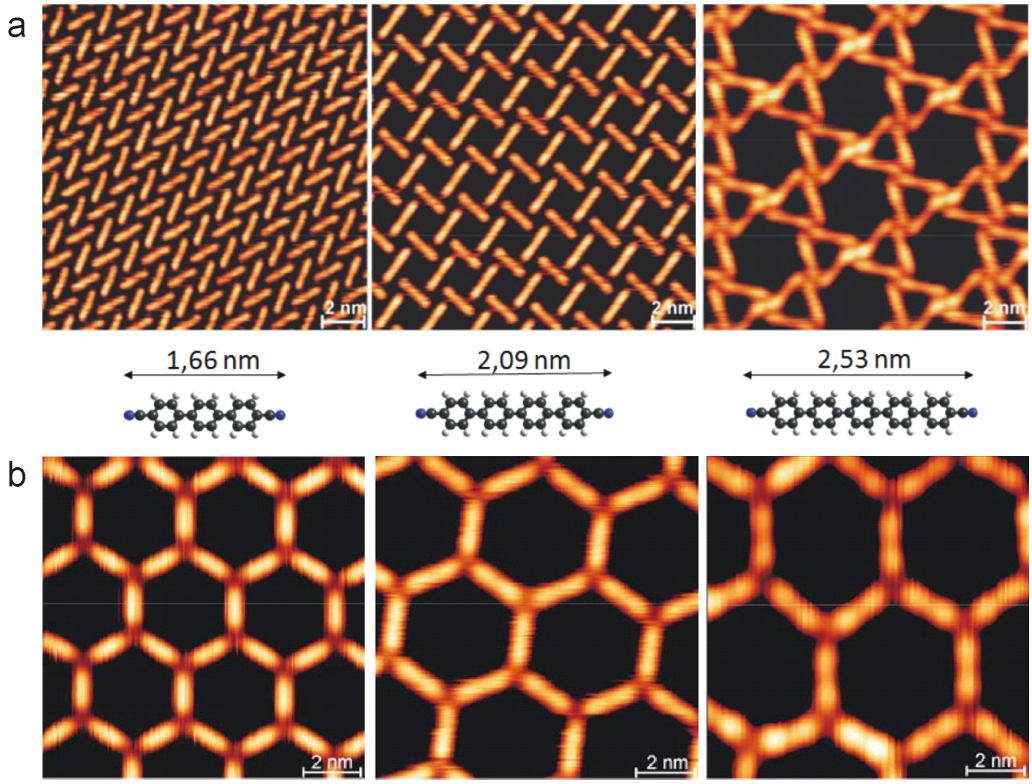

Figure 1.4: Supramolecular structures of dicarbonitrile oligophenyls with different backbone length on Ag(111) studied by STM. **(a)** Molecular pattern formation with three, four and five phenyl rings in the molecular backbone. **(b)** Metal-organic pattern formation with varying cavity size. Images adopted from refs. [46, 89].

In contrast to the high variability of supramolecular networks stabilized by interaction with hydrogen, metal-ligand mediated networks feature solely one bond motive: a three fold coordination via a central Co atom (see figure 1.4 *b*). The CN groups point star like towards the central metal atom. Detailed analysis of the adsorption position of the molecules and the Co atom showed that the structures are commensurate with the substrate and their backbones are oriented along the high symmetry direction of the substrate [47, 52]. The pattern extends in the μm range with a high regularity in a honeycomb structure featuring a variable cavity size based on the molecular backbone length. In the case of a terphenyl the Co coverage had been strongly varied. Local Co deficiency results in a regular six-fold coordination star like structure. Space limitations herein lead to a fully reticulated disordered network [90].

1.4 Surface Mobility

Dynamical phenomena [3, 92] like rotation [93, 94], diffusion [95] and conformational change [96] are important issues especially in self-assembly processes on surfaces.

Detailed knowledge about the dynamics of the system, growth and nucleation processes as well as adsorption sites of complex molecules is essential to predetermine the supramolecular structure and to functionalize surfaces. In surface pattern formations especially rotational and conformational degrees of freedom are important. Geometric constrains can influence the resulting pattern or lead to metastable phases. The migration of molecules and atoms on surfaces can be explained by the very simple picture provided by Volmer and Langmuir [97, 98]. He suggests that, molecules at low enough temperature on solid surfaces are bond to the surface atoms and oscillate about their equilibrium position. By increasing the temperature the molecules increase their amplitude of oscillation. Therewith it will occur more and more often that an adsorbed molecule jumps to an adjacent adsorption site. Adjacent adsorption sites are separated by an energy barrier E_m, the migration barrier. It is assumed that subsequent jumps are uncorrelated. To perform diffusion or rotation on the surface the molecule has to overcome a barrier. With increasing temperature the energy provided to activate the reaction is increasing as well and the corresponding rates rise exponentially. This description of surface migration is still valid today. Nevertheless in recent years experimental and theoretical characterization provides a more detailed understanding of the processes [95, 99–109]. Most surface diffusion processes can be described in good approximation by the reaction rate theories usually implemented for chemical reactions. Transition state theory predicts [110] that these rates follow an Arrhenius law [111]

$$\Gamma = v_0 exp\left(\frac{-E_a}{k_b T}\right) \tag{1.2}$$

Where E_a is the activation Energy, T the temperature, k_B the Boltzman constant and v_0 an temperature dependent pre-factor defined by $v_0 = \frac{(k_B T)}{h} e^{(\Delta S/k_b)}$. With the STM it became possible to visualize atoms and single molecules. By using a variable temperature STM, adsorbates can be tracked continuously at different temperatures. By the evaluation of many events and by analyzing their dynamics, one can determine the activation energy and the pre-factor of a given system.
In recent years a detailed insight into dynamics of adsorbates at variable temperature was accumulated ranging from single atoms and metal clusters to complex molecules on various surfaces. The diffusion of single molecules is a well explored dynamical surface process. Earlier studies focused on acetylene on Pd(111) [112] and Cu(001) [94], PVBA on Pd(110) [113], C60 on Pd(110) [114] and decacyclene on Cu(110) [115]. Advanced studies revealed the existence and importance of long distance jumps of decacyclene and hexatert-butyl decacyclene. Herein it was also demonstrated that the diffusion constant can be significantly increased by lifting

the molecules from the surface by substituents [116]. Molecular movement and its observation became also interesting while constructing "nanocars" and "turning wheels" [117–120].

1.5 Thesis Overview

The main topic of this thesis is the investigation and characterization of one and two dimensional organic and metal-organic networks utilizing pathways of supramolecular engineering. More specifically, we studied the adsorption of dicarbonitrile terphenyl (mNC-pPh$_3$-mCN and mNC-pPh$_3$-pCN) molecules on noble metal surfaces such as Ag(111) and Cu(111). Oligophenyls are an interesting class of molecules due to their physical properties. Functional carbonitrile (CN) groups substituted in different positions can influence the adsorption properties and self-assembly behavior of the molecule. Self-assembly processes on surfaces are not fully understood and we are far away to predetermine the resulting structures. Nevertheless CN especially in presence of transition metal atoms provides a toolbox for interesting and telling experiments.
Experiments presented in this thesis have been studied primarily by means of scanning tunneling microscopy (STM) in ultra high vacuum (UHV) conditions at variable temperature. Metal surfaces have been selected since STM experiments require a conducting substrate. The close-packed surface of Ag(111)and Cu(111) have a low atomic corrugation and a threefold symmetry, ideal to study the interaction of the adsorbates. Their different chemical reactivity provides a further parameter to influence the self-assembly particularly with regard to the influence of the mobile surface atoms on the resolved molecular pattern. Further insight into the chemical state and the adsorption geometry on the surface could be revealed by complementary X-ray absorption surface science techniques such as X-ray photoelectron spectroscopy (XPS) and near edge X-ray absorption fine structure (NEXAFS) spectroscopy.
Chapter 1, the introduction provides an insight to the topic and the motivation of the thesis. Fundamental principles of supramolecular engineering will also be explained and the group of oligophenyl molecules are introduced.
In chapter 2 all relevant experimental methods used in this project are described in combination with a brief theoretical description of their operation principle. In particular STM, XPS and NEXAFS spectroscopy are addressed.
Chapter 3 comprises details of the experiments and the experimental results conducted during the thesis. It is divided into five sections, whereby the first three sections are subject to the molecule mNC-pPh$_3$-mCN, presenting its adsorption on

the Ag(111) and Cu(111) surface at room and low temperature. Self-assembled 1D-ribbons and networks will be presented with the molecule adsorbed coplanar with its extended π-system in the molecular backbone to the sample surface. We will show that the molecular orientation can be influenced by the molecular coverage. Furthermore robust metal-organic 2D random networks with distinct nodal motifs will be presented providing design criteria for disordered 2D solids. In section four of chapter 3 we introduce the molecule mNC-pPh$_3$-pCN adsorbed on Ag(111) which is the link between the linear functionalized oligophenyls presented by U. Schlickum et. al in recent studies and the fully asymmetric functionalized oligophenyls presented in the beginning of this chapter. The change of one substituent position alters the arising supramolecular networks. We will further describe a hybrid molecular network of hydrogen-bond and metal-coordinated motifs as well as a fully reticulated metal-organic network. Additional experiments on functional prophyrins with pyridine endgroups will be presented in section five providing an insight into the dynamical behavior of the species on the Cu(111) surface.

Chapter 2

Experimental Methods

2.1 The Scanning Tunneling Microscope

A brief introduction into the theoretical background of the scanning tunneling microscopy (STM) is given to enable the reader to understand the principles of the STM image formation and its limitations.
The Scanning Tunneling Microscope from G. Binnig and H. Rohrer invented in 1981 [5] presents one of the most powerful tools in surface science and marked the beginning of scanning probe microscopy. Early tunneling experiments with solids related to the topic date back in the 1960s, where I. Giaever used a tunneling barrier to measure the energy gap in superconductors [121].Bardeen [122] outlined the theoretical concept to describe the tunneling process between two electrodes, from a many body point of view.
Figure 2.1 depicts the principle STM configuration. The central part is a piezo-tube scanning an atomically sharp tip, which in most cases is made of tungsten, platinum-iridium alloy or gold, over a conducting sample surface. While applying a bias voltage between tip and substrate, the atomically sharp tip is approached to the surface, until a tunneling current can be measured (approx. 1 nA at typically 5 to 20 Ådistance). The tunneling current exhibits an exponential dependence to the distance of the surface, which permits the resolution of atomic features.
There are two main ways to operate an STM. (1) In the constant-height mode the tip scans the sample surface with constant height and the electronic records the changes in the tunneling current. This mode offers the possibility to achieve fast scans, but bears the risk of tip crashes with the surface, especially on rough surfaces. (2) In the constant-current mode, the tunneling current I_t is compared to a given current by a feedback circuit. The feedback loop provides a correction voltage to the piezo-tube scanner to adjust the height of the tip with respect to the surface to

keep the current constant. The signal of the feedback-loop and the x-y position of the tip are recorded while scanning the surface.

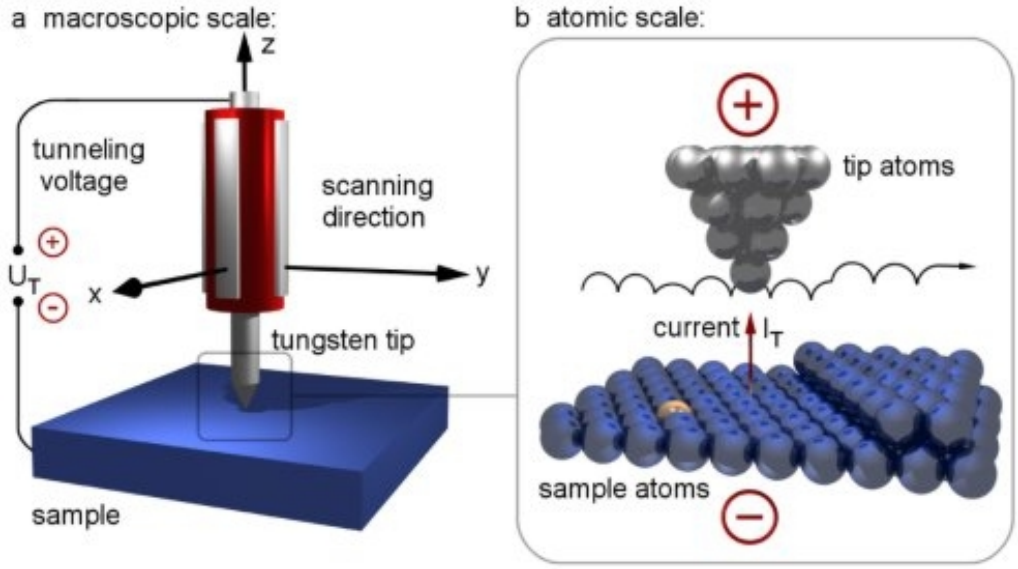

Figure 2.1: STM configuration based on a piezo-tube guiding an atomically sharp tungsten tip over the conducting sample surface. At a given distance it is possible to measure a tunneling current between tip and sample which represents a convolution of surface topography and local density of states. Graphic adapted from ref. [123].

The tunneling process from electrons through a potential barrier is a purely quantum mechanical effect. In classical physics an electron is not allowed to cross a potential barrier higher than its energy. However, in quantum mechanics, particles are described by wave functions, which can penetrate a potential barrier, where their spatial probability density $|\psi(x,t)|^2$ decays exponentially. If the potential barrier is sufficiently small there will be a finite probability for the electron to be found beyond the gap, as depicted in figure 2.2 instead of being reflected at the potential barrier. By applying a bias voltage V, the Fermi levels of the two electrodes are shifted in respect to each other and electrons from the occupied states of one electrode can tunnel into the unoccupied states of the second electrode. Hence, a tunneling current I_t can be detected. The probability of finding an electron beyond the potential barrier with a thickness d is subject to an exponential decay expressed in a simplified equation for the tunneling current I_t (under assumption $E < V$)

$$I_t \propto \exp^{-2\kappa d} \tag{2.1}$$

with

$$\kappa = \sqrt{\frac{2m(V-E)}{\hbar^2}} \tag{2.2}$$

where m is the mass of an electron, $\hbar$ is the reduced Plank constant ($\hbar = \frac{h}{2\pi}$), E is the energy of the electrons and V is the height of the potential in the barrier.

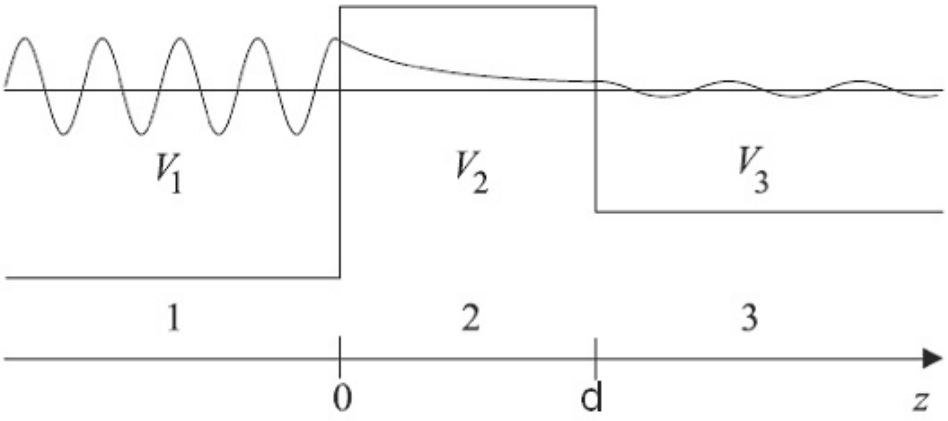

Figure 2.2: Sketch of the wave function describing tunneling through a 1D rectangular potential barrier of the width d, for the situation $E < V_2$ where V is the potential barrier height.

To yield sufficient tunneling events small distances between tip and surface are required. The exponential dependency of the tunneling current to the distance leads to an enormous sensitivity. By changing the tip-sample distance about one Å the current changes one order of magnitude. One of the challenges in STM was to achieve the necessary stability, to control the tip position on top of the sample with a residual Å resolution. This was achieved by employing piezo elements to control the movement of the tip and eliminating mechanical vibrations of STM components. By scanning the tip over the substrate in constant-current or constant-hight mode and recording the tunneling current, the topography of a surface can be imaged.

2.1.1 STM theory

Until present there is no exact theoretical treatment of the tunneling process in STM, and it is virtually impossible to achieve. The main reason is that the geometry of the tip apex is not known and is therefore hard to model. The exact shape of the tip changes not only from preparation to preparation, but typically during the scan as well.

Historically, there were several approaches to model the tunneling current between two electrodes measured in the 1960's. There are theoretical approximations to describe the origin of the tunneling current (I_t), which showed that I_t is proportional to the density of states and an exponentially dependent tunneling parameter. The exponential behavior given in equation (2.1) only uses one dimensional tunneling

and describes the potential barrier as a rectangular barrier. Due to the very small overlap of the wave functions Bardeen proposed a new perturbation theory approximation [122]. He explained the tunneling between two electrodes based on the approximation that the wave functions of the two electrodes do not interfere. He calculated the corresponding matrix element to

$$M_{tS} = \frac{\hbar^2}{2m} \int_S \left(\psi_S^* \vec{\nabla} \psi_t - \psi_t \vec{\nabla} \psi_S^* \right) d\vec{S} \tag{2.3}$$

where M_{tS} is determined by the overlap of the surface wave functions of the two subsystems at a separation surface S and ψ_t and ψ_S are the wave functions of tip and sample, respectively. At the STM, we have a similar situation, with a potential barrier and two electrodes, where one is the substrate and the other the atomically sharp tip. Utilizing the Bardeen matrix element, Tersoff and Hamann developed their STM theory [124, 125]. Up to the present this elementary theory is one of the most used descriptions due to its simplicity and straightforward interpretation of STM images it provides, which for most cases works as an adequate approximation. The current can be calculated from the matrix element (2.3). Given that all experiments are deducted at room temperature or slightly above, the Fermi-function can be replaced by a step function. This leads to the equation similar to first order perturbation theory:

$$I_t = \frac{2\pi e^2}{\hbar} V_j \sum_{t,S} |M_{t,S}|^2 \delta(E_t - E_F) \delta(E_S - E_F) \tag{2.4}$$

where V_j is the junction voltage applied to the sample and E_F the Fermi energy of the tip and sample, which in this approximation is assumed to be the same. The δ-functions show, that only elastic tunneling is taken into account. To describe the surface wave function Tersoff and Hamann extended Bardeen's model by using a two dimensional Bloch expansion

$$\psi_S \left(\vec{r_\parallel}, z \right) = \Omega_S^{-\frac{1}{2}} exp \left(i\vec{k_\parallel} \cdot \vec{r_\parallel} \right) \sum_{\vec{G}} a_{\vec{G}}(z) \exp \left(i\vec{G} \cdot \vec{r_\parallel} \right) \tag{2.5}$$

where $\vec{r_\parallel}$ is an in-plane oriented vector, $\vec{k_\parallel}$ the Bloch-wave vector, Ω_S the normalized volume of the sample, $\vec{G}$ the reciprocal surface lattice vector and $a_{\vec{G}}(z)$ the expression for the decaying wave reaching the potential barrier. The decaying wave can be described by solving the Schrödinger equation perpendicular to the surface, where ψ_S has to be a solution. Given that the z dependence of the surface wave function can be written as

$$\psi_S\left(\vec{r_\parallel}, z\right) = \Omega_S^{-\frac{1}{2}} \sum_{\vec{G}} a_{\vec{G}}(z) \exp\left(-\sqrt{\kappa^2 + |\vec{k}_{\vec{G}}|^2} z\right) \exp\left(i\vec{k}_{\vec{G}} \cdot \vec{r_\parallel}\right) \tag{2.6}$$

where κ is the same as in equation 2.2. and $\vec{k}_{\vec{G}} = \vec{k}_\parallel + \vec{G}$.
To build the tip wave function, one has to generate an adequate model, because the actual atomic structure of the tip is not defined. Tersoff and Hamann solved this problem via modeling the tip as locally spherical potential with the center at $\vec{r_0}$ and the radius R (see figure 2.4). The emerging tip wave function is assumed to be a s-wave

$$\psi_t\left(\vec{r}\right) = \Omega_t^{-\frac{1}{2}} C_t \kappa R \exp(\kappa R) \frac{\exp\left(-\kappa|\vec{r} - \vec{r_0}\right)}{\kappa|\vec{r} - \vec{r_0}|} \tag{2.7}$$

where Ω_t is the normalized volume of the tip apex and C_t a constant defined by $\psi_t = \Omega^{-\frac{1}{2}} C_t$. Due to the model of the tip and the subsequently following wave function, it is now possible to solve the matrix element, which leads to the expression

$$I_t = V_j \left[\Omega_t^{-1} \sum_t \delta(E_t - E_F)\right] \left[\sum_S |\psi_S\left(\vec{r_0}\right)|^2 \delta(E_S - E_F)\right] \times \frac{8\pi^3 e^2}{m^2} \exp(-2\kappa R)(C_t R)^2. \tag{2.8}$$

Here the first term in brackets accounts for the tip local density of states ρ_t (LDOS) [1] at the Fermi level, and the second expresses the LDOS of the sample surface ρ_S at the Fermi level relative to the center of the tip. According to this approximation a constant tip DOS leads to the conclusion that the overall conductance is dependent on the surface LDOS. If one assumes both densities of state as constant the expression simplifies to the same exponential term as in equation (2.1)

$$I_t \propto V_j \rho_t \rho_S \exp^{-2\kappa R} \tag{2.9}$$

.

This leads to the following model presented in figure 2.3. If a negative voltage is applied to the tip the electrons tunnel from the occupied tip states to the unoccupied sample states. The resultant current is the tunneling current I_t presented in equation (2.9) which decays exponentially with increasing tip sample distance d and is a function of the LDOS of the tip-surface system. Accordingly, surface LDOS changes

[1] The Density of states (DOS) is the sum over all states I with energy E
The local density of states (LDOS) is furthermore weighted by the square of the wave functions ψ_i ,yielding also a space dependence.

in the energy window below the bias voltage will be followed by the tip (in case of constant current).

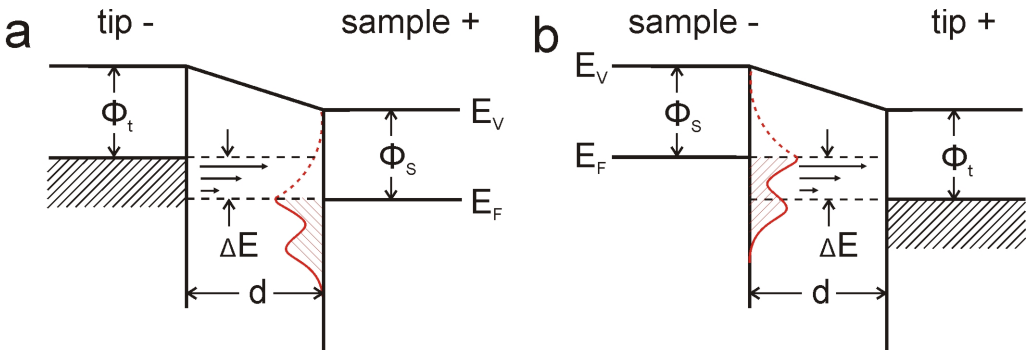

Figure 2.3: Energy diagram for the tunneling junction between tip and sample conventionalized as electrodes. The vertical axis depicts the energy and the horizontal axis the distance. **(a)** Shows the density of states of the tip and the sample, where a negative bias is applied to the tip. Accordingly the electrons in the junction with the width d tunnel from the occupied tip states into the unoccupied sample states. **(b)** The electrons tunnel from the occupied sample states into the unoccupied tip states. Φ_S and Φ_t are the work functions of the electrodes. The arrows indicate the voltage dependent tunneling probability.

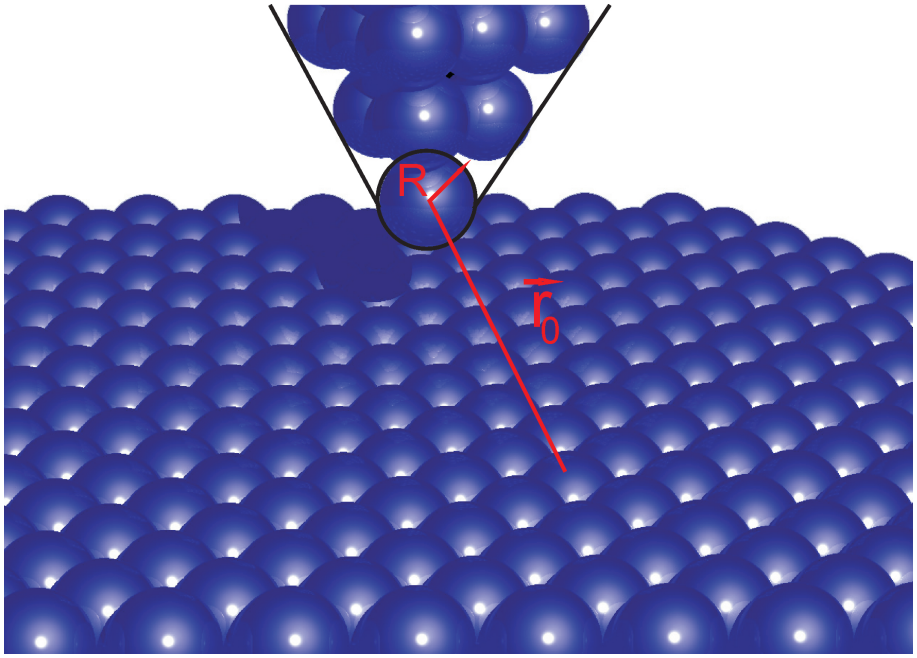

Figure 2.4: Model of the Tersoff Haman approximation, where R is the radius of the spherical potential representing the tip and $\vec{r}_0$ the position of the tip center.

The constant LDOS of the tip is a rough approximation especially since the size of the apex of the tip is subject to quantum mechanical effects due to a partially reduced dimensionality. One of the main issues with an s-wave approximation is that

a modulation of the LDOS at the atomic scale can not be explained, contradicting atomic resolution on close-packed metals found in experiment [126, 127]. Some advanced theories [128, 129] explain atomic resolution by introducing different tip models. Chen [128] modeled the tip with the d_{z^2} state, showing thereby the ability to resolve the LDOS on an atomic scale. The theory outlined above can not describe the oxides and adsorbates, due to the band gap of oxide layers or adsorbates the current equation loses its validity.

2.1.2 Imaging of Adsorbates

Constant current images contain a convolution of topography and the LDOS which can complicate their interpretation. Different adsorbates can produce different height signals, i.e. O on Pt(111) [130] or N on Fe(100) [131]. For example an adsorbed CO molecule can appear as protrusion or depression on the surface depending on the functionalisation of the tip [132]. It was also found that the adsorption position of a CO molecule on Pt(111) influences its appearance [133]. Before the first images of molecules on metal surface had been published it was not clear if it would be possible at all to probe and resolve molecules by STM. The tunneling current is an integral over the interval $[E_F,\ E_F + eV]$, where E_F is the Fermi-energy and eV applied bias voltage. Most organic molecules exhibit a wide gap between the highest occupied molecular orbital (HOMO) and the lowest unoccupied molecular orbital (LUMO). Adsorbed on the surface they can still be several eV away from the Fermi-level. However adsorbed molecules influence the LDOS because they interact with the continuum states of the conduction band even, if their states are far away from the given energy window [134, 135]. For weakly coupled molecules it can happen that the molecular states are barely broadened, hence if the molecules are far away from the tunneling interval the tunneling current is not affected by the molecules. For chemisorbed species Newns and Anderson describe in a model the emergence of a broad band with a contribution at the Fermi-level LDOS [136, 137]. The emergence of the molecular contrast was the first time explained by Lang, who proved the Tersoff-Harmann model valid for atomic adsorbates [138, 139]. The height contrast of adsorbates in STM can be explained when a small contribution of a broadened molecular orbital is in the energetic window given by the tunneling bias. The variation of the tunneling voltage can alter the appearance of the molecule in the STM image due to the changes of the integration area and accessibility of the molecular orbitals. For example in figure 2.5 a metal-organic self-assembled structure is displayed where the rod-like protrusions are molecules arranged star-like around a center metal atom. The left image is recorded at a bias voltage of 0.3 V and the right

image at 0.9 V. By increasing the voltage in the center of the circular structure a dot like protrusion becomes visible, which is a Co adatom. The change is reversible and not due to changes in the tip structure. Variations in the imaging of molecular states were also found elsewhere [140–143]. Adsorbates are imaged as protrusions or depressions depending on how they modify the LDOS. A general rule is that with increasing electronegativity or decreasing polarizibility of the adsorbate they tend to be imaged as depression [144, 145]. Strong influences on the appearance and imaging quality is governed by the tip itself. It is easily conceivable that a sharp apex generates a higher spatial resolution than a broad tip due to the exponential decay of the tunneling current. Besides the apex shape the tip stability is a serious issue. Not only parts of the tip can break off altering the apex and thus the appearance, but also atoms and molecules can adsorb on the tip and lead to instabilities in the tunneling current. Molecules transfered to the tip result often in unreproducible imaging conditions, but it has been reported that one can also increase the resolution with a modified tip apex. Tautz et. al. revealed a deeper insight into different phenylring based molecules by achieving intra-molecular resolution [146]. Additional molecular hydrogen was dosed to the coplanar adsorbed molecules and the resulting images suggested even chemical resolution.

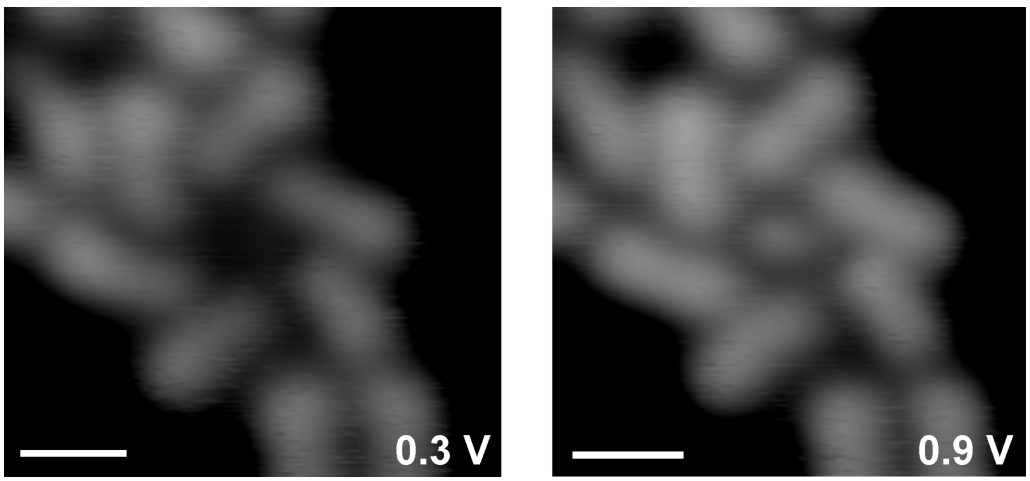

Figure 2.5: STM image of metal-organic pattern at different bias influencing the appearance of the appearing structure. The scale bar accounts for 1 nm.

2.1.3 Setup of the Aarhus STM

To understand not only the final structure of the assembly, but also the dynamics of adsorbates a stable, fast scanning STM that is working over a range of temperatures is required. The Aarhus 150 STM, designed by the scanning probe microscopy group at the University of Aarhus and commercialized by Specs™ was devised for these

applications. Its main advantage is its stability, which arises from the compact design and the small dimensions of the piezo-tube scanner. The STM's overall stability is crucial to keep the basic distance between the STM tip and the single crystal surface constant on the picometer scale. With this instrument it is possible to scan images of 200x200 Å^2 with a resolution of 512x512 pixels in less than a minute. The measurements can be achieved in a temperature range from 100 to 400 K, offering the possibility to influence the mobility of the molecules on the surface. To observe single molecules and molecular lattices, well-defined conditions are a prerequisite for the experiments. It is necessary to work in an ultra-high vacuum (UHV) chamber. The present chamber was custom designed by Dr. Alexander Weber-Bargioni in our group to accomplish the experiments in our field of interest. It includes a preparation chamber with the possibility to evaporate molecules with an organic molecular beam evaporator (OMBE) onto the sample surface and adding metal atoms using a metal beam evaporator (MBE). The vibration insulation of the chamber is achieved by using a passive air damping system by Newport™. Within the work in Prof. Barth's group the assembly of the whole instrumentation was completed, tested and calibrated.

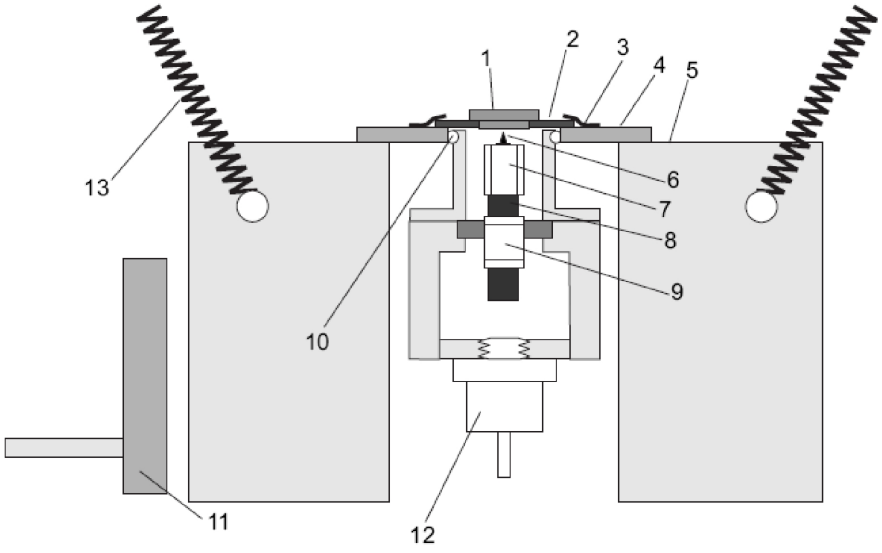

Figure 2.6: Cross-section overview of the Aarhus STM: Legend: **(1)** sample in sample holder; **(2)** sample holder; **(3)** leaf springs; **(4)** top plate **(5)** aluminum housing; **(6)** single crystal tungsten wire; **(7)** scanner piezo tube; **(8)** SiC rod; **(9)** inchworm piezo motor; **(10)** quartz balls; **(11)** cold finger; **(12)** Zener diode and **(13)** suspending springs [147].

Figure 2.6 shows a cross-section of the side view of the STM: The sample, a metal single crystal (1) is mounted on a custom made molybdenum sample-holder (2), which fits on the top plate and is clamped by two leaf springs (3) mounted on

the top plate (4). This part yield the steady position between the tip (6) and the sample. The tip made out of a tungsten wire has been sharpened by electrochemical etching. The interior STM design consists of the scanner piezo tube (7), partitioned into four quadrants oriented along the tube axis, which afford the x-, y- and z movement by applying an antisymmetric voltage. This scanner is attached to the top of a SiC rod (8) which fits precisely into the so-called inchworm motor (9). Quartz or zirconium-oxide spheres provide thermal and electrical insulation of the inner scanner-unit to the housing (5). For experiments below room temperature, the scanner part had to be decoupled from the housing (5) to ensure the proper working of the inchworm motor under varying temperature conditions. A Zener diode (12) keeps the scanning part at room temperature during low temperature experiments. To reach low temperatures the cold finger (11) is cooled with liquid nitrogen using a flow cryostat, cooling the aluminum housing (5) and therewith the sample.
The UHV chamber was designed to satisfy our experimental needs. It is divided into two parts, one for the preparation and one for the measurements, separated by a gate valve. This separation is useful to generate well defined conditions during the measurements in the STM-chamber as well as to keep the STM tip clean during the preparation of the sample in the neighboring chamber. The system operates at a base pressure of 2×10^{-10} mbar during the measurements. This enables atomically clean conditions required to resolve the interaction of specific atoms and molecules without contaminations.
Figure 2.7 depicts the chamber in blue and the main attached instruments in bronze. On the STM-chamber an ion-gun (12) is mounted in line above the STM (4) to clean the STM tip, especially after extensive scanning on samples decorated with molecules. Furthermore a load-lock is attached to transfer samples into the chamber without breaking the vacuum. In situ reactions with different gases are possible due to the leak-valve (10). The depot (9) in the preparation chamber (2), stores up to five sample holders and contains an electron beam heater to anneal the samples. The sample preparation procedure is explained in detail in the next section 2.1.4. To clean the sample a sputter ion-gun (12) is aligned with the center of the preparation chamber as well as an OMBE (5) and MBE (6). The OMBE and the MBE provide molecules and metal adatoms, respectively, in a high purity and controlled manner in oder to investigate submonolayer adsorbate coverages. Both evaporators can be withdrawn and separated by a gate valve from chamber to exchange the molecules or metals without breaking the vacuum. Furthermore an Auger electron spectrometer is mounted (11). To move the sample out of the depot into the preparation position and further into the STM three manipulators (14, 15, 16) are installed.

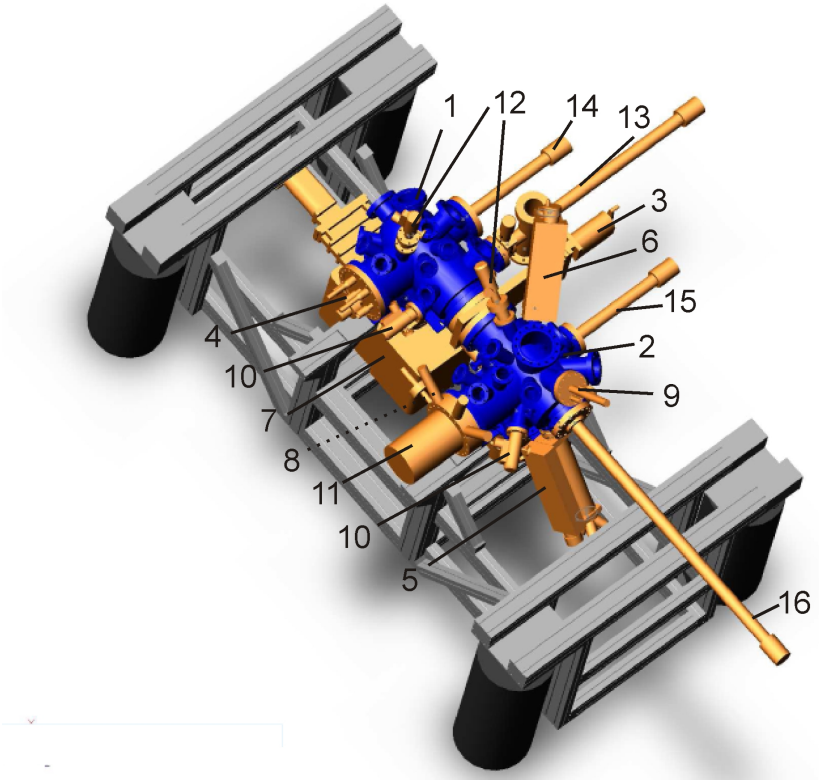

Figure 2.7: Schematic drawing of the STM-assembly consisting of the chamber with attached parts, the frame (grey) and the external damping system (black). Legend: **(1)** STM-chamber; **(2)** preparation-chamber; **(3)** middle gate valve; **(4)** Aarhus-STM; **(5)** organic molecule beam evaporator (OMBE); **(6)** metal beam evaporator (MBE); **(7)** Ion-getter pump; **(8)** turbo-molecular pump; **(9)** depot and electron beam heater; **(10)** leak-valve; **(11)** Auger electron spectrometer; **(12)** ion sputter gun; **(13)** load-lock; **(14)** short transfer arm STM-chamber; **(15)** short transfer arm preparation chamber; **(16)** long transfer arm.

An important factor to work in well defined conditions is the vacuum system, keeping the sample contamination as low as possible. Therefore different pump stages are engaged to establish a base pressure of 2×10^{-10} mbar. Figure 2.8 presents the model of the vacuum system for Aarhus STM. The green highlighted areas have a base pressure of 2×10^{-10} mbar pumped by a 300 l/s turbo-molecular pump in combination with an ion-getter pump, whereas the area inked in blue, the high vacuum area, works at a base pressure of 1×10^{-8} mbar provided by a 70 l/s turbo-molecular pump. The OMBE, the MBE and the load-lock can be connected to the UHV and HV part of the vacuum system in order to change the molecules, the metal source or the sample itself. For pumping the chamber after ventilation and as an exhaust a membrane pump is employed (highlighted in light grey). The preparation chamber as well as the measuring chamber and the evaporators are baked at about 100°C for 48 hours in order to desorb water after ventilation.

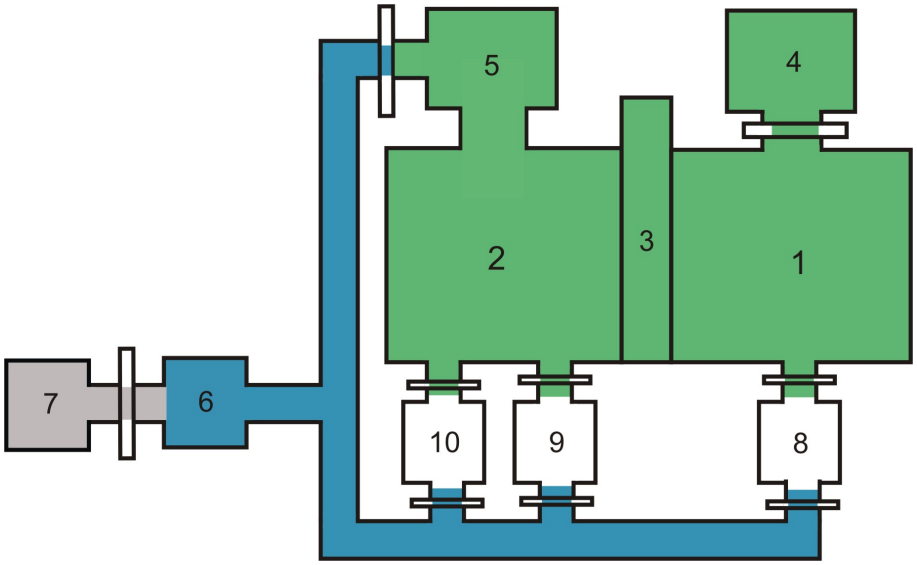

Figure 2.8: Schematic drawing of the vacuum system. Legend: **(1)** STM-chamber; **(2)** preparation-chamber; **(3)** middle gate-valve; **(4)** ion-getter pump; **(5)** turbo-molecular pump; **(6)** turbo-molecular pump - rough part; **(7)** double membrane pump; **(8)** load lock; **(9)** organic molecule beam evaporator (OMBE); **(10)** metal beam evaporator (MBE). The colors depict the different vacuum stages, where grey highlights a pressure of $\sim$ 1 mbar and blue $\sim 10^{-8}$ mbar, together they are the rough vacuum part. The green colored are has a base pressure of $\sim 10^{-10}$ mbar.

2.1.4 Preparation Procedures

The constitution of a smooth and clean sample surface is the basis for all our experiments where molecules are deposited on atomically flat surfaces. Therefore the single metal crystals are transferred into the UHV-chamber where the surface needs to be cleaned and smoothened to receive atomically flat terraces. Flat and clean surfaces are important for several reasons: First, to characterize the quality of a tip using e.g. the apparent sharpness of an imaged atomic step edge; second, to facilitate the scanning over the surface and preventing the tip to crash. This would lead to a change of the tip apex and therewith alter the imaging conditions; third and most importantly, to provide well defined environments for the molecules and atoms evaporated on the surface. For our experiments we employed Cu(111) and Ag(111) single crystals. Both samples provide a similar geometric structure, yet exhibiting a different chemical reactivity. Measurements on the bare crystals image their hexagonal surface structure and allow to see the atomic structure for calibrating the STM. In particular, the piezo constants were calibrated measuring the monoatomic step height and the lattice constants of the Cu(111) and Ag(111).
The preparation of these crystals is divided in two parts: First the sputtering, i.e. surface ablation by an argon ion (Ar^+) beam. In the second step the induced sur-

face roughness is reduced to atomically flat terraces by annealing. Both procedures are conducted with the sample inserted into the heating position of the parking lot. During the sputtering cycle several monolayers of the substrate are removed, leaving ideally only pure material on the sample surface. This is especially important to be carried out thoroughly when inserting a new sample into the UHV-chamber, to remove oxide layers and impurities.
Therefore argon gas is inserted into the chamber to a pressure of 2×10^{-5} mbar. The argon atoms are ionized in the ion sputter-gun and accelerated towards the sample with a potential of 0.8 kV. The intensity of the sputtering Ar^+ beam is measured via the Ar^+ current on the sample by placing a multimeter between the e-beam sample bias supply and the grounding of the whole chamber. The sputtering current used here was typically ~ 14 μA.
By heating the sample to the homologous temperature the sample surface is smoothened. The sample is heated to the desired temperature by an electron beam combined with a thermocouple mounted at the sample clamp. Depending on the sputtering time and therewith roughness of the surface, the annealing time has to be varied. A typical cleaning procedure of Cu(111) after the deposition of molecules is the following:

- Sputtering with 2×10^{-5} mbar argon pressure, an accelerating voltage of 0.8 kV and 20 mA sputtering current running at the ion gun for 30 min
- Annealing at 750 K for 20 min
- Sputtering with 2×10^{-5} mbar argon pressure and an accelerating voltage of 0.8 kV 15 min
- Annealing at 720 K for 10 min
- Sputtering with 2×10^{-5} mbar argon pressure and an accelerating voltage of 0.8 kV for 10 min
- Annealing at 670 K for 10 min

The annealing temperatures for the Ag(111) preparation were reduced to 700 to 650 K, respectively, due to the lower melting temperature compared to Cu(111). The annealing temperature for the second and third cleaning cycle was decreased to prevent the diffusion of impurities from the sample volume towards the surface. The surface diffusion at these slightly decreased temperatures is still sufficient to smoothen the surface. Subsequently molecules and metal adatoms have been evaporated after verifying a clean and smooth surface with the STM.

To evaporate molecules a Knudsen-cell is used, where the molecules are heated in a quartz crucible to provide a small vapor pressure in an isothermal enclosure. The deposition rate is very stable, determined by the temperature of the enclosure which is controlled using a thermocouple. The OMBE provided by Dodecon nanotechnology GmbH is able to store four crucibles. Each crucible is temperature independent due to separate heating filaments and the possibility of a flow-cooling. The evaporation temperatures and exposure times used for the several molecules are indicated in the related experiment.
The MBE was built in house and is equipped with a tungsten filament, which heats a metal wire, wrapped around the tungsten filament. For various experiments different metals can be inserted easily by changing the filament. To assure a well defined beam the filament is shielded. A small hole in the cover, facing the sample, provides a homogeneous beam of metal atoms. The evaporation flux has been determined by different STM measurements. The employed metal and evaporation time is determined in the related experiments.

In addition to a reproducible, high quality sample preparation, the tip shape and stability is critical to achieve high quality images. However, the tip forming process lacks control and reproducibility. In our case the tip consist of an electro-chemical etched tungsten wire. The etching is performed with a 2-molar aqueous sodium hydroxide (NaOH) solution, drawn in figure 2.9.

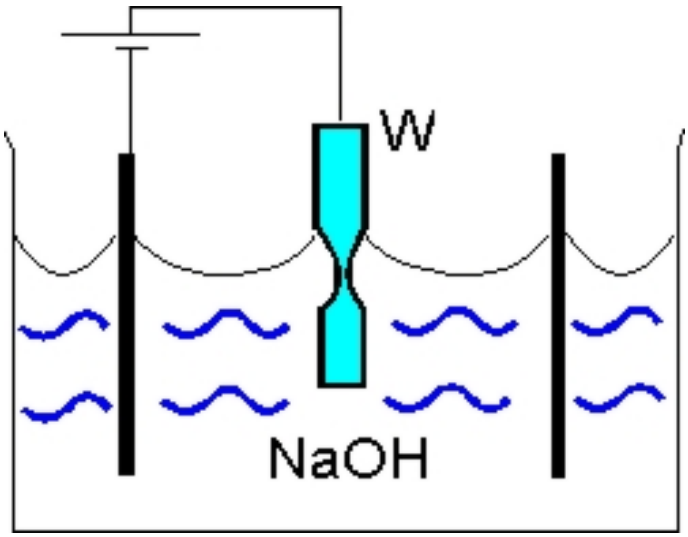

Figure 2.9: Schematic drawing of tungsten tip etching via NaOH-solvent and Al anode.

The anode is an aluminum bar and the cathode is the tungsten wire. On the interface of solution and gaseous phase the etching process is strongest, reducing the wire until it is separated, leaving a sharp tip [148]. Hydrofluoric acid is used to remove the leftover oxide. Due to the high reactivity of tungsten the oxide

layer forms again fairly quick, until the tip is transferred into the vacuum. In order to remove this residual oxide layer and to achieve more reproducible tunneling conditions, the tip has to be sputtered. Since the tip cannot be exchanged in situ in the Aarhus STM setup an ion sputter-gun is mounted over the scanner tube in line with the piezo element to sputter the tip on a regular basis, removing residues also remained from scanning. To prevent the sputtering of the scanner tube a cover plate with a 2 mm hole in its center is used which is placed instead of the sample. The tip is moved with the inchworm motor through the hole of the cover further into the ion-beam. The sputter current can be measured directly from the tip by measuring the tunnel current against the ground. Typically we sputter with a current of ~ 0.1 μA for $\sim$ 15 minutes. Depending on the thickness of the oxide-layer the sputter-time might be increased. Another effective way, apart from dipping the tip into the substrate, is the use of field emission between the tip and a conductive sample. Due to the high voltages required during the field-emission and the delicate thin wiring inside the STM, it is essential to set up this process very careful to prevent burning the STM wiring.

The field emission procedure is accomplished as follows: A conductive sample is placed in the measurement position and the tip is approached to the surface. Before applying the high field, the tip has to be retracted to about $\sim$ 100 nm. As already mentioned the wiring inside the STM is very fragile. A resistor (10 MΩ) is placed in series to the tunneling junction to protect the wiring, even if the tip contacts the sample, and a multimeter to monitor the applied current, as depicted in figure 2.10.

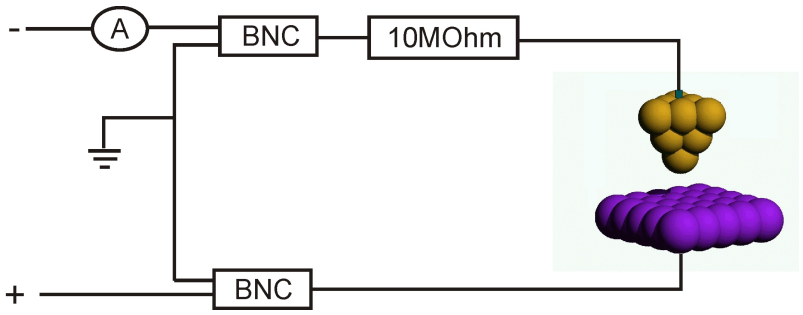

Figure 2.10: Circuit for the field emission

A negative potential is applied to the tip and a positive to the sample. The current between tip and sample can be measured, after the electrical field on the apex of the tip is high enough ($\sim$109 V/m) to emit electrons. Common parameters for the field emission are 500 V and 20 μA. As a result of the tip modification a change in the applied current is observable. When the current becomes stable, the tip apex can be assumed somewhat sharp and the field emission is complete. The

tip sharpening during this process is based on the assumption that the smaller the apex radius, the higher the electrical field and the easier it is to emit electrons. The high field increases the local current at the tip apex ripping off eventual residuals on the tip as well. Due to the material deposited from the tip onto the sample one should abstain from scanning over the sample surface used for emission.
This procedure is by no means a reproducible apex formation method, however it creates typically a sharp and stable tip with a reasonable resolution. It often can be still useful to dip the tip into the metal substrate to achieve with the pulled out material an atomically sharp tip and a cover with the sample material. Due to adhesive forces the sample material is pulled out of the sample and creates a cone, which can be mono-atomic in some cases. An analogy of this process is to pull of a spoon out of a honey jar. To cover the tip from all sides similarly with the substrate material, one can move the tip in a square across the surface. This incorporates the advantage that, the work-function of tip and substrate are similar. Due to the geometry difference of tip and substrate they will never be exactly the same.

2.1.5 Low Temperature STM

In order to immobilize the implemented adsorbates completely complementary experiments on a low temperature STM were performed at 6 K. The LT-STM [149] is also part of the Physics Department E20 at the TU-München. The LT-STM with its associated bath cryostat is implemented to a UHV chamber working at a base pressure of 1×10^{-10} mbar custom designed by A. Schiffrin and W. Auwärter to fulfill our needs and equipped with various tools for surface preparation. The LT-STM is a so called Besocke-type [150] designed at the ″Freie Universität Berlin″ by G. Meyer [149, 151] and commercially available by CreaTec [152].
Figure 2.11 gives a detailed overview on the LT-STM setup with the piezo unit in the center. It consist of four cylindrical piezos, three outer and one center piezo (see figure 2.11). The outer piezos ramp a copper plate with the center piezo in the middle. Sapphire half-spheres mounted on top of the outer piezos provide thermal and electrical insulation. The copper ramp is not flat but separated in three equivalent planes of 2 degrees gradient each. The outer piezos are in contact with one plane and rotate the copper ramp by moment of inertia drive resulting in a movement of the central piezo towards or away from the sample surface. The tip scanning the surface is made of a tungsten wire etched (see section 2.1.4) to provide a preferably sharp apex and can be scanned in three modes over the surface. First by lateral and vertical movement of the center piezo. Second by lateral and vertical movement of the outer three piezos and third by lateral scanning of the center tube

while the z-movement is assisted by the outer piezos. In the current experiments the first method was implemented. In measuring position the STM unit hangs from springs and vibrations are damped by an Eddy current magnet. The insulation against mechanical vibrations is essential for high resolution images and scanning tunneling spectroscopy (STS). The sample holder is placed beneath the outer piezos. The central unit is surrounded by a shield providing insulation of thermal radiation. To cool the system, the central unit and the inner shield are connected to a liquid N_2 shielded ^{4}He bath cryostat. A Zener diode provides the possibility to tune the sample temperature between 6 K and approx. 300 K. Experiments carried out with this system were accomplished all at 6 K. At 6 K the actuators perform a voltage to displacement ratio in the order of 10 Å per V, allowing for a pm accurate positioning of the tip. To follow the height variations on the surface the constant height mode was used resolving the topography of the sample surface as a 2D matrix.

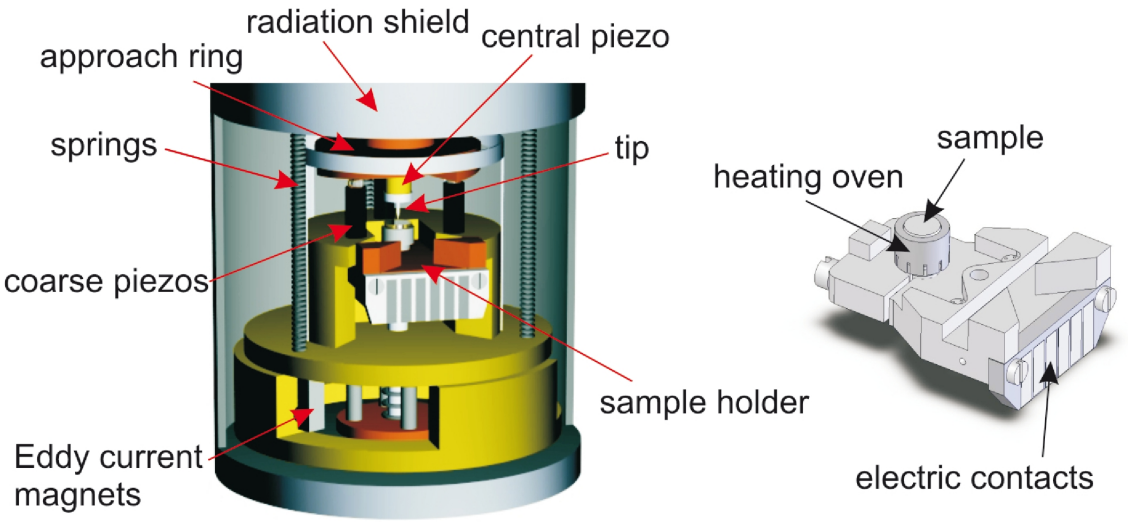

Figure 2.11: Model of LT-STM scanning unit and the corresponding sample holder. Reproduced from [151]

The UHV chamber is separated into a preparation chamber and a measuring chamber. The first is equipped with state of the art surface science technique tools for in-situ sample preparation and characterization, such as Ar^+ sputtering source, metal beam epitaxy (MBE) cell, organic molecule epitaxy (OMBE) source, quadrupole mass spectrometer (QMS) and several leak valves for controlled gas admission. To assure surface homogeneity and to achieve extended islands on the single crystal, the sample can be annealed up to 800 K by resistive heating. A further detailed description of the setup can be found elsewhere [151, 153].

2.2 Synchrotron Studies

The following part will provide an overview on the complementary experimental methods such as X-ray photoelectron spectroscopy (XPS) and near edge X-ray absorption fine structure (NEXAFS) spectroscopy. The according experiments have been performed at the synchrotron light source BESSY-II in Berlin at the HE-SGM beam line guided by Dr. Florian Klappenberger and in collaboration with Dr. Thomas Strunskus, Dr. Alexej Nevedov and Prof. Christof Wöll. The sample preparation and molecule evaporation was performed in the same way as in the STM UHV-chamber in order to maintain similar surface conditions. The samples for the NEXAFS spectroscopic measurements have been prepared under the same conditions as for the STM and XPS measurements.

2.2.1 X-ray Photoelectron Spectroscopy (XPS)

The STM is a powerful tool to provide an insight to the nanoscale and on topographic information. Also chemical information of small organic molecules on a conducting surface can be analyzed to some extent by studying the adsorbate vibrational mode utilizing scanning tunneling spectroscopy (STS). Most experiments of this thesis have been performed at room temperature where the mobility and the thermal vibrations of small adsorbates prohibit STS measurements. To perform chemical analysis of the adsorbed species over an integrated surface area XPS measurements have been performed. In our experiments we focused on the carbon 1s edge to resolve changes in the oxidation state of the phenyl rings. The nitrogen 1s edge from the carbonitrile group was the second area of interest to determine the changes in the oxidation state while interacting with the surface and metal adatoms. The XPS experiments were conducted at the synchrotron facility due to the high intensity and its monochromatic light providing a strong signal from the molecular pattern, which, to some extend is in the submonolayer range. In contrast to a lab X-ray source the photon energy is tunable with higher resolution.

The physical principle of the XPS technique is comparatively simple. The incoming photon knocks out a metal of an atom via the photoelectric effect explained by Einstein in 1905. The energy of the photon $h\nu$ is transferred to the atom and as long as the energy is higher than the work function of the material an electron with kinetic Energy E_{kin} can be emitted. Due to the low energy of the photons the penetration depth of the resulting photoelectrons is low resulting in a high surface sensitivity [110, 154]. The surface sensitivity can be increased by reducing the photon energy and varying the incident photon beam at grazing angle. However

the main reason for the high surface sensitivity is the short mean free path for an electron in a solid, which is in the order of nm. The ejected electrons are detected by an analyzer where the kinetic energy of the electron is measured. The kinetic energy of the detected electron is correlated to the binding energy in the atom by

$$E_{kin} = h\nu - E_b - \phi_S. \tag{2.10}$$

Where E_b stands for the binding energy and ϕ_S for the material's workfunction. The binding energy of the electron is the difference between the Fermi energy E_F and the energy of the emerging electron state and is specific for every element and shell position, hence providing the possibility for element specific analysis [155]. By analyzing the peak intensities in a recorded spectrum the stoichiometric ratio between the atomic species can be determined, since their cross-sections for photoionization is not correlated. The energy of the core electron provides also information about the local chemical environment, thus one can determine changes in oxidation- and protonation-state of a specific element. If for example a valence electron is removed from the atom the binding energy of the core level electrons increases leading to a so called chemical shift in the spectrum. For our experiments XPS will be employed to analyze the variation of self-assembled molecular layers. Especially metal surfaces can screen the positive molecular core which leads to a weaker bonded core electron. This effect is caused by Coulombic screening of the conduction band electrons. The closer the atom is located to the surface the stronger the resulting screening. The resulting shift is called Madelung shift. The chemical shift E_{chem} and Madelung shift E_{Mad} can be summarized in the equation for the effective binding energy

$$E_{bin}^{eff} = E_b + \Delta E_{chem} + \Delta E_{Mad} + \Delta E_r^{int} + \Delta E_r^{ext}. \tag{2.11}$$

E_r^{int} and E_r^{ext} account for relaxation effects related to the core and valence electrons. The measured flux of 1s photoelectrons can be convoluted with competitive processes like emission and radiative electron hole recombination which prevents a straightforward interpretation of the results. Emitted electrons may interact resulting in a low energy secondary electron. Furthermore electron hole relaxation can affect the photoelectron current. The application of a retardation potential in front of the electron analyzer can be beneficial to discriminate secondary electrons. Especially while analyzing the C 1s edge of aromatic systems at high molecular coverage inelastic events, so-called "shake up" processes may occur, as a result from inelastically excitation of valence electrons. Also the splitting of features due to spin

orbit coupling must be taken into consideration. Therefore careful and critical data treatment is essential.

2.2.2 Near Edge X-ray Absorption Fine Structure Spectroscopy (NEXAFS)

Informations governed by XPS are significant for the analysis of the chemical state of the adsorbate but rather uneligible to explore geometrical aspects of the molecular adsorption. NEXAFS spectroscopy alike XPS is a sensitive tool to probe the chemical environment of adsorbed species. In contrast to XPS where occupied molecular states are probed, NEXAFS spectroscopy analyzes unoccupied states. Additionally intramolecular properties as bond length and type and relative orientations of the different functional groups can be studied. Within this project we used the NEXAFS technique to explore the orientation of π orbitals.

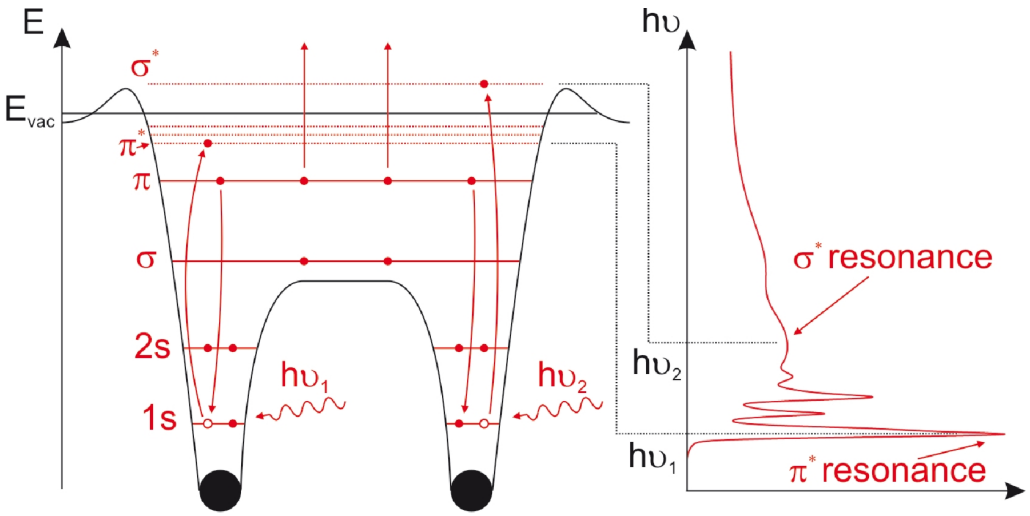

Figure 2.12: Model of the secondary Auger electron emission in a two-atomic molecule with different radiation energy $h\nu_1$ and $h\nu_2$ resulting in the characteristic NEXAFS spectra with π^* and σ^* resonances.

The fundamental principle of this technique is the absorption of a photon with the energy $h\nu$ by the molecular core level close to the absorption edge (within $\sim$ 30 eV) resulting in an excitation into unoccupied molecular orbitals. These processes are highly sensible to the orientation of the unoccupied molecular orbital with respect to the incident photon beam. The excitation for the core electrons of a diatomic molecule is depicted in figure 2.12. Upon absorption of an incident photon the 1s electron can be promoted to the unoccupied π^* orbital as long as $h\nu$ exceeds the energy of the π^* orbital and remains lower than the ionization potential ($IP = E_{vac} - E_{1s}$). To fill the remaining hole with an electron from a π orbital decays

while transferring its releases its excess energy to another electron in the valance band, which is emitted subsequently as secondary Auger electron. The decay energy can also be emitted by fluorescence. If $h\nu > E_{vac}$ the electron from the 1s state can be excited in the σ^* state, a virtual bound state with σ symmetry showing a broad resonance due to its short lifetime. By increasing the photon energy to $h\nu >> E_{vac}$ electrons would be directly photoemitted like in XPS.
In NEXAFS, the emitted secondary Auger electrons are detected since it is a measure for the number of absorbed photons. The energy of the photons is scanned and an absorption peak arises whenever a core electron can be excited into an unoccupied molecular orbital thus determining the fine structure of the molecule. A "fingerprint" of the molecule and the chemical environment is generated consequently.
To minimize the influence of artifacts from competitive processes, such as photoemitted and inelastically scattered electrons, a retardation potential is situated before the electron detector. The detected intensity $I(h\nu)$ is proportional to the probability of the core level electron in a ψ_i orbital to be excited into the unoccupied ψ_f orbital by photon absorption.

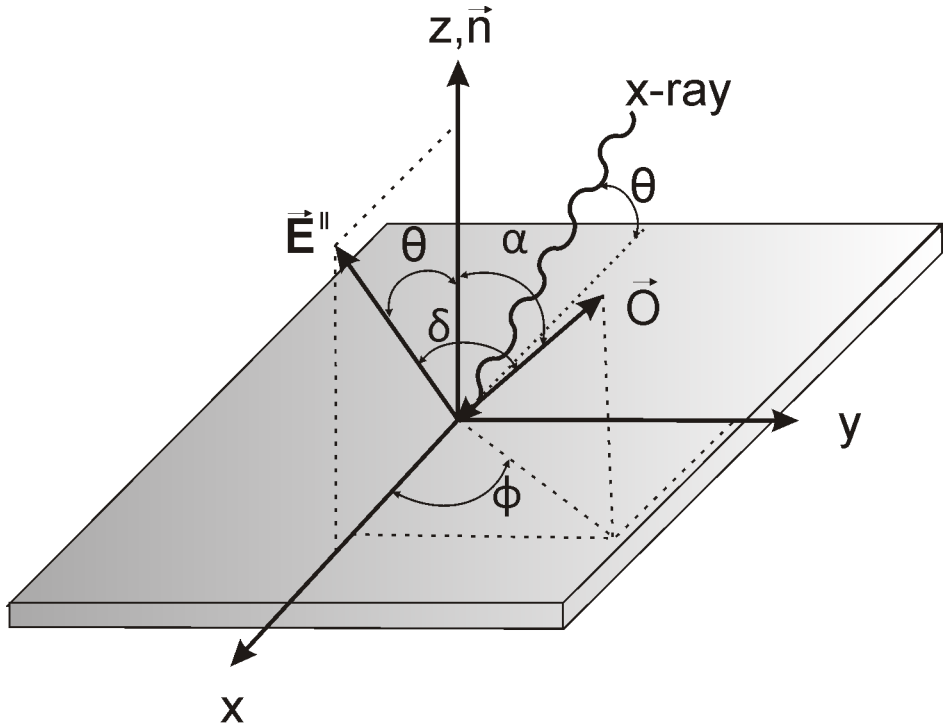

Figure 2.13: Coordination system defining the incident of the X-ray beam onto the molecular orbitals. The X-ray beam exhibits an angle θ with the surface plane and is polarized $\vec{E}$ in the x - z plane. The vector $\vec{O}$ defines the molecular orbital and is characterized by a polar angle α and an azimuthal angle ϕ. The drawing is adapted from [156].

Within the conducted experiments we focused on the C 1s and N 1s absorption

edge. The corresponding 1s orbital has a spherical symmetry. Therefore the resulting $I(h\nu)$ is subject to the overlap between the X-rays electric field vector $\vec{E}$ and the orientation of the unoccupied state ψ_f. Synchrotron radiation provides highly polarized light. The polarization angle of the incident photon beam is known and hence the intensity distribution of $I(h\nu)$ can provide information about the orientation of the molecule and its functional groups. The direction of the highest intensity for the 1s to π^* transition can be approximated by $I_\nu = cos^2\delta$. Where ν denotes the π^* vector final state and δ is the angle between the electric field vector $\vec{E}$ and the direction $\vec{O}$ of the final state molecular orbital. For a system similar to the one displayed in figure 2.13, where the incident photon beam is in x - z plane and z parallel to the surface normal, the resulting intensity can be written as

$$I_\nu = cos^2\alpha + sin^2\theta\ sin^2\alpha\ cos^2\alpha + 2sin\alpha\ cos\alpha\ sin\theta\ cos\theta\ cos\phi. \tag{2.12}$$

The incident photon beam exhibits an angle θ to the surface plane hence the k-vector of $\vec{E}$ has an angle θ to the surface normal. Further α is the polar angle and ϕ is the azimuthal angle of the π^* vector. The symmetry of the employed surface can simplify the equation (2.12) by eliminating the azimuthal dependence. The employed Ag(111) and Cu(111) surfaces exhibit a threefold symmetry with its high symmetry directions separated by 60°. For threefold or higher symmetry $cos^2\phi$ the azimuthal component averages to $\frac{1}{2}$ [156] and the equation (2.12) can be simplified to

$$I_\nu = cos^2\theta + cos^2\alpha + \frac{1}{2}sin^2\theta\ sin^2\alpha. \tag{2.13}$$

After identification of the resonances in the NEXAFS spectra one can vary the incident angle of the photon beam and gain information on the π^* orientation. Due to fluctuations of the recorded signal and the individual absorption characteristic of the X-ray optics the NEXAFS signal has to be normalized. The NEXAFS spectroscopic measurements presented within this thesis were recorded in partial yield mode (C 1s 150 eV; N 1s 250 eV). Simultaneously a characteristic peak from a carbon contaminated gold grid is registered as a reference. A constant background signal and the spectrum of a clean Ag(111) or Cu(111) crystal have been subtracted from all recorded spectra. Finally all intensities were normalized to an edge jump of 1 [157]. The resulting $I(h\nu)$ spectra for an energy $h\nu < IP$ can be assigned to $1s \rightarrow \pi^*$ transition and result in sharp peaks as visible in the NEXAFS spectra of figure 2.12. Detailed analysis and correlations between different incident angles can be performed by fitting the observed peaks with Voigt functions or Gaussians functions. Subsequently the resolved intensities for the different incident angles can be

compared with theoretical calculations of the intensity distribution to reconstruct the orientation of the according orbital on the substrate.

Chapter 3

Investigated Systems

In this chapter the experimental observations and data interpretation achieved during the thesis are presented. In part one we focus on self-assembled networks mediated by interaction with hydrogen and the molecular orientation on the Ag(111) surface. Subsequent evaporation of metal adatoms is evaluated in part two resulting in a random glassy network with distinct three- and fourfold bond motifs. The increase of the molecular coverage on Cu(111) drives a reorientation of the molecules from nearly planar to perpendicular. In part four of this chapter the hydrogen-bond and metal adatom mediated self-assembly process of a second functionalized oligophenyl have been investigated. Here the position of a functional carbonitrile moiety is changed resulting in an asymmetric molecule. Additionally we investigated the dynamic behavior of porphyrin molecules with pyridyl endgroups which will be addressed in part five.
Part one of this chapter corresponds to reference three in the publication list, part two corresponds to reference four and main elements of part five are published in reference seven.

3.1 Supramolecular Organization and Chiral Resolution of *p*-Terphenyl *m*-Dicarbonitrile on the Ag(111) Surface

The supramolecular organization and layer formation of the non-linear, pro chiral molecule $[1,1';4',1'']-$terphenyl$-3,3''$-dicarbonitrile (mNC$-pPh_3-m$ CN) adsorbed on the Ag(111) surface is investigated by scanning tunneling microscopy (STM) and near-edge X-ray absorption fine-structure spectroscopy (NEXAFS). Upon two-dimensional (2D) confinement the molecules are deconvoluted in three stereoisomers, that is, two mirror-symmetric *trans*- and one *cis*-species. STM measurements reveal large and regular islands following room temperature deposition, whereby NEXAFS confirms a flat adsorption geometry with the electronic π-system parallel to the surface plane. The ordering within the expressed supramolecular arrays reflects a substrate templating effect, steric constraints and the operation of weak lateral interactions mainly originating from the carbonitrile (CN) endgroups. High-resolution data at room temperature reveal enantiormorphic characteristics of the molecular packing schemes in different domains of the arrays, indicative of chiral resolution during the 2D molecular self-assembly process. At submonolayer coverage supramolecular islands coexist with a disordered fluid phase of highly mobile molecules. Following thermal quenching (down to 6 K) we find extended supramolecular ribbons stabilized again by attractive and directional non-covalent interactions, the formation of which reflects a chiral resolution of *trans*-species.

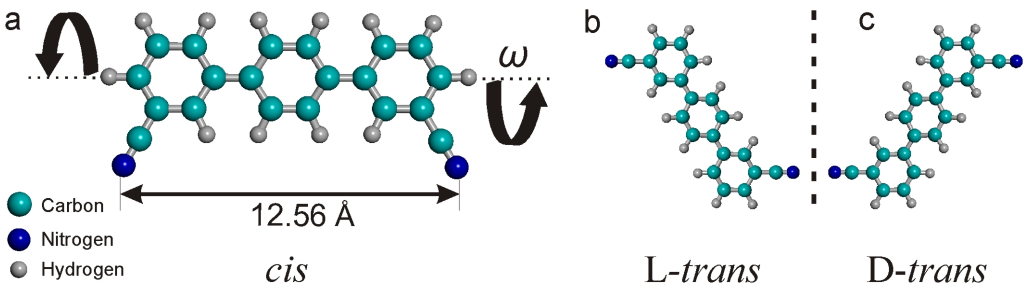

Figure 3.1: Molecular model of the $[1,1';4',1'']$ – *terphenyl* – $3,3''$-dicarbonitrile (mNC$-pPh_3-m$CN). On the left the *cis* conformation with the rotation angle ω is presented. By rotating the phenyl ring about this angle two mirror-symmetric entities emerge upon surface confinement, pictured on the right (L- and D-*trans*).

3.1.1 Introduction

The control of supramolecular self-assembly at interfaces is a promising avenue for the design of low-dimensional nanoscale architectures [3, 4, 158, 159]. A variety of synthesis protocols, using electrostatic interactions [160–162], hydrogen bonding [44,163–168] or metal-ligand interactions [51,95,169–171] have been explored. In two dimensions, the bonding capabilities of two interacting CN groups were successfully employed to steer the self-assembly of substituted porphyrins on Au(111) [20]. Depending on the position of the CN substituents, triangular clusters, tetramers, and supramolecular wires evolve. In different work, the CN group controlled structure formation by interaction with alkoxy groups [172].

Recently, we employed linear ditopic dicarbonitrile-polyphenyl molecular building blocks and studied their self-assembly on the Ag(111) surface [46,47]. Topologically different supramolecular structures evolve depending on the backbone length. In particular, selecting species containing three to six phenyl groups led to the formation of close-packed layers or different chiral open networks including a Kagomé network. All investigated networks turned out to be commensurate with the underlying atomic lattice. Furthermore dicarbonitrile linkers were successfully employed for metal-directed assembly of 2D coordination networks on Ag(111). Hereby we encountered striking differences depending on the symmetry of the linker. When linear species were employed, with the CN moiety at *para* positions, highly regular open nanomeshes with tunable pore sizes were fabricated [52, 89]. The pertaining convergent assembly is in direct contrast to the divergent scenarios leading to random coordination networks when using a linker with CN moieties at *meta* positions [173]. Herein, we focus on the 2D supramolecular assembly of this linker itself. It is depicted in Scheme 3.1 and consists of three phenyl rings connected via C−C σ-bonds, with two CN groups in the *meta*-position on the outer side of the terminating phenyl rings. The angle ω describes the molecule backbone rotation around the σ-bond between the phenyl rings. In the crystal structure for *para*-terphenyl the central phenyl ring is tilted about $\pm$ 27° with respect to both outer phenyl rings, which are parallel [83].

On noble metal surfaces, such as Ag(111), extended π-systems are well known to preferentially adsorb parallel to the substrate. The CN groups tends to a metal complexation and acts as an anchoring point for the molecule, enhancing the stability on the sample at ambient temperatures [83]. 2D confinement in a flat geometry furthermore implies the deconvolution in three stereoisomers. Thus, upon 2D confinement the molecule isomerizes into a *cis* and two *trans* enantiomers due to the symmetry breaking effect of the surface and a special 2D chirality scenario is

encountered that has not been described so far [174–181]. The natural composition of the pertaining two-dimensional gas can be assumed to be 50% *cis* and 25 % for each mirror-symmetric *trans* onformation [173, 182]. Our results indicate that the 2D layer formation of these molecules reflects a chiral resolution of these surface enantiomers. Moreover, we investigated the thermal quenching of a fluid phase consisting of highly mobile molecules that coexists with compact islands at 300 K. It notably condensates into extended supramolecular ribbons, representing enantiopure assemblies from the *trans*-species.

Experimental Methods & **Materials**

The STM experiments were performed on a Ag(111) single crystal in ultrahigh vacuum providing well-defined conditions. Before running the experiments, the sample was cleaned thoroughly by repeated Ar^+ sputtering cycles with an energy of 1.0 keV and a typical sputter current of 10 μA for 15 min. The sputtering was followed by annealing at 770 K for 10 min. Subsequently the molecules have been deposited by organic molecular beam epitaxy (OMBE) from a quartz crucible held at 500 K after prudent degassing, while the sample was kept at room temperature. The pressure during evaporation never exceeded 1×10^{-9} mbar. The molecular flow was about 0.14 ML min^{-1}, as derived from the STM measurements to be. The cooling rate for the low-temperature experiments was approximately 1 Ks^{-1} in the decisive temperature interval 300-100 K.
The synthesis of the rod-like *m*NC-*p*Ph$_3$-*m*CN molecule was developed according the published procedure by coupling of bis(iodobenzene) and two equivalents of 3-phenylboronic acid under typical Suzuki conditions with 10 mol % Pd(0) [183]. The geometry of the free molecule was calculated in the semi-empirical AM1 framework. Room-temperature STM measurements were performed in a custom-designed ultra-high vacuum apparatus equipped with a commercially available Aarhus 150 variable temperature STM (cf. www.specs.de) and standard tools for in situ sample preparation (see section 2.1.4). All measurements were carried out at a base pressure below 5×10^{-10} mbar. STM topographic images were obtained with an electrochemically etched tungsten tip and bias voltages between -1.5 and $+1.5$ V applied to the sample. Data were recorded in constant-current imaging mode. Low-temperature STM measurements were performed with a Besocke-type low-temperature (LT) STM from Createc (cf. www.createc.de and [149]) at ca. 6 K, housed in a custom-designed ultra-high vacuum chamber with a base pressure lower than 2×10^{-10} mbar [184]. Similar scanning parameters, as in the Aarhus STM, have been applied. All presented STM topographic images were processed with the

WSXM SPM program [185]. The images presented in figures 3.2 *a*, 3.3 *b* and 3.4 were measured with the Aarhus-type STM. Figures 3.3 *a*, 3.5 and 3.7 comprise micrographs recorded with the LT-STM.
The near-edge X-ray absorption fine-structure (NEXAFS) spectroscopy measurements were carried out at the HE-SGM beam line located at BESSY II in Berlin providing highly monochromatic light with a linear polarization of 82 %. Molecules were deposited at room temperature after verifying surface cleanness by repeated NEXAFS spectra recorded at the C1s and N1s K edge. To minimize X-ray mediated damage to the molecules the sample was cooled down to 110 K for the measurement [186].

3.1.2 Results & Discussion

Following deposition with the substrate at room temperature, the molecules self-assemble in well-ordered layer structures. A section of a close-packed island build by the dicarbonitrile linker units is shown in figure 3.2 *a*. The individual molecules are resolved as rod-like protrusions, that is, the imaging is dominated by the carbon backbone. The brick-like pattern formed shows a high regularity. The islands extend over large areas without defects or an apparent moiré pattern. Even the step edges are covered without formation mismatch. This strongly suggests a commensurate structure, similar to the networks obtained with *para*-polyphenyl-*para*-dicarbonitrile (*p*NC-*p*Ph$_x$-*p*NC)linear analogs [46, 47, 52, 89]. However, the superstructure formed with the present *para*-terphenyl-*meta*-dicarbonitrile (*m*NC-*p*Ph$_3$-*m*NC) clearly contrasts that of the *p*NC-*p*Ph$_x$-*p*NC [46, 47], which fact directly evidences the decisive role of the functional CN endgroups in the pertaining arrangements.
High-resolution STM images and careful data analysis enable us to propose a structural model of the molecular adsorption shown in figure 3.2 *b*, despite the fact that generally the placement of the CN groups can not be unambiguously assigned by STM. The displayed unit cell has a rhombic shape with a edge length of 15.3(± 0.5) Å and 9.3(± 0.5) Å, respectively, and an implicit angle of 48°. The island structure of the molecules forms a highly regular pattern determined by the vectors $\vec{a}$ and $\vec{b}$ and the embedded unit cell. The molecular backbone is not perfectly aligned with $\vec{a}$, but tilted slightly clockwise by about 5°, most probably due to the steric repulsion of the hydrogens in the meta position and the molecular asymmetry. By contrast, for linear *p*NC-*p*Ph$_x$-*p*NC molecules with x = 3, 4, 5, and 6 on the same substrate orientations along high-symmetry substrate directions prevail [46, 47, 52, 89]. With respect to the ⟨-110⟩ high-symmetry directions of the underlying substrate the molecular main axis is rotated by 15° counter-clockwise.

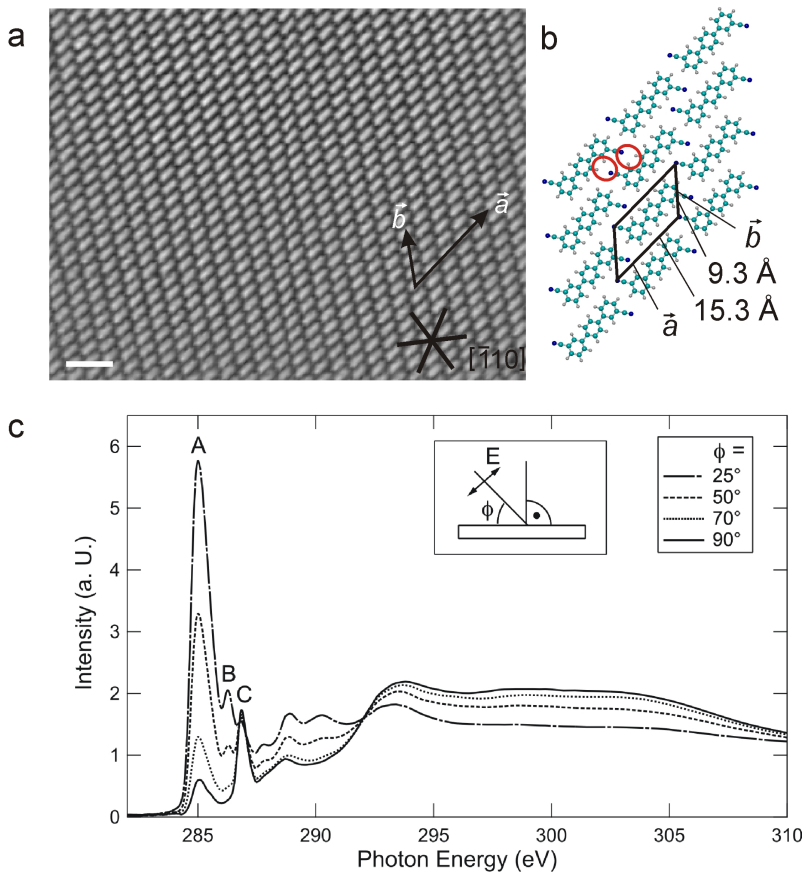

Figure 3.2: STM overview of a molecular island with a molecular model and X-ray absorption data. **a)** Overview on a dense packed highly ordered molecular island on the Ag(111) substrate. The atomistic model in **(b)** gives an insight into the bonding scheme. **c)** NEXAFS measurements on the C1s edge demonstrate a strong dichroism indicating a well-ordered monolayer. The angle dependence of the intensities of the different peaks reveal a flat laying π-system (peak A) and CN groups parallel to the substrate (peaks B and C).

The molecules in the island layer are assumed to occur in the *trans* conformation. They interact with the next neighbor via the CN group developing two non-covalent bonds with next-neighbor phenyl moieties, marked with the grey ellipses in figure 3.2 *b*. The $N\cdots$H distances are about 2.3 Å. Similar binding properties and distance have been reported for CN-terminated adsorbed porphyrins and were supported by ab initio calculations [187], as well as for adsorbed pNC-pPh$_x$-pNC species [46,47,52,89]. Due to the high electronegativity of the nitrogen, even a dipolar character of the bond is conceivable, [188] similar to related compounds in the gas [189] and crystalline phases [190]. This considerations clearly favors the proposed arrangement of *trans* species, where the orientation of adjacent CN-groups is anti-parallel. By contrast with the *cis* species, an energetically unfavorable proximity of nitrogen atoms bearing an electron lone pair and a parallel orientation of adjacent CN-groups would

exist.

In order to test our assumption of the geometry of the adsorbed molecules we performed NEXAFS measurements at the C1s edge, displayed in figure 3.2 *c*. In general, the spectra are similar to benzene spectra with a series of sharp peaks in the π^* region and one peak in the σ^* (294 eV) region [20]. The angle-dependent series exhibits a pronounced dichroism in the whole energy range evidencing a highly ordered adlayer with all molecules in a very similar conformation. From the comparison with the benzene spectra [191], it becomes clear that peak A (at 285 eV) originates from the lowest phenyl-ring-related π^* resonance and thus comprises information about the average orientation of the phenyl backbone. Furthermore, we attribute the additional peaks B (286.3 eV) and C (286.9 eV), which are not present for benzene, to the two perpendicular π orbitals of the CN triple bond. Resonance B is shifted to lower energy with respect to resonance C due to the interaction with the phenyl π system [192]. Together the two features allow one to determine the orientation of the CN group independently from the phenyl signals. The decreasing intensity at elevated angle ϕ (the angle between the E-vector of the synchrotron radiation and the surface normal) of peaks A and B as well as the increasing intensity of peak C clearly indicate that the molecules are adsorbed flat on the surface. In more detail, the deviation from the perfect planar conformation assumed in Scheme 3.1 can be described by a rotation around the σ-bonds of the long molecular axis by approximately 20°, which is a reasonable value for *para*-polyphenyl molecules [193].

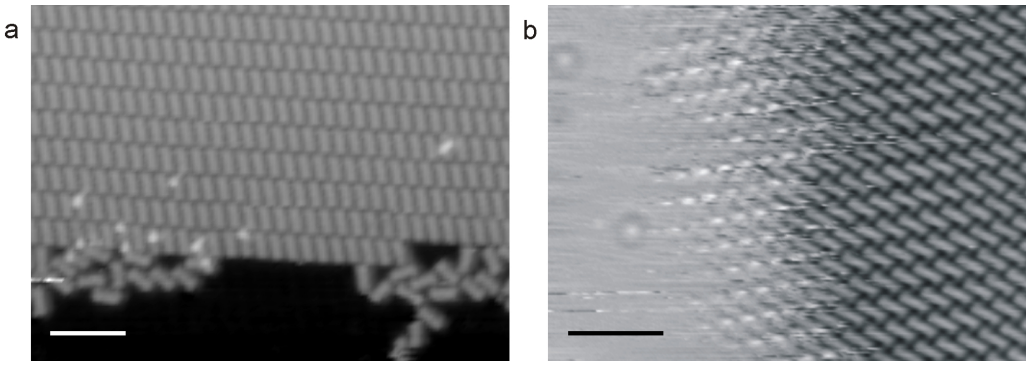

Figure 3.3: STM images of the island border structure at different temperatures. **a)** On Ag(111) after room-temperature-assembly and cool-down to 6 K the edge-mobility is frozen and the edge decoration evidences the condensation of mobile species. **b)** On Cu(111) at 300 K fluctuating edges indicate appreciable mobility of linkers and coexistence with a 2D fluid in open areas. Scale bars 4 nm.

At room temperature, isolated molecules on the Ag(111) surface exhibit a high diffusivity, expressed in a molecular surface fluid at submonolayer coverages. Ac-

cordingly, the island boarders are in a dynamic equilibrium with the fluid phase in open terraces, whereas the interior section of the island remains stable. This is shown for both the Ag(111) and Cu(111) surfaces in figure 3.3, where on the one hand the fluctuation of an island border at 300 K is clearly discernible, and on the other hand the irregular decoration of island edges with molecules from the fluid following substrate cooling. With the Cu(111) surface, the island patches are smaller than on Ag(111) and even single molecules on steps and defects can be observed. For Ag(111) submonolayer preparations measured at room temperature the mobility zone at the island edges is very extended (10 nm range), which fact is attributed to the weaker surface interactions compared to a copper substrate.

A detailed view into the packing schemes of molecular assemblies in different domains and several preparations reveals the occurrence of six orientations of the molecular brick-like structure, shown in figure 3.4. Due to the threefold symmetry of the substrate and the two molecular *trans*-conformations six island formations are expected. We propose that all structure formation is based on the balance between surface epitaxial fit and non-covalent lateral interactions (compare the atomistic model proposed in figure 3.2 *b*. Furthermore the 2D chirality of the molecules needs to be considered, which allows for several bonding motifs because of the different positioning of the reactive CN endgroups. In the upper part of figure 3.4 the L-*trans* phases are depicted. The mirrored D-*trans* islands are each depicted underneath. Every column includes the particular mirror symmetric formation, whereby the mirror axis is given each with one of the crystal high symmetry directions [180]. L-*trans* molecules, exhibiting a clockwise tilt for the molecules and the unit cell, respectively, with respect to the high symmetry direction indicated by an arrow; whereas D-*trans* molecules feature a counter-clockwise tilting. Each island consists of only one conformation and thus represents an enantiomorphic entity due to a 2D chiral resolution.

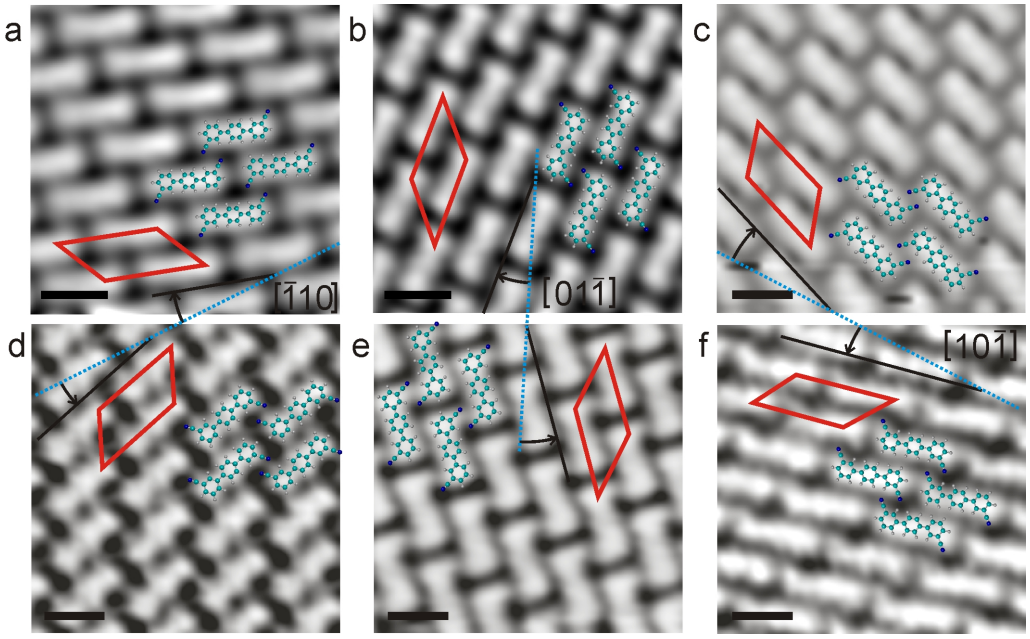

Figure 3.4: High-resolution STM images of molecular islands at room temperature. Due to the surface threefold symmetry and L- and D-*trans* (upper and lower column, respectively) molecular conformation, six-island orientation can be expected. Following the model in figure 3.1, **a-c)** are composed of L-*trans* molecules, whereas images **(d)** - **(e)** consist of D-*trans* molecules. Scale bars 1 nm.

It should be noted that both intermolecular and molecule-substrate interactions are crucial for the successful self-assembly of the reported structures: The CN determined packing scheme points to considerable attractive intermolecular forces, while the six orientations of the molecular domains relative to the substrate together with the commensurate island structure (as inferred from the dimensions of the unit cell and a lacking moiré pattern) indicate non-negligible molecule- substrate interactions. Most of the structures investigated displayed a packing scheme that can be explained with these ordering principles implying exclusively the two *trans*-species. However, islands exist with different packing schemes, such as the one in figure 3.3 for the Ag(111) surface, that can be better explained with the chaining of *cis*-conformers. Unfortunately the large extension of the islands prevented from a statistical analysis regarding the equal distribution of all island structures and surface stereoisomers. The influence of the substrate is also obvious when the low coverage system is thermally quenched to low temperatures (6 K), where entities from the molecular fluid deduced above condense notably into molecular ribbons. Because these assemblies are not perfectly ordered they represent metastable configurations due to kinetic limitations in the 2D aggregation processes. The formed ribbons are oriented along the three high symmetry orientations of the substrate (marked with the black star in the lower right corner in figure 3.5 *a*). They can extend up to more than 100 nm,

whereby for each direction two different chiralities are observed. In the shown STM image a mirror-symmetry axis (white line) demonstrates the two opposite molecular conformations of D-*trans* and L-*trans*. Thus altogether six dominating structural orientations are visible. Besides this, defect structures are observed in rare cases, which are interpreted as interconnections between the stable 1D ribbons. They are significantly shorter and may be an indication for the flexibility of entire chain segments.

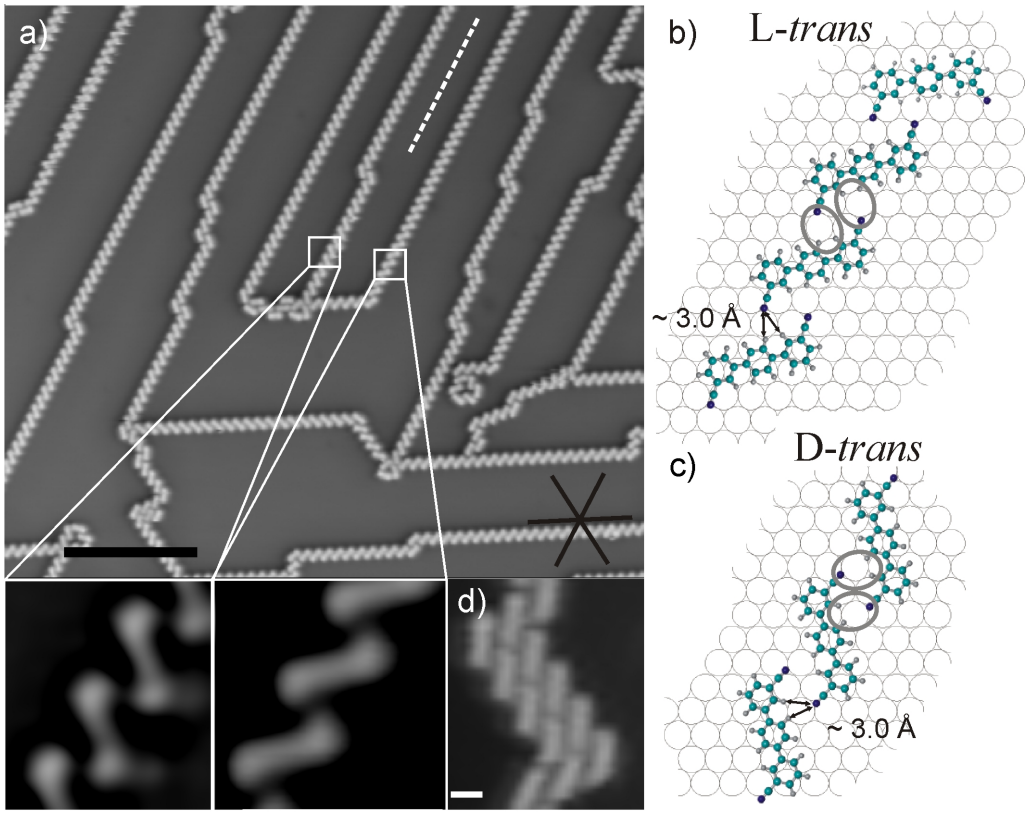

Figure 3.5: Set of STM images and atomistic structure model: **a)** high-resolution image of linker molecules assembled in a linear structure imaged at 6 K on Ag(111) with a coverage of 0.1 ML. A mirror axis (white line) helps to visualize the chirality of the assembled ribbons. The high symmetry orientations of the substrate are marked in the bottom right corner. Scale bar: 14 nm. **b-c)** Structural model of the linear phase with interatomic distances. **d)** Island patches evolve with increasing molecular coverage. Scale bar: 1 nm.

High-resolution images have been recorded to clarify the bonding scheme in the linear structure. The periodicity of the ribbon is 11.5 (± 0.5) Å, that is, similar to the one in the island formation. The data allow us to propose an atomistic model of L-*trans* conformation lines featuring planar molecules like in the island structure that is displayed in figure 3.5 *b*. The CN groups point towards phenyl hydrogens of the neighbouring molecule. The pertaining $N\cdots H$ distance is slightly above 3 Å,

which is consistent with a recent analysis of nanoporous network structures consisting of sexiphenyl with two CN groups in the *meta* position [52, 89]. The atomistic model features the position of the nitrogen in the hollow site of the substrate achieving commensurate assembly consistent with the measured molecular orientation and distances. Our model is in agreement for D- and L-*trans* conformation, whereas the molecular backbone of the L-*trans* is tilted clockwise by ca. 12° from the propagation direction of the 1D ribbon and the D-*trans* counter-clockwise, respectively. Only rarely are *cis* species incorporated in the ribbon structures. Their presence in characteristic defects where lateral shifts occur is modeled in figure 3.5 *b*.

Thus the condensation of the molecular fluid upon thermal quenching and the pertaining 2D self-assembly is a chiroselective process. In the fluid phase, where the density is low and molecules are rarely in contact with each other, it must be assumed that a thermal equilibrium distribution with equal proportion of *cis* and *trans* species prevails [173]. However, during the condensation the intermolecular interactions might render the *trans* conformation more favorable. Note that the expression of the ribbons points to a limited mass transport in the assembly. It implies on the one hand a chiral resolution of the two different *trans* species. Hereby the coexistence of mirror-symmetric ribbons from both *trans* species in large terraces excludes a self-replication process in their formation, which contrasts findings with related systems [194]. On the other hand, the minor proportion of *cis* species that could be identified can be understood as a hint that during the self-assembly a dynamic chiral switching process is possible, that is, the rotation of a cyanophenyl moiety about the molecular axis occurs driving a *cis*-*trans* transformation. This is in agreement with previous observations of complex adsorbed organic molecules where chiral switching could be correlated with spontaneous conformational changes [181]. Furthermore on close-packed noble metal surfaces the interaction between phenyl rings and the substrate is relatively weak, such that reorientations of rotatable phenyl moieties are possible [195]. Note that a lift from the surface in cluster formation was already demonstrated in ab initio calculations for adsorbed benzonitrile [187].

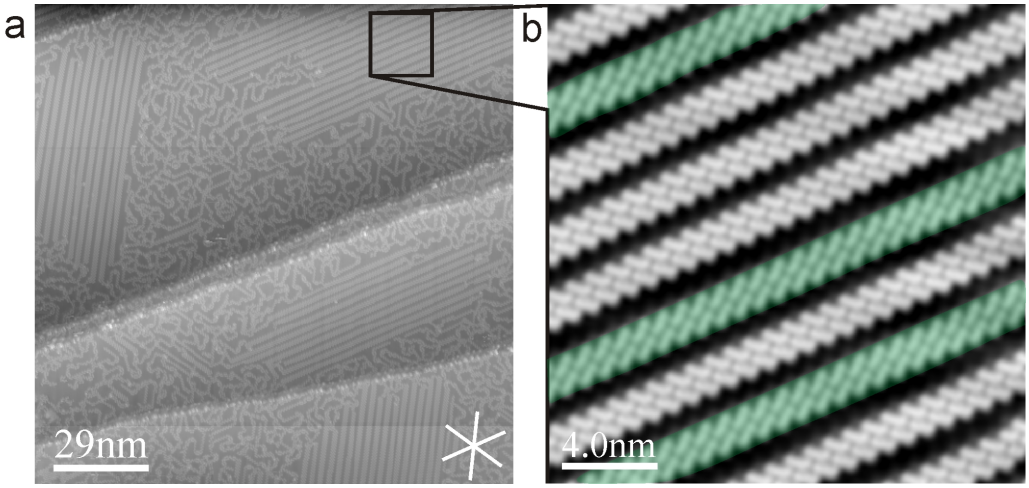

Figure 3.6: Molecular network with increased coverage (0.6 ML) on Ag(111). **(a)** Overview on several terraces covered with ordered and disordered areas of molecular islands. The white cross marks the substrate orientation (UT = -1 V, IT = 0.14nA, 6 K). **(b)** High resolution STM image of the ordered molecular pattern reveals 1 dimensional racemic molecular rows. The green superimposed areas are assembled by D-*trans* enantiomers (UT = -1 V, IT = 0.094 nA, 6 K).

In figure 3.5 *a* the coverage is about 0.1 ML. By increasing the coverage at first small islands can be found, which seem to evolve from two adjoining ribbons. In figure 3.5 *d* the transition from a one-dimensional to a two-dimensional structure is depicted. The islands can extend over large areas to stacked molecular chains by increasing the molecular coverage. Figure 3.6 *a* shows an overview on several terraces with a molecular coverage of about 0.6 ML with additional Co adatoms evaporated on top. Clearly we can distinguish between highly ordered areas and disordered areas. Metal-organic bond motives dominate the disordered area and hydrogen bond mediated structures the ordered structure. The different areas arise since the network can not be fully reticulated due to a Co minority. The not metal coordinated molecules are accompanied in a 2D fluid at room temperature form a surface gas and form the chains while cooling. The chain formation indicates a limited mass transport during self-assembly and chiral resolution. We focus here on the ordered areas. According to the substrate orientation marked by the white cross the ordered islands are oriented with their chains along the crystal high symmetry direction. High resolution STM images reveal that the 1D chains are assembled by stacked molecular ribbons like in figure 3.5 *a*. The molecular rows exhibit the same binding motive consisting of molecules with the same chirality. Consequently two different molecular orientations in the ribbons can be found. The D-*trans* enantiomer is colored with green to highlight the according areas. The distances between corresponding rows is about 1 nm which could be caused by the preferential adsorp-

tion site on the substrate. It is well known that adsorbates change the surface state. The chain structures presented here could be interesting, since they reduce the surface state between the chains to 1 dimension like demonstrated by Schiffrin et. al. [11]. Similar observations have been published recently by Kühne et. al. for cyano functionalized oligophenyl molecules assembled in metal-organic and organic networks. The direction of the molecular main axis in the 1D ribbons and 1D islands is not exactly the same as in the linear structure, presumably due to the interaction with the neighboring ribbons. Hence the island is different from the linear structure. Further molecules exhibiting a *cis* conformation occur especially on the step edges and on unusual/border positions, such as the outer right and left molecule in figures 3.5 *b,d*.

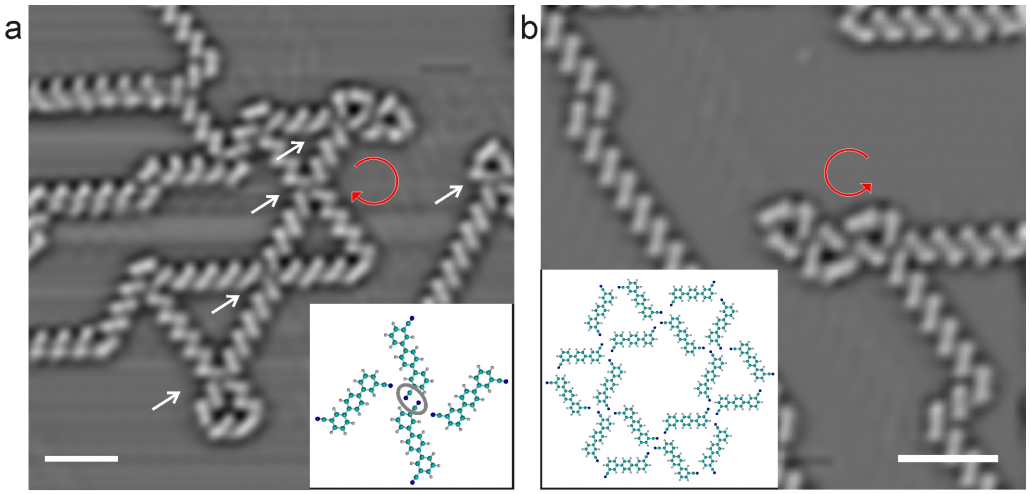

Figure 3.7: Supramolecular structures, exhibiting chiral nodal motifs. **a)** At intersections of the ribbons, chiral structures with a counter clockwise rotation can be found (marked with the white arrows). In **(b)** a similar bond motif is displayed with a clockwise rotation. The motifs resembles those identified in the Kagomé like superstructure with linear building blocks (see refs. [7, 8]), which could be assembled as depicted in the inset with the molecules used herein. Scale bar: 4 nm.

Both enantiomers of the *trans* specimen were found to assemble in the typical linear 1D chiral structures. At intersections of 1D ribbons with the same chirality, 2D chiral nodal motifs arise. In figure 3.7 *a* the D-*trans* conformation resembles a counter-clockwise rotating "windmill" structure at the intersections marked with white arrows. The nodes in these 2D structures consist of two different binding motifs, as illustrated in the inset. The positioning of two of the CN groups suggests a dipole interaction with an antiparallel orientation (marked with a grey circle). The second bonding motif is more hydrogen-bridge like, similar to the ribbon and island formation. A dominant orientation resulting in the dipolar bond was not observed. Figure 3.7 *b* features the windmill motif as well. However, being composed of L-*trans*

molecules, the sense of rotation is inverted. By merging several equally oriented windmill motives more complex structures can be created (inset of figure 3.7 *b*). Three windmill motifs are connected forming a sector of a circular structure. This motif is alike a structure formed by five and six phenyl dicarbonitrile molecules on Ag(111) where they form regular Kagomé-like structures over wide areas [47, 52]. Furthermore in the island structure as well as in the 1D ribbon formation, the D-*trans* molecule is rotated clockwise and the L-*trans* counter clockwise, respectively. In combination with the initial state of island formation (figure 3.5 *d*) the depicted atomistic model for the island formation is corroborated. Hence over wide areas a racemic distribution of molecular arrangement by means of the island pattern could be evidenced.

3.1.3 Conclusion

We presented a study addressing the supramolecular organization and layer formation of the non-linear, prochiral molecule $[1, 1'; 4', 1'']$-terphenyl-$3, 3''$-dicarbonitrile adsorbed on the Ag(111) surface. Our combined STM and NEXAFS investigations provide novel insights in the 2D self-assembly of this prochiral species that upon surface confinement deconvolutes in three stereoisomers, that is, two mirror-symmetric *trans*- and one *cis*-species. STM measurements reveal large and regular islands following room temperature deposition, whereby NEXAFS confirms a flat adsorption geometry with the electronic π-system and functional CN end groups parallel to the surface plane. The ordering within the densely packed supramolecular arrays reflects a substrate templating effect, steric constraints, and the operation of weak lateral interactions between the functional end groups. The expressed bonding motifs suggest both mutual interactions between CN and phenyl moieties. Chiral resolution processes in the self-assembly lead to enantiormophic characteristics of the molecular packing schemes in different domains of the arrays. Notably a set of six brick-like arrangements could be identified comprising rotational domains of three *trans* species with two mirror-symmetric configurations each. At submonolayer coverage supramolecular islands coexist with a disordered fluid phase of highly mobile molecules. Following thermal quenching, we find extended supramolecular ribbons stabilized again by attractive and directional non-covalent interactions driven by CN endgroups. The ribbon formation reflects an exclusive chiral resolution of *trans* species.

3.2 Random 2D String Networks based on Divergent Coordination Assembly

The bulk properties of glasses and amorphous materials have been studied widely, but the determination of their structural details at the molecular level is hindered by the lack of long-range order. Recently, two-dimensional, supramolecular random networks were assembled on surfaces, and the identification of elementary structural motifs and defects has provided insights into the intriguing nature of disordered materials. So far, however, such networks have been obtained with homomolecular hydrogen-bonded systems of limited stability. Here we explore robust, disordered coordination networks that incorporate transition-metal centres. Cobalt atoms were co-deposited on metal surfaces with a ditopic linker that is nonlinear, prochiral (deconvoluted in three stereoisomers on two-dimensional confinement) and bears terminal carbonitrile (CN) groups. *In situ* scanning tunneling microscopy revealed the formation of a set of coordination nodes of similar energy that drives a divergent assembly scenario. The expressed string formation and bifurcation motifs result in a random reticulation of the entire surface.

3.2.1 Introduction

Understanding the nature of condensed disordered systems represents one of the challenging tasks for twenty-first century science [196–199]. Traditional experimental tools that rely on ensemble averaging have provided many important insights into the fascinating properties of glasses and amorphous solids, but to identify local order characteristics requires imaging techniques that address the individual constituents and topological defects. The direct, molecular-level investigation of random networks became possible with two-dimensional (2D) supramolecular systems assembled on well-defined surfaces amenable to *in situ* observation using scanning tunneling microscopy (STM).

For instance, a series of elementary structural motifs that reflect hydrogen-bonding multiplicity was identified in kinetically trapped random networks obtained with nonsymmetrical cytosine molecules on a Au(111) surface under vacuum conditions at low temperatures [200]. At the solid-liquid interfaces, rod-like molecular building blocks with four peripheric, isophthalic functional endgroups were shown to form porous networks that displayed orientational symmetry, but simultaneously lacked

large-scale translational order [201, 202]. Such molecular random tilings, in which the density of spatially fluctuating defects is rather low, can be regarded as entropically stabilized phases that represent 2D glasses [201, 203].

Here we report an STM investigation of robust, disordered coordination networks that comprise interconnected polymeric strings and multiple ramification motifs. We used the nonlinear prochiral ditopic linker deconvoluted in three stereoisomers on surface confinement introduced in scheme 3.1. Coordination assembly was induced by co-deposited cobalt atoms, which engaged in lateral metal-ligand interactions with the linker dicarbonitrile endgroups. The resulting complex networks are based on a set of distinct three- and fourfold cobalt-CN nodal coordination motifs of similar energy that result in bifurcation or string formation. Thus, symmetry deconvolution of the linker and coordination multiplicity entails divergent assembly with concomitant random reticulation of the entire surface. An important feature of coordination interactions is their appreciable bonding strength, typically significantly higher than that of hydrogen bonds. In the present study this is exploited to meet the important criterion of room-temperature stability regarding open, random networks namely irregular, 2D, reticulated surface architectures that comprise voids.
The highly symmetric ditopic or tritopic linkers used thus far on low-index metal surfaces favor the encountered convergent protocols, in which a unique or a small number of bonding motifs within the formed structures are at the origin of extended, regular supramolecular arrangements. Thus, translational symmetry, size and shape control can be achieved for polymeric or network structures. By contrast, with the nonlinear prochiral linker used at present the symmetry-breaking effect of the surface, in conjunction with the predominant, coexisting three- and fourfold coordination nodes that are close in energy, generates a multiplicity of distinct network elements that do not organize in a regular pattern.

Experimental Methods & Materials

The experiments were performed like described in the previous part using a variable-temperature and a low-temperature STM, respectively. The used Cu(111) and Ag(111) substrates were prepared by standard procedures. The molecules were deposited from a quartz crucible in an organic molecular-beam epitaxy source at 480 K, with the substrate kept at 300 K. Subsequently, submonolayer molecular films were exposed to a beam of cobalt atoms for the coordination assembly, whereby the linker-metal ratio was adjusted to < 3. To equilibrate the resulting surface networks, the samples were annealed to 300-350 K; the higher temperatures led to thermal des-

orption of linkers not engaged in lateral coordination bonds. After preparation, the sample was transferred *in situ* and STM data were acquired at T = 300 K and 6 K. The images presented in figures 3.8, 3.9 and 3.10 were measured with the Aarhus-type STM. The images of figure 3.11 were recorded with the LT-STM.

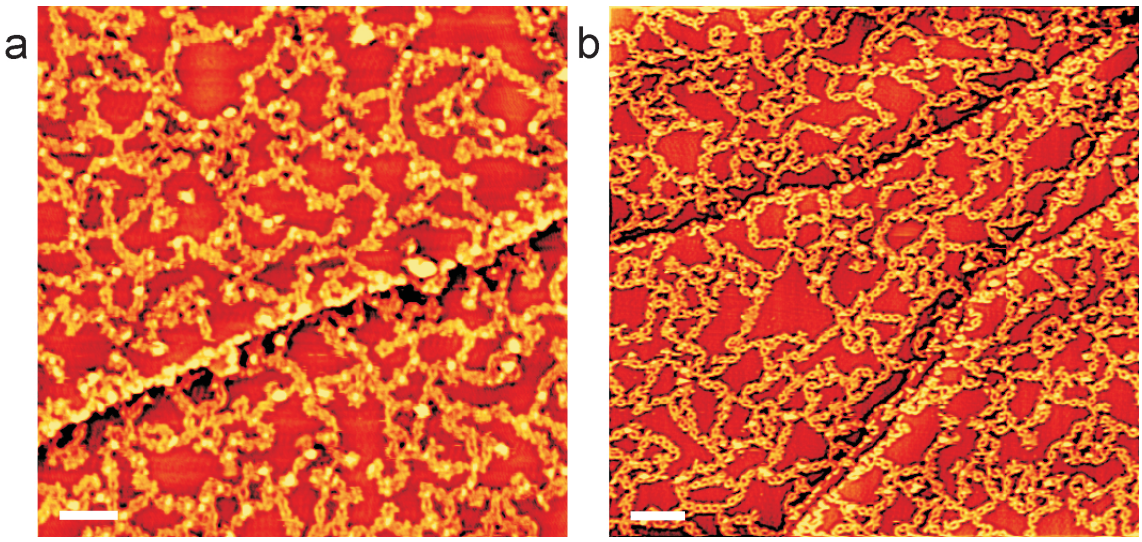

Figure 3.8: STM images of random coordination string networks. The co-deposition of cobalt atoms and nonlinear dicarbonitrile linkers on close-packed Ag(111) **(a)** and Cu(111) **(b)** surfaces leads to the formation of random networks. Sample bias voltage (V_B) = 1.2 V, tunneling current (I_T) = 0.1 nA; recorded at 300 K. Scale bars: 10 nm.

3.2.2 Results & Discussion

Random network formation

Specifically, we used a ditopic linker, introduced previously in section 3.1.1. The rod-like *p*-terphenyl-*m*-dicarbonitrile (*m*NC-Ph$_3$-*m*CN) (Scheme 3.1), with a distance of 12.56 Å between the terminal nitrogen atoms of the CN moieties. Because the ditopic linker's functional endgroups are at its periphery, many different interconnection modes between network elements are expressed, which represent either coordination strings or bifurcation nodes. On the level of stereoconformers the natural composition of the pertaining 2D fluid at low coverages can be assumed to be 50% *cis* and 25% for each of the mirror-symmetric *trans* conformations.
STM overview images of typical coordination networks after Co-directed assembly of the linkers on Cu(111) and Ag(111) are reproduced in figure 3.8. The data reveal irregular networks on both surfaces, which consist of meandering strings interconnected by a variety of nodes. The networks do not display mesoscale order, in marked contrast to the highly regular nanomeshes obtained with ditopic linear

linker analogues [52,89]. However, they are built up by a limited number of distinct coordination motifs and present coordination nodes that clearly show short-range order. Accordingly, they can be designated as 2D, glassy coordination networks.
The formation of very similar random networks on substrates with ∼10% difference in surface lattice constants (4.08 versus 3.55 Å) indicates construction principles whereby the epitaxial fit does not have a decisive role in the structural evolution. Therefore, the assembly of pure linker layers on both substrates gives densely packed extended islands, the order of which reflects non-covalent lateral interactions between CN endgroups and aromatic moieties [46]. The island formation and their step edge fluctuation at 300 K (see figure 3.3) give further evidence that high molecular mobility prevails during the coordination assembly conducted in the 300-350 K range. The morphology of the random networks presented here is thus dominated by the availability of different conformers and adaptive coordination motifs. The compact protrusions in figure 3.8 are small cobalt clusters that show cobalt excess during network formation; that is, metal center deficiency can be ruled out as a factor that determines network characteristics.

Coordination motifs and network morphology

A high-resolution STM image that reveals molecular positioning within the coordination strings and their intersections is reproduced in figure 3.9. First, here we can identify and assess the distribution of surface conformers. A statistical analysis of random coordination networks performed for a series of such images revealed that the natural ratio of a 2D surface gas is roughly conserved (∼60% *cis* and ∼20% for each *trans* species). The slight deviation detected from the ideal composition might be caused, in part, by diastereomeric discrimination during gas-phase deposition related to the mutual orientation of functional groups and the small *cis-trans* conversion barrier (6 kJ mol^{-1}) related to a carbon-carbon biphenyl rotation [204]. This indicates that during network assembly the linkers rarely change their conformation and are stabilized preferentially by surface and lateral interactions. Second, the data clearly reveal the coexistence of nodal motifs with three- or fourfold coordination of cobalt centers by CN ligands. The encountered coordination nodes can be separated into bifurcation motifs and chain motifs, which occur for three- and fourfold cobalt coordination. The predominant bifurcation motifs are of the fourfold *cis-cis*-Co-*trans-trans* (labeled *cc•tt*) and the threefold Co-*trans-trans-trans* (*•ttt*) node families (figure 3.9 *b,c*). Their corresponding models are given in aside, respectively, and were found in our data sets in both possible mirror-symmetric configurations (see appendix part C figure 4.6).

Furthermore, formation of the random string network requires the existence of chain motifs. They are identified readily in figure 3.10, but are even more pronounced in preparations at slightly reduced coverages, such as that depicted in figure 3.10 *a*. The predominant chain-forming coordination nodes are of the families *cis-cis*-Co-*cis-cis* (cc•cc), modeled in figure 3.10 *e* and *cis-cis*-Co-*trans* (cc•t), modeled in figure 3.10 *f*.

The proportion of threefold-coordinated nodes in a given network is typically significantly higher than that of fourfold-coordinated nodes, which is supported by density functional theory results that indicate an energetic preference for threefold coordination of cobalt centers by CN functional groups on noble metal surfaces. The calculations revealed that in the presence of a silver substrate (modeled by a silver cluster) this preference is the result of a small energy difference between three- and fourfold cobalt coordination of only 90 meV per coordination node (in contrast to the situation for isolated planar nodes, in which the preference is inverted in favor of fourfold coordination) [52]. The pertaining binding energies per ligand amount to ∼0.7 and ∼0.5 eV for threefold versus fourfold coordination, respectively; taking into account the bonding to the subjacent silver cluster, a small total energy difference results.

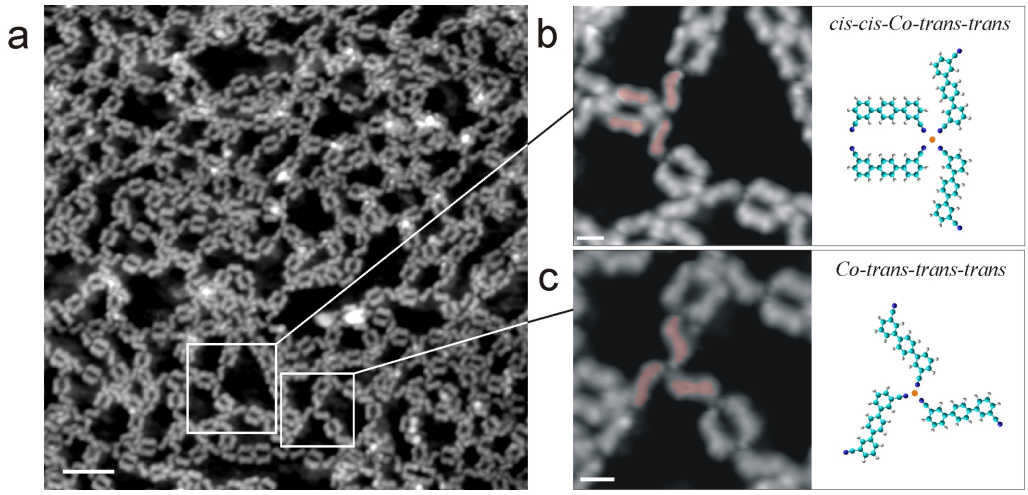

Figure 3.9: Molecular-resolution STM images of a disordered coordination network on Ag(111). **a)**, Coordination motifs that underlie the random network with coexisting three- and fourfold coordination nodes. $V_B = 1.2$ V, $I_T = 0.1$ nA; recorded at 6 K. Scale bar: 5 nm. **b, c)**, Magnified views showing the dominant bifurcation motifs (circled) with their corresponding models, *cis-cis*-Co-*trans-trans* bifurcation (*cc•tt*) **(b)** and Co-*trans-trans-trans* bifurcation (•*ttt*) **(c)**. Scale bar: 1 nm. Light blue spheres: C; dark blue spheres: N; white spheres: H; orange spheres: Co.

Importantly, the calculations apply equally well to linear and bent linkers because

the change in symmetry does not affect the arrangement of the functional groups in direct proximity to the coordination node. For steric reasons, molecular strings that incorporate a sequence of three- or fourfold coordination nodes cannot be realized with the linear linkers. In the case of linear dicarbonitrile molecules, the energy difference thus promotes highly regular honeycomb structures that exclusively feature threefold coordination after the convergent coordination assembly at room temperature [52,89]. Only under conditions associated with kinetic limitations (∼250 K, see appendix B figure 4.2) was the expression of a defective honeycomb structure with a minority of fourfold coordination nodes observed (that is, self-correction with the elimination of defective arrangements is fully operational at 300 K). By contrast, the formation of random networks with bent linkers under conditions in which yet higher energy barriers can be overcome (temperatures up to 350 K), in conjunction with their high surface mobility and the similarity of the coordination motifs, signals that kinetic limitations do not dominate the ordering scenario. Thus, the small energy difference, in combination with the stereochemical deconvolution of the different molecule configurations (an opportunity not present for the linear equivalents), favors the expression of random string networks.
The predominance of a set of specific coordination motifs and the expression of a random, reticulated structure that spreads out over large areas reflects a dynamic, divergent assembly scenario, in which the reversibility of the metal-ligand interactions interferes decisively. This directly contrasts the principles that underlie the on-surface synthesis of branched polymeric nanostructures, which are trapped kinetically and have geometric properties dictated by the irreversible formation of covalent bonds [162, 205, 206]. Accordingly, there are to date no reports of covalent bond formation on surfaces used to fabricate well-ordered molecular nanoarchitectures.

Statistics and 2D chirality considerations

A coordination-node statistical analysis derived from data series representative of the situation depicted in figure 3.9 is shown in table 3.1. For simplicity, the *cis*- and *trans*-enantiomers (rather than the *cis*-, D-*trans*- and L-*trans*-enantiomers) are pooled. The dominating chain motifs (cc•c, cc•t and cc•cc) represent 50% of the realized possibilities, and predominant bifurcation motifs (*cc•tt*, *•ttt*, *cc•ct* and *•tttt*) account for 43%. Linkers attached to cobalt clusters were excluded, and 5% of the nodes have coordination numbers that exceed four.

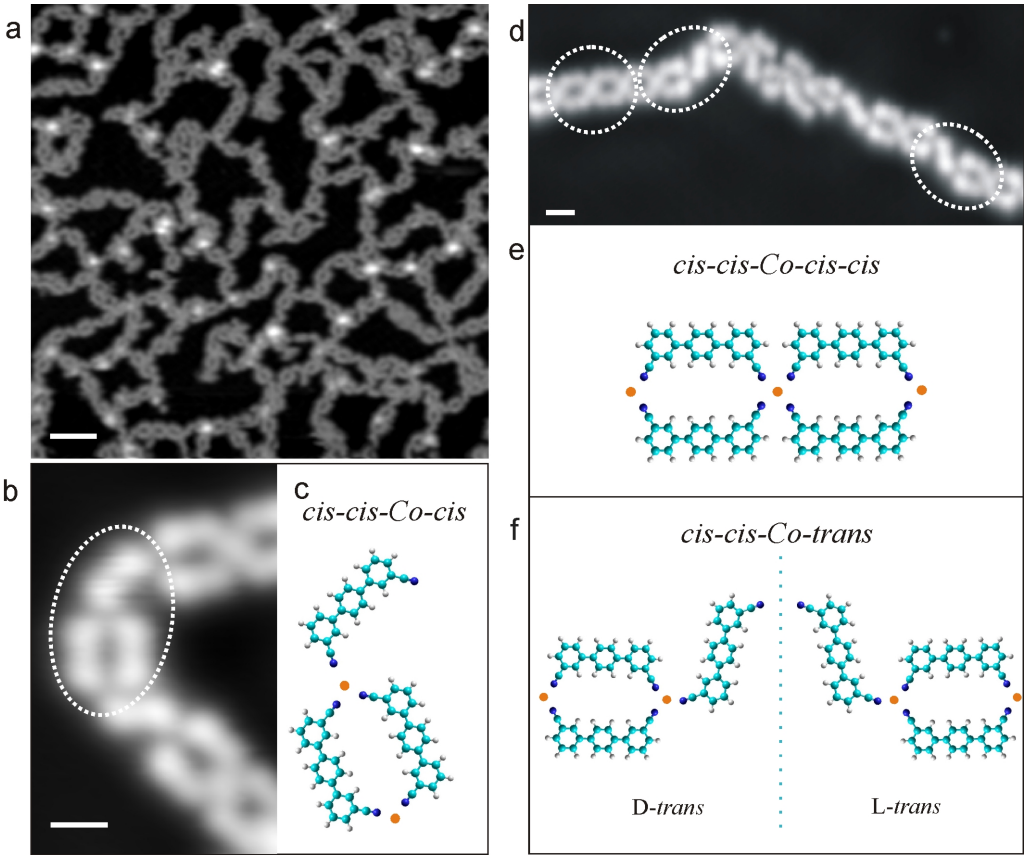

Figure 3.10: Random coordination string networks on Ag(111). **a)**, High-resolution STM image that emphasizes the string characteristics on Ag(111). V_B = 1.2 V; I_T = 0.1 nA; recorded at 6 K. Scale bar: 5 nm. **b, c)**, Magnified chain with a threefold cobalt-coordination motif (**b**, circled) and a schematic representation of the corresponding *cis-cis*-Co-*cis* (cc•c) kink **(c)**. Scale bar: 1 nm. **d-f)**, Magnified chain with fourfold cobalt-coordination motifs (**d**, circled) and schematic representations of the circled kinks, *cis-cis*-Co-*cis-cis* (*cc•cc*) chain motif **(e)** and two mirror-symmetric configurations of *cis-cis*-Co-*trans* (*cc•t*) bifurcation motifs **(f)**. Scale bar: 1 nm. Light blue spheres: C; dark blue spheres: N; white spheres: H; orange spheres: Co.

A surprising result of the network-node analysis is that motifs equivalent from purely statistical considerations do not appear with equal probability. For instance, the units required to build either *cc•t* or *c•tt* configurations are similarly abundant in a 2D fluid of linkers. The evident preference for the chaining *cc•t* unit after coordination with cobalt must be associated with the selection mechanisms that operate during the network assembly, which presumably implies, for instance, the interference of mobile metal-molecule subunits [207], and rotational movements of the (coordinated) linkers or weak lateral interactions between them, for example between CN groups and aromatic moieties [46]. For a full clarification of this intriguing behavior further studies of network formation *in situ* and of complementary kinetic Monte-Carlo simulations are suggested.

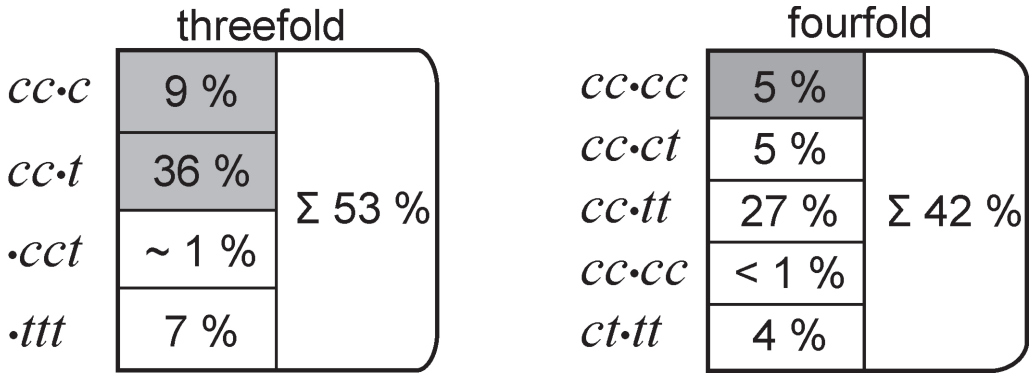

Table 3.1: Coordination-node statistics that summarize the possible families of three- and fourfold nodal motifs. 2D chirality of pertaining conformers and nodal motifs are pooled, the dominating chain motifs are given and the amount of higher coordination nodes is minor and has been neglected. The background of the chaining motives are grey and for bifurcation motives white, respectively.

Furthermore, 2D chirality represents an additional central aspect for the network topology, because the expression of the coordination nodes accounts for organizational chirality [174, 208], which has topological consequences. For instance, either left or right-handed windmill motifs can be realized with mononuclear, threefold cobalt coordination by *cis*-conformers on surfaces (model given in the appendix C figure 4.6). Consequently, the families summarized in table 3.1 present a library of 94 different coordination motifs in total, following the concept presented by Lehn [30]. The complete tabulation of all nodes with differentiated chirality signatures provided in the appendix D shows that the families of three- and fourfold coordination nodes provide 24 and 70 motifs, respectively. This dynamic library is available, in principle, for network formation and allows many surface reticulation possibilities. Thus, the interplay of local order induced by the metal-ligand interactions and the multiple levels of isomerism and chirality creates a topological conundrum to which the system′s response is random reticulation. Accordingly, in contrast to the scenario of highly convergent, metal-directed surface coordination assembly with linear dicarbonitrile species [52, 89], the 2D stereoisomerism of the linker discussed instructs a divergent assembly route. The use of a 2D chiral linker *per se* is not necessarily sufficient for a random network formation; in previous studies we identified cases in which asymmetric molecular backbones merely led to distortions in surface coordination networks that showed a unique nodal motif [170, 209]. Furthermore, chiral coordination nodes, for instance identified in networks with mononuclear iron-phenolate coordination motifs, can account for various cavity types in porous networks [210]. The node composition found in the amorphous network has to satisfy the natural

ratio of available conformers and co-determines the order of the network through the ratio between bifurcation motifs and chain-forming motifs. Whereas highly ordered structures that contain the natural ratio between the three surface conformers can be proposed (see the phase shown, as an example, in appendix A figure 4.1), the inherent disorder of networks reported here is evidence for a 2D glassy state that is, its constituents congeal during network formation and do not achieve a regular phase. Consequently, free-energy minimization during network formation does not bestow a homogeneous super lattice, in striking contrast to the high regularity achieved with linear building blocks and identical local coordination interactions. Taking into account the potentiating effect on the number of nodal motifs that arise from symmetry considerations (see tabulation in appendix D), the weight of the entropic term must be affected substantially by the chiral nature of the linkers. It is suggested that this term (beyond the binding-energy consideration of elementary structural motifs [200] (see the discussion above)) is of general importance in the expression of 2D supramolecular random networks [201, 203].

For the string networks discussed here, a further characteristic of the coordination motifs is metal-ligand bond length. The linker′s electronic structure is affected only weakly by the subjacent silver lattice [52, 89, 207], so we can assume that the encountered conformers are close to the geometry of isolated species. The models represented in figures 3.9 and 3.10 take this into account, on the basis of which we estimate a cobalt-CN bond distance of ∼2 Å, similar to values found for 2D cobalt-CN nanomeshes with linear linkers [52, 89] and related 3D compounds [211]. In isolated coordination compounds or 3D networks, changes in electronic properties are expected with different coordination numbers. In agreement, the STM measurements also point to differences regarding the electronic structure of threefold versus fourfold coordinated metal centers. Whereas typically the latter are imaged as protrusions (that is, provide a substantial contribution to the surface local density of states), the cobalt atom with triple CN coordination is mostly transparent [52, 89]. This signals the existence of a 2D analogue to conventional bulk, mixed-valence coordination polymers or networks, although one must keep in mind that the electronic structure of the cobalt centers is influenced by the underlying metal substrate [95, 159, 212].

Molecular manipulation with an STM tip

To obtain further insight into the nature of the coordination strings and nodes, molecular manipulation experiments were carried out. To this end, in constant-current mode the STM tip was moved laterally across a molecule that terminated a chain segment. Thereby, the tip-sample distance controlled by the tunneling resis-

tance R was reduced, starting from normal imaging conditions in which the network is generally unaffected by the scanning procedure (R = 1.8 GΩ) and continuing until a displacement of the molecule was observed (R = 2.5 MΩ). In figure 3.11 we compare selected states prior to and after such manipulation steps. Figure 3.11 *a,b* indicate that the terminal molecule can flip during the manipulation procedure while being attached to the linking node continuously, as the observed change in angle is consistent with a rotation of the linker about the CN-cobalt connection. Figure 3.11 *c,d* demonstrate the displacement of an entire string, which is leveraged about a threefold coordination mode without breaking. Thus, the lateral metal-ligand interactions override the substrate bonding at specific sites, which confirms the minor impact of the surface atomic lattice on the random networks. It is suggested that this important feature gives the flexibility apparently required for network assembly. To introduce structural flexibility in surface-confined supramolecular arrangements an alternative possibility is the use of flexible molecular species, with which a certain level of adaptiveness can also be achieved [195, 213, 214].

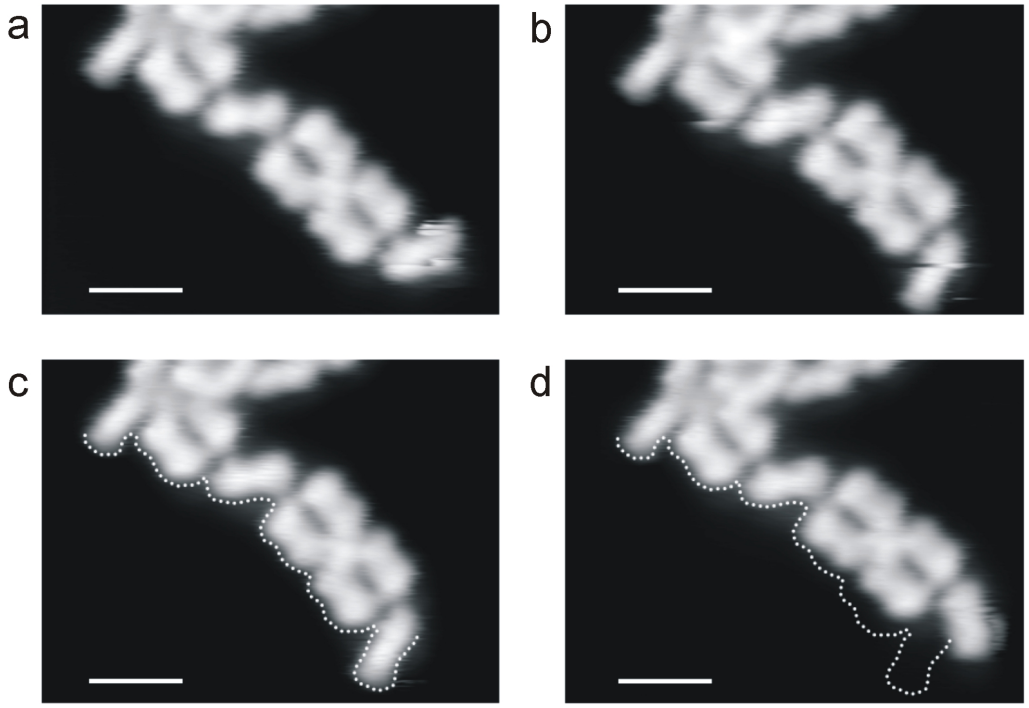

Figure 3.11: Molecular manipulation experiments. **a, b)**, a linker at the end of a coordination string was manipulated with a STM tip (performed at 8 K) to flip it between the initial **(a)** and final states **(b)** as the tip was moved laterally across the terminal molecule. **c, d)** The displacement of the entire chain segment is shown. Imaging parameters, V_B = 20.2 mV, I_T = 0.11 nA; for manipulation, V_B = 250 mV, I_T = 20 nA. Scale bars: 2 nm.

It is interesting to compare our findings with the recently reported hydrogen-

bonded random networks from cytosine molecules self-assembled on the Au(111) surface [200]. With this system, multiple elementary coupling motifs, notably different hydrogen bonded filament and ring arrangements of the flat-lying molecules, could be identified also. The mutual orientation of the network constituents is determined by the availability of many hydrogen-bond donor and acceptor groups within the same molecule. By contrast, the coordination nodal motifs presented here are based on the interaction of just one functional molecular endgroup and single metal adatoms. Thus, they give different local, short-range order characteristics (that is, the regular arrangement of CN groups around cobalt centers), and both the disposition for ramification and string formation can be explained by the linker asymmetry and organizational chirality. Furthermore, the embedded metal centers represent coordinatively unsaturated sites [95, 159] that can provide distinct functional properties [212]. In addition, the higher stability of cobalt-nitrogen coordinative bonds compared to the weak hydrogen bonds used previously [200] means that room-temperature stability of the open, disordered topology formed is achieved. This is an important aspect in view of the potential applications of 2D glassy coordination networks.

3.2.3 Conclusion

We report here a full spatial and structural elucidation of disordered coordination architectures using STM to probe directly the arrangements at the molecular level. Our results reveal the divergent assembly of random string networks on planar surfaces using a prochiral, ditopic linker that forms metal-ligand bonds with cobalt centers. The use of coordination interactions renders robust disordered network structures that incorporate distinct bifurcation and string motifs based on a scenario mediated by reversible metal-ligand interactions. The connection between molecular symmetry, on-surface metal-ligand interactions and energetic similarity of the predominant three- and fourfold coordination nodes provides design criteria for the engineering of disordered 2D solids. It is suggested that string networks with randomization and multiple coordination motifs present a new route towards a distinct class of robust, adaptive compounds and network topologies situated between so-called metal-organic frameworks and covalent polymers.

3.3 Reorientation of Molecular Layers of Asymmetric Dicarbonitrile Oligophenyls

In recent years a variety of studies on molecular self-assembly on different surfaces has been published. The major part aims to understand the principles behind self-assembling phenomena. The evolving structures are significantly influenced by the molecular coverage and the ratio between the different employed species. Here we present a study on changes of a molecular pattern assembled by oligophenyl molecules functionalized with CN endgroups on Cu(111) at room temperature. We were able to follow the changes by means of scanning tunneling microscope, near-edge X-ray absorption fine structure spectroscopy and X-ray photoelectron spectroscopy. The molecular orientation changes from a coplanar adsorbed brick-like structure to an upright standing linear pattern with increasing coverage.

3.3.1 Introduction

Thin molecular films have attracted high interest over the last decade due to their possible application as organic light emitting devices (LEDs) [215–218], organic semiconductors [219–221], in photovoltaics [222] and in non-linear optics [223]. Decisive factors for the performance of organic-LEDs (OLEDs) are the electron injection from the substrate into the molecular conduction band and the transport within the molecular layer. Molecular π-stacking of aromatic systems is an appropriate way to increase the in-plane charge mobility [224], proven in experiments [225] and by theory [226].

We report here on coverage-induced orientational changes resulting in a reorganization of the self-assembled molecular pattern studied by scanning tunneling microscopy (STM), near-edge X-ray absorption fine structure (NEXAFS) spectroscopy and X-ray photoelectron spectroscopy (XPS). The measurements have been conducted employing the Cu(111) single crystal surface with molecular coverages varying from sub-monolayer to multilayer. In the regime of 0.3 - 0.7 monolayer (ML) at room temperature (RT) stable organic self-assembled networks prevail. We define a monolayer as a completely covered sample surface with flat adsorbed molecules oriented parallel with their π-system to the surface. The single molecule in the self-assembled network is adsorbed with its molecular backbone coplanar on the surface. The molecular structure transforms with increasing coverage to a metal

adatom mediated and by π-π interaction supported molecular pattern where the molecular π-system is lifted off the surface. The interaction between the substrate and the organic species in the evolving phase even suggests a rehybridisation of the functional carbonitrile group. We succeeded in triggering the orientational change of the single molecules resulting in the formation of a new self-assembled molecular network and observed this by means of NEXAFS, XPS and STM.

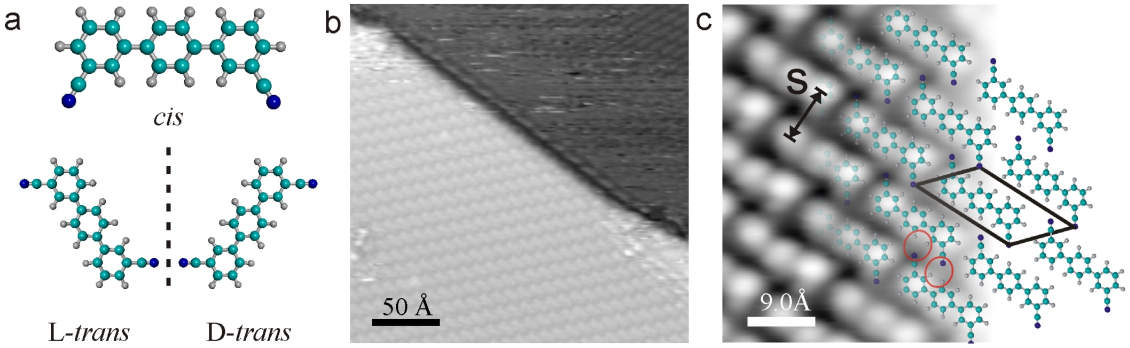

Figure 3.12: Molecular model and STM images of a organic supramolecular network at room temperature (RT). **(a)** Atomistic model of the $[1,1';4',1'']$-terphenyl-$3,3''$ - dicarbonitrile (*m*NC-*p*Ph$_3$-*m*CN) molecule in *cis* and *trans* conformation. Carbon is marked with green, nitrogen with blue and hydrogen with white spheres. **(b)** STM image of a brick-like network on Cu(111). The darker area shows a 2D surface fluid on a lower step-edge. **(c)** High-resolution STM image of the brick-like molecular pattern superimposed with the atomistic model, whereby the interacting N and H atoms are marked with red circles. The unit cell has a size of 15.3×9.3 ($\pm$ 0.5) Å^2 and the distance between the molecular rows s is 6.9 ($\pm$ 0.5) Å.

Experimental Methods & Materials

All STM measurements were conducted in the Aarhus type STM. The Cu(111) sample was cleaned like explained in section 2.1.4. Subsequently the *m*NC-*p*Ph$_3$-*m*CN molecule was evaporated by means of organic molecular beam epitaxy from a quartz crucible at 440 K while the sample was held at RT. The measurements were performed at RT.

The NEXAFS and XPS measurements were performed at the HE-SGM beamline at the BESSY-II synchrotron in Berlin. The employed apparatus works at a base pressure of 1×10^{-10} mbar and in order to obtain comparable results as during the STM measurements the sample preparation have been performed in the same manner. To reduce beam damage especially at high molecular coverage, the sample was held at $\approx$ 160 K while measuring. Multilayer samples were studied with monochromator slit widths of 100 μm resulting in an energy resolution of 0.2 eV for the C1s and 0.3 eV for the N1s edge. Sub-monolayer and monolayer preparations were performed

with a slit width of 200 μm corresponding to an energy resolution of 0.4 eV for the C1s and 0.6 eV for the N1s edge. The data treatment was performed following the procedures described in ref. [157].

3.3.2 Results & Discussion

For our experiments a prochiral ditopic polyphenyl molecule has been investigated with complementary surface science techniques. We will present comprehensive STM investigations supported by NEXAFS and XPS. An atomistic model of the nonlinear ditopic $[1,1';4',1'']$-terphenyl-$3,3''$-dicarbonitrile molecule (mNC-pPh$_3$-mCN) is depicted in figure 3.12 *a*. It consists of three phenyl rings forming the linear molecular backbone and a carbonitrile (CN) group placed in *meta* position on each of the outer phenyl rings. The σ-bonds between the phenyl rings allow for a rotation of the phenyl rings around the molecular backbone-axis. Due to the rotational degree of freedom a *cis* and a *trans* species exists. In the gas phase an equal distribution between *cis* and *trans* isomers can be estimated [173, 182, 227].

STM measurements

On the employed Cu(111) metal substrates the molecule initially assembles in a highly regular supramolecular pattern as depicted in figure 3.12 *b*. The image shows two terraces. The lower terrace (dark area) supports a molecular surface gas, since at RT the single molecule on the bare metal surface is highly mobile. The brighter upper terrace is covered with a self-assembled molecular layer. A single molecule appears as a rod like protrusion (bright) originating from the extended π-backbone. The molecules are aligned one after another and each line is stacked on top of the last one resembling a brick wall, therefore we call it a brick-like structure. The pattern formation is surrounded by a 2D molecular surface fluid, whereas the borders of the islands are in dynamic equilibrium with the surface fluid. Recent experiments showed, that while cooling down the gas phase condenses into 1D ribbons oriented along the high symmetry direction of the crystal. The 1D ribbons are constructed of *trans* molecules. Due to the surface symmetry breaking effect upon adsorption, the *trans* isomer separates in a left- (L) and right- (D) handed species (see figure 3.12 *a*). Figure 3.12 *c* shows a high-resolution STM image of the brick-like network in detail superimposed with an atomistic model of the molecular pattern. We know from earlier measurements that the assembly consists of homochiral *trans* isomers whereby the interaction (marked with the red circle) is mediated by the CN group

towards the H of an adjacent molecule (see section 3. Due to the threefold symmetry of the substrate and the existence of D− and L-*trans* isomers six pattern orientations can be found. The pattern formation on Cu(111) is strongly dependent to the coverage. After dosing a small amount of molecules (<0.1 ML) on the substrate the step edges are decorated first, as one can still see on the lower side of the step-edge proceeding through figure 3.12 *b*. With increasing coverage islands start to form at RT at about 0.3 to 0.7 ML and large extended highly regular homochiral molecular networks evolve. This brick-like structure is similar to the one on Ag(111) (see section 3). Annealing experiments on Cu(111) of a submonolayer coverage revealed the formation of a metal-organic network similar to the one found after Co coevaporation.

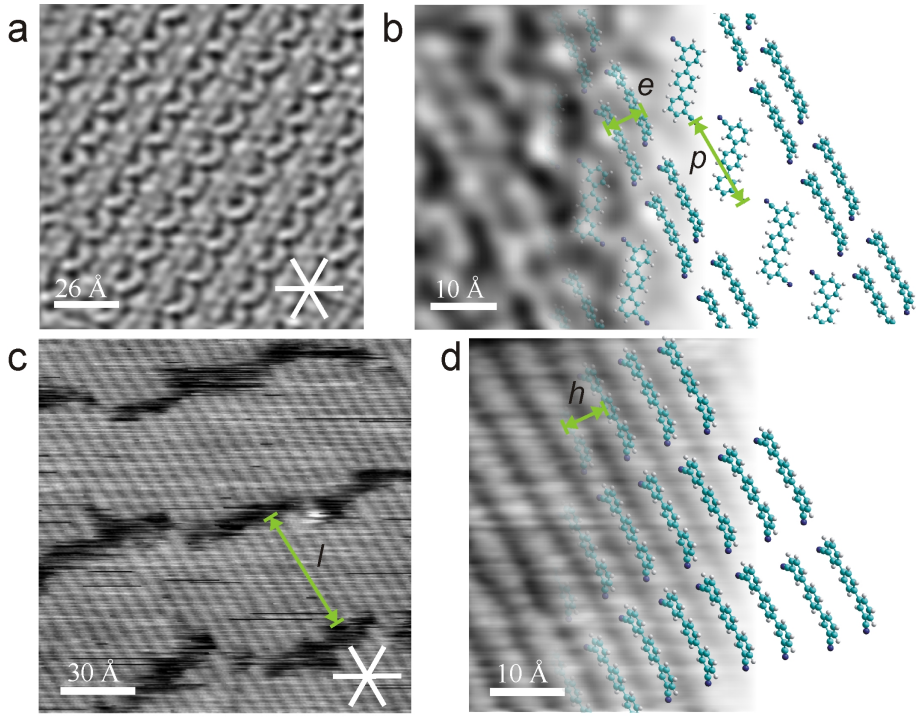

Figure 3.13: Molecular resolution STM images of the coverage dependent assemblies of mNC-pPh$_3$-mCN on Cu(111) at RT partially superimposed by atomistic models. **(a)** The molecular pattern formed at 0.8 ML coverage incorporates a linear and a zig-zag structure and is oriented along one of the high-symmetry directions of the substrate, marked with the white cross. **(b)** High-resolution STM image of the combined linear and zig-zag structure superimposed with an atomistic model. The linear structure exhibits a separation of e = 5.7 (± 0.5) Å between each line and the zig-zag structure a periodicity of p = 14.9 (± 0.5) Å. **(c)** STM image of a preparation at a coverage of 1 ML with exclusive linear structure oriented along the high symmetry direction of the substrate. The linear motive features an average length of l = 51.2 (± 0.5) Å. **(d)** High-resolution STM image of the linear motive exhibiting an inter-lines distance of h 5.2 (± 0.5) Å superimposed with the corresponding atomistic model.

By increasing the molecular coverage on Cu(111) changes in the brick-like structure can be observed. Figure 3.13 *a* shows a STM image of a sample with a coverage of ≈ 0.8 ML. It consist of a regular sequence of linear ribbons and zig-zag elements parallel to each other. The ribbons alternate with zig-zag assemblies depicted as in the topograph. An analysis of a large amount of chains showed that linear structures beside each other can been found, but a zig-zag motive is always confined by two ribbons. Each linear ribbon is oriented along a substrate high-symmetry direction (indicated with the white cross) and contains two single strings separated by a distance d of 5.7 (± 0.5) Å(see figure 3.13 *b*). The zig-zag arrangement features a periodicity of p = 14.9 (± 0.5) Å. Our assignment of the molecular geometry is superimposed onto the high-resolution STM image of figure 3.13 *b* with an atomistic

model. The linear structure consists of *cis* isomers pointing with their CN groups towards the sample surface while the phenyl rings stand upright pointing away from the substrate. We suggest the CN groups to point towards the surface due to their high affinity towards Cu [52, 95, 228, 229]. The orientation of the phenyl rings almost "perpendicular" to the surface is motivated by the short inter-line distance e of 5.7 ($\pm$ 0.5) Å. Kwon et. al. showed for an oxadiazole derivate a similar behavior resulting in an interline distance of 4.8 Å [230]. The zig-zag structure is supposed to be planar on the surface like the brick structure.
By increasing the coverage to about 1 ML the molecular assembly changes as depicted in figure 3.13 *c*. Now a wavy striped pattern with a novel linear structure arises having an average length l = 51.2 ($\pm$ 0.5) Å, which corresponds to the length of three molecules. All linear motives are oriented along the high-symmetry directions of the surface. The lines are interrupted by narrow trenches which appear in the image as dark regions and lead to a zebra-like texture emerging on a larger scale. However, in the high resolution image (see figure 3.13 *c*) no molecular contrast can be seen within the molecular lines making it difficult to explore the molecular assembly. The inter-line spacing h is determined to 5.2 ($\pm$ 0.5) Å and is smaller than the spacing of the former ribbons. Our tentative model is superimposed on top of the experimental pattern formation (see figure 3.13 *c*). The model is motivated by the agreement of the average value of l and the molecular dimensions. The distance h is too small to assume a coplanar adsorption of the molecular backbone leading to a line separation s of 6.9 ($\pm$ 0.5) Å (see figure 3.12 *c*). The clear separation of the string motifs and the affinity of the CN groups towards the metal substrate supports our model where the CN groups point to and the phenyl backbone lift off the surface. The molecular density in the linear structure compared to the brick-like structure is increased. Thus we ascribe the dark junctions interjecting the linear structure to stress relief boundaries evolving from a limitation in the mobility of the molecular pattern. In order to show the dynamic behavior of the molecule reorientation we present in Appendix B figure 4.4 and 4.5. Temperature treatment of the brick-like as well as the zig-zag and linear structure up to $\approx$ 400 K on Cu(111) results in similar metal-organic pattern formations explained in section 3.1.3.

NEXAFS measurements

For a further evaluation of the coverage dependent molecular orientation in the organic adlayer NEXAFS measurements have been performed. Earlier NEXAFS investigations with the *m*NC-*p*Ph$_3$-*m*CN molecule on Ag(111) indicated a flat adsorbtion geometry with the π-system almost parallel to the surface. This result has

been found for sub-monolayer (see figure 3.2), monolayer (see appendix F figure 4.13) and multilayer (see appendix F figure 4.14) coverage. Since the low-coverage structure on Cu(111) appears while STM measurements with the same pattern as the corresponding layer on Ag(111), NEXAFS measurements in a sub-monolayer regime have been performed to compare the pattern formations on the two substrates. Subsequently the coverage was increased stepwise to follow possible changes in the molecular pattern.

In order to explain the main features arrising from the NEXAFS spectra we present in figure 3.14 *a* the intensity of the C1s signal for photon energies between 280 and 340 eV plotted for three different incident angles of the X-ray beam (20° in black, 53° in red and 90° in blue) at multilayer coverage. A layer thickness of 7 ML was evaluated from the absolute adsorption edge signal height. The incident angle (θ) of the X-ray beam and hence of the E-vector with respect to the sample surface-normal ($\vec{n}$) is marked by the inset in figure 3.14 *a*. In the π^* area the spectrum shows three peaks at 284.9 eV, 286.2 eV and 286.7 eV named π_1, π_2 and π_3. The sharp resonance π_1 and the features at 288.7 and 290 eV can be found at similar energies in benzene and oligophenyl [191, 231–233]. The features π_2 and π_3 are not present for benzene and oligophenyl, thus we assign them to the CN group. Recent work published by Klappenberger et. al. showed similar resonances for pNC-pPh$_x$-pCN molecules with varying backbone length [234]. E. Arras calculated by means of first principle DFT the ground-state orbitals and the according energies displayed in figure 3.14 *c*. The calculation identifies three orbital states π_1, π_2 and π_3. π_1 and π_2 are oriented out of the molecular backbone plane and exhibit a B_2 symmetry. π_3 features a B_1 symmetry oriented in the molecular backbone plane perpendicular to π_1 and π_2.

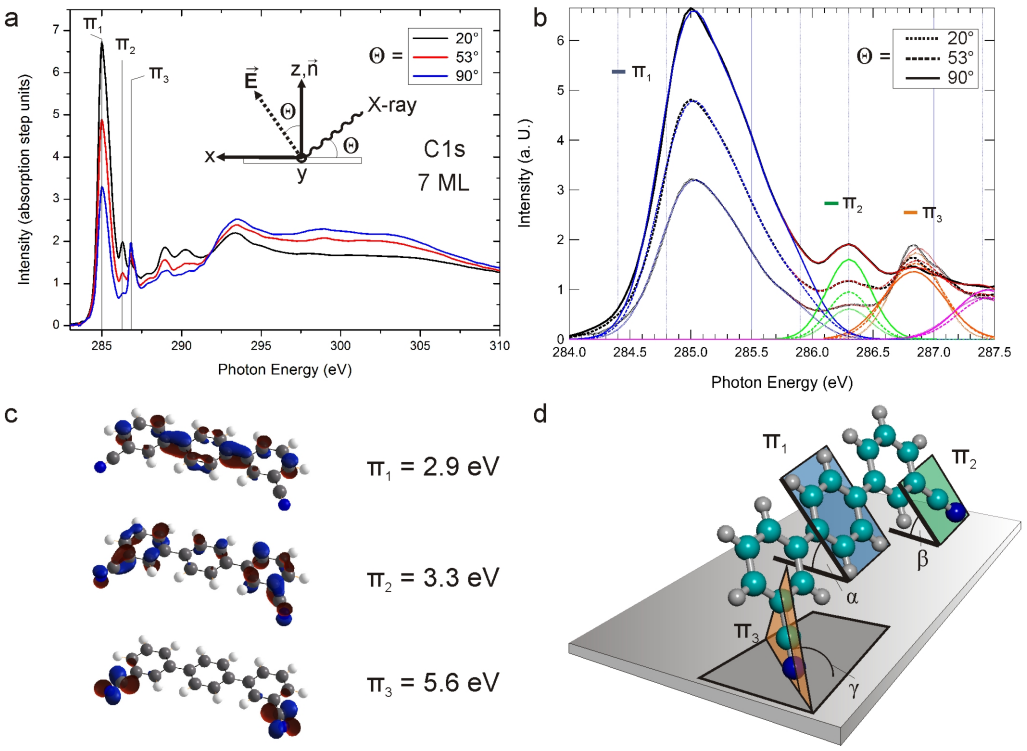

Figure 3.14: Overview on the angle dependent experimental NEXAFS C1s spectra on *m*NC-*p*Ph$_3$-*m*CN and illustration of the probed molecular orbitals. **(a)** NEXAFS C1s spectra with alternating X-ray incident angle (θ) of a multilayer of *m*NC-*p*Ph$_3$-*m*CN on Cu(111) at 160 K. The evaluated peaks are marked in the π^*-region of the spectra (π_1, π_2, π_3). The inset shows the experimental arrangement, where $\vec{E}$ is the polarization vector of the incident X-ray beam, θ the incident angle and y the rotation axis for the experiment. **(b)** Detail of the area of interest in the π^* region with varying incident angle (20°, 53°, 90°). A fit procedure based on a Gauss-function provides a resulting resonance distribution (red) and an angle dependent intensity for the peaks π_1 (blue), π_2 (green) and π_3 (orange). **(c)** Calculated ground-state orbitals corresponding to the peaks in the π^* area of the NEXAFS spectra. **(d)** Model of the molecular orientation on the surface.

For the analysis of the molecular orientation with respect to the surface we concentrate on the π^* region. In order to provide a better insight towards the molecular orientation and the molecular orbitals figure 3.14 *d* presents a set of angles characterizing the orientation of the molecule to the surface. The angles resolved from the NEXAFS analysis are directly linked to this model. The planes π_1 and π_2 represent the projected planes of the π_1 and π_2 orbitals. The angles α and β represent the tilt angle of the plane to the surface. The steric repulsion of the phenyl rings in the molecular backbone influencing the resolved angles will be taken into account. The plane π_3 which represents the π_3 orbital is oriented perpendicular to π_2-plane and along the orientation of the CN group. The angle γ describes the angle to the metal surface [191]. If the molecule is adsorbed flat with its molecular backbone on the surface the angles α and β would be near 0° and γ would be close to 90°. In

contrast, if the molecule is adsorbed perpendicular with its molecular backbone to the surface the angle α and β would be near 90°, but the angle γ would be around 60°. The angle γ results from the tilt of the CN group out of the molecular backbone plane in *meta* position. For the interpretation of the molecular orbitals regarding the phenyl ring and the CN group we refer to calculations by Rangan et. al. and Piantek et. al. employing a benzonitrile [235] and dimetacyano azobenzene [236].
The sharp peaks, the apparent dichroism and the intensity difference between the different incident angles in figure 3.14 *a* and *b*, confirm a highly ordered organic layer. The peak intensity of the resonances π_1 and π_2 decrease with increasing incident angle of the X-ray beam while the intensity of π_3 is increasing. In order to evaluate the acquired spectra we fitted the resonance shape according to ref [157]. A Gaussian function was used to fit the peak position and to resolve the intensity of each peak. Subsequent we kept the relative energy shift and peak width constant to achieve a comparable shape per spectral part. An example of the analysis of the π^* region is depicted in figure 3.14 *b*. This detailed spectra comprises three different incident angles (20°, 53° and 90°). The constitutive peaks of π_1 are fitted in blue, for π_2 in green and for π_3 in orange. The relative width of the peak π_1 is assigned to the excitation of different C1s initial states defined for the different carbon atoms of the phenyl rings [234, 237]. The variation of the incident angle causes changes in the peak intensity which can be evaluated from the fit resulting in the three angles (α, β, γ) presented in figure 3.14 *d*.
In the NEXAFS spectra of figure 3.14 *b* a strong decrease of the peak π_1 with increasing incident angle can be observed, likewise the intensity of peak π_2 is decreasing. The decrease of both peaks (π_1 and π_2) is not surprising, since the orbitals are assumed to be coplanar (see figure 3.14 *c,d*). For the same variation of the incident angle of the X-ray beam the intensity of peak π_3 increases. Hence the molecular orbital subject to the CN group is not oriented coplanar to the single crystal surface. In conclusion for the multilayer coverage the peaks π_1 and π_2 result in an angle $\alpha = \beta = 35° \pm 5°$ and π_3 in an angle γ of $55° \pm 5°$. Thus the NEXAFS analysis of the π^* orbitals at multilayer molecular coverage indicates a regular structure with highly ordered molecules adsorbed almost parallel with its π_1 and π_2 planes on the metal surface. The reason for the fairly large angles α and β could be the steric repulsion between the phenyl rings inducing a ring twist, especially in molecular layers far from the metal substrate. STM measurements by Braun et. al. showed a twist of the adjacent phenyl rings in the molecular backbone due to steric repulsion and influences of the adsorption site [238].
In figure 3.15 *a* the NEXAFS C1s spectra for a molecular coverage of 0.5 ML is

depicted. The peak π_1 is the characteristic feature of the spectrum and comparable to the multilayer preparation presented in figure 3.14 *a*. The resonances of π_2 and π_3 appear clearly again. A strong dichroism again suggests a high degree of ordering in the molecular layer. The angles resolved from the analysis of the intensity distribution are $\alpha = 20° \pm 5°$, $\beta = 25° \pm 5°$ and $\gamma = 55° \pm 5$. Including the experimental error and the steric repulsion the resolved angles of the NEXAFS analysis clearly confirm the near-to coplanar adsorption in the brick-like structure found within the STM measurements on Cu(111). These results agree with earlier measurements on Ag(111) (see figure 3.2) and accord to measurements on *p*NC-*p*Ph$_x$-*p*CN and oligophenyls without functional moieties [231]. They are in good agreement with multilayer preparation presented in figure 3.14 *a* and with earlier multilayer experiments on Ag(111) (see appendix F figure 4.13). The molecules in the sub-monolayer are oriented more coplanar to the surface than in the multilayer.

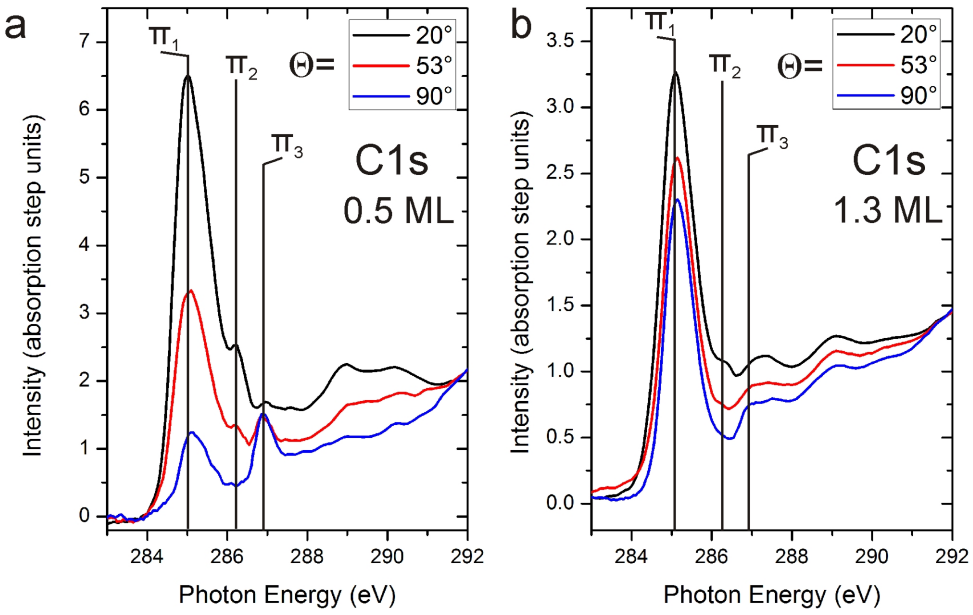

Figure 3.15: Angle dependent high resolution NEXAFS spectra of *m*NC-*p*Ph$_3$-*m*CN with increasing coverage on Cu(111). **(a)** NEXAFS spectra of the π^* area with 0.5 ML molecular coverage. **(b)** NEXAFS spectra of the π^* area with $\approx$ 1.3 ML molecular coverage.

The NEXAFS C1s spectra presented in figure 3.15 *b* were recorded for a molecular coverage of about 1.3 ML grown at RT. Still the shape of the spectra is dominated by the π_1 resonance emerging from the molecular phenyl backbone. However in contrast to the previous 0.5 ML coverage distinct changes can be found. The dichroism

is clearly smaller. The resonance of π_2 and the intensity of π_3 are reduced. The changes in the NEXAFS spectra become most prominent after the analysis of the normalized peak intensities. The previously (in the sub-monolayer) small angles for α and β raised to α=45° ± 5° and β = 40° ± 5°. Meanwhile the angle indicating π_3 is reduced to $\gamma = 50° \pm 5°$. These changes indicate that the molecular backbone lifts off from the surface while increasing the molecular coverage and support the structural changes seen in the STM. In detail, with the increase of α and β the π_1 and π_2 planes tilt away from the metal surface. These angles can not arise just from the measurement error and steric repulsion in the phenyl backbone.
The orientation of the molecules in the multilayer is not entirely coplanar with their phenyl backbone to the surface. The angles for $\pi_{1,2}$ (see figure 3.14) deduced from NEXAFS experiments at multilayer coverage are comparatively high and could be explained as follows. We know from earlier multilayer measurements on Ag(111) that the molecules arrange flat with small twist between adjacent phenyl rings caused by steric hindrance (see appendix F figure 4.14). We assume a similar packing scheme for the multilayer on Cu(111) as well, indicating a gradual change in the adsorption of the different molecular layers.
Additional to the NEXAFS C1s data, spectra at the N1s edge have been recorded presented in figure 3.16 *a-c*. All outlined data were acquired from the same preparations as the C1s spectra. In figure 3.16 *a* a molecular multilayer with ≈ 7 ML coverage is presented. Two π^* resonances at 399.3 eV and 400.1 eV are the prominent features of the NEXAFS N1s spectra. They belong to the two π^* orbitals of the CN (π_2, π_3) mentioned before (see figure 3.14 *c, d*). Both orbitals are oriented perpendicular to each other as shown in figure 3.14 *c, d*. In the range of 401 eV to 403 eV another resonance is visible in the multilayer (see figure 3.16 *a*) which corresponds to a π^* resonance oriented parallel to the π_3 plane [235]. The resonances π_2 and π_3 agree with DFT calculations of Carniato et. al. in the gas phase [192] and results by Rangan et. al. on Si(001) [235]. The analysis of the molecular adsorption site is focused on the first two resonances, which exhibit a strong dichroism. The data analysis of the resonance intensity for the multilayer preparation reveals an angle $\beta = 40° \pm 5°$ and $\gamma = 70° \pm 5°$ for the π_2 and π_3 plane to the metallic surface. This is in good agreement with the data of the C1s region presented in figure 3.14 *a*.

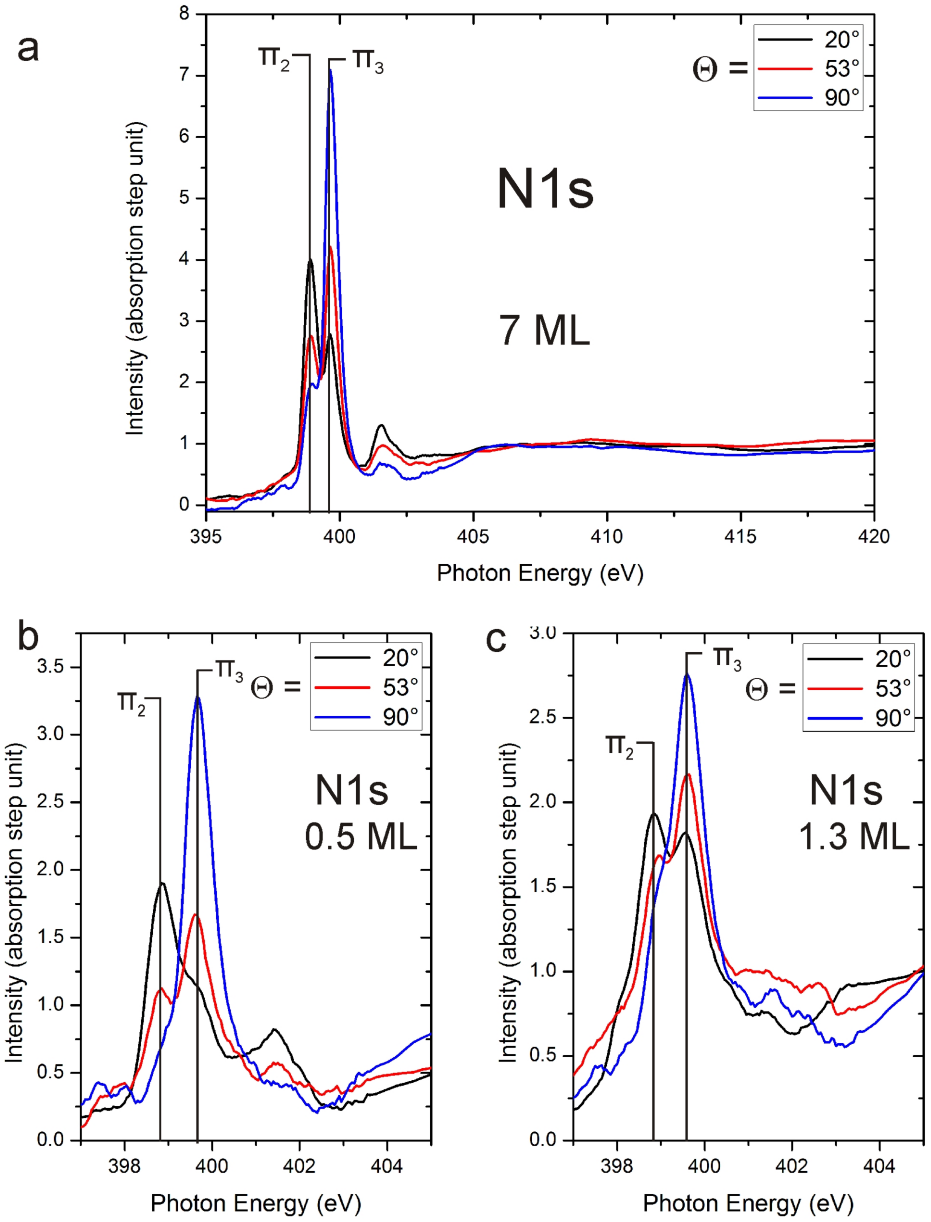

Figure 3.16: Angle dependent NEXAFS N1s spectra at 20°, 53° and 90° on Cu(111) with different molecular coverage of *m*NC-*p*Ph$_3$-*m*CN at 160 K. π_2 and π_3 are the prominent features resulting from the carbonitrile group. **(a)** Overview NEXAFS N1s spectra with about 7 ML molecular coverage. **(b)** Angle dependent NEXAFS spectra with 0.5 ML molecular coverage. **(c)** N1s spectra with a molecular coverage of about 1.3 ML at different photon incident angles (Θ).

		0.7 ML	1.3 ML	7 ML
C1s	$\alpha \pm 5°$	20	40	40
	$\beta \pm 5°$	25	45	35
	$\gamma \pm 5°$	70	50	55
N1s	$\beta \pm 5°$	30	45	35
	$\gamma \pm 5°$	70	60	65

Table 3.2: Overview on the angles resolved by NEXAFS analysis on the C1s and N1s edge, determining the orientation of the molecule on the surface.

Figure 3.16 *b* presents NEXAFS N1s spectra of the sub-monolayer regime (0.5 ML). The shape of the resonance distribution is comparable to the multilayer, but the differences of the intensities are enhanced. For example if θ is 90° the π_2 resonance almost vanishes and the π_3 resonance is reduced at $\theta = 20°$ appearing just as a shoulder. This suggests an orientation of the π_2 plane comparatively coplanar to the metal surface. The analysis of the resonances revealed an angle β of $30° \pm 5°$ and γ of $70° \pm 5°$ and supports a coplanar adsorption of the molecules.
The increase of the coverage to $\approx$ 1.3 ML depicted in figure 3.16 *c* changes the resonance intensities. The analysis of the changes reveals an angle $\beta = 45° \pm 5°$ and $\gamma = 60° \pm 5°$ accounting like the analysis of the intensity distribution of the C1s edge in figure 3.15 *b* for a tilt of the π_2 plane away from the sample surface.
The NEXAFS N1s spectra for all three molecular coverages were found to be comparable with their C1s analogons confirming the tilt of the entire molecule and hence the phenyl backbone lifts off from the surface according to the molecular coverage. Table 3.2 presents an overview on all resolved angles in the NEXAFS analysis.

XPS measurements

Along with the NEXAFS spectra XPS data have been acquired for the N1s and C1s edge. Figure 3.17 *a* presents an overview on subsequent XP spectra on the N1s edge performed at RT with increasing coverage ranging from 0.5 ML to $\approx$ 7 ML. For the first preparation with 0.5 ML (upper graph, lower curve) one peak is prominent at 399.5 eV (N_a) which we assign to a single species of N adsorbed on the Cu(111) substrate. Recent XPS measurements by Piantek of azobenzene derivates on Cu(001) exhibited a peak at 399.6 eV interpreted as a physisorbed species [236] and Rangan et. al. found on Si(001) for benzonitrile a peak at 399.5 eV [235]. The presented STM data (figure 3.12 *b,c*) agree with the homogeneity of the surface layer just like the NEXAFS spectra. At 0.5 ML a tiny side peak N_b is visible at 398 eV, which could arise from the adsorption of the molecules on step edges resulting in a

stronger interaction with the Cu atoms.

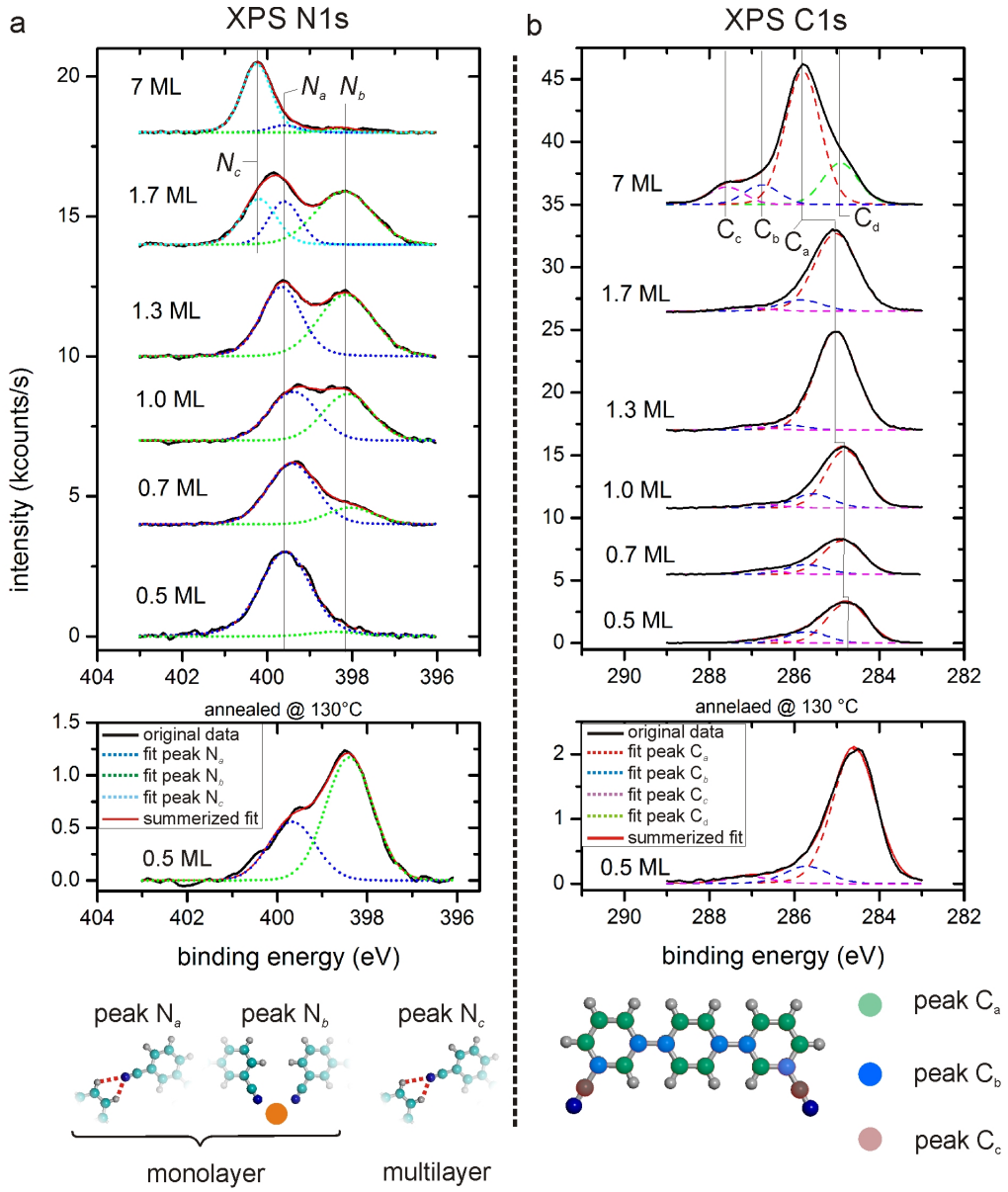

Figure 3.17: XP spectra of *m*NC-*p*Ph$_3$-*m*CN on Cu(111) with increasing molecular coverage at 160 K. **(a)** N1s XP spectra from 0.5 to 7 ML. On the bottom a XP spectra with a molecular coverage of 0.5 ML annealed to 400 K is depicted. The atomistic models at the bottom display possible interaction sites of the N resulting in the different peaks (N_a, N_b, N_c). **(b)** C1s XP spectra from 0.5 to 7 ML. On the bottom a XP spectra for a 0.5 ML preparation annealed to 400 K is depicted. The atomistic model groups the C atoms of the *m*NC-*p*Ph$_3$-*m*CN molecule resulting in the different peaks of the XP spectra (C_a, C_b, C_c).

By increasing the molecular coverage the area of peak N_b increases compared to peak N_a. At 1.7 ML a third peak N_c at 400.2 eV arises. In the multilayer just one peak at 400.2 eV is prominent which we assign to the N in the CN not in contact with

the surface. In order to understand the origin of peak N_b an annealing experiment up to 400 K was conducted based on a preparation with 0.5 ML coverage. The resulting spectrum is presented in the lower panel of figure 3.17 *a*.
By annealing the sample, the number of Cu surface adatoms is increased [239, 240]. STM measurements suggest, that the dicarbonitrile molecules remain on the surface while coordinating to Cu adatoms forming three− and fourfold coordination motives incorporated in an porous 2D metal organic network [89, 173]. Due to the coordination of the CN groups to the Cu adatom the screening of the N core electrons is increased the resulting peak is shifted compared to the brick-like structure to lower energies. Thus, we assign the peak N_b with an energy of 398.4 eV in the annealed preparation to a Cu coordination of the N species. Atomistic models on the bottom of figure 3.17 *a* illustrate our understanding of the surrounding of the N resulting in the different peaks.
During the measurements with increasing coverage the number of mobile Cu surface adatoms obviously is not as high as during annealing. However, metal coordination of N containing endgroups was proved at RT as well [241]. The growth of peak N_b in our measurements takes place in two ways. As shown for figure 3.13 *b* with increasing coverage the highly regular brick-like structure transforms into a combination of a linear and a zig-zag structure. Herein we propose a mixture of bond motives. In the zig-zag structure the molecules are connected by the interaction of adjacent N and H atoms. The molecules arranged in the linear structure point with their functional moieties towards the surface, i.e., the N of the functional group moves closer to the surface resulting in a stronger screening of the core electrons. Thus we assign the peak N_b to the signal of the Cu-N metal-ligand bonding.

		N_a	N_b	N_c	C_a	C_b	C_c
0.5 ML	energy $[eV]$	399.6	398.4		284.8	285.7	286.8
	area [%]	94.3	5.2		72.8	18.9	6.7
0.7 ML	energy $[eV]$	399.4	398		284.9	285.8	286.6
	area [%]	79.4	21.0		73.4	18.5	8.2
1 ML	energy $[eV]$	399.4	398.1		284.8	285.6	286.8
	area [%]	51.2	48.6		76.3	18.3	4.8
1.3 ML	energy $[eV]$	399.6	398.1		285.0	286.16	287.0
	area [%]	44.9	54.3		92.2	4.5	3.1
1.7 ML	energy $[eV]$	399.6	398.2	400.2	285.0	285.8	287.1
	area [%]	22.3	50.1	27.1	84.4	12.2	3.7
7 ML	energy $[eV]$	399.6	398.2	400.25	285.8	286.8	287.6
	area [%]	8.9	5.7	87.4	86.1	7.4	4.5

Table 3.3: Peak position for the evaluated peaks of the N1s and C1s XP spectra in combination with the related area enclosed in the fit curve.

As we demonstrated for the STM measurements increasing molecular coverage changes the surface pattern into a linear structure (see figure 3.13 *c,d*) and the zig-zag structure vanishes. In the XPS data we assign these changes to the growth of the peak N_b in the range of 0.7 to 1 ML molecular coverage, which is subject to the movement of the N closer to the surface while the molecular backbone planes π_1 and π_2 tilt away from the surface. A rehybridization of the carbonitrile group as shown for benzonitrile on Si(001) by Rangan et. al. could not be evidenced clearly [235]. But the broadening of peak N_b towards lower binding energy suggests a strong coupling of the CN species.

The XP spectra also have been analyzed on the C1s edge in an energy range of 280 to 290 eV. The best fit for the resolved spectra was achieved with three peaks for the coverage of 0.5 to 1.7 ML and with 4 peaks for the multilayer coverage. For the spectra with a molecular coverage of 0.5 ML the main peak is at 284.8 eV (see figure 3.17 *b* upper panel). Besides this two additional peaks can be evaluated at 285.7 eV and 286.8 eV. The peaks result from the different environments of the carbon in the molecule. The major part of the carbon atoms (12) are part of the phenyl ring exhibiting two covalent bond sites towards neighboring carbon atoms and one bond to a hydrogen atom(C_a). A second species (C_b) is covalently bond to three adjacent carbon atoms, 6 carbon atoms altogether. We assign a third species (C_c) to the C atom the CN group. The different species are depicted at the bottom of figure 3.17 *b*.

At low coverage like at 0.5 ML the main peak is positioned at 284.8 eV. Due to the highest intensity and in comparison with benzene and oligophenyl measurements

[242–245] we attribute this peak to C_a. The low energy of C_a could be a hint for a plane π_1 and π_2 adsorbed coplanar to the surface since this would result in a strong screening of the phenyl backbone by the surface. The C atoms we assign for the C_c species are subject to a strong interaction with the N atom, due to the high electron affinity of the N the core electrons in comparison to the C_b species are bond stronger to the core resulting in a XPS signal shifted to higher energies. Therefore we assign the peak with the highest energy to C_c.

With increasing coverage the three peaks $C_{a,b,c}$ shift towards higher kinetic energy. In the multilayer (7 ML) preparation the energy of peak C_a is shifted to 285.8 eV which we assign to the absence of the screening resulting from the metal surface [242, 243]. The shift of peak C_a takes place in two steps: initially it is small while increasing the coverage from 0.5 to 1.7 ML and becomes more pronounced for the multilayer regime. The first shift indicates a reduced screening of the molecular backbone by the surface which could result from the lift of the molecules off the surface. A second hint for this rotation is the reduction of peak C_c in comparison to the main peak C_a. We assign this to a shorter distance of the N to the surface (0.7 - 1.7 ML regime). A similar behavior can be seen in the spectra (figure 3.17 *b*) of the preparation with 0.5 ML molecular coverage annealed at 400 K. Here the peak C_c is reduced compared to C_a due to the metal coordination of the molecules. However the peaks are not shifted towards higher energies, which is a further hint on a flat adsorption on this sample and a lifted structure for coverage of about 1 - 1.7 ML. At high molecular coverage (7 ML) a fourth peak C_d emerges. We assign this peak to the contribution of molecular layers close to the surface.

Finally we propose an atomistic model concerning the positioning of the molecules in the linear structure at increased molecular coverage. Figure 3.18 presents our model with the phenyl backbone almost perpendicular oriented to the sample surface. A view perpendicular on the upright standing molecule is presented in figure 3.18 *a* and a side view along the molecular backbone direction in figure 3.18 *b*. For every linear segment we propose three molecules adsorbed with their CN groups on the hollow site of the metal surface. The length of a linear segment of 51.2 ($\pm$ 0.5) Å allows just three molecules, since a single species measures about 13 ($\pm$ 0.5) Å. The repulsive forces between the CN groups would prevent the adsorption of the two CN groups of adjacent molecules in neighboring hollow sites. Thus we placed the CN group to the next hollow site establishing an inter-lines distance of 5.2 ($\pm$ 0.5) Å. The length of the model fits well with the STM measurements. Between the molecules in a chain segment no molecular contrast or disruption is visible (see figure 3.13 *c,d*). The distance between the molecules suggests a host in the junction connecting the two

molecules, which could be provided by a Cu adatom. On the Cu(111) single crystal surface a large number of mobile surface atoms is available [239]. Furthermore, investigations with tetracyanoethylene (TCNE) on Cu(100) by Crommie et. al. revealed strong interactions between the adsorbate and surface resulting in a strong structural modification of the Cu(100), so called buckling [246].
We are not certain about the metal incorporation in the molecular structure, since the number of Cu atoms embedded in the structure is fairly high. The Cu adatoms could adsorb between the two CN groups. Here they could serve as an anchor for the molecules increasing the stability of the chain segment. As well the adatoms would explain the non-existent contrast in the chains which could be at a result of the molecular movement at RT as well. Another hint for metal incorporation into the linear motive is given by experiments on Ag(111) with increased coverage and additional Co adatoms resulting in a similar structure (see Appendix B figure 4.5). Without the additional metal adatoms the structure can not be found.
The interceptions between the chains (see figure 3.13 *c*) we assign to stress relief boundaries, which could be subject to the changes in the density of the molecular structure. Another possible explanation could be the surface buckling which would provide a natural explanation for the stress-domain pattern formation. In figure 3.18 *b* a view along the molecular backbone direction of the line structure is depicted. The neighboring rows could stabilize the structure by $\pi - \pi$ interaction between the aromatic backbone (marked with the red arrow), which has been reported in the literature up to distances of 4.8 Å [230]. π stacking in this system is not the main driving force, but increases the overall stability. The reorientation of the molecule in the linear pattern is a result of increased molecular coverage effecting packing constrains in combination with an altered balance of molecule-molecule and molecule-adsorbate interaction. At the same coverage on a Ag(111)sample the reorientation could not be evidenced. However subsequent Co coevaporation results in the described dynamical structure reorientation.

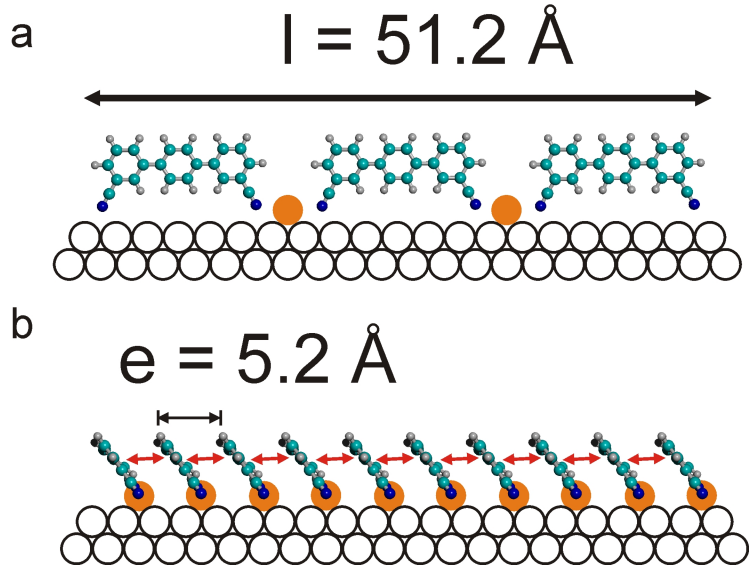

Figure 3.18: Atomistic model of the adsorption of *m*NC-*p*Ph$_3$-*m*CN on Cu(111) at increased molecular coverage. **(a)** Frontal side view of the molecular assembly with the phenyl backbone oriented almost perpendicular to the substrate and Cu adatoms (orange) between the molecules. **(b)** Side view into the in-line perspective of the molecular assembly with a distance between the chains of 5.2 (± 0.5) Å. The metal adatoms (orange) adsorb in hollow position.

3.3.3 Conclusion

In summary the results of the experiments reveal the change of the molecular orientation subject to the molecular coverage and the position of the functional moiety. Hence, by fine tuning of the employed sample, the molecular coverage, the functional groups and their position on the molecule, the orientation of the molecular backbone on the surface can be altered. The orientational changes observed by means of STM, XPS and NEXAFS give insight into the high affinity of CN substituents to Cu(111).

3.4 Competing Interactions in Surface Reticulation with a Prochiral Dicarbonitrile Linker

In recent experiments linear oligophenyls have been employed to create self-assembled molecular patterns on metal surfaces. In order to influence and steer the structure formation the molecules were functionalized with carbonitrile (CN) groups in specific sites. Two different species were studied until now: linear species with two CN groups in *para* position (*p*NC-*p*Ph$_x$-*p*CN) [10, 46, 47, 52, 88–90] and a non-linear species with its functional groups in *meta* position of the outer phenyl rings (*m*NC-*p*Ph$_3$-*m*CN) [173, 227]. Especially in metal-organic networks the resolved patterns exhibit striking differences. The *p*NC-*p*Ph$_x$-*p*CN molecules form highly regular honey-comb meshes on Ag(111) extended over wide areas with a predominant threefold coordination of the metal center [52, 90]. In contrast the *m*NC-*p*Ph$_3$-*m*CN molecules self-assemble in an open porous 2D random metal-organic network at the very same surface [173] with metal coordination centers in three- and fourfold coordination distributed in an equal ratio. A third species is introduced here to obtain better insight regarding the different behavior of the molecular subunits while metal coordination. We reduced the intermolecular degrees of freedom by substituting one CN group in *para* and one group in *meta* position, respectively. This results in two different organic supramolecular networks, whereby one exhibits a chiroselectivity. After coevaporating small amounts of Co a hybrid network comprising both hydrogen and coordination bond motifs was studied. Intriguingly, the CN group substituted in *para* position is favored for the metal coordination, whereas the *meta* substituted CN group remains in hydrogen bonding. An increase of the metal adatom ratio eventually promotes the self-assembly of a RT stable 2D random metal-organic network.

3.4.1 Introduction

We report here on $[1, 1'; 4', 1'']-$terphenyl$-3, 4''-$dicarbonitrile (*p*NC-*p*Ph$_3$-*m*CN) molecules (see figure 3.19) adsorbed on Ag(111) at low temperature (6 K) and room temperature (RT) studied by scanning tunneling microscopy (STM). Upon adsorption on a surface the prochiral molecule deconvolutes into two enantiomers and assembles in two organic structures named phase A and phase B. Each of the two structures is commensurate with the surface and is built of a homochiral dimer

motif constructing the pattern, respectively. Phase A is a RT-stable dense packed chevron like pattern containing both enantiomers in equal ratio. Phase B exhibits a hexagonal porous structure consisting of only one enantiomer and is not stable at RT. By coevaporating Co atoms a robust RT-stable 2D random network is formed. Surprisingly selective metal-ligand interactions lead to the preferred coordination of the functional group in *para* position to the Co forming a threefold star-like motive. These trimers interact weakly via the *meta* CN units and the phenyl ring hydrogen of adjacent molecules. When saturating the structure with Co adatoms also the *meta* positioned CN groups coordinate to the metal and a RT-stable fully reticulated metal-organic network evolves. In this disordered network three- and fourfold coordination of Co coexists featuring a diverse reactivity of possible Co reaction centers based on their degree of coordination.

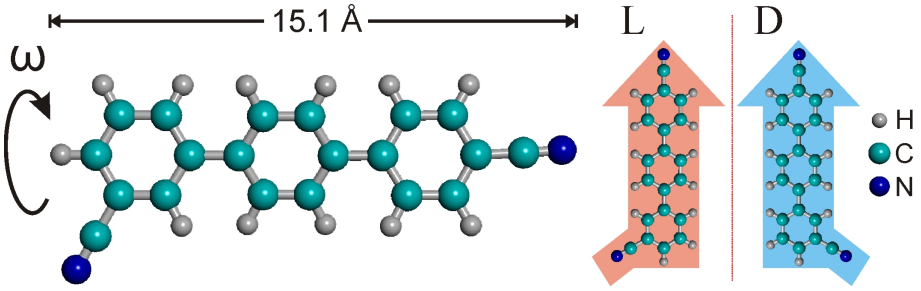

Figure 3.19: Atomistic model of $[1,1';4',1'']-$terphenyl$-3,4''-$dicarbonitrile (pNC-pPh_3-mCN) with an approximate length of 15.1 ($\pm$ 0.5) Å. ω is the rotation angle of the phenyl ring about the σ bond to the molecular backbone. Adsorbed on the surface the molecule deconvolutes into two enantiomers a L- and D-type marked with the red and blue arrow.

Experimental Methods & Materials

The synthesis of the rod-like $[1,1';4',1'']-$ terphenyl$-3,4''-$dicarbonitrile molecule was developed according to the published procedure by coupling bis-iodobenzene and two equivalents of 3-phenylboronic acid under typical Suzuki conditions with 10 mol% Pd(0). The geometry of the free molecule was calculated in the semi-empirical AM1 framework. STM images have been manipulated with WsxM [185]. The experiments were performed using a variable-temperature and a low-temperature STM (see section 2.1.4) using the same setting like explained in part one of this chapter. The employed Ag(111) substrate was prepared by standard procedures (cycles of Ar^+ sputtering and annealing) to obtain extended, flat terraces separated by monoatomic steps. The molecules were deposited from a quartz crucible in an organic molecular-beam epitaxial source at 450 K, with the substrate kept at 300 K. Subsequently, the submonolayers of the molecular films were exposed to a beam

of cobalt (Co) atoms, whereby the molecule-metal ratio was adjusted. After the preparation, the sample was transferred *in situ* to the STM where the topography was recorded at T = 300 K and 6 K. The images presented in figure 3.23 *a,b* were measured with the Aarhus-type STM. Figures 3.20 *a,b,c* and 3.21 *a,b* comprise micrographs recorded with the LT-STM.
First principale calculations were performed to further investigate the particular binding properties of $[1,1';4',1'']-$ terphenyl$-3,4''-$dicarbonitrile molecules. In order to simplify both the calculations and the interpretations, the substrate was not considered, and only the intermolecular binding was studied. It was done using the Projector Augmented-Wave (PAW) approach as implemented in the ABINIT code [247, 248], within the Local Density Approximation (LDA) for the exchange-correlation energy. The cutoff energy used is 30 Ry. Periodic boundary conditions were applied, and a minimal void spacing of 8 Å is present between image molecules, ensuring an error lower than 10 meV/molecule as drawn from convergence checks. All atoms are in the same plane, and full relaxation is allowed inside this plane.

3.4.2 Results & Discussion

Organic supramolecular network

Figure 3.20 *a* shows a STM topography overview at 6 K of the structures formed by the non-linear ditopic linker after deposition of 0.5 ML on a Ag(111) surface at 300 K. The molecule consists of three phenyl rings forming the molecular backbone connected by a rotatable σ-bond. Two reactive CN groups at the outer phenyl rings on *meta* and *para* position, respectively, enable the molecule to form 2D supramolecular networks [46, 52, 89]. Upon adsorption the prochiral molecule isomerizes into a leavus (L) and a dexter (D) enantiomer. To distinguish between these two isomers we marked the L- with red and the D-species with blue arrows. The arrowhead points into the direction of the *para* oriented CN group, whereas the direction of the *meta* CN group is labeled by the short tail pointing either left or right. After deposition a natural ratio of 50% D and 50% L can be assumed to be present on the surface [182]. On the surface the molecule is imaged as rod like protrusion with a length of $\approx$ 13 Å and an apparent height of 1 Å. Polyphenyl molecules are well known to adsorb preferentially with their π-system parallel to the substrate on noble metal surfaces such as Ag(111). At low coverage the molecules decorate preferentially the bottom side of the step edges. This suggests a high mobility of the molecules at RT. With increasing coverage the molecules assemble in islands.
The overview image (see figure 3.20 *a*) shows three terraces with two different molec-

ular patterns. A dense packed layer (phase A) in yellow and a honeycomb pattern (phase B) marked grey and blue are identified. Phase A has a coverage of 0.98 Mol/nm^2 which is significantly higher than of phase B (0.64 Mol/nm^2). In either phase the regular pattern is disturbed close to the step edges. Nevertheless, the lower step edge (marked with an arrow) seems to be the starting point for nucleation, since the first immobilized molecules are found here. The islands are extended over wide areas (μm^2 range) in a highly regular manner, just limited by the terrace size. We exclusively found one specific structure at a given terrace. RT-experiments show, that phase A is RT stable but phase B not. A 2D surface fluid of highly mobile molecules is present between the dense packed islands at RT. Phase B seems to grow from the gas phase while cooling the sample to 6 K.

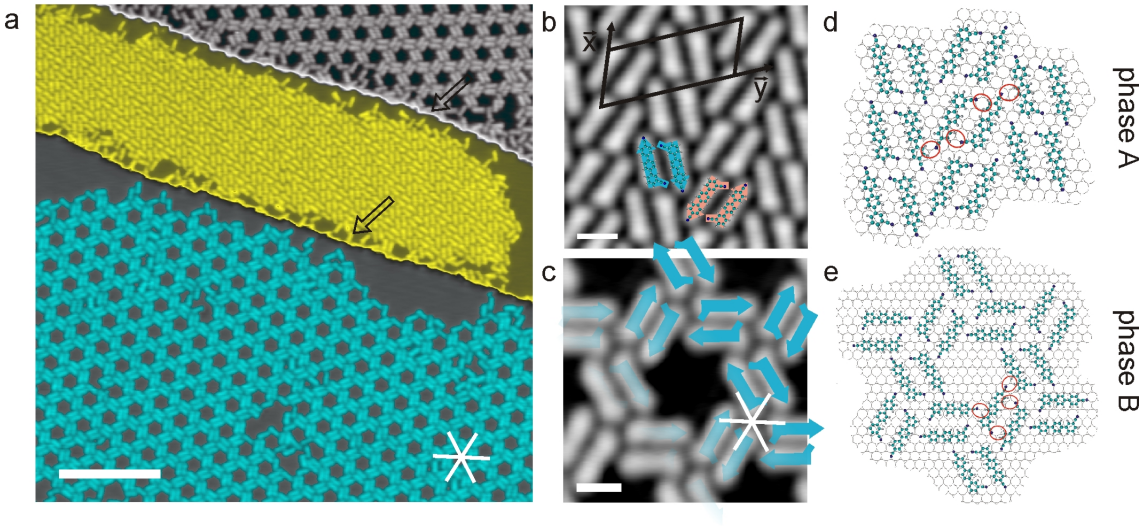

Figure 3.20: Molecular self-assembly of nonlinear dicarbonitrile linkers on Ag(111) at 6 K visualized by STM. **(a)** Two phases are visible on different terraces (U$_t$ = -0.6 V, I_t = 0.21 nA, scale bar 11 nm). The high symmetry directions of the surface are marked by the white star. **(b)** The dense-packed structure can be found in six orientations and exhibits a unit cell of 13.7×29.5 (± 0.5) Å^2 (U_t = -0.06 V, I_t = 0.41 nA, scale bar 1 nm). **(c)** A hexagonal chiral phase comprised of only one enantiomer (D) of the molecule (U_t = -0.05 V, I_t = 0.1 nA, scale bar 1 nm). **(d)** Atomistic model of the dense packed structure represented in **(a)** and **(b)**. **(e)** Atomistic model of the porous phase represented in **(a)** and **(c)**.

For detailed structure analysis high resolution low temperature STM images have been generated revealing a chevron like formation in phase A (Fig.3.20 *b*) and a porous hexagonal structure in phase B (Fig. 3.20 *c*). Phase A exhibits a basic bond motive (blue marked arrows in Fig. 3.19 *b*) comprising two molecules with the same chirality aligned parallel and interacting by $N\cdots$H bond formation between the *meta* positioned CN group and two hydrogen atoms of the neighboring

molecule phenyl ring. An atomistic model is depicted in figure 3.20 *d* and reflects our understanding of the position of the single molecule on the surface. The model is based on careful measurements of intermolecular distances and angles between the molecules combined with the knowledge that the preferred CN adsorption site is the hollow position. The organic bond motif forms the central dimer, visible in the atomistic model and marked with red circles. The bond distance within the dimer (2.2 Å) tends to be smaller compared to the distance between adjacent dimers (2.5 Å). The distances are consistent with ab initio calculations on CN terminated adsorbed porphyrins [187] and comparable to recent experiments on similar dicarbonitrile polyphenyl species [47, 52, 227]. Phase A contains both enantiomers in an equal distribution, in contrast to experiments presented in section 3, where the prochiral *m*NC-*p*Ph$_x$-*m*CN led to a close packed organic formation featuring chiral resolution.

A unit cell with a size of 13.7 × 29.5 (± 0.5) Å^2 is identified (Fig. 3.20 *b*) contains two mirror-symmetric dimers. Vector $\vec{x}$ is pointing into the direction of identical dimer rows. Three orientations plus their mirror symmetric counterparts exist reflecting the substrate threefold symmetry. $\vec{x}$ is tilted about 10° away from the substrate high symmetry direction. Even with the 10° tilt of the high symmetry direction the structures are commensurate. The fact, that phase B is exclusively built from only one enantiomer indicates that the molecules can change their chirality during network formation. This can only be achieved by a rotation of the phenyl ring with the CN-group in *meta* position parallel to the σ-bond connection of two adjacent phenyl rings. The feasibility of this rotary motion is supported by recent findings where complex adsorbed molecules undergo similar conformational changes [181]. The weak interaction of the phenyl ring with the substrate supports a rotary motion as well [195, 249]. The necessary surface lift off has been simulated for benzonitrile [187]. The absence of a moiré pattern and the extended defect free islands of phase A indicate a structure commensurate to the surface lattice. The white cross in the figure marks the single crystal orientation.

In phase B the dimer motive can be identified as well. Figure 3.20 *c* shows a high resolution image of the grey area in the overview (figure 3.20 *a*) superimposed with a structural model indicating the orientation and the chirality of the presented molecules. The formation consists of D molecules exclusively implying a chiral resolution during the self-assembly process. The dimer is oriented along the substrate high symmetry direction, marked with the white cross. The three dimer orientations merge in one point and form the central motive of phase B which builds a highly regular organic honeycomb structure. The blue area of figure 3.20 *a* is the

same structure composed of dimer motifs assembled by L molecules. The molecular backbone of the single molecule in the blue colored phase B is not oriented along the substrates high symmetry direction but tilted away 20° counter-clockwise. However, both orientations are commensurate with the substrate presented in figure 3.20 *e*. The pore size of the hexagons is ≈ 10 nm^2. To a small amount the pores host guest molecules but the homogeneity remains unaffected by the additional molecules. Defects have generally been found due to dislocations in the substrate or near step edges.

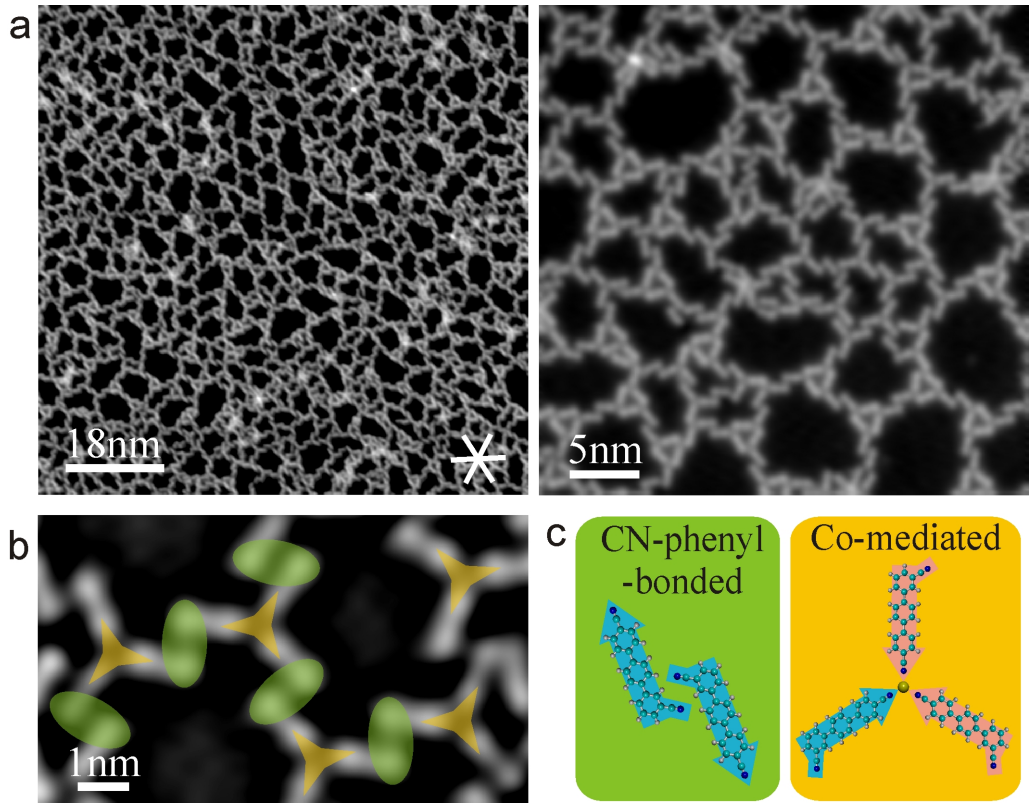

Figure 3.21: Hybrid Co coordinated and CN-phenyl random porous network visualized with STM at 6 K. **(a)** Two STM overview images on the structure after coevaporation of only a small amount of Co adatoms (U_t = -0.6 V, I_t = 0.11 nA). **(b)** High resolution topographic image of the structure combined with a superimposed color scheme marking the bond-nature. Green marks the CN-phenyl motive and yellow the Co-coordination (U_t = -1.0 V, I_t = 0.2 nA). **(c)** The atomistic model of the bond motifs are highlighted with the same color code to clarify the bond / chirality relation found in the network.

Selective metal-ligand interactions in a molecular network

The homogeneity and long range order of the organic formation vanishes after dosing a small amount of Co on top of 0.4 ML molecules and an open porous network depicted in figure 3.21 *a* occurs. From the image a ratio of 1:3 (Co : molecules) was evaluated. The network comprises a combination of Co coordinated and CN

to hydrogen oriented motifs showing pores with a size from 5 nm^2 to 50 nm^2. Surprisingly the Co is almost exclusively coordinated to the *para* positioned CN group building threefold star-like structures with metal coordination. For clarification the network had been inked (Fig. 3.21 *b*) to distinguish the different bond types. The star-like trimers are marked in yellow and they are non-covalently connected to adjacent trimers with the residual uncoordinated CN group in *meta* position (marked with green). A preferred bond site of the nitrogen towards the phenyl hydrogen could hardly be estimated, but the nitrogen favors to bind between two hydrogens of adjacent phenyl rings. The structure as a whole is not RT stable, however, at RT stable star-like metal-organic formations could be found diffusing on the surface (see Appendix B figure 4.3). The combined movement of the metal-organic motifs indicates a strong interaction of the Co, whereas an influence of the surface atomic lattice on the random network formation could not be observed.

Figure 3.21 *c* depicts an atomistic model of the two dominant bond motifs (CN-Ph interaction in green and a Co-coordination marked yellow). The CN group points towards the hydrogen atoms of a neighboring molecule. The yellow marked Co-coordination occurs here in a threefold manner exclusively. The motive is already known from hexagonal networks employing molecules with two *para* positioned CN groups and variable chain length (3 to 6 phenyl rings) [47, 90]. The star-like formation of the Co-coordinated structure exists with all combinations of enantiomers, however the interaction between the trimers is strongly dependent on the chirality of the molecules. Hence an ordered structure is hardly to be expected.

For the specific ratio of Co and molecules presented here the majority of the *para* CN groups are coordinated to metal centers. The lose *meta* CN groups are at RT potentially able to rotate about the σ-bond and can adapt to neighboring molecules establishing a $N^{\cdots}$H formation while cooling down.

In order to evaluated the origin of the different affinity of *para* and *meta* group towards the metal center first principle density functional theory calculations have been performed for molecular dimers by E. Arras at TUM-E20. For the analysis we tried to evaluate the respective bond strength per molecule in a hydrogen mediated formation. In figure 3.22 we present the most prominent bond formations for CN groups in *meta* and *para* position. The according energies per binding are specified in table 3.4. It is clearly visible, that the *m*-*m* motif features the highest binding energy. This binding motif offers as well a geometrical stabilization resulting in two non-covalent bonds influencing each other similar to a chelate reaction [250]. Hence we assume the different affinity of the CN groups to the metal adatoms is reflecting a free energy minimization of the entire molecule formation.

	p-m	m-m	p-p	p-p-p
E_B [meV]	340	600	436	310

Table 3.4: Evaluation of the energy per binding (E_B), calculated by first principle DFT calculation for the molecular motifs shown in figure 3.22. For the *p-m* binding motif the position of the CN group towards the adjacent molecule is essential and therefore varies between 220 and 340 meV.

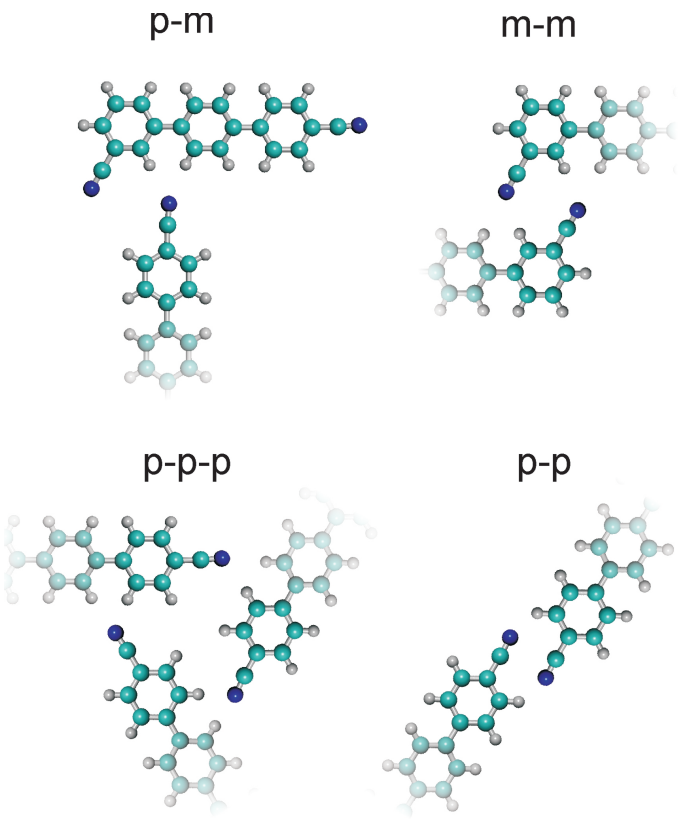

Figure 3.22: Atomistic model of the four most prominent CN-phenyl bond motifs displaying the positions evaluated by means of first principle DFT calculations.

Fully reticulated metal-organic network

By increasing the amount of Co in the molecular pattern a completely reticulated metal-organic network evolves. The preparation depicted in figure 3.23 *a* is characterized by an oversupply of Co resulting in a saturated metal-organic network formation. The Co-coordination is now the exclusive binding motive stabilizing the network. Herewith the stability increases and the network becomes RT stable. We can identify only few typical coordination motifs on a short scale. However no long range order exists. Bright spots on the surface are Co clusters and indicate excess of Co. A typical arrangement is illustrated in figure 3.23 *b* showing three- and four-fold coordinated chain motifs. Besides the chain motifs bifurcation motifs of the

pattern have been found exhibiting three- and fourfold coordination as well. A low molecular coverage leads to an enhanced number of chain motifs and by increasing the molecular coverage the bifurcation becomes more favorable. In contrast to the hybride network, described above, the fraction of the threefold coordination motifs dramatically dropped from almost 100% to 56%.

An overview on the node distribution evaluated from the preparation depicted in figure 3.23 *a* is shown in table 3.5. DFT calculations for a linear phenyl ring tailored with two CN groups on opposite sides indicates a energy preference for the threefold coordination of about 90 meV per coordination node [52]. In the present experiment the molecules exhibit an almost equal ratio between three- and fourfold coordination. The increased ratio of the fourfold coordination motive most probably arises from the preferential formation of metal-organic dimers (MOD). These MOD represent the main motive in the pattern and consists of two homochiral molecules aligned anti-parallel with their backbones and connected by a Co adatom between the CN groups. The atomistic model in figure 3.23 *c* displays two characteristic node formations predominant in the network including the MOD formation. The former predominant star-like formation is not a decisive structural motive anymore. For *m*-NC-*p*Ph$_3$-*m*NC a similar dimer formation was found [227] where the *meta* groups point towards each other and are coordinated by a Co adatom. Here the *meta* positioned CN groups coordinate with the Co metal adatom as well as the *para* CN group of the neighboring molecule resulting in a stable interaction of adjacent molecules. A single dimer only comprises one enantiomer, nevertheless the natural ratio between the two surface induced enantiomers is preserved in the overall structure. In contrast to the organic network, the influence of the chirality is confined to the interaction of two molecules constructing a MOD. The coordination of either functional group disables the backbone rotation and the adaptation of the chiral isomers. Therewith the entire character of adsorbate-substrate and adsorbate-adsorbate interaction is changed from commensurate organic structure with weak intermolecular interactions towards predominant metal coordination.

coordination number	three-fold	four-fold	five-fold	six-fold
fraction [%]	55.9	31.5	8.4	4

Table 3.5: Evaluation of the node distribution in the Co saturated molecular network shown in figure 3.23 *a*.

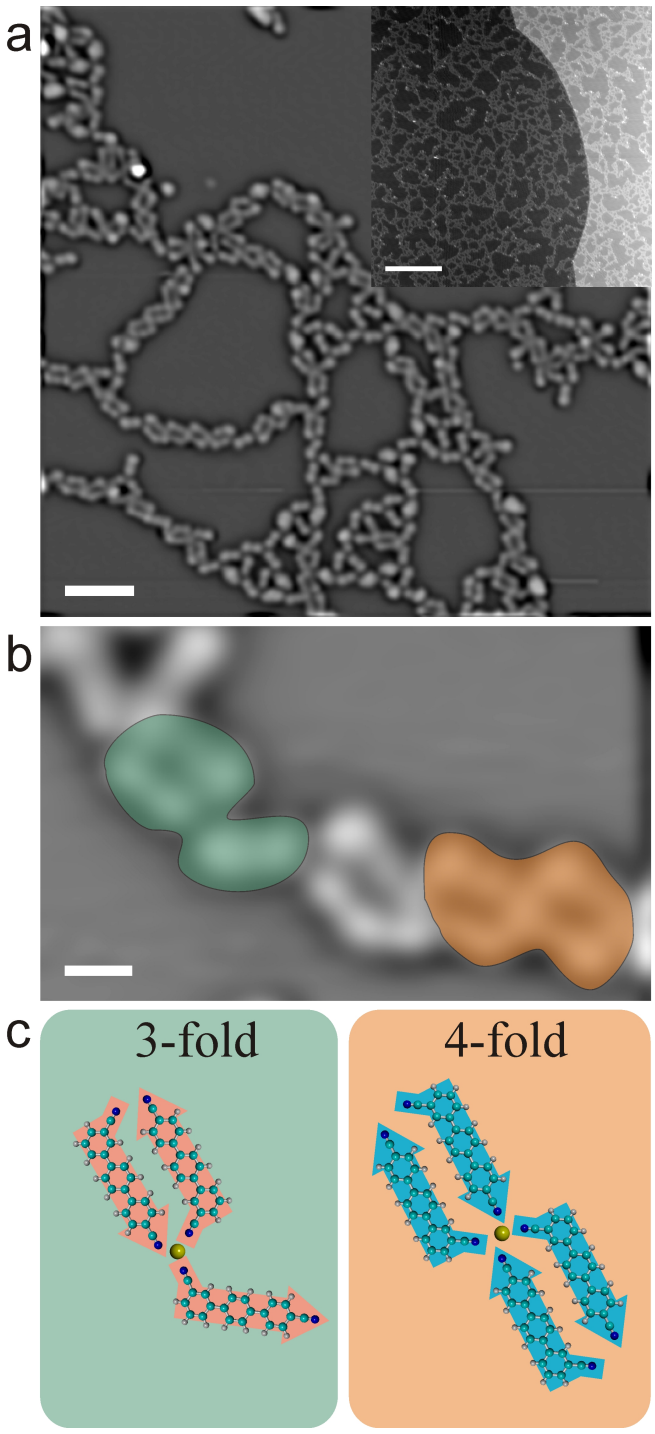

Figure 3.23: Molecular resolution STM image of a Co mediated reticulated metal-organic network formation. **(a)** Overview image on the open porous Co-coordinated network built up by repeated metal coordination motifs. The inset shows the metal-coordination network on a large scale (U_t = -0.66 V, I_t = 0.1 nA, scale bar 5 nm and 140 nm for the inset, 6 K). **(b)** High resolution image of the main bond motifs (U_t = -1.0 V, I_t = 0.2 nA, scale bar 1 nm, 6 K). **(c)** Atomistic model of typical three- and fourfold coordination motifs.

3.4.3 Conclusion

We studied the supramolecular and metal-directed assembly of the ditopic *p*NC-*p*Ph$_3$-*m*CN linker molecule on Ag(111) with STM at 6 K and room temperature. Our results reveal two isomers of the molecule on the surface forming two different layer structures, whereby phase B is enantioselective and phase A features the molecular isomers in equal ratio. The arrangement of the molecules in homochiral phases and the adaptation to adjacent molecules accounts for the rotation of the phenyl ring about the molecular backbone on the surface.

The coevaporation of metal adatoms reveals a structure with partial metal-organic binding which is not RT stable. Here the functional moieties of the molecule at *para* and *meta* position favor metal-ligand or CN-Ph interactions, respectively, in order to minimize the structure free energy. Additional Co evaporation created a fully reticulated robust metal-organic network constructed by distinct three- and fourfold nodal motifs. The structure features no long-range order similar to recent observations with a related asymmetric linker [173]. A central metal-organic dimer motif is the predominant subunit.

3.5 Additional Experiments on Porphyrin Molecules

3.5.1 Dimerisation boosts 1D Mobility of Conformationally Adapted Porphyrins on a Hexagonal Surface Atomic Lattice

Additional to the presented experiments concerning oligophenyl molecules we employed porphyrin molecules in order to determine the diffusion on metal surfaces and to get an insight on the adsorption site and the binding scheme between the molecules at room temperature as well as after temperature treatment. At first we employed temperature-controlled fast-scanning tunneling microscopy to monitor the diffusion of tetra-pyridyl-porphyrin (H_2-TPyP) molecules on the Cu(111) surface. The data reveal unidirectional thermal migration of conformationally adapted monomers in the 300-360 K temperature range. Surprisingly equally oriented molecules spontaneously form dimers that feature a drastically increased one-dimensional diffusivity. The analysis of the bonding and mobility characteristics indicates that this boost is driven by a collective transport mechanism of a metallosupramolecular complex. Annealing of H_2-TPyP molecules on the Cu(111) surface at 390 K leads to a molecular chain formation. The chain length herein is strongly related to the annealing time. Subsequent heating to 450 K results in the deprotonation of the porphyrin macrocycle accompanied by changes in the molecular appearance as well as slight changes in the molecular network.

Introduction

Here we present a scanning tunneling microscopy (STM) study on the mobility of the exemplary tetra-pyridyl-porphyrin (H_2-TPyP) on Cu(111). H_2-TPyP presents flexibility and internal degrees of freedom, as demonstrated in Figure 3.24. Our data reveal a direct correlation of conformational surface alignment and diffusion anisotropy. Moreover we observed how equally oriented H_2-TPyP upon rapprochement spontaneously form dimeric units that feature a drastically increased 1D diffusivity. This striking mobility boost directly contrasts expectations from a description of molecular surface migration in an independent particle model. The dimer formation is associated with the functional pyridyl moieties affinity to copper adatoms,

whence a coordinative coupling motif is suggested that mediates a collective transport mechanism of a metallo-supramolecular complex.

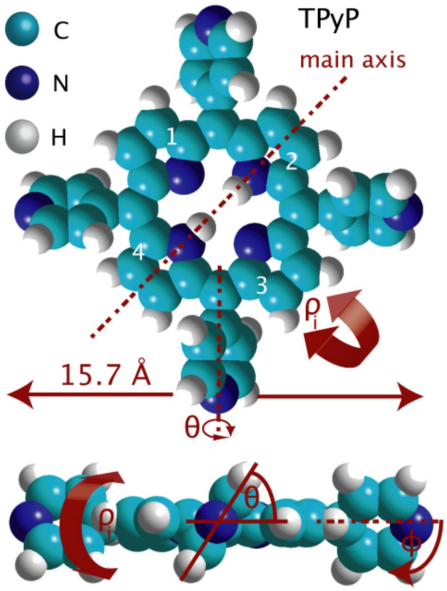

Figure 3.24: The top view model (upper panel) highlights the central porphyrin macrocycle and the four pyridyl groups. The side view (lower panel) displays the dihedral angle, θ, and the inclination angle, ρ, that determine the orientation of the terminal groups. The bending of the macrocycle is described by the angles ϕ.

Experimental Methods & Materials

The pre-preparation of the Cu(111) crystal was succeeded likewise described earlier. A submonolayer of H_2-TPyP was deposited by organic molecule beam epitaxy from a thoroughly degassed quartz crucible at 618 K. The images were acquired employing a variable-temperature Aarhus type 150 STM [116, 251] which was heated and equilibrated at a specific temperature in the 300 - 360 K range. The topography data was obtained with a tungsten tip in the constant current mode, typically at $U_t = 1$ V and currents below 1 nA ($I_t = 0.1$ nA) with an acquisition time of 12-14 s/image for the diffusion studies. In the employed high tunneling resistance regime ($R_T = 10\ \Omega$) the molecules' thermal surface motions were uninfluenced by the STM measurement process [113, 116, 251].

Results and Discussion

Upon adsorption on the Cu(111) substrate the H_2-TPyP molecules undergo a conformational adaptation resulting in a twofold symmetric configuration [252]. Following this we define the molecular main axis parallel to the long side of the rectangular envelope in the STM topography. Analyzing more than 8500 diffusion events

at different temperatures reveals exclusively unidirectional motion of the H_2-TPyP molecules. Figure 3.25 *b* shows the first image of a movie sequence comprising 250 frames recorded at 338 K. To demonstrate the unidirectionality of the adsorbate motion the image to image displacements and the averaged trajectories have been analyzed and are displayed in Figure 3.25 *c*. The motion is clearly unidirectional along the molecular main axis and thus follows exactly the high-symmetry directions of the hexagonal substrate. This is to our knowledge the first direct observation of a conformation-induced diffusion anisotropy of an adsorbed flexible molecular species. The adsorbed molecules have a certain chance to collide with each other during their 1D random walk. In the case of such an event their mutual orientation plays a crucial role for the mobility of the resulting aggregate. When the H_2-TPyP species molecular axes' points in different directions a reduced mobility is observed. However, if two colliding molecules are aligned in parallel with a displacement perpendicular to their motion direction such that just two pyridyl endgroups come together, metastable dimers evolve. These dimers are intriguingly much more mobile than the single molecules, while the unidirectional motion characteristics are retained. To visualize this mobility boost, five consecutive STM images are displayed in Figure 3.26, separated by a time lapse of 14 s. This selection from a series of more than 1000 images recorded at 338 K shows four monomers and one dimer simultaneously. Each entities displacement between consecutive frames is marked by an arrow. Between all subsequent frames, the dimer realizes a net displacement of several lattice sites, whereas only one of the four monomers performs a one-lattice-site hop (frame four to five).

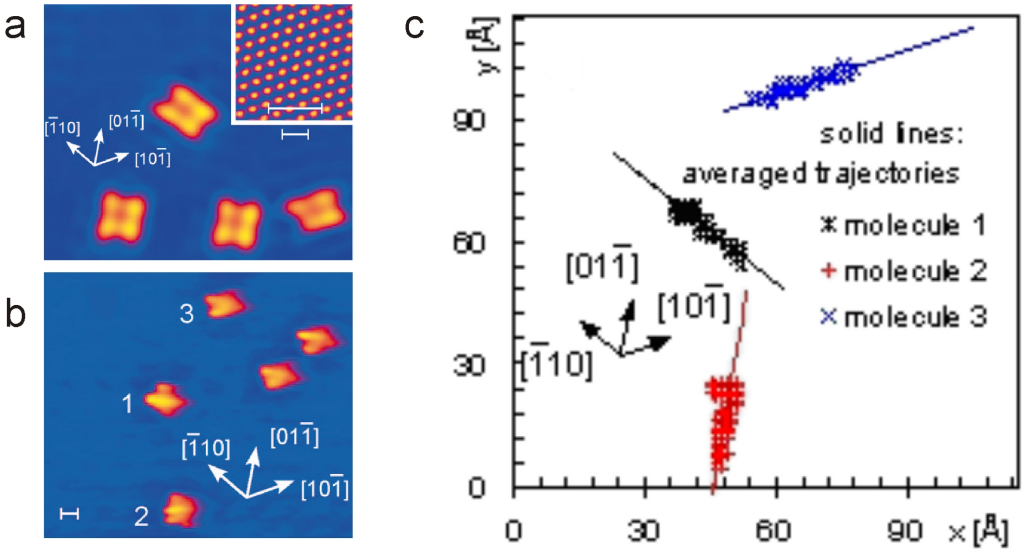

Figure 3.25: **(a)** Adsorption site and bonding configuration of H_2-TPyP on Cu(111): The overview STM image shows several H_2-TPyP monomers at 300 K with the molecular anisotropy axis indicated. Inset: Atomic resolution image of the substrate. **(b), (c)** Anisotropic thermal motion of H_2-TPyP at T = 338 K. **(b)** Initial frame of 250 consecutive images used for the trajectory analysis depicted in **(c)**. The averaged trajectories extracted from image-to-image displacements of the three molecules enumerated in **(b)** reveal anisotropic motion along high-symmetry substrate directions. Scale bars 1 nm each.

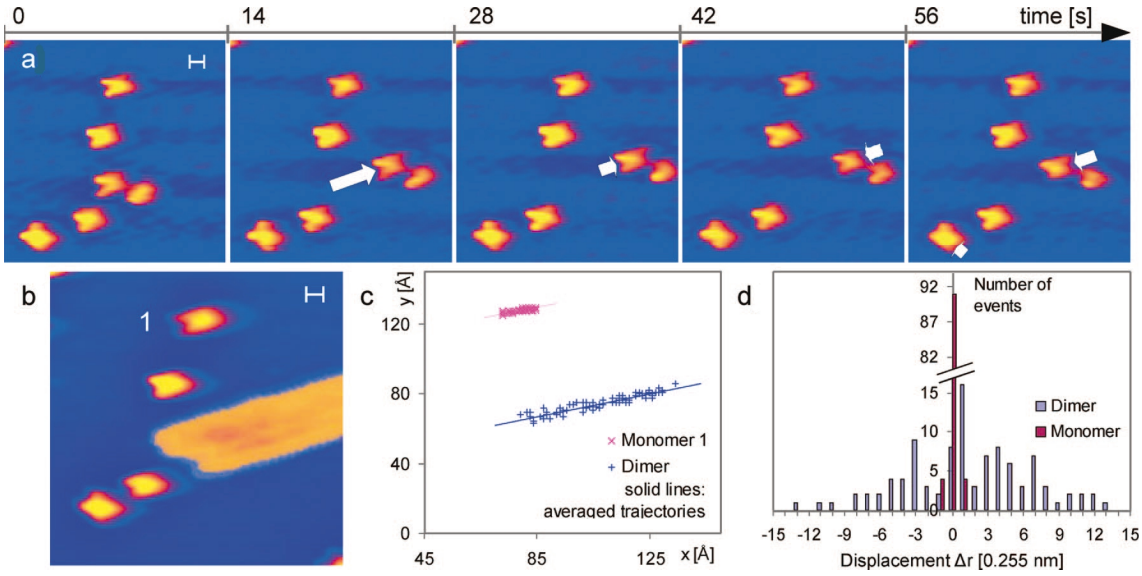

Figure 3.26: **a.)** Stills from an STM movie revealing the formation of a H_2-TPyP dimer with increased mobility at T = 338 K. Arrows indicate image-to-image displacements, for the dimer [+14; +4; -2; -5] in units of lattice spacing a = 2.55 Å] and for the monomer [+1], respectively. **(b)** Average over 100 images; the broad stripe represents all the dimer's positions. The plot in **(c)** represents extracted displacements of monomers and dimers from 99 image-to-image comparisons. The averaged trajectories visualize agitation along the [10$\bar{1}$] axis. **(d)** Corresponding net displacement histogram for monomers and dimers after 14 s each.

To emphasize the drastic differences in mobility, Figure 3.26 *b* shows a superposition of 100 individual images. The broad stripe whose envelope is indicated, beginning at the right end and reaching well into the middle of the image, is the area covered by the moving dimer (an STM movie visualizing the system dynamics can be found at www.e20.physik.tu-muenchen.de/Galerie). Also the trajectories analysis shown in Figure 3.26 *c* clearly demonstrates that the dimers' unidirectional motion is conserved while the respective mean square displacement is drastically increased compared to diffusion of isolated molecules. This behavior could be further substantiated in the jump-distance analysis considering 100 sequential images with moving monomers and dimers, respectively. The corresponding displacement histogram is reproduced in Figure 3.26 *d*. While imaging with a rate of 1 frame per 14 s the dimers show a net displacement of up to 14 lattice sites whereas the monomers show hardly any movement at all.
In order to systematically assess the dynamics of the unidirectional motion processes, single-molecule diffusion studies at different temperatures in the range 300 - 360 K have been performed. The mean square displacement $\langle(\Delta r)^2\rangle$ occurring within a time interval t was evaluated for each molecule to determine the hopping rate [253]:

$$h = frac\big\langle(\Delta r)^2\big\rangle\langle\lambda\rangle^2 \cdot t$$

The jump length of H_2-TPyP monomers corresponds to one lattice spacing (2.55 Å) and thus can be measured in integer multiples of it, leading to:

$$h = frac\big\langle(\Delta r')^2\big\rangle t$$

The obtained hopping rates were found to obey an Arrhenius law, in agreement with the thus far generally encountered behavior for surface diffusion of large molecules [32, 113, 116], i.e.,

$$h(t) = A \cdot e^{-\frac{E}{kT}}.$$

For the monomer diffusion we determined a migration barrier of $E_m = 0.96 \pm 0.09$ eV and a prefactor of $A_m = 1.4 \times 10^{12\pm1.4}$ Hz (extracted from the plot in Figure 3.27 .

The Arrhenius analysis for the dimers (assuming discrete single lattice unit displacements for their migration, as directly confirmed for moving dimers at 294 K) results within error bars in the same migration energy barrier as observed for the monomers. By contrast, the prefactor correlated to the dimer diffusion is increased by two orders of magnitude, i.e., $E_d = 0.94 \pm 0.03$ eV and $A_d = 1.9 \times 10^{14\pm0.5}$ Hz.

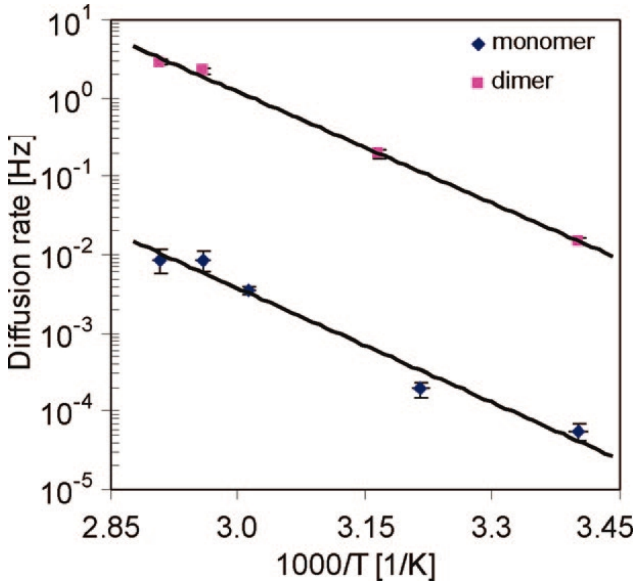

Figure 3.27: Arrhenius diagram for monomer and dimer motion in the 300 - 360 K temperature range. For monomer diffusion there is a migration barrier of $E_m = 0.96 \pm 0.09$ eV and a prefactor $A_m = 1.4 \times 10^{12\pm1.4}$ Hz , for the dimers $E_d = 0.94 \pm 0.03$ eV and $A_d = 1.9 \times 10^{14\pm0.5}$ Hz.

The first step for an understanding of the different diffusion characteristics is to clarify the nature of the dimer formation. The nitrogen atoms of pyridyl groups are partially negatively charged. Accordingly for H_2-TPyP adsorption on nonreactive noble metal surfaces such as Ag(111) these terminal groups tend to avoid each other [254]. By contrast, the presently encountered stable dimers are obviously interconnected through their pyridil groups and can be examined up to the maximum investigated temperature of approximately 360 K, indicating appreciable attractive interactions.

It is well known that on the low-index Cu surfaces thermally generated adatoms exist that can be engaged in the metal-directed assembly of 2D coordination compounds [252, 255]. Indeed, the affinity of the functional pyridyl groups to metal centers is a widely employed motif for metallo-supramolecular architecture [210]. This strongly suggests that the H_2-TPyP dimers are in fact stabilized by metal-ligand interactions with a Cu surface atom located between the pyridyl moieties. This interpretation is supported by high-resolution STM data and the corresponding atomistic model for the dimer reproduced in Figure 3.28 *a,b* respectively. The effect of Cu adatoms interfering in the molecular organization can be similarly recognized when annealing the sample to temperatures exceeding 400 K, whereupon well-aligned H_2-TPyP strings evolve (see Figure 3.29 *b-d* and 3.28 *d*. Within the chain segments H_2-TPyPs of exclusively the same conformational alignment (i.e., with parallel molecular axes) are linked by the coordinative coupling of now both

pyridyl endgroups. For the formation of these arrangements rotational molecular motions or diffusion events along directions off the easy diffusion axis must occur, that are made possible by the increased thermal energy [252, 255].

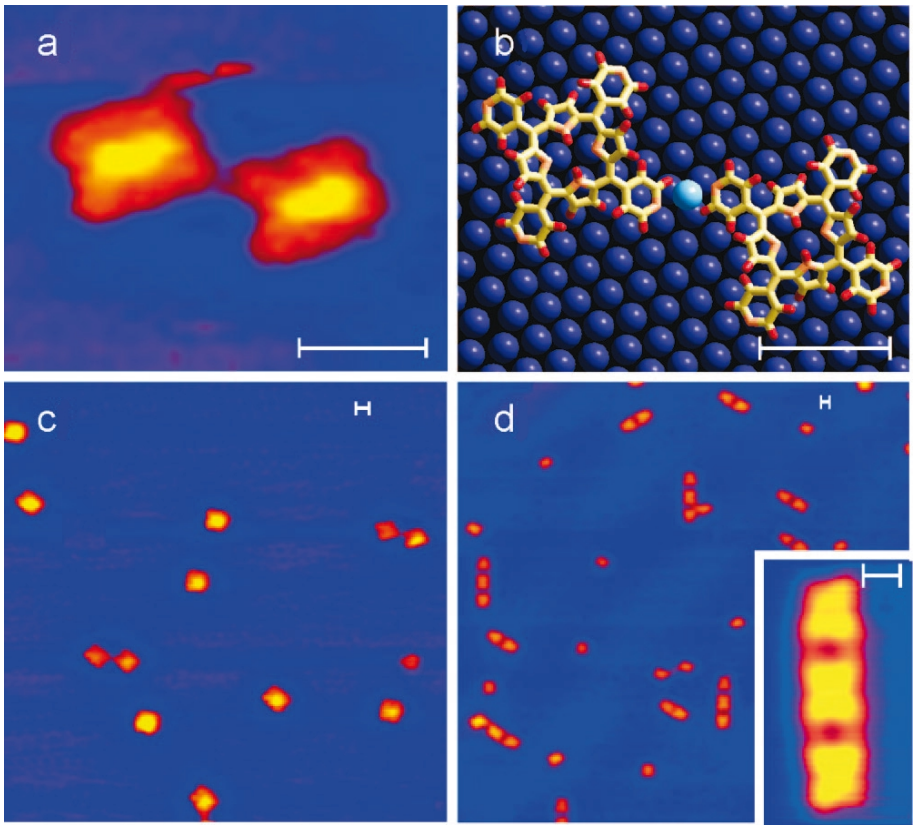

Figure 3.28: **(a)** High-resolution STM image of a H_2-TPyP dimer and **(b)** corresponding structure model showing a Cu adatom coordinated by the pyridyl ligands. **(c)** 'Overview image showing the coexistence of several dimers and individual molecules. **(d)** Upon annealing to T = 414 K for $\sim$ 30 min supramolecular strings evolve in a conformation-dependent metal-directed assembly where two pyridyl endgroups are linked (imaged at 300 K). Scale bars 1 nm each.

The microscopic understanding of the dimer mobility boost is considered as follows. Substrate-mediated or other attractive interactions of independently moving adsorbed molecules are expected to decrease their mobility [256] which directly contrasts our observations. A weakened interaction of the terminal pyridyl groups to the substrate due to additional lateral adatom coordination as well as a displacement of the dimer forming H_2-TPyPs from their preferred adsorption sites might be involved in this intriguing dynamic process. Furthermore the diffusivity enhancement for dimer motions indicates a qualitative change of the physics underlying the thermal migration. It is presumably related to collective motion mechanisms which have been previously encountered for adsorbed metallic clusters [257], CO

dimers on Cu(110) [258] or Au atomic strings in electrochemical environments [259]. Further theoretical work is called to develop a complete picture of the delicate interplay between molecular conformational surface adaptation, chemisorptive and lateral metal-ligand interactions that eventually determines the complex energy landscape experienced by the present porphyrin monomers and dimers.

1D metal-organic ribbon formation after annealing

In addition to the diffusion experiments implementing H_2-TPyP we conducted investigations addressing the formation of self-assembled structures. By dosing H_2-TPyP molecules on a Cu(111) surface kept at 300 K the molecules stay separated and barely interact with adjacent molecules. In figure 3.29 *a* single molecules are visible exhibiting the well known sandwich like shape with its main axis along the high symmetry direction of the crystal like explained above [241, 260].
At RT just randomly diffusion events of single molecules take place. With increasing temperature the hopping rate raises exponentially increasing the possibility of molecular interactions. Figure 3.29 *b* depicts an STM image after temperature treatment at 390 K for 10 min. The molecules now arrange preferentially in 1D molecular ribbons with an average length of 2.24 molecules. The molecular ribbons are oriented along the high symmetry direction of the substrate alike the single molecules accounting for a stationary adsorption site. The chains extended by increasing the annealing time to 20 and 80 min depicted in figure 3.29 *c* and *d*. After 20 min the average chain length is 2.56 molecules and after 80 min 3.24 molecules. Further annealing did not increase the chain length notably regarding this coverage. The coverage in the preparation of figure 3.29 *b*-*d* is about 0.3 ML, whereas we refer a full monolayer to a dense packed pattern of coplanar adsorbed molecules.
The statistical evaluation of the temperature treatment is depicted in figure 3.30. We analyzed the molecular ribbon length distribution for different annealing times. Subsequently we outlined the data in separate graphs. Three steps of annealing have been preceded with 10 min (red), 20 min (green) and 80 min (blue). According to extended annealing the single molecule portion decreased significantly from more than 27 % down to 5 %. The chain fraction incorporating two molecules is comparable after 10 and 20 min of annealing, but decreased for the benefit of chains containing 3 molecules after 80 min. After 80 min 13 % of the molecules found on the surface are subject to fivefold chains leading to the question of the movement and assembling of smaller chain segments. From earlier measurements in a temperature range of 300 K to 360 K we know that single molecules diffuse along their main axis and rotate at elevated temperatures from one substrate high symmetry

direction to the next. Hence while proceeding a random walk along the mandatory directions the single molecule could adopt to adjacent molecules and chains. The chain growth starts on the bare surface as well as on the step edges were single immobilized molecules could be found. With increased temperature we assume a diffusion of chain segments as well incorporating two or three molecules. Furthermore we assume, ones the molecules are bond via the metal coordination between both pyridyl groups the chains remain stable while annealing. For better comparison each chain distribution has been fitted with a Poisson distribution presented in each chart. All three Poisson fit curves have been added to the chart evaluated after 80 min annealing. The comparison of the fit lines shows the increased chain length from 2.24, 2.56 to 3.24 molecules in average.

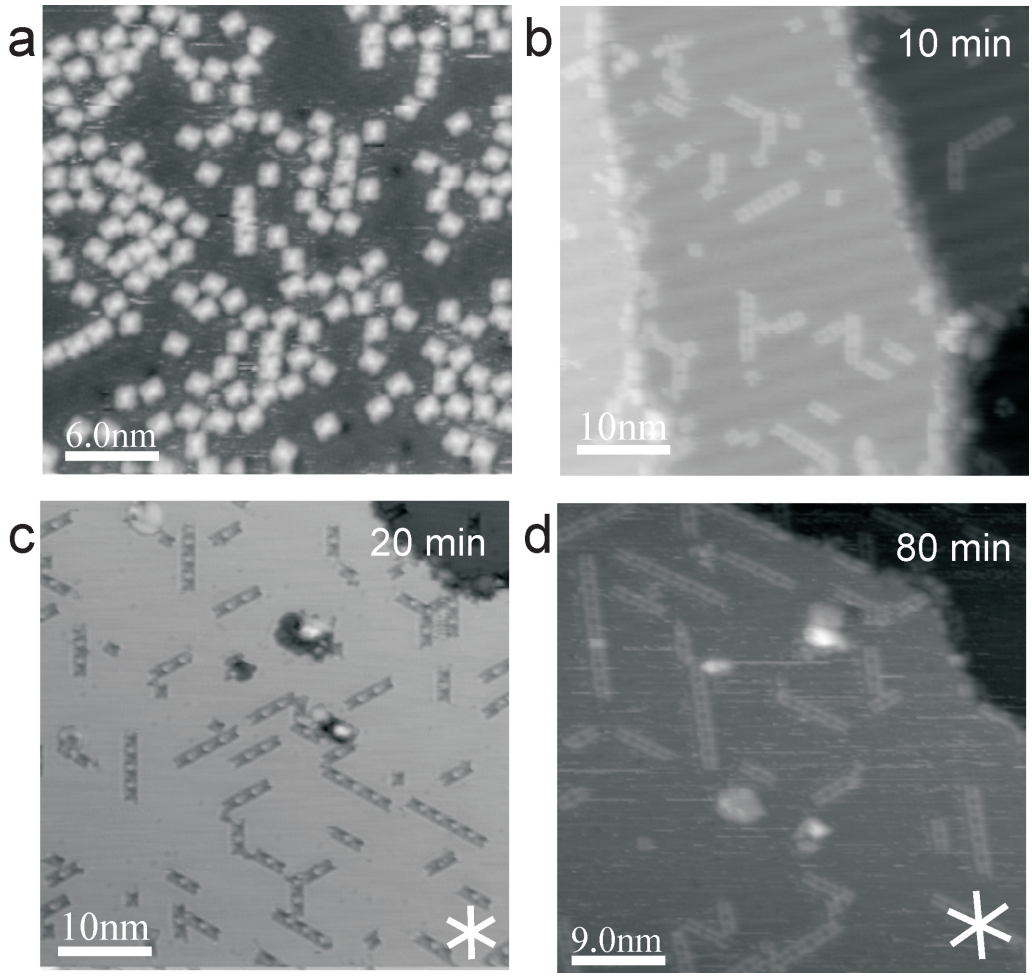

Figure 3.29: In consecutive experiments H_2-TPyP molecules on Cu(111) have been annealed up to 80 min at 390 K exhibiting increasing chain length. **(a)** H_2-TPyP molecules deposited at RT feature a single molecule appearance. **(b-d)** STM images of H_2-TPyP after different annealing times (10min, 20 min, 80 min).

Even at higher coverages longer chains could not be observed. Figure 3.31 *a* presents the H_2-TPyP molecule on Cu(111) with a coverage of about 0.4 ML after annealing for 30 min at 390K. In the image preferentially short segments are visible. An extended honey-comb formation could not be evidenced. Due to the high coverage an unusual binding motive can be seen, marked in green. The chain motive is not the exclusive bond motive anymore, bifurcations can be seen with three molecules coordinated via the pyridyl group and tilted each 60° to another. The inset of figure 3.31 *a* shows a high resolution image of a H_2-TPyP molecule with its typical two bright lobes in the center reflecting the molecular main axis. The bright lobes result from the so called saddle shape formation of the molecule subject to the conformational adaption to the surface [260]. The bright features are surrounded by four lobs identified as the pyridyl legs. The pyridyl groups are well known to coordinate with metal adatoms [28, 261]. On the Cu(111) surface especially while annealing an enhanced number of Cu atoms diffuses on the surface deriving from heat evaporation of the step edges [239]. The Cu coordinates with the pyridyl groups enabling the molecule to adopt to an adjacent molecule via a Cu bridge. In figure 3.31 *a* and *e* these chain motives are apparent. To form linear motives the molecules have to be parallel with their main axis and positioned on the same atomistic row. The rotation of a single molecule from one substrate high symmetry direction towards another was already described earlier. Molecules oriented in different directions form metal-organic structures as well. They coordinate about one edge visible in the green marked areas of figure 3.31 *a*. Based on this motive honey comb formations were found on a small scale.

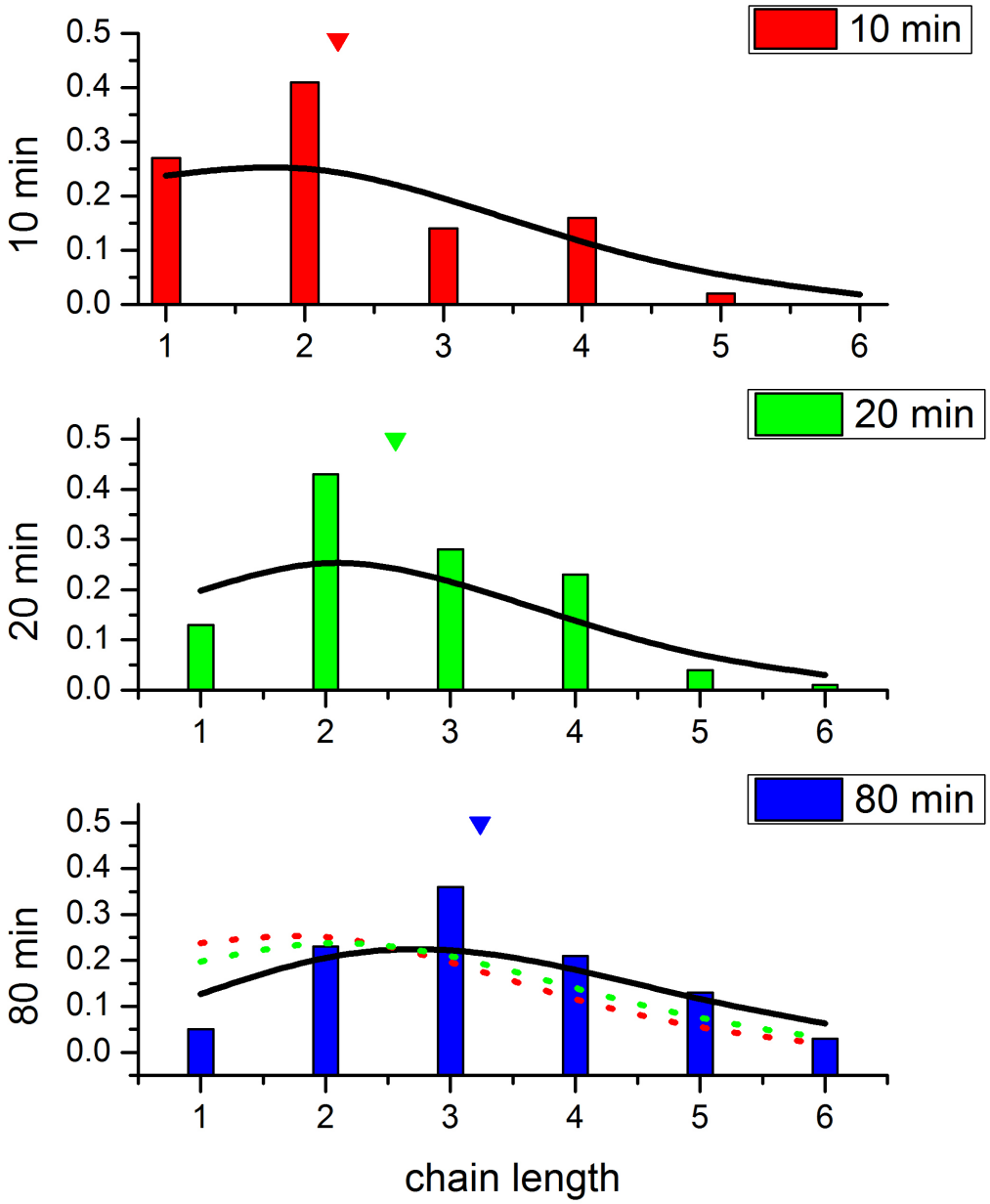

Figure 3.30: Statistical evaluation of the 1D molecular ribbon growth after 10 min (red), 20 min (green) and 80 min (blue) of annealing at 390 K. Every chart is superimposed with a Poisson distribution (black). For better comparison all three Poisson fits are plotted in the chart depicting the distribution after 80 min annealing. The colored triangles mark the average chain length subject to the annealing time.

The detailed description of the adsorption site of the molecule on the underlying atomic lattice is challenging since in normal conditions molecules and substrate atoms can't be resolved in the same time. The exact position of the H_2-TPyPs was determined based on LT-STM measurements utilizing CO molecules as markers [260]. Subsequently an atomistic model could be evaluated depicted in figure 3.31 *c*. The center of the molecule is found in bridge position, whereas the center

hydrogen atoms are oriented along the high symmetry direction of the substrate. Between two molecules a distance of 15.5 Å was measured accounting for a bond distance of 2.5 Å between the N in the functional pyridyl group and the Cu atom. The connecting Cu molecule sits in hollow position [260].

Taking a closer look bright lobes are visible in the chaining motives between some molecules (figure 3.31 *a* red area). While measuring the distance between the centers of two adjacent molecules a variation in the distance becomes apparent. The molecules aligned via the bright lobes exhibit a periodicity of 18.5 Å, whereas the centers of the molecules connected without the bright lobes are separated by 15.5 Å. Regarding to Ref. [262] and [260] the difference can be explained by an additional Cu atom. Thus we assume for the metal coordination of two H_2-TPyPs exhibiting bright lobes between the molecules two Cu atoms connecting the pophyrins. Each Cu atom here is adsorbed in hollow position. The bond distance of N towards Cu is about 1.9 Å, which is in very good agreement with theoretical predictions [20]. A corresponding atomistic model is depicted in figure 3.31 *d*. The appearance of the double Cu bridge can be explained by the combined diffusion of the porphyrin and the Cu adatoms coordinated to the N in the functional groups.

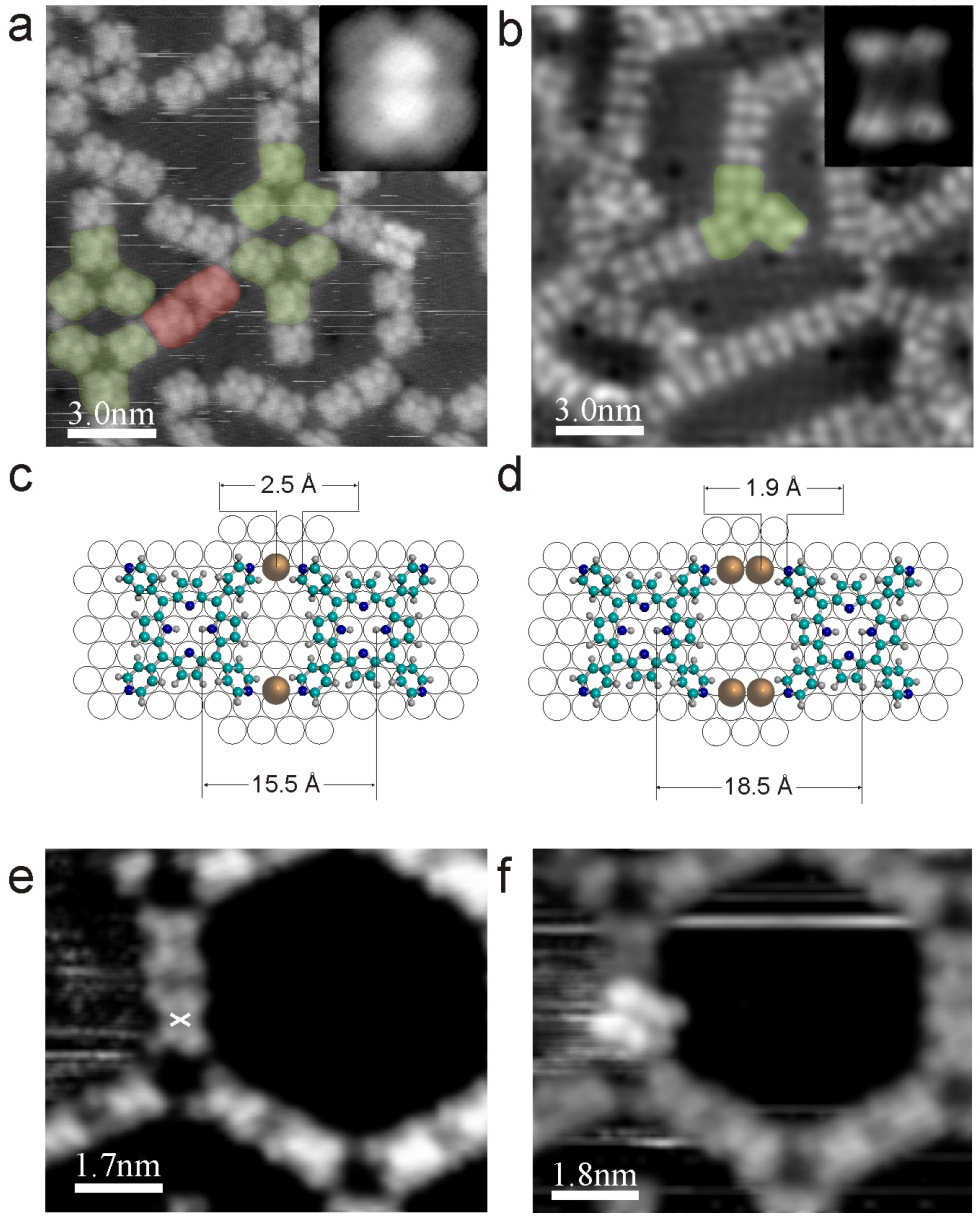

Figure 3.31: Metal-organic network formation of H_2-TPyP molecules on Cu(111) at RT. **(a)** STM image of H_2-TPyP molecules exhibiting two binding schemes (linear and bifurcation). The inset presents a high resolution STM image of H_2-TPyP. **(b)** Temperature induced deprotonation of the porphyrin macrocycle after annealing to 450 K. The inset presents a high resolution image of the deprotonated porphyrin. **(c)-(d)** Atomistic model of the Cu coordinated H_2-TPyP enclosing one and two metal atoms respectively. **(e)-(f)** Tip induced deprotonation of a H_2-TPyP molecule induced by a 4.9 V pulse changing the molecular appearance and orientation on the metal surface.

Temperature and tip induced deprotonation of H_2-TPyP

Annealing up to 450 K strongly alters the appearance of the molecules. In figure 3.31 *b* a change in the molecular structure can be seen. The bright center lobes

of the sandwich like structure disappeared and just four square like lobes remain accounting for a constitutional change in the molecule. A detailed view on the deprotonated molecule is depicted in the inset of figure 3.31 *b*. Since the effect was probed after several tip formings it is not related to changes of the tip apex. Klappenberger and co-workers revealed by incorporating NEXAFS and XP spectra techniques that the change is based on the deprotonation of the center hydrogen atoms [260]. Apart from that, the conformation of the molecule remains the same. Thus, the structural change appearing in the STM image is manly an electronic effect. The deprotonation seems to have no influence on the chain formation but changes in the bifurcation bond motive are visible (marked with green in figure 3.31 *b*). The edge to edge bond of the pyridyl legs mediated by a Cu adatom is vanished. Now the bright lob assigning for the pyridyl group is oriented to the center of the adjacent molecule. The lobes point towards an adjacent molecule appear higher in the STM image than the one pointing to the bare surface. The deprotonation of the center hydrogen atoms is not just possible by annealing. Tip induced bias pulses over the center of the molecule resulted in the same effect locally and controllable for a single molecule. Figure 3.31 *e* and *f* are consecutive images. By placing a 4.9 V bias pulse on the center of the molecule marked with the white *x* the molecule changes its appearance and position. The molecule now exhibits the typical cloverleaf structure found for molecules annealed to a temperature > 450 K. As well the position of the molecule seems to be rotated pointing with the lobe towards the center of the adjacent molecule.

Conclusion

In conclusion, we demonstrated that the conformational surface adaptation of large organic molecules strongly interferes with the diffusion characteristics. The saddle-shape of the studied tetra-pyridyl-porphyrin leads on the high-symmetry Cu(111) substrate to unidirectional diffusion up to ~ 360 K. The H_2-TPyPs functional pyridyl endgroups are essential for the adsorbate-substrate interaction and can capture thermal Cu adatom and form a dimeric coordination complex with another adsorbed porphyrin. When consisting of equally oriented H_2-TPyPs, these dimers show a drastically increased diffusivity which is again unidirectional. This phenomenon is ascribed to a collective motion mechanism of the entire supermolecule on the underlying copper atomic lattice. It is suggested that these observations are important to steer self-assembly processes for supramolecular architectures on surfaces [3, 92] and develop a comprehensive understanding of the physics underlying the transport processes of complex adsorbed species and aggregates theory.

Upon annealing in a temperature range of 300 - 470 K three different phases of the H_2-TPyP could be resolved. At RT the molecules are predominantly separated on the surface. By annealing the sample to 390 K 1D metal-organic ribbon formation could be created, whereas the chain length is determined by the annealing time. The metal-organic bond motive could be assigned to a metal coordination between thermal Cu surface atoms and and functional pyridyl groups. A third phase arises after annealing to > 450 K. Characteristic changes of the molecule appearance are subject to the deprotonation of the molecular macrocycle resulting in changes of the electronic structure of the molecule.

3.5.2 From 1D Metal-Organic Ribbons into a 2D Surface-Fluid, following the Movement of Molecular Chains on the Cu(111) Surface.

In the past decade enormous effort was put to reveal self-assembly and self-recognition processes leading to a basic understanding of hydrogen bond networks [44, 166, 180, 194], dipole-dipole and Van der Waals interaction [20, 69, 263], metal-coordination [52, 89, 227] mediated networks and covalent bond pattern formation [205]. Information about the stability of the molecule and their formations as well as information about diffusion properties and restrictions can be found by employing variable temperature STM measurements [32, 113, 116, 253]. Employing statistical data analysis the hopping rate and the diffusion barrier could be evaluated. Here we present the movement and melting behavior of a porphyrin derivate (BCA-235) forming 1D metal-organic ribbons on Cu(111).

Introduction

The interaction of molecular entities is strongly dependent on the substituents (ct. chapter 1). By changing the functional groups the properties of the arising network can be predetermined to some amount. The porphyrin molecules implemented in the previous experiments with H_2-TPyP have four pyridine end-groups substituted on the macrocycle, providing four possible binding sites. In the following experiment the porphyrin macrocycle incorporates a zinc (Zn) atom and the substituents are altered into two *tert*-butyl and two pyridyl substituents. The pyridyl group is selected to steer the metal-organic interaction. Hence the possible binding sites are reduced to allow for chain formation.
In recent experiments Heim et. al. found a metal-organic coordination pattern constructed by the BCA-235 on Cu(111) and Ag(111) with additional Cu adatoms

at 6 K [264, 265]. Here we investigated the stability of the metal-organic coordination binding of pyridine functionalized porphyrin molecules by increasing the sample temperature stepwise. We could follow the gradual ″melting″ of the 1D molecular structure. The starting point of our experiments has been the measurement at 180 K where the molecular structure is immobilized. At 210 K the first motion of single molecules in terminating chain positions could be visualized and was followed by the movement of entire chain segments at 240 K. Here the assembly and reassembly of molecular chains could be studied as well. Further increase of the temperature (300 K) leads to the formation of a molecular surface gas. With raising temperature (320 K) the gas-fraction becomes dominant and immobile molecules are just visible on step edges and defects.

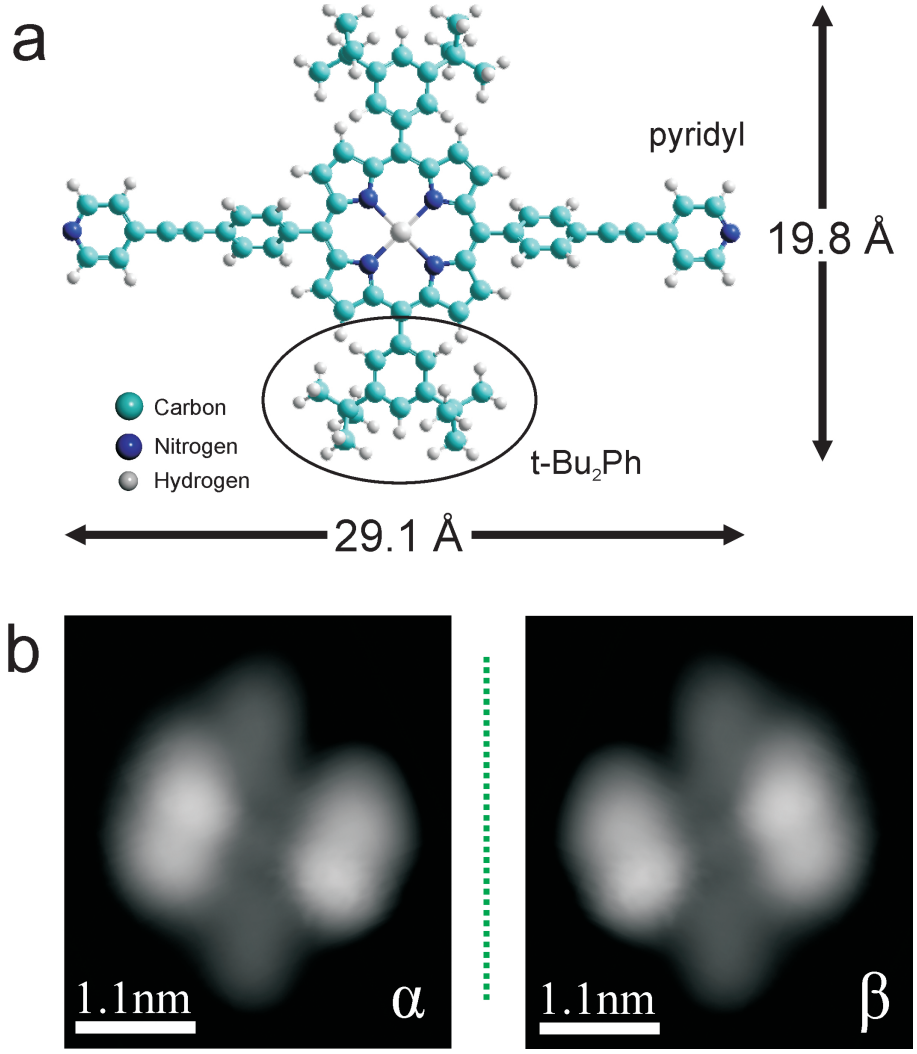

Figure 3.32: Atomistic model and high resolution STM image of a porphyrin derivate (BCA-235). **(a)** Atomistic model of the BCA-235 molecule with two pyridyl groups and two 3,5-de-*tert*-butyl (*t-Bu*$_2$Ph) on opposite sides. **(b)** High resolution STM image of the porphyrin molecule in the chiral conformation α and conformation β on Cu(111) at 6 K. The green dotted line displays the mirror symmetric plane.

The porphyrin derivate (BCA-235) presented in figure 3.32 *a* is based on a tetrapyrrolic core with a Zn center. Two different functional groups are substituted in *meso*-position, two phen-1,4-diylethynylpyridyl groups in 5,15 position and two 3,5-di-*tert*-butyl (*t-Bu*$_2$Ph) substituents in 10,20 position. The *meso*-groups are free to rotate about the macrocycle-phenyl axis within the limits of steric repulsion. The substrate influences the rotation of the *meso*-groups based on π-orbital metal interaction, atomic corrugation and the geometric structure of the surface. Typically the macrocycle is found to be distorted due to intermolecular hindrance [266] into a saddle shape [43, 252, 267]. High resolution STM studies at low temperature resolve two conformational isomers α and β emerging from the rotation of the butyl groups

off the molecular plane and by the folding of teh pyridyl legs [264, 265, 268] shown in figure 3.32 *b*. The asymmetric shape of the two isomers can easily be seen. The left molecule we further refer to as isomer α and the right isomer we further refer to as β. The bright lobes in the horizontal axis result from the butyl groups [20, 269] and the pyridyl legs appear as elongated lobes oriented along the vertical axis. The lower side of the butyl group is rotated to the surface.

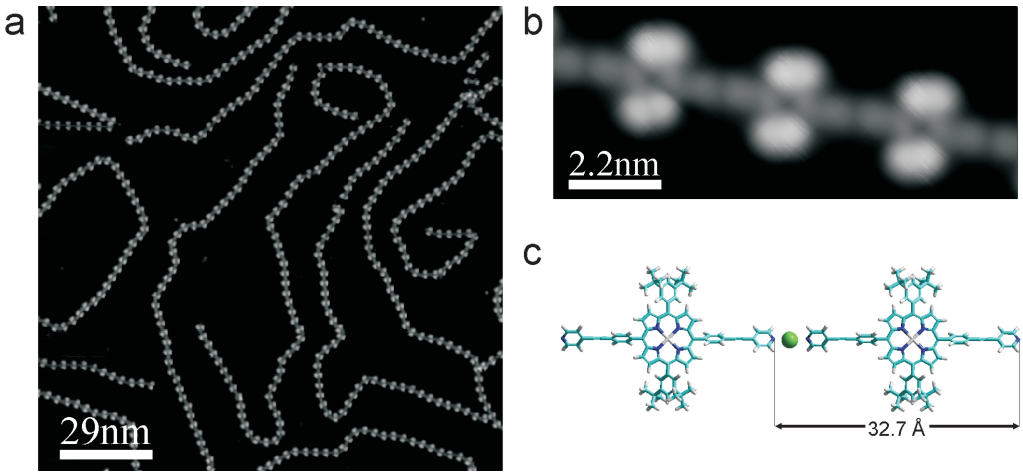

Figure 3.33: Metal organic chain formation on Cu(111) at 6K. **(a)** Overview on the 1D string formation of BCA-235 by metal coordination. **(b)** High resolution STM image of the metal-organic binding motive. **(c)** Atomistic model of the metal-organic binding motive exhibiting a length of 32.7 Å.

After dosing the molecule on the Cu(111) substrate kept at 350 K elongated 1D chain like structures emerge. Figure 3.33 *a* shows an STM overview image on the structure resolved at 6 K with a coverage of about 0.2 ML. Elongated curved structures with variable length and a width of 19.5 Å can be seen. By combining linear and curved segments the structure appears highly flexible. Careful data treatment by D. Heim et. al. revealed clearly periodic features wherein the chains are aligned in a corridor of $\pm 15°$ with respect to the substrate high symmetry direction and exhibit a molecular center to center distance of 32.7 Å [265]. Preferentially even at higher coverage the chains tend to avoid interaction with each other indicating repulsive forces among the chains. Further analysis revealed a metal coordination of the adjacent molecule in the chain by Cu surface atoms [239]. This model could be supported by the Cu to N distance of 1.8 $\pm$0.2 Å which is in very good agreement with measurements by Lin et. al. and [159] theoretical DFT calculations revealing a distance of 1.9 Å [241].

Results & Discussion

At low temperature tip manipulation experiments revealed a strong intermolecular coupling of the metal-organic chains. By dragging the tip over the surface in a controlled manner single molecules on the end of a chain and whole chain segments could be manipulated [265]. Chain movement can be promoted as well by increasing the temperature. Figure 3.34 *a* shows consecutive STM images at 180 K featuring a metal-organic ribbon formation. The structure is stable and the single molecules incorporated in a chain can easily be discriminated. The comparison of the consecutive images reveals at some points small changes of the chain position. The area highlighted red includes a molecule with a free coordination site. From one image to the next we can see the movement of the molecule about the metal coordination towards the adjacent molecule. In the yellow inked area molecular chain movements while scanning are shown. This could be due to the tip influence, since the comparison of a series of consecutive images revealed no significant chain movements at 180 K. The movement of more than single molecules could be observed at a temperature of 210 K presented in figure 3.34 *b*. The red areas again highlight the location of molecular movement. We can now follow the motion for every single coordinated molecule from on image to the next.
By increasing the temperature to 240 K the motion of large molecular chains can be verified. The red marked areas show lose chain segments migrating over the surface. The blue surrounded area highlights a pore varying the enclosed area by embedding new molecules into the chain. We can follow the reorganization of the chain segments itself. The green area in the lower part of figure 3.35 *a* presents in the first and second image the breaking of the metal-coordination bond. In the third image of figure 3.35 *a* the lose chain ends coordinate forming a new chain segment. Highlighted in red the movement of a lose chain end is visible migrating in the consecutive images. Further dis- and reassembly migrations can be found in the two other green marked areas. By increasing the temperature to 270 K (figure 3.35 *b*) the chain segments change completely from one image to the next. The migration and reorganization can be tracked by starting from step edges or impurities. In some small areas the structure can not be resolved any more due to the fast movement of the chain segments and single molecules. We highlight this areas red and associate them with a 2D surface fluid. Further increasing of the substrate temperature increases the areas filled with the surface fluid. At 300 K (figure 3.35 *c*) it covers about one third of the image as can seen by the red areas. Up to now the placement of the chain segments on the surface was random. Starting from 300 K the chains preferentially start at step edges and impurities and migrate about

their anchor point. These findings become even more pronounced by increasing the temperature up to 320 K. Here the surface fluid is the dominant phase and molecular chains, fixed by their anchoring point can be hardly seen (figure 3.35 *d*). The area covered by a surface fluid is notably larger clarifying the reallocation of the dominant 1D-phase to highly mobile surface gas. Further temperature elevation to 360 K reduces the chain fraction to almost zero. Molecules only can be found on step edges and dislocations and form comparatively short chains of two or three molecules. By increasing the temperature from 180 to 360 K we could thus follow the melting of a metal-organic superstructure.

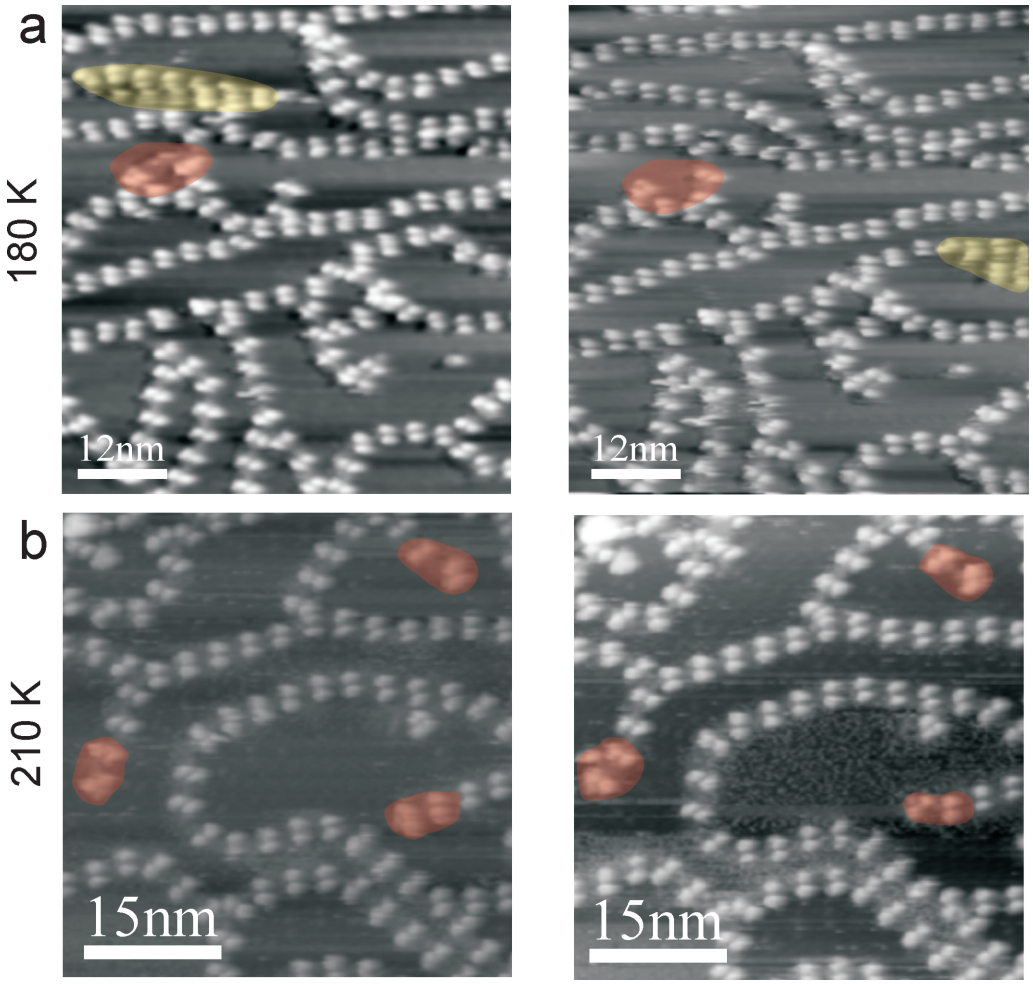

Figure 3.34: STM overview images on the movement of the molecular assembly of BCA-235 at increasing temperature in the range of 180 K to 210 K on Cu(111). **(a)** Consecutive STM images of molecular chain segments at 180 K exhibiting slight movements (yellow, red). **(b)** Movement of the molecular chains at 210 K (red).

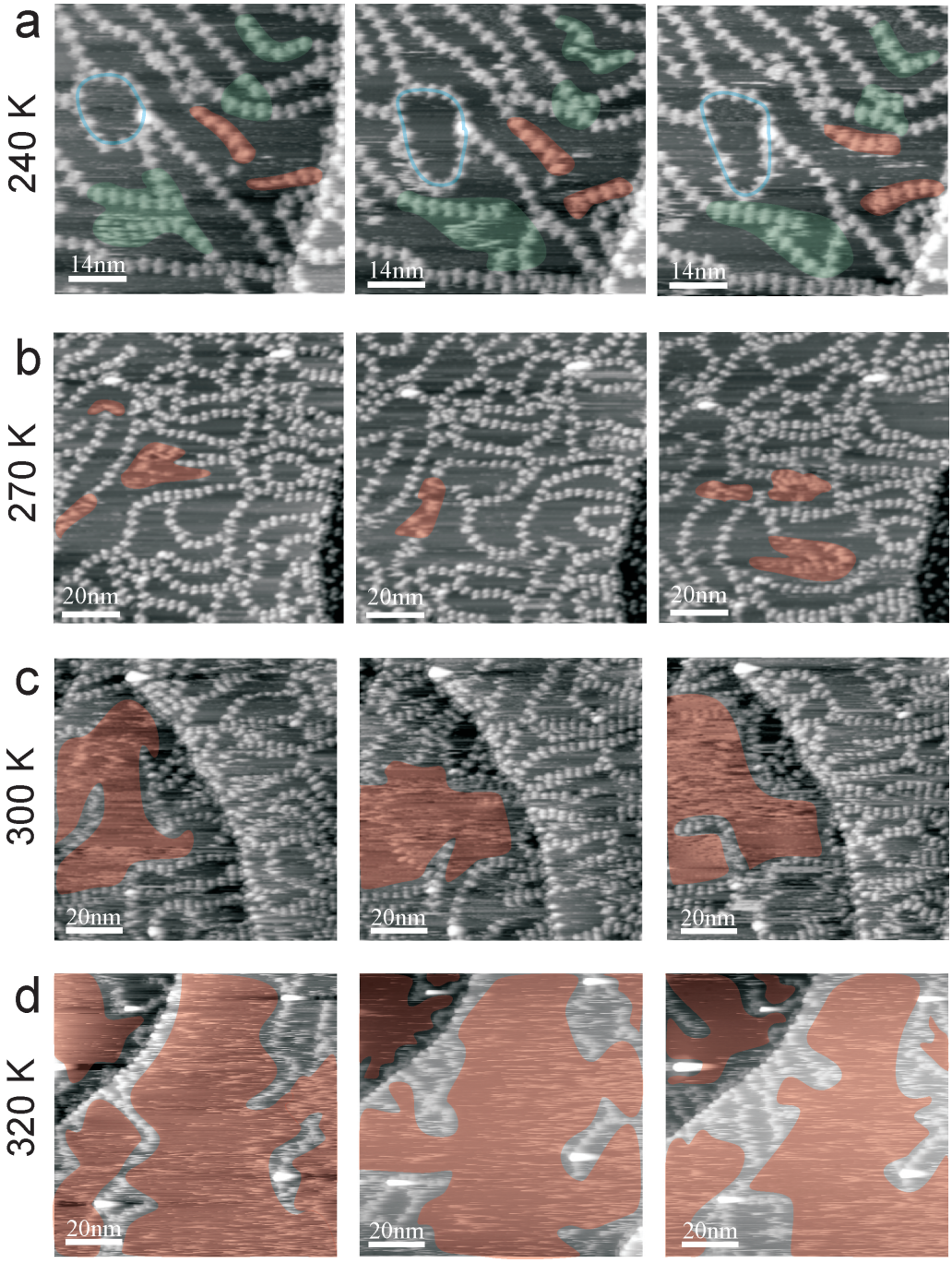

Figure 3.35: Overview STM images of the self-assembled molecular structure of BCA-235 and its melting with increasing temperature from of 240 K to 320 K on Cu(111). **(a)** STM image series of molecular chain movements (red, blue) and molecular bond breaking and rearrangement (green) at 240 K with a time lap of ≈ 50 sec. **(b)** Consecutive STM images with a time lap of ≈ 60 sec. exhibiting mobility of almost every chain segment at 270 K including bond breaking and reassembly. The red highlighted area depicts molecular movement under the tip. **(c)** STM overview images of migrating metal-organic chain segments in dynamic equilibrium with a molecular surface fluid (red) at 300 K. The time lap between the images in ≈ 80 sec. **(d)** Image series of 1D molecular structure and a surface fluid (red) at 320 K with a time lap of ≈ 50 sec.

The movement of a single molecule on the surface has been explored experimentally [93–95] and theoretically [75, 103, 104, 109]. These investigations suggested a reduced mobility of agglomerates in comparison to single molecules. Already at 210 K molecules coordinated just on one side perform movements about this bearing point. Whereas entire chain segments start migrating only with increasing temperature. This implies, that a temperature of 210 K exceeds already the diffusion barrier for a single molecule. For the present system we can distinguish three situations. At 6 K the entire 2D metal-organic network is immobilized. In a distinct temperature range between 210 and 310 K metal-organic chains migrate about the surface. In the third state the thermal energy is high enough to break the metal-organic coordination motive, thus maintaining a surface fluid.

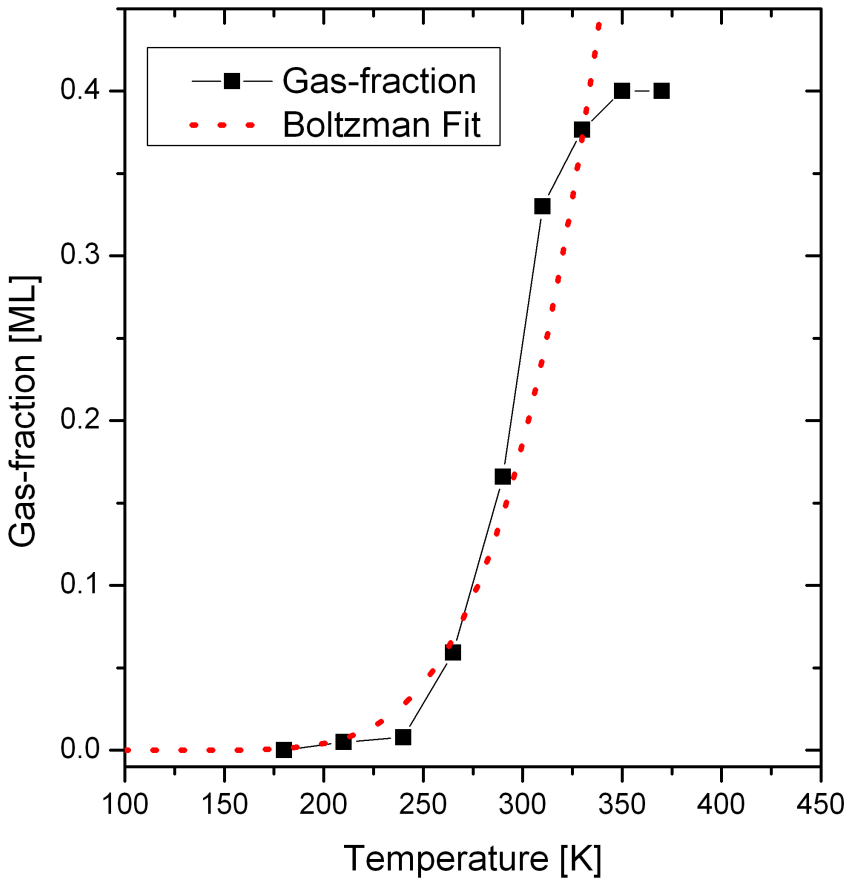

Figure 3.36: Transition of a metal-organic network to the gas phase with increasing temperature on Cu(111). The fluid fraction is limited by the fraction of the molecules measured in the condensed phase.

The fraction of metal organic chains have been evaluated for the according temperatures in order to give an estimation of the energy of the metal-organic bond motive. Single molecules bond to the step edge were not considered due to their altered binding energy. Figure 3.36 presents the ratio between condensed phase and gas phase in a temperature range from 180 - 360 K. The resolved data show a melting zone from 250 to 350 K. Subsequently the entire structure is melted and just single molecules bond to step edges or dislocations remain visible on the surface. The gradient of the slope is an expression for the conversion at the decisive point. In order to analyze the bond energy between the metal-organic chain segments we fitted the distribution with a Boltzman distribution

$$N_j = N_0 g_j e^{-\frac{E_j}{k_B T}} \tag{3.1}$$

where N_j is the number of particles in the gas fraction, N_0 is the number of available particles, g_j is the level of degeneracy, E_j the binding energy, k_B the Boltzman factor and T the temperature. The function follows the data well in the melting zone, but is not able to describe the area when the slope is flattening due to the confined reservoir of molecular chains. We evaluated a bond energy of roughly 0.2 eV. We are aware, that the accuracy of this value is not reliable, but well suited for an approximation. However, the value evaluated for the binding energy are in the order of magnitude of metal-ligand interactions [4]. Based on their flexibility [265] and rigidity up to 240 K this metal-organic network could serve for connecting nanoscale objects [270]. The implementation of Co adatoms instead of Cu could increase the bond strength in order to develop room temperature stability.

Conclusion

By increasing the temperature from 180 - 320 K we investigated the movement and melting behavior of metal-organic ribbons formed by BCA-235 coordinated with Cu surface atoms on Cu(111). We depicted the movement of entire metal-organic chain segments in a temperature range of 210 - 300 K, as well as the formation and dissociation of the 1D ribbons. With increasing temperature (>300 K) the structure dissociates in a gas phase. During the melting process a bond energy between the Cu adatoms and the pyridine group could be roughly approximated.

Chapter 4

Summary

In this thesis the engineering of novel robust surfaces functionalized with carbonitrile substituted oligophenyl molecules and porphyrin derivates employing supramolecular strategies is presented. Self-assembly on a molecular level on the close-packed noble metal surfaces Ag(111) and Cu(111) was investigated in order to understand the underlying adsorbate-adsorbate and adsorbate-substrate interaction. Supporting X-ray photoelectron spectroscopy and near-edge absorption fine structure spectroscopy have been performed to provide a deeper insight on the chemical nature of the molecular patterns. The prochiral species $[1,1';4',1'']-$terphenyl$-3,3''-$ dicarbonitrile (mNC-pPh$_3$-mCN) self-assembles into supramolecular ribbons and islands, where the high symmetry directions of the substrate steers the directionality of the homochiral assembly. This ribbon and island formations indicate, that the outer phenyl rings can freely rotate and adopt the functional CN groups to an adjacent molecular pattern. Dynamical changes in self-assembled molecular structures are barely understood. Here we were able to follow the orientational changes of the molecular pattern by STM, XPS and NEXAFS technique, where the high affinity of the carbonitrile substituent [209] to the metal Cu(111)substrate is a crucial factor. Variation in the molecular coverage (> 0.7 ML) forces a reorientation of the supramolecular island pattern on Cu(111).

By employing molecular units and metal adatoms we succeeded in creating versatile metal-ligand molecular structures serving as a model system for disordered 2D solids. Cobalt coevaporation drives the emergence of a fully reticulated room temperature stable 2D random metal-organic network. The coexistence of three- and fourfold coordination motifs goes beyond results for linear dicarbo-oligophenyls [52], where threefold coordination prevails. Our investigations provided hints for different oxidation states of the metal center which could serve as a selective anchoring point for catalytical reactions.

Recent experiments [46, 47, 52, 89] employed oligophenyls with different backbone length and substituted carbonitrile group in *para* position. In order to close the gap between *m*NC-*p*Ph$_3$-*m*CN employed in this thesis and *p*NC-*p*Ph$_x$-*p*CN, a novel molecule with its carbonitrile groups in *para* and *meta* position has been investigated. Two supramolecular organic layer arise where one exhibits a chevron-like motif similar to earlier measurements with linear oligophenyls [46]. Also a porous hexagonal phase could be found which is enantiopure. Enantioselective processes have been observed in recent studies in specific systems at the molecular level [70]. They are promising starting points for chiroselective heterogenous catalytic applications. Cobalt coevaporation leads to the formation of an open porous 2D disordered metal-organic network comparable to the assembly found for *m*NC-*p*Ph$_3$-*m*CN. In both systems a ditopic metal-organic dimer represents a highly stable smallest subunit. The rotational and directional degree of freedom provided by the molecular species *m*NC-*p*Ph$_3$-*m*CN and *p*NC-*p*Ph$_3$-*m*CN results in a metal-organic network highly adaptable to a local environment due to a large number of possible nodal motifs and its small stable subunits.

Additional to the oligophenyl molecules we investigated the diffusion behavior of H$_2$-TPyP on Cu(111) in a temperature range of 300 to 360 K. Here we found a directional guidance of the molecules by the underlying substrate which allows only for a 1D lateral movement along the $\langle 110 \rangle$ directions. This behavior is a direct consequence of molecular conformational adaptation to the surface. The H$_2$-TPyP can form dimers by coordinating via Cu surface adatom. Intriguingly this dimerisation increases the diffusion rate drastically. Annealing to 420 K results in a metal-organic molecular chain formation, where Cu surface atoms connect the neighboring molecules. Further annealing revealed electronical changes in the molecule caused by the deprotonation of the porphyrin macrocyle hydrogen atoms. The deprotonation could be triggered with tip bias pulses as well. Finally we investigated the behavior of the metal-organic chains formed by the porphyrin derivate BCA-235 on Cu(111) with increasing temperature. Between 180 K and 360 K we were able to track the movement of the metal-organic chains followed by a dissociation of the chains into a surface liquid.

Publication List

1. M. Marschall, J. Reichert, K. Diller, A. Nefedow, Ch. Wöll, S. Klytskaya, M. Ruben, F. Klappenberger, J.V. Barth, Reorientation of Molecular Layers of Asymmetric Dicarbonitrile Oligophenyls. *to be published*

2. M. Marschall, J. Reichert, D. Ecija, W. Auwärter, E. Arras, S. Klytskaya, M. Ruben, J.V. Barth, Competing Interactions in Surface Reticulation with a Prochiral Dicarbonitrile Linker. *to be published*

3. F. Klappenberger, D. Kühne, M. Marschall, S. Neppl, S.; Krenner, A. Nefedov, T. Strunskus, K. Fink, Ch. Wöll, S. Klyatskaya, O. Fuhr, M. Ruben, J.V. and Barth, Uniform π-system alignment in thin films of template-grown dicarbonitrile-oligophenyls. *Advanced Functional Materials*, 21-7, 1631-1641 (2011)

4. S. Klyatskaya, F. Klappenberger, U. Schlickum, D. Kühne, M. Marschall, J. Reichert, R. Decker, W. Krenner, G. Zoppellaro, H. Brune, J.V. Barth, M. Ruben, Surface-confined self-assembly of di-carbonitrile polyphenyls. *Advanced Functional Materials*, 21-7, 1230-1240 (2011)

5. M. Marschall, J. Reichert, K. Seufert, W. Auwärter, F. Klappenberger, A. Weber-Bargioni, S. Klyatskaya, G. Zoppellaro, A. Nefedov, T. Strunskus, Ch. Woll, M. Ruben, J.V. Barth, Supramolecular organization and chiral resolution of p-terphenyl-m-dicarbonitrile on the Ag(111) surface. *Chem Phys Chem*, (2010) 11, 1446-51.

6. M. Marschall, J. Reichert, A. Weber-Bargioni, K. Seufert, W. Auwärter, S. Klyatskaya, G. Zoppellaro, M. Ruben, J.V. Barth, Random two-dimensio- nal string networks based on divergent coordination assembly. *Nature Chemistry*,

(2010) 2, 131-137.

7. J. Reichert, A. Schiffrin, W. Auwärter, A. Weber-Bargioni, M. Marschall, M. Dell'Angela, D. Cvetko, G. Bavdek, A. Cossaro, A. Morgante, J.V. Barth, L-Tyrosine on Ag(111): Universality of the amino acid 2D zwitterionic bonding scheme. *ACS Nano*, (2010) 4, 1218-26.

8. A. Schiffrin, J. Reichert, Y. Pennec, W. Auwärter, A. Weber-Bargioni, M. Marschall, M. Dell'Angela, D. Cvetko, G. Bavdek, A. Cossaro, A. Morgante, J.V. Barth, Self-assembly of L-methionine on Cu(111): Steering enantiomorphic biomolecular nanostructures by substrate reactivity and thermal activation. *The Journal of Physical Chemistry C* (2009) 113, 12101-12108.

9. M. Eichberger, M. Marschall, J. Reichert, A. Weber-Bargioni, W. Auwärter, R.L. Wang, H.J. Kreuzer, Y. Pennec, A. Schiffrin, J.V. Barth, Dimerization boosts 1D mobility of conformationally adapted porphyrins on a hexagonal surface atomic lattice. *Nano Letters* (2008) 8, 4608-13.

10. F. Klappenberger, A. Weber-Bargioni, W. Auwärter, M. Marschall, A. Schiffrin, J.V. Barth, Temperature dependence of conformation, chemical state, and metal-directed assembly of tetrapyridyl-porphyrin on Cu(111) *Journal of Chemical Physics* (2008) 129, 214702.

Appendix

A. Hypothetical regular network with threefold coordination nodes and 2D isomer balanced stochiometry

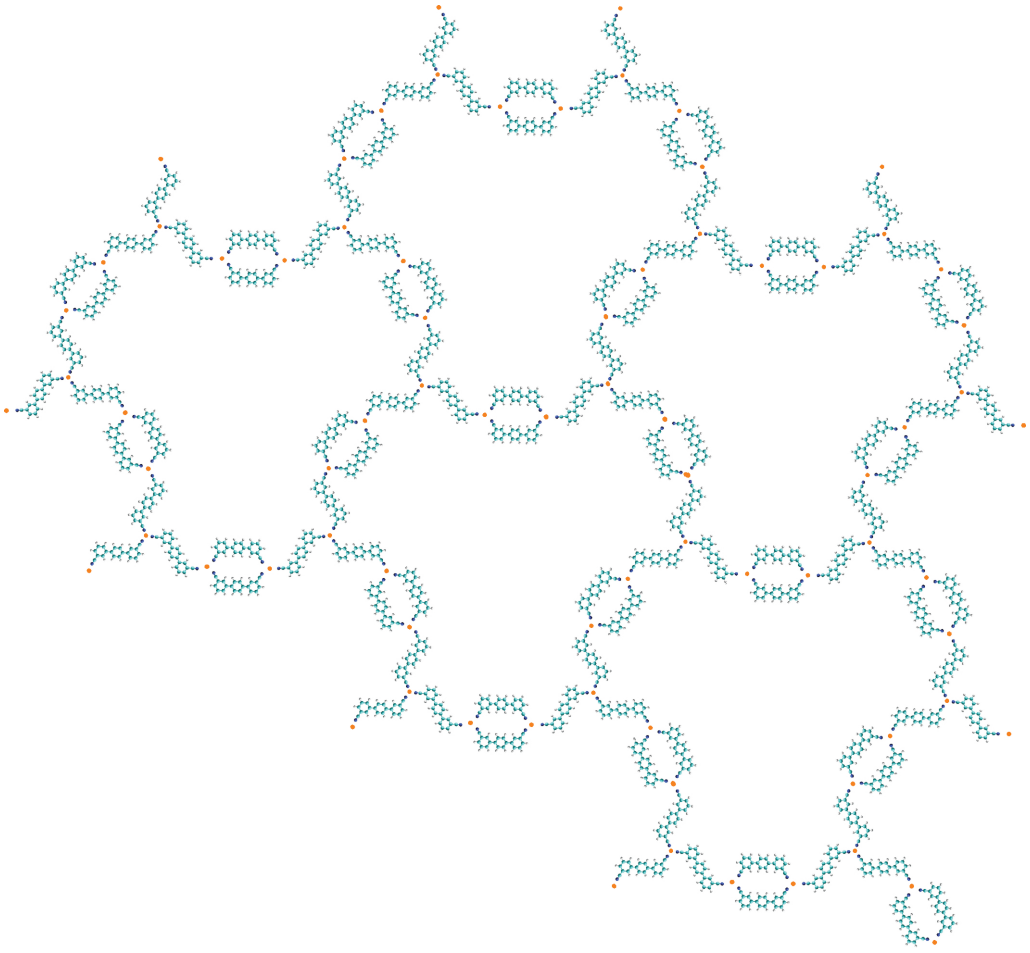

Figure 4.1: Hypothetical regular network of the *m*NC-*p*Ph$_3$-*m*CN molecule with threefold coordination nodes and 2D isomer balanced stochiometry.

B. Additional STM images

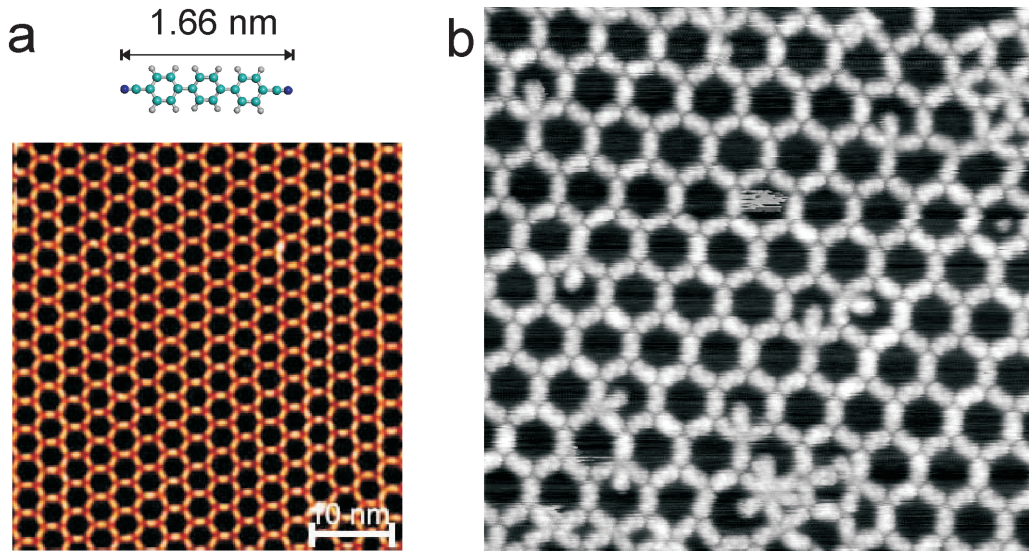

Figure 4.2: **(a)** Highly regular honeycomb lattice of the shown linear dicarbonitrile-terphenyl linker analog following convergent metal-directed assembly - equilibrated at 300 K with the exclusive formation of nodes with threefold coordination. **(b)** Coordination assembly under conditions where kinetic limitations interfere: at 250 K the expression of characteristic defects in the honeycomb lattice occurs, notably in the form of the marked fourfold coordinated cobalt centers (30 x 30 nm^2, V_B = -1 V, I_T = 0.08 nA; image courtesy of Uta Schlickum).

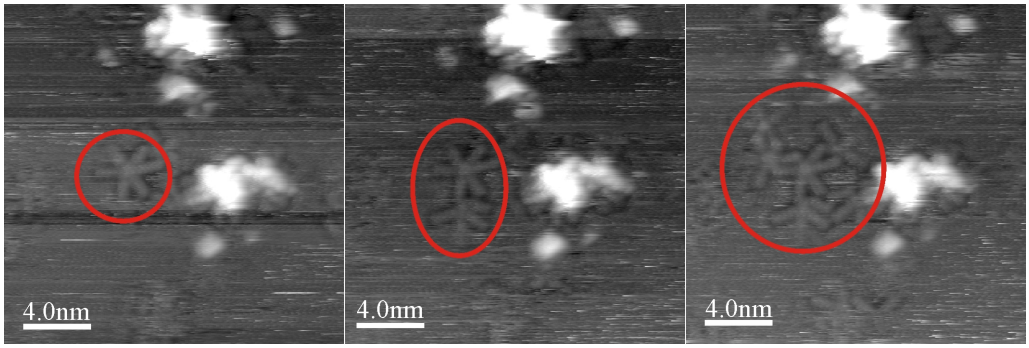

Figure 4.3: Co coordinated *p*NC-*p*Ph_3-*m*CN molecules at room temperature forming a meta-stable star-like structure.

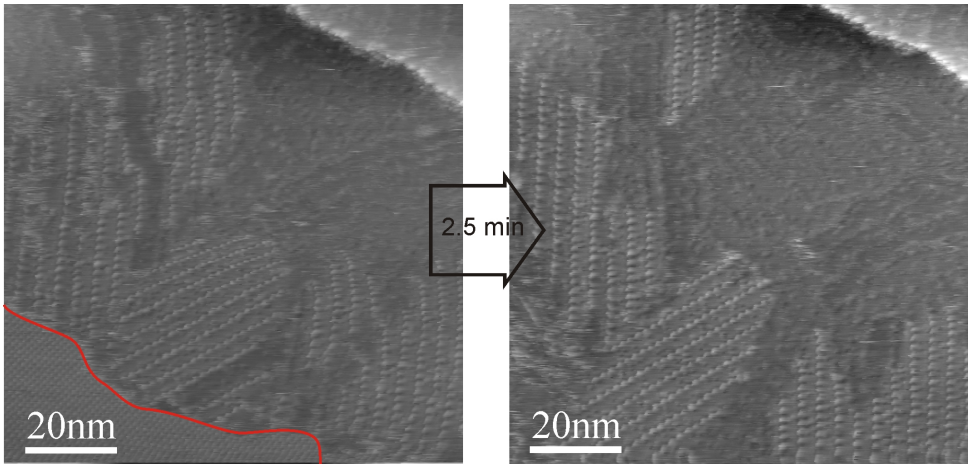

Figure 4.4: Consecutive overview STM images of the *m*NC-*p*Ph$_3$-*m*CN molecule co-evaporated with Co on Cu(111) at RT exhibiting dynamic changes of the molecular orientation from the brick-like (highlighted in red) structure to a linear structure.

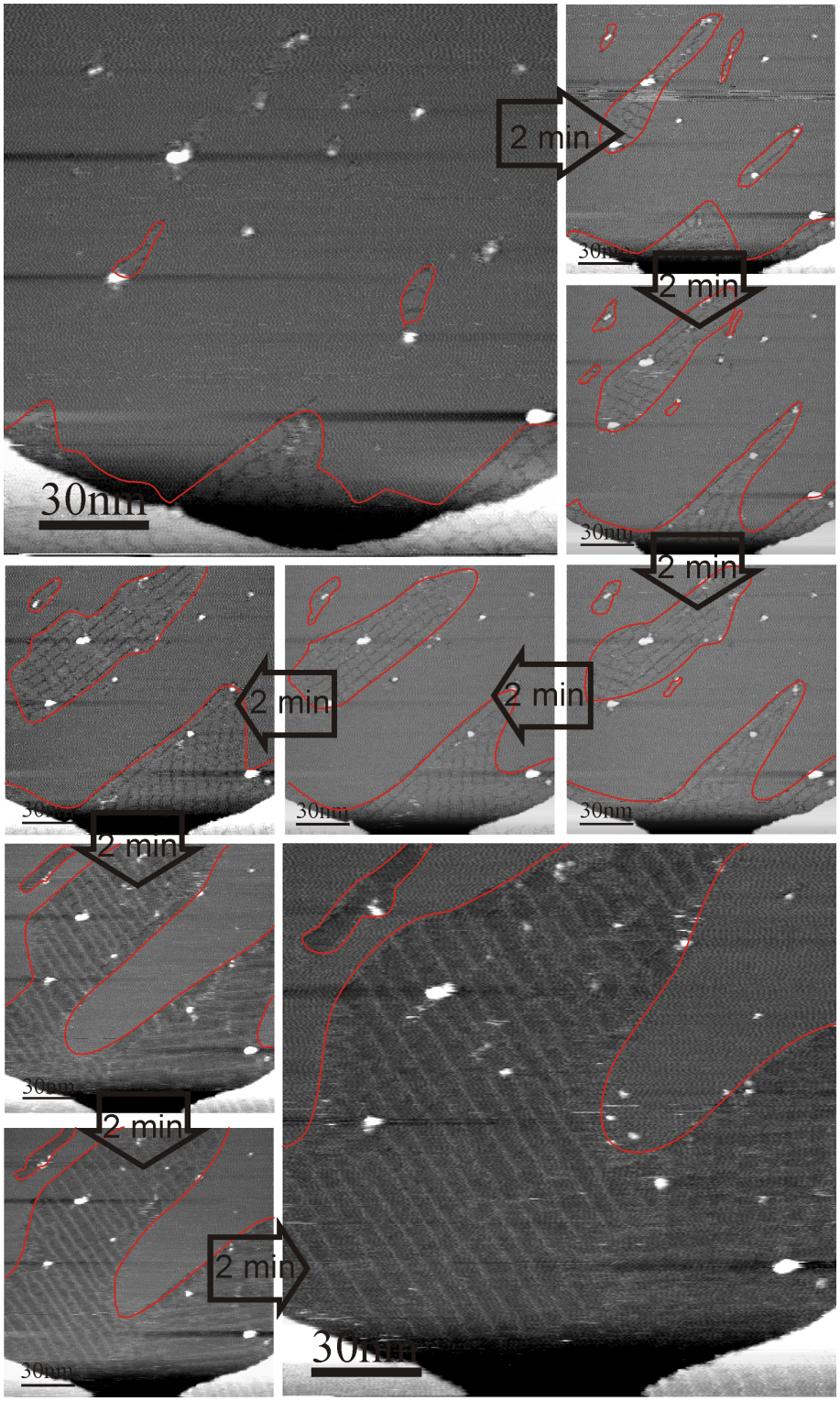

Figure 4.5: Consecutive overview STM images of the *m*NC-*p*Ph$_3$-*m*CN molecule co-evaporated with Co on Ag(111) at RT exhibiting dynamic changes of the molecular orientation. The evolving linear structure with the molecules oriented coplanar with their molecular backbone to the surface are highlighted in red.

C. Organizational chiral windmill motif with *trans*- or *cis*- configuration linkers and threefold Co coordination

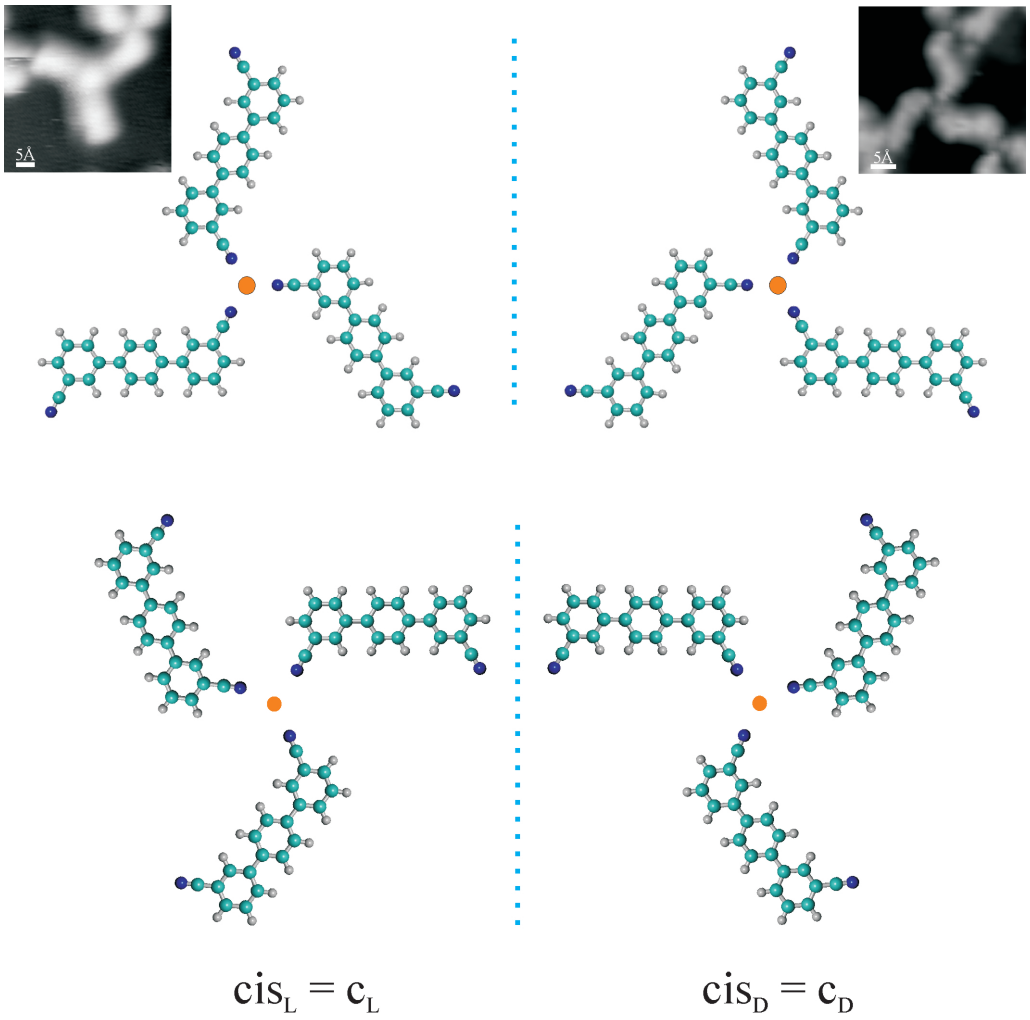

Figure 4.6: Four atomistic models build the mirror symmetric counter parts of Co threefold coordinated *cis* and *trans* windmill structures. Due to the side selectivity a *cis* molecule exhibits a directionality and hence chirelity is inserted to the molecular structure (cis$_L$ and cis$_D$).

D. Survey of all possible 2D *m*NC-*p*Ph$_3$-*m*CN + Co coordination motifs

I. Threefold coordination motifs:

Redundant motifs are excluded.

{ccc}: 4

$c_L c_L c_L$ $c_L c_L c_D$
$c_L c_D c_D$ $c_D c_D c_D$

{ttt}: 4

$t_L t_L t_L$ $t_L t_L t_D$
$t_L t_D t_D$ $t_D t_D t_D$

{cct}: 8

$c_L c_L t_L$ $c_D c_L t_L$
$c_D c_D t_L$ $c_L c_D t_L$
$c_D c_D t_D$ $c_L c_D t_D$
$c_D c_L t_D$ $c_L c_L t_D$

{ctt}: 8

$c_L t_L t_L$ $c_D t_L t_L$
$c_D t_D t_L$ $c_L t_D t_L$
$c_D t_D t_D$ $c_L t_D t_D$
$c_D t_L t_D$ $c_L t_L t_D$

$\sum_{3-fold} = 24$

II. Fourfold coordination motifs

Redundant motifs are excluded.

{cccc}: 6

$c_L c_L c_L c_L$ $c_L c_L c_L c_D$
$c_L c_L c_D c_D$ $c_L c_D c_L c_D$
$c_L c_D c_D c_D$ $c_D c_D c_D c_D$

{ccct}: 16

$c_L c_L c_L t_L$ $c_D c_L c_L t_L$ $c_L c_D c_L t_L$ $c_L c_L c_D t_L$
$c_D c_D c_L t_L$ $c_D c_L c_D t_L$ $c_L c_D c_D t_L$ $c_D c_D c_D t_L$
$c_L c_L c_L t_D$ $c_D c_L c_L t_D$ $c_L c_D c_L t_D$ $c_L c_L c_D t_D$
$c_D c_D c_L t_D$ $c_D c_L c_D t_D$ $c_L c_D c_D t_D$ $c_D c_D c_D t_D$

{cctt}: 16

$c_L c_L t_L t_L$	$c_D c_L t_L t_L$	$c_L c_D t_L t_L$	$c_L c_L t_D t_L$
$c_D c_D t_L t_L$	$c_D c_L t_D t_L$	$c_L c_D t_D t_L$	$c_D c_D t_D t_L$
$c_L c_L t_L t_D$	$c_D c_L t_L t_D$	$c_L c_D t_L t_D$	$c_L c_L t_D t_D$
$c_D c_D t_L t_D$	$c_D c_L t_D t_D$	$c_L c_D t_D t_D$	$c_D c_D t_D t_D$

{cttt}: 16

$c_L c_L t_L t_L$	$c_D c_L t_L t_L$	$c_L c_D t_L t_L$	$c_L c_L t_D t_L$
$c_D c_D t_L t_L$	$c_D c_L t_D t_L$	$c_L c_D t_D t_L$	$c_D c_D t_D t_L$
$c_L c_L t_L t_D$	$c_D c_L t_L t_D$	$c_L c_D t_L t_D$	$c_L c_L t_D t_D$
$c_D c_D t_L t_D$	$c_D c_L t_D t_D$	$c_L c_D t_D t_D$	$c_D c_D t_D t_D$

{ctct}: 10

$c_L t_L c_L t_L$	$c_D t_L c_L t_L$	$c_L c_D c_L t_L$	$c_D t_D c_L t_D$
$c_D t_D c_L t_L$	$c_D t_L c_D t_L$	$c_L c_D c_D t_L$	$c_D t_D c_D t_L$
$c_L c_D c_L t_D$	$c_D t_D c_D t_D$		

{tttt}: 6

$t_L t_L t_L t_L$	$t_L t_L t_L t_D$		
$t_L t_L t_D t_D$	$t_L t_D t_L t_D$		
$t_L t_D t_D t_D$	$t_D t_D t_D t_D$		

$\sum_{4-fold} = 70$

$\Longrightarrow \sum_{3+4-fold} = 94$

III. Geometrical representation of three- and fourfold coordination nodes classified as above

threefold coordination nodes

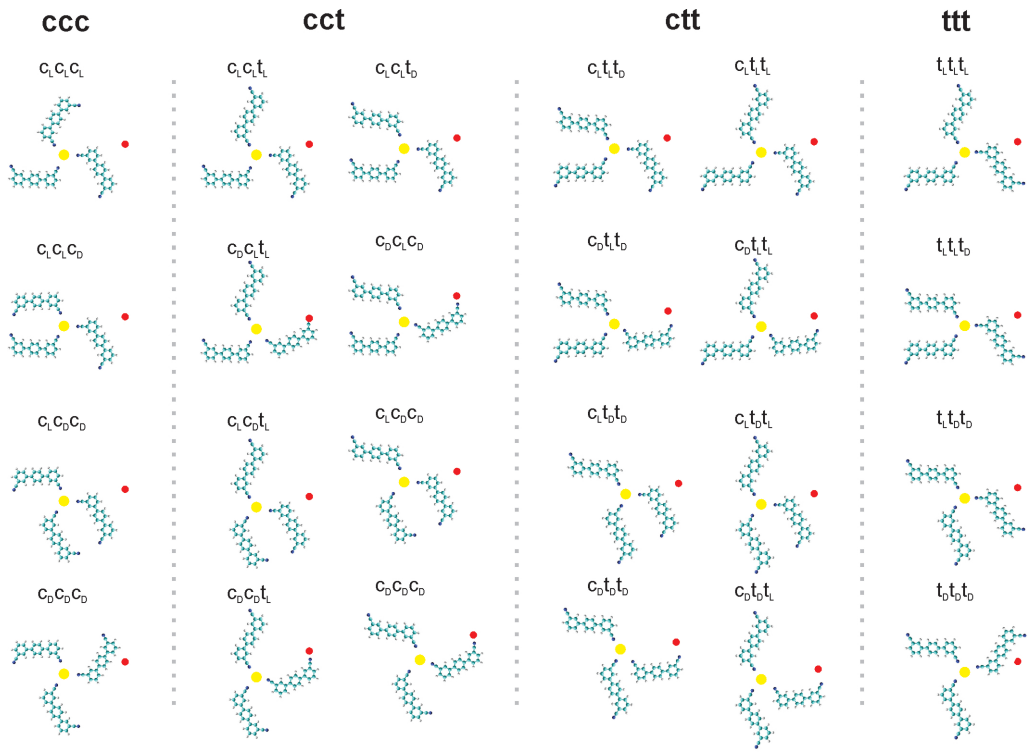

Figure 4.7: Atomistic model of threefold metal-organic nodal motifs. The metal center is marked yellow, the carbon atoms in the molecule cyan, nitrogen blue and hydrogen white. The red dot aside of every nodal motif highlights the starting point for the nomenclature.

fourfold coordination nodes

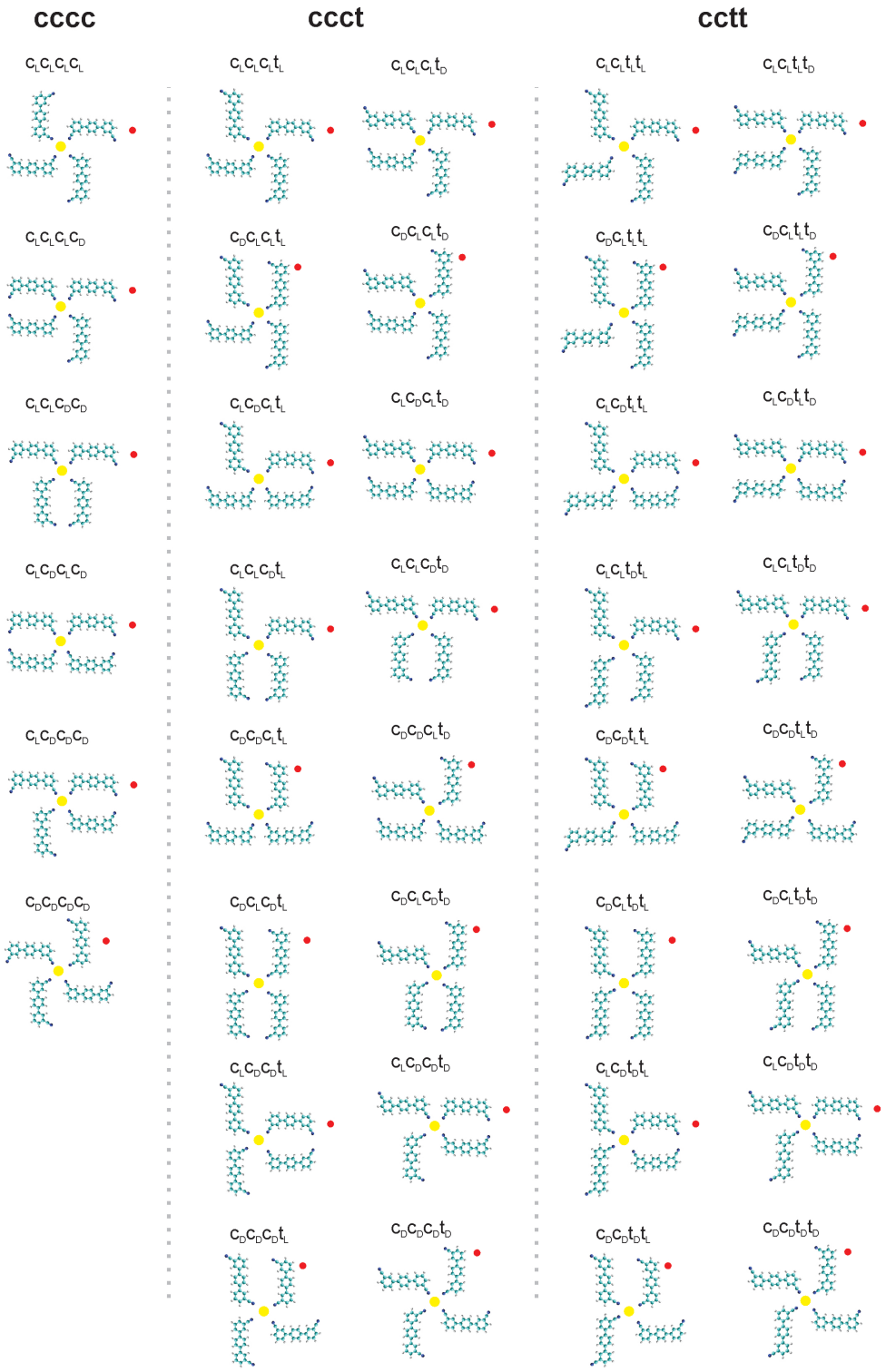

Figure 4.8: Atomistic model of fourfold metal-organic nodal motifs. The metal center is marked yellow, the carbon atoms in the molecule cyan, nitrogen blue and hydrogen white. The red dot aside of every nodal motif highlights the starting point for the nomenclature.

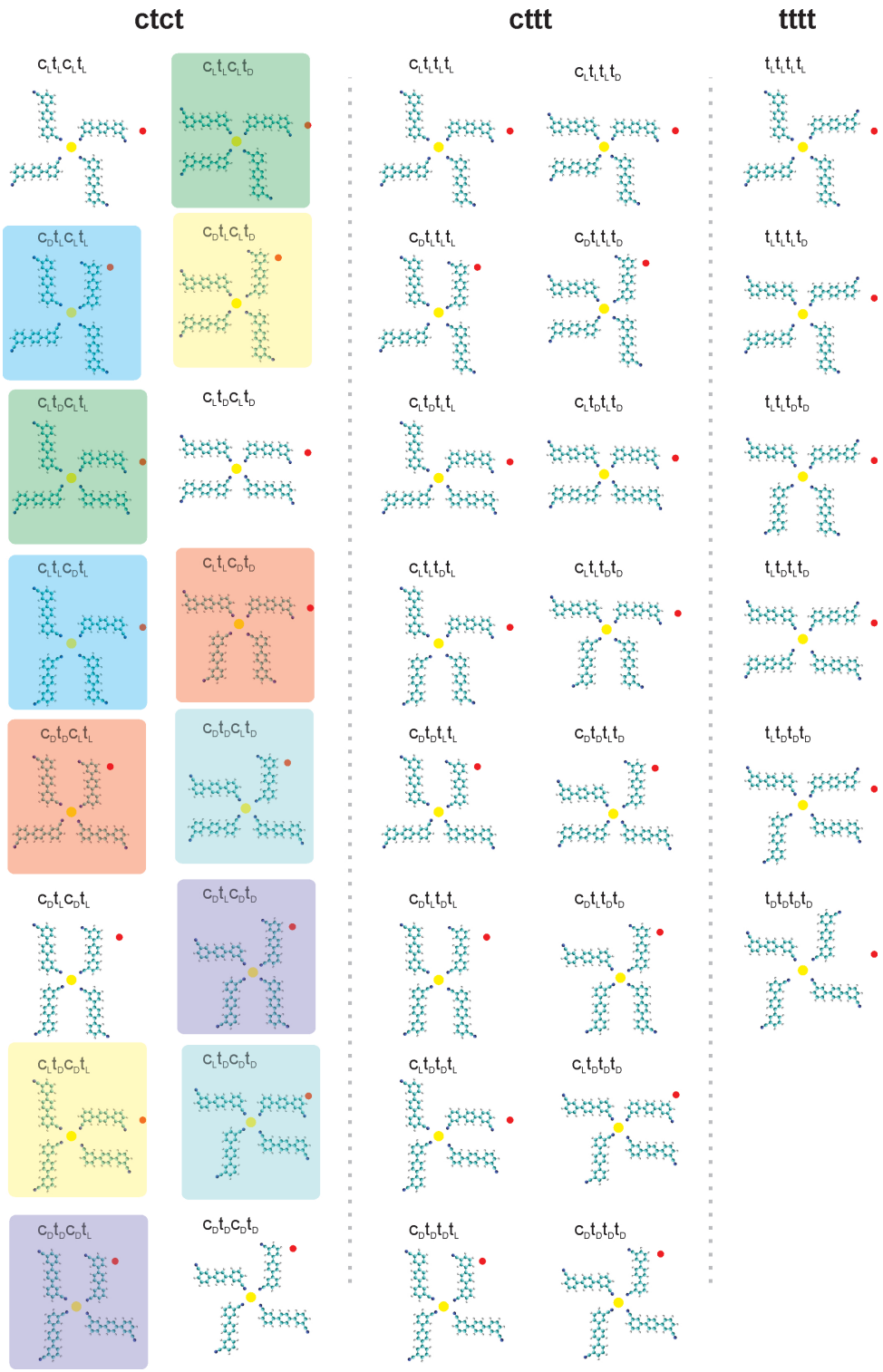

Figure 4.9: Atomistic model of fourfold metal-organic nodal motifs. The color code of the highlighted motifs marks redundant nodal motifs. The metal center is marked yellow, the carbon atoms in the molecule cyan, nitrogen blue and hydrogen white. The red dot aside of every nodal motif highlights the starting point for the nomenclature.

E. Survey of all possible 2D Co-*p*NC-*p*Ph$_3$-*m*CN coordination motifs

The molecule *p*NC-*p*Ph$_3$-*m*CN comprises a directionality concerning the functional CN moities substituted in *para* (p) and *meta* (m) position. Hence in order to provide a full overview on the nodal motifs we have to distinguish between *para* CN group and *meta* CN group coordinated to the Co center.

I. Threefold coordination motifs:
Redundant motifs are excluded.

{ppp}: 4

$p_D p_D p_D$ $p_D p_D p_L$
$p_D p_L p_L$ $p_L p_L p_L$

{mmm}: 4

$p_D m_D p_D$ $p_D m_D p_L$
$p_D m_L p_L$ $p_L m_L p_L$

{ppm}: 8

$p_D p_D m_D$ $p_D p_D m_L$
$p_D p_L m_L$ $p_L p_L m_L$
$p_L p_L m_D$ $p_L p_D m_D$
$p_D p_L m_D$ $p_L p_D m_L$

{pmm}: 8

$p_D m_D m_D$ $p_D m_D m_L$
$p_D m_L m_L$ $p_L m_L m_L$
$p_L m_L m_D$ $p_L m_D m_D$
$p_D m_L m_D$ $p_L m_D m_L$

$\sum_{3-fold} = 24$

II. Fourfold coordination motifs:
Redundant motifs are excluded.

{pppp}: 6

$p_D p_D p_D p_D$ $p_D p_D p_D p_L$ $p_D p_D p_L p_L$
$p_D p_L p_L p_L$ $p_L p_L p_L p_L$ $p_L p_D p_L p_D$

{mmmm}: 6

$m_D m_D m_D m_D$ $m_D m_D m_D m_L$ $m_D m_D m_L m_L$
$m_D m_L m_L m_L$ $m_L m_L m_L m_L$ $m_L m_D m_L m_D$

{pppm}: 16

$p_D p_D p_D m_D$ $p_L p_D p_D m_D$ $p_D p_L p_D m_D$ $p_D p_D p_L m_D$
$p_L p_D p_L m_D$ $p_D p_L p_L m_D$ $p_L p_L p_D m_D$ $p_L p_L p_L m_D$
$p_D p_D p_D m_L$ $p_L p_D p_D m_L$ $p_D p_L p_D m_L$ $p_D p_D p_L m_L$
$p_L p_D p_L m_L$ $p_D p_L p_L m_L$ $p_L p_L p_D m_L$ $p_L p_L p_L m_L$

{ppmm}: 16

$p_D p_D m_D m_D$ $p_L p_D m_D m_D$ $p_D p_L m_D m_D$ $p_D p_D m_L m_D$
$p_L p_D m_L m_D$ $p_D p_L m_L m_D$ $p_L p_L m_D m_D$ $p_L p_L m_L m_D$
$p_D p_D m_D m_L$ $p_L p_D m_D m_L$ $p_D p_L m_D m_L$ $p_D p_D m_L m_L$
$p_L p_D m_L m_L$ $p_D p_L m_L m_L$ $p_L p_L m_D m_L$ $p_L p_L m_L m_L$

{pmpm}: 12

$p_D m_D p_D m_D$ $p_L m_D p_D m_D$ $p_D m_L p_D m_D$ $p_D m_D p_L m_D$
$p_L m_D p_L m_D$ $p_D m_L p_L m_D$ $p_L m_L p_D m_D$ $p_L m_L p_L m_D$
$p_D m_L p_D m_L$ $p_D m_L p_L m_L$ $p_L m_L p_D m_L$ $p_L m_L p_L m_L$

{pmmm}: 16

$p_D m_D m_D m_D$ $p_L m_D m_D m_D$ $p_D m_L m_D m_D$ $p_D m_D m_L m_D$
$p_L m_D m_L m_D$ $p_D m_L m_L m_D$ $p_L m_L m_D m_D$ $p_L m_L m_L m_D$
$p_D m_D m_D m_L$ $p_L m_D m_D m_L$ $p_D m_L m_D m_L$ $p_D m_D m_L m_L$
$p_L m_D m_L m_L$ $p_D m_L m_L m_L$ $p_L m_L m_D m_L$ $p_L m_L m_L m_L$

$\sum_{4-fold} = 70$

$\Longrightarrow \sum_{3+4-fold} = 94$

III. Geometrical representation of three- and fourfold coordination nodes classified as above

threefold coordination nodes

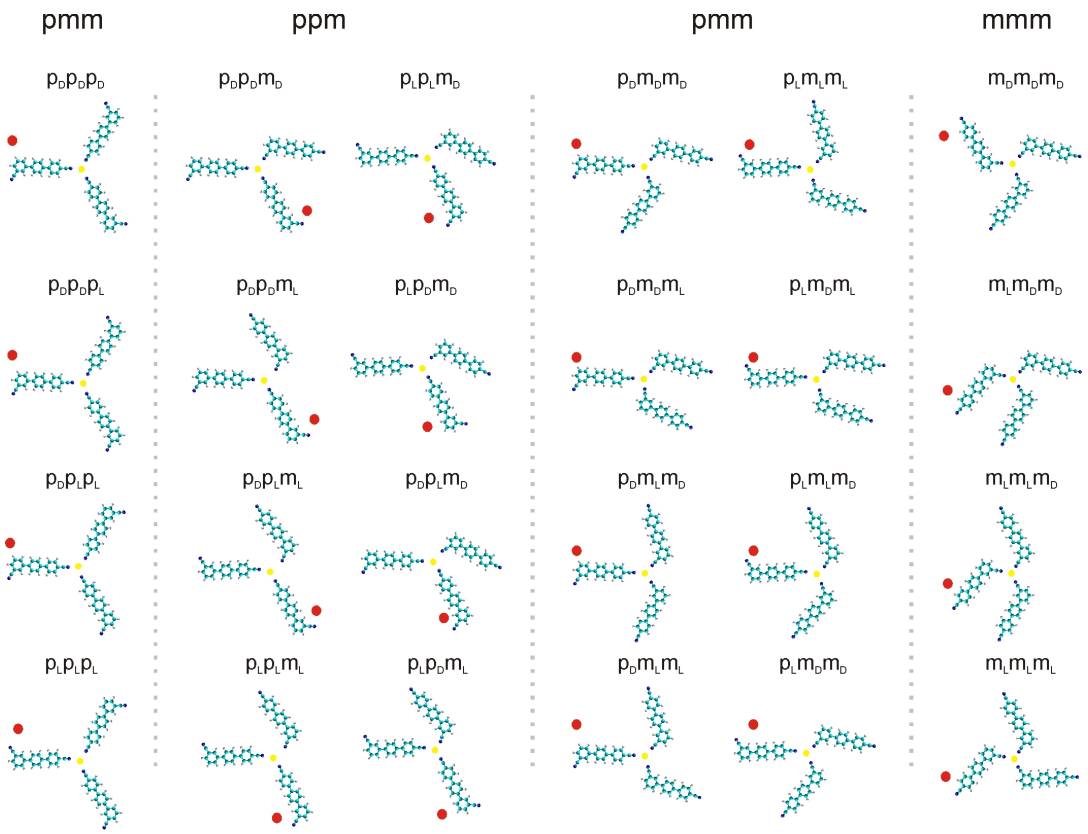

Figure 4.10: Atomistic model of threefold metal-organic nodal motifs. The metal center is marked yellow, the carbon atoms in the molecule cyan, nitrogen blue and hydrogen white. The red dot aside of every nodal motif highlights the starting point for the nomenclature.

fourfold coordination nodes

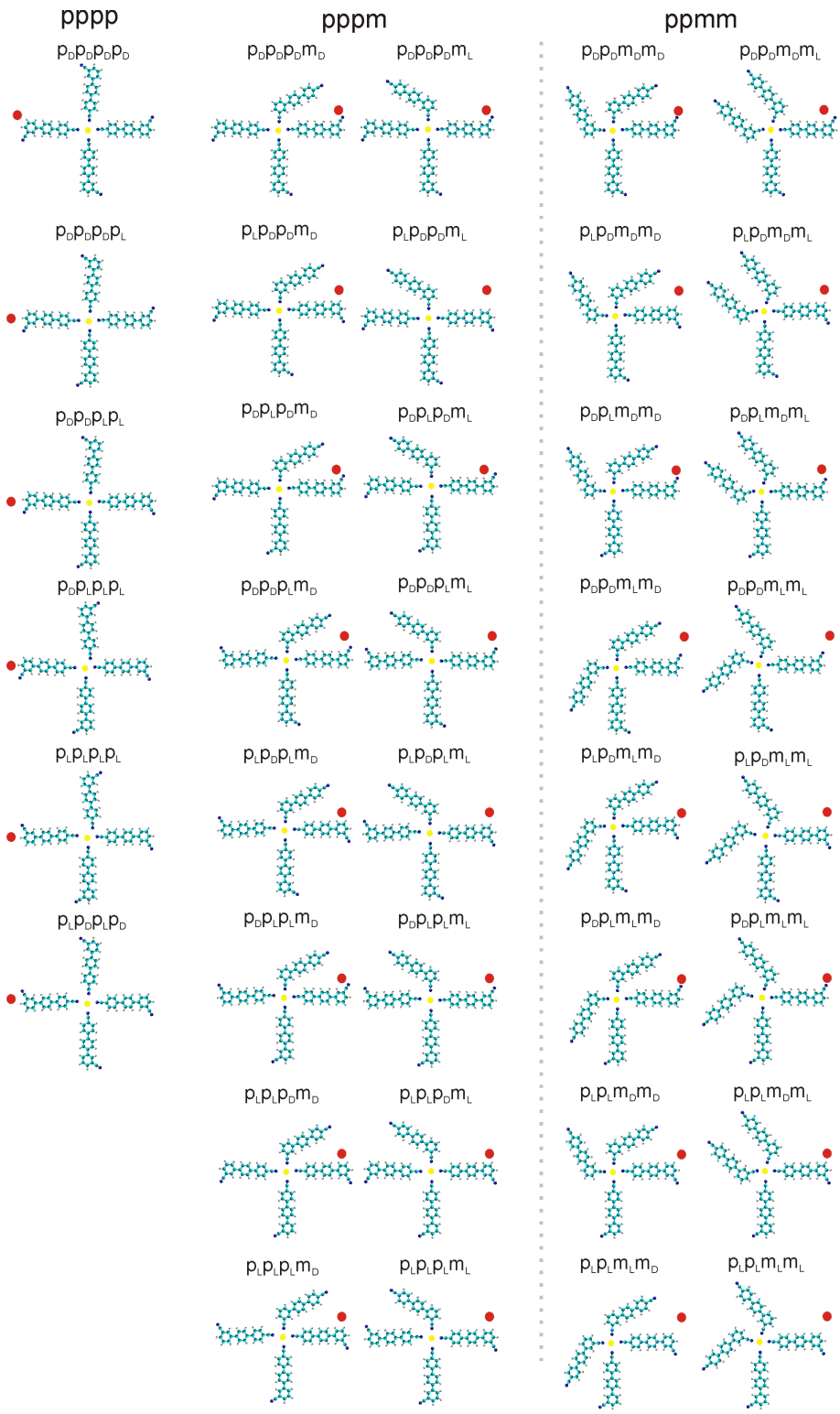

Figure 4.11: Atomistic model of fourfold metal-organic nodal motifs. The metal center is marked yellow, the carbon atoms in the molecule cyan, nitrogen blue and hydrogen white. The red dot aside of every nodal motif highlights the starting point for the nomenclature.

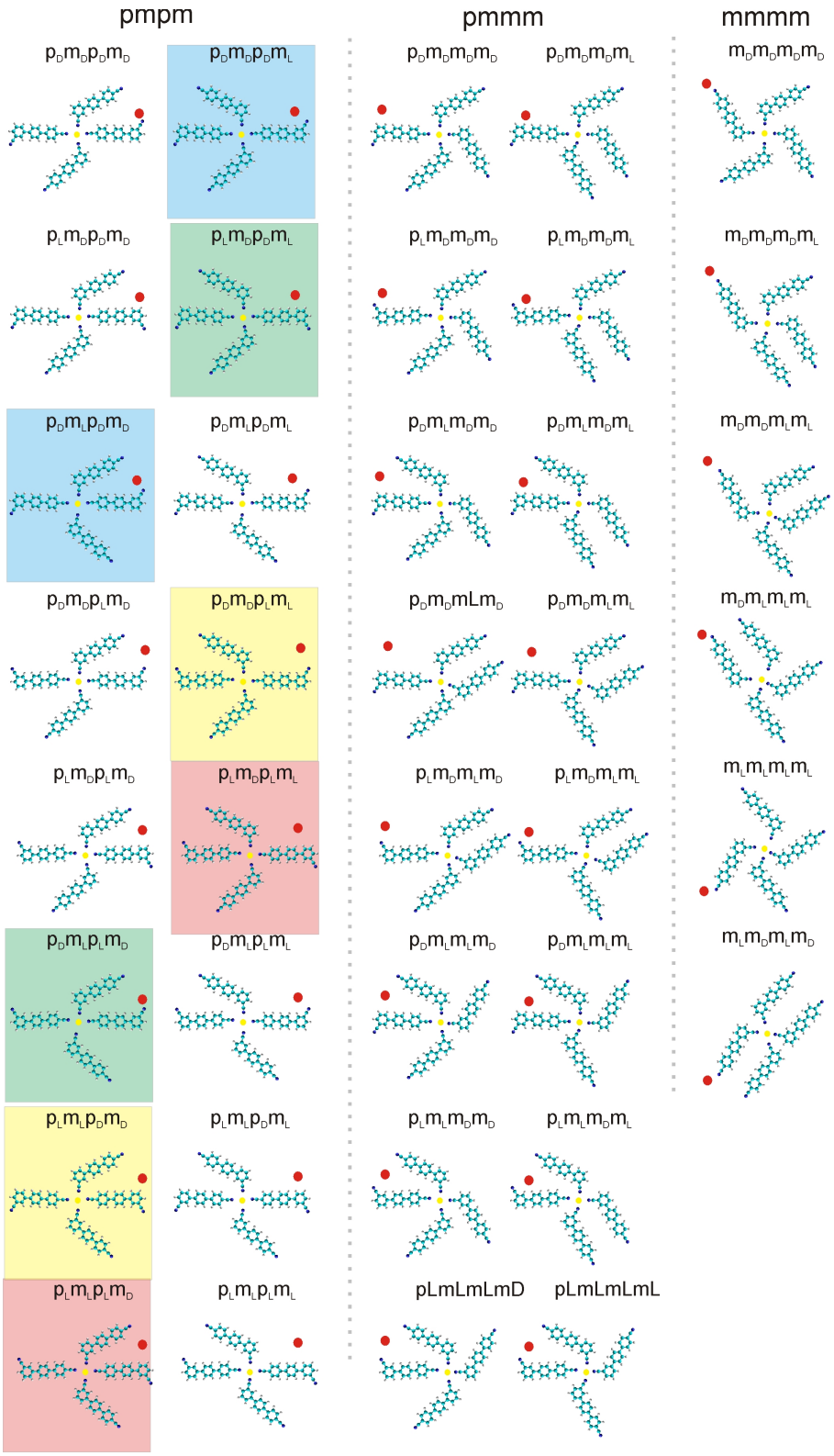

Figure 4.12: Atomistic model of fourfold metal-organic nodal motifs. The color code of the highlighted motifs marks redundant nodal motifs. The metal center is marked yellow, the carbon atoms in the molecule cyan, nitrogen blue and hydrogen white. The red dot aside of every nodal motif highlights the starting point for the nomenclature.

F. Additional NEXAFS measurements

I. *m*NC-*p*Ph$_3$-*m*CN monolayer on Ag(111)

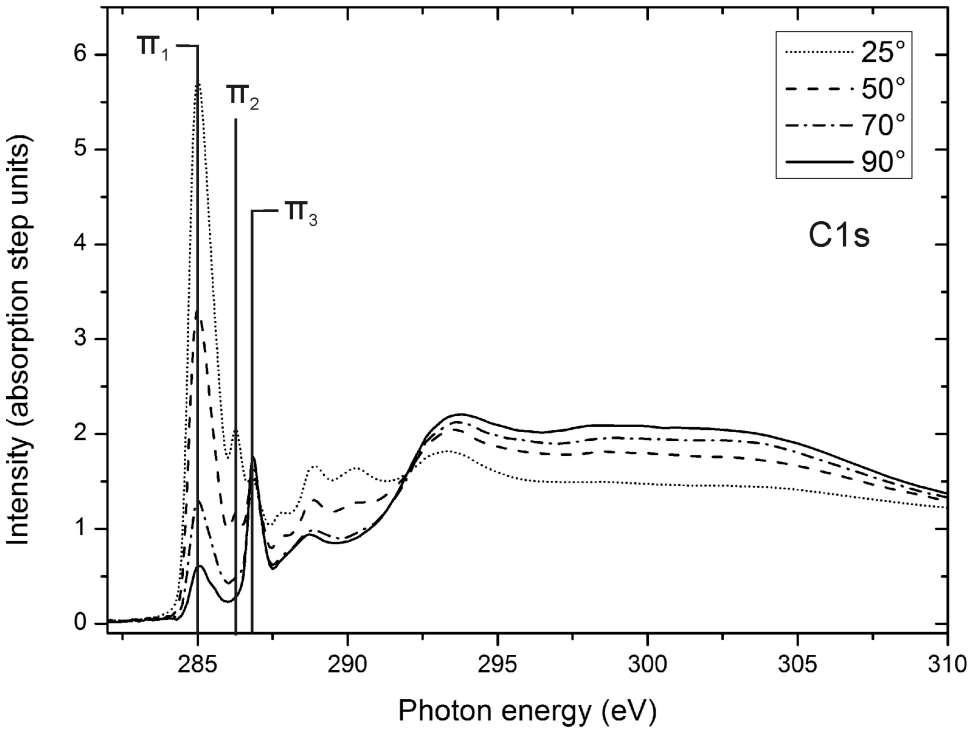

Figure 4.13: Angle dependent NEXAFS C1s spectra of *m*NC-*p*Ph$_3$-*m*CN monolayer complementing the measurements presented in chapter 3 and 3.2.3 on Ag(111).The peaks π_1, π_2 and π_3 refer to figure 3.14.

II. *m*NC-*p*Ph$_3$-*m*CN multilayer on Ag(111)

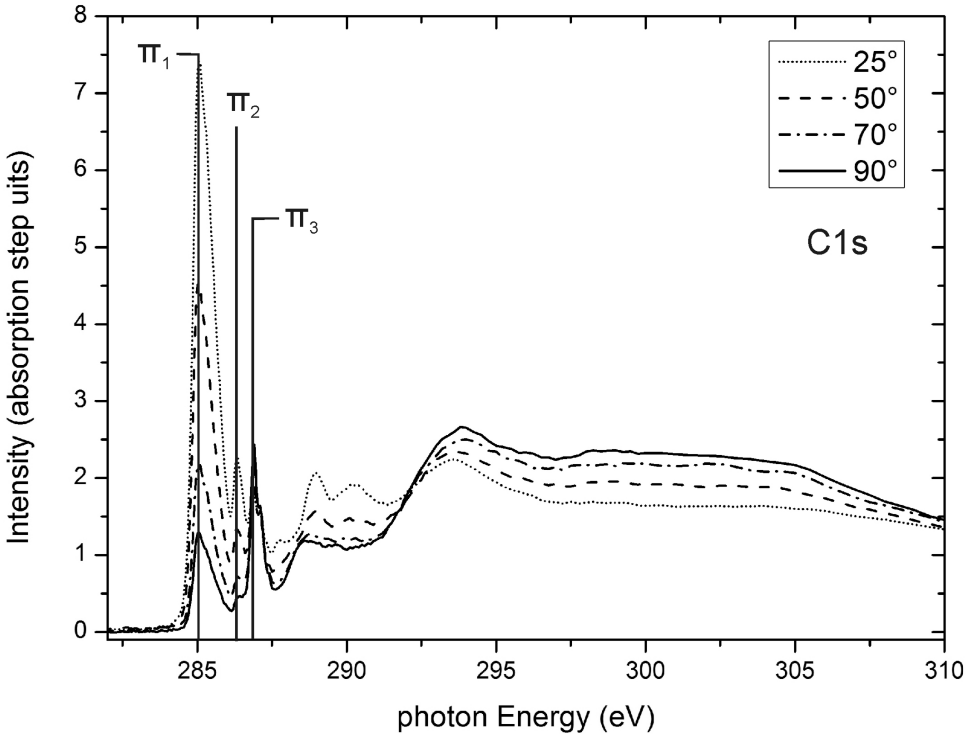

Figure 4.14: Angle dependent NEXAFS C1s spectra of *m*NC-*p*Ph$_3$-*m*CN multilayer complementing the measurements presented in chapter 3 and 3.2.3 on Ag(111).The peaks π_1, π_2 and π_3 refer to figure 3.14.

Bibliography

[1] F. I. Bohrer, C. N. Colesniuc, J. Park, M. E. Ruidiaz, I. K. Schuller, A. C. Kummel, and W. C. Trogler. Comparative gas sensing in cobalt, nickel, copper, zinc, and metal-free phthalocyanine chemiresistors. *Journal of the American Chemical Society*, 131(2):478–485, 2009.

[2] I. A. Cody. Low energy surfaces for reduced corrosion and fouling. *U.S. patent 0219598 A1*, 2005.

[3] J. V. Barth, G. Costantini, and K. Kern. Engineering atomic and molecular nanostructures at surfaces. *Nature*, 437(7059):671–679, 2005.

[4] J. V. Barth. Molecular architectonic on metal surfaces. *Annual Review of Physical Chemistry*, 58(1):375–407, 2007.

[5] G. Binnig and H. Rohrer. Vacuum tunnel microscope. *Helvetica Physica Acta*, 55(2):128–128, 1982.

[6] G. Binnig and H. Rohrer. Scanning tunneling microscopy - from birth to adolescence. *Reviews of Modern Physics*, 59(3):615–625, 1987.

[7] E. Ritter, R. J. Behm, G. Pötschke, and J. Wintterlin. Direct observation of a nucleation and growth process on an atomic scale. *Surface Science*, 181(1-2):403–411, 1987.

[8] M. Grill, L.and Dyer, L. Lafferentz, M. Persson, M. V. Peters, and S. Hecht. Nano-architectures by covalent assembly of molecular building blocks. *Nature Nano*, 2(11):687–691, 2007.

[9] M. F. Crommie, C. P. Lutz, and D. M. Eigler. Confinement of electrons to quantum corrals on a metal-surface. *Science*, 262(5131):218–220, 1993.

[10] F. Klappenberger, D. Kühne, W. Krenner, I. Silanes, A. Arnau, F. J. García de Abajo, S. Klyatskaya, M. Ruben, and J. V. Barth. Tunable quantum dot arrays

formed from self-assembled metal-organic networks. *Physical Review Letters*, 106(2):026802, 2011.

[11] A. Schiffrin, J. Reichert, W. Auwärter, G. Jahnz, Y. Pennec, A. Weber-Bargioni, V. S. Stepanyuk, L. Niebergall, P. Bruno, and J. V. Barth. Self-aligning atomic strings in surface-supported biomolecular gratings. *Physical Review B*, 78(3):035424, 2008.

[12] S. W. Hla and K. H. Rieder. Stm control of chemical reactions: Single-molecule synthesis. *Annual Review of Physical Chemistry*, 54:307–330, 2003.

[13] G. Dujardin, R. E. Walkup, and P. Avouris. Dissociation of individual molecules with electrons from the tip of a scanning tunneling microscope. *Science*, 255(5049):1232–1235, 1992.

[14] B. C. Stipe, M. A. Rezaei, W. Ho, S. Gao, M. Persson, and B. I. Lundqvist. Single-molecule dissociation by tunneling electrons. *Physical Review Letters*, 78(23):4410–4413, 1997.

[15] X. H. Lu, M. Grobis, K. H. Khoo, S. G. Louie, and M. F. Crommie. Spatially mapping the spectral density of a single c-60 molecule. *Physical Review Letters*, 90(9):–, 2003.

[16] L. A. Bumm, J. J. Arnold, M. T. Cygan, T. D. Dunbar, T. P. Burgin, L. Jones, D. L. Allara, J. M. Tour, and P. S. Weiss. Are single molecular wires conducting? *Science*, 271(5256):1705–1707, 1996.

[17] R. Wiesendanger, H. J. Güntherodt, G. Güntherodt, R. J. Gambino, and R. Ruf. Observation of vacuum tunneling of spin-polarized electrons with the scanning tunneling microscope. *Physical Review Letters*, 65(2):247, 1990.

[18] R. Wiesendanger, I. V. Shvets, D. Bürgler, G. Tarrach, H. J. Guntherodt, and J. M. D. Coey. Evidence for selective imaging of different magnetic ions on the atomic scale by using a scanning tunnelling microscope with a ferromagnetic probe tip. *EPL (Europhysics Letters)*, 19(2):141, 1992.

[19] S. Heinze, M. Bode, A. Kubetzka, O. Pietzsch, X. Nie, S. Blügel, and R. Wiesendanger. Real-space imaging of two-dimensional antiferromagnetism on the atomic scale. *Science*, 288(5472):1805–1808, 2000.

[20] T. Yokoyama, S. Yokoyama, T. Kamikado, Yo. Okuno, and S. Mashiko. Selective assembly on a surface of supramolecular aggregates with controlled size and shape. *Nature*, 413(6856):619–621, 2001.

[21] A. A. Dhirani, R. W. Zehner, R. P. Hsung, P. Guyot-Sionnest, and L. R. Sita. Self-assembly of conjugated molecular rods: A high-resolution stm study. *Journal of the American Chemical Society*, 118(13):3319–3320, 1996.

[22] K. L. Prime and G. M. Whitesides. Self-assembled organic monolayers - model systems for studying adsorption of proteins at surfaces. *Science*, 252(5009):1164–1167, 1991.

[23] Y. Xia, J. A. Rogers, K. E. Paul, and G. M. Whitesides. Unconventional methods for fabricating and patterning nanostructures. *Chemical Reviews*, 99(7):1823–1848, 1999.

[24] Intel Corporation. *http://www.intel.com/pressroom/archive/releases/2010/20100201comp.html*.

[25] T. Ito and S. Okazaki. Pushing the limits of lithography. *Nature*, 406(6799):1027–1031, 2000.

[26] P. Ehrlich. *Collected studies on Immunity.* Wiley, New York, 1906.

[27] A. Werner. *Zeitschrift der Anorganishcen Chemie*, 3, 1893.

[28] A. Langner et. al. Self-recognition and self-selection in multicomponent supramolecular coordination networks on surfaces. *Proc. Natl Acad. Sci. USA*, 104:17927–17930, 2007.

[29] J.M. Lehn. *Biomimetic Chemistry.* Elesiver, Amsterdam, 1983.

[30] J.M. Lehn. *Supramolecular Chemistry.* VCH, Weinheim, 1995.

[31] J. M. Lehn. Supramolecular chemistry-scope and perspectives molecules, supermolecules, and molecular devices (nobel lecture). *Angewandte Chemie International Edition*, 27(1):89–112, 1988.

[32] J. V. Barth. Transport of adsorbates at metal surfaces: From thermal migration to hot precursors. *Surface Science Reports*, 40(3-5):75–149, 2000.

[33] M. Simard, D. Su, and J. D. Wuest. Use of hydrogen bonds to control molecular aggregation. self-assembly of three-dimensional networks with large chambers. *Journal of the American Chemical Society*, 113(12):4696–4698, 1991.

[34] G.M. Whitesides, J.P. Mathias, and C.T. Seto. Molecular self-assembly and nanochemistry: a chemical strategy for the synthesis of nanostructures. *Science*, 254(5036):1312–1319, 1991.

[35] K. A. Sharp, A. Nicholls, R. F. Fine, and B. Honig. Reconciling the magnitude of the microscopic and macroscopic hydrophobic effects. *Science*, 252(5002):106–109, 1991.

[36] A. Klug. From macromolecules to biological assemblies (nobel lecture). *Angewandte Chemie International Edition*, 22(8):565–582, 1983.

[37] Margaret C. Etter. Encoding and decoding hydrogen-bond patterns of organic compounds. *Accounts of Chemical Research*, 23(4):120–126, 1990.

[38] W. L. Jorgensen and J. Pranata. Importance of secondary interactions in triply hydrogen bonded complexes: guanine-cytosine vs uracil-2,6-diaminopyridine. *Journal of the American Chemical Society*, 112(5):2008–2010, 1990.

[39] G.R. Desiraju. *Crystal Engineering: The Design of Organic Solids*. Elsevier, Amsterdam, 1989.

[40] J. Pranata, S. G. Wierschke, and W. L. Jorgensen. Opls potential functions for nucleotide bases. relative association constants of hydrogen-bonded base pairs in chloroform. *Journal of the American Chemical Society*, 113(8):2810–2819, 1991.

[41] M. Bailey and C. J. Brown. The crystal structure of terephthalic acid. *Acta Crystallographica*, 22(3):387–391, 1967.

[42] M. Sledz, J. Janczak, and R. Kubiak. New crystalline modification of terephthalic acid. *Journal of Molecular Structure*, 595(1-3):77–82, 2001.

[43] T. Yokoyama, T. Kamikado, S. Yokoyama, and S. Mashiko. Conformation selective assembly of carboxyphenyl substituted porphyrins on au (111). *The Journal of Chemical Physics*, 121(23):11993–11997, 2004.

[44] J. A. Theobald, N. S. Oxtoby, M. A. Phillips, N. R. Champness, and P. H. Beton. Controlling molecular deposition and layer structure with supramolecular surface assemblies. *Nature*, 424(6952):1029–1031, 2003.

[45] E. Fischer. Synthese der mannose und lävulose. *Berichte der Deutschen Chemischen Gesellschaft*, 23:370?394, 1894.

[46] U. Schlickum, R. Decker, F. Klappenberger, G. Zoppellaro, S. Klyatskaya, W. Auwärter, S. Neppl, K. Kern, H. Brune, M. Ruben, and J. V. Barth. Chiral kagome lattice from simple ditopic molecular bricks. *Journal of the American Chemical Society*, 130:11778–11782, 2008.

[47] D. Kühne, F. Klappenberger, R. Decker, U. Schlickum, H. Brune, S. Klyatskaya, M. Ruben, and J. V. Barth. Self-assembly of nanoporous chiral networks with varying symmetry from sexiphenyl-dicarbonitrile on ag(111). *The Journal of Physical Chemistry C*, 113(41):17851–17859, 2009.

[48] B. Dietrich, J. M. Lehn, and J. P. Sauvage. Les cryptates. *Tetrahedron Letters*, 10(34):2889–2892, 1969.

[49] B. Dietrich, J. M. Lehn, J. P. Sauvage, and J. Blanzat. Cryptates–x : Syntheses et proprietes physiques de systemes diaza-polyoxa-macrobicycliques. *Tetrahedron*, 29(11):1629–1645, 1973.

[50] S. Roche, J. A. Thomas, and L. J. Yellowlees. A highly coupled ruiii-ruii system incorporating sulfur donor ligands. *Chemical Communications*, (14):1429–1430, 1998.

[51] S. Stepanow, M. Lingenfelder, A. Dmitriev, H. Spillmann, E. Delvigne, N. Lin, X. Deng, Ch. Cai, J. V. Barth, and K. Kern. Steering molecular organization and host-guest interactions using two-dimensional nanoporous coordination systems. *Nature Materials*, 3(4):229–233, 2004.

[52] U. Schlickum, R. Decker, F. Klappenberger, G. Zoppellaro, S. Klyatskaya, M. Ruben, I. Silanes, A. Arnau, K. Kern, H. Brune, and J. V. Barth. Metal-organic honeycomb nanomeshes with tunable cavity size. *Nano Lett*, 7(12):3813–7, 2007.

[53] J. Monod, J. P. Changeux, and F. J. Allosteric proteins and cellular control systems. *Journal of Molecular Biology*, 6(4):306–329, 1963.

[54] G. Gagnaire, A. Jeunet, and J. L. Pierre. An artificial allosteric system without metal cation binding : regulation of dipolar splitting in a biradical by a neutral molecular substrate. *Tetrahedron Letters*, 32(18):2021–2024, 1991.

[55] J. C. Rodríguez-Ubis, O. Juanes, and E. Brunet. A simple polyheterotopic molecular receptor derived from bispyrazolylmethane showing negative allosteric co-operation of zn(ii). *Tetrahedron Letters*, 35(8):1295–1298, 1994.

[56] V. Toupance, T.and Ahsen and J. Simon. Ionoelectronics. cation-induced nonlinear complexation: Crown ether- and poly(ethylene oxide)-substituted lutetium bisphthalocyanines. *Journal of the American Chemical Society*, 116(12):5352–5361, 1994.

[57] J. Rebek. Binding forces, equilibria and rates: new models for enzymic catalysis. *Accounts of Chemical Research*, 17(7):258–264, 1984.

[58] B. Liu, M. Ma, D. Zacher, A. Bétard, K. Yusenko, N. Metzler-Nolte, Ch. Wöll, and R.A. Fischer. Chemistry of surmofs: Layer-selective installation of functional groups and post-synthetic covalent modification probed by fluorescence microscopy. *Journal of the American Chemical Society*, 133(6):1734–1737, 2011.

[59] D. Écija, W. Auwärter, S. Vijayaraghavan, K. Seufert, F. Bischoff, K. Tashiro, and J. V. Barth. Assembly and manipulation of rotatable cerium porphyrinato sandwich complexes on a surface. *Angewandte Chemie International Edition*, 50(17):3872–3877, 2011.

[60] L. Addadi, Z. Berkovitch-Yellin, I. Weissbuch, J. van Mil, L. J. W. Shimon, M. Lahav, and L. Leiserowitz. Growth and dissolution of organic crystals with tailor-made inhibitors implications in stereochemistry and materials science. *Angewandte Chemie International Edition*, 24(6):466–485, 1985.

[61] C. J. Eckhardt, N. M. Peachey, D. R. Swanson, J. M. Takacs, M. A. Khan, X. Gong, J. H. Kim, J. Wang, and R. A. Uphaus. Separation of chiral phases in monolayer crystals of racemic amphiphiles. *Nature*, 362(6421):614–616, 1993.

[62] S. De Feyter, P. C. M. Grim, M. Rücker, P. Vanoppen, Ch. Meiners, M. Sieffert, S. Valiyaveettil, K. Müllen, and F. C. De Schryver. Expression of chirality by achiral coadsorbed molecules in chiral monolayers observed by stm. *Angewandte Chemie International Edition*, 37(9):1223–1226, 1998.

[63] F. Stevens, D. J. Dyer, and D. M. Walba. Direct observation of enantiomorphous monolayer crystals from enantiomers by scanning tunneling microscopy. *Angewandte Chemie International Edition*, 35(8):900–901, 1996.

[64] S. Sowerby, W. Heckl, and G. Petersen. Chiral symmetry breaking during the self-assembly of monolayers from achiral purine molecules. *Journal of Molecular Evolution*, 43(5):419–424, 1996.

[65] R. M. Hazen, T. R. Filley, and G. A. Goodfriend. Selective adsorption of l- and d-amino acids on calcite: Implications for biochemical homochirality. *Proceedings of the National Academy of Sciences of the United States of America*, 98(10):5487–5490, 2001.

[66] D.B. Cline. *Physical Origin of Homochirality in Life*. AIP Press, Woodbury / New York, 1996.

[67] H. Fang, L. C. Giancarlo, and G. W. Flynn. Direct determination of the chirality of organic molecules by scanning tunneling microscopy. *The Journal of Physical Chemistry B*, 102(38):7311–7315, 1998.

[68] G. P. Lopinski, D. J. Moffatt, D. D. M. Wayner, and R. A. Wolkow. Determination of the absolute chirality of individual adsorbed molecules using the scanning tunnelling microscope. *Nature*, 392(6679):909–911, 1998.

[69] M. Böhringer, K. Morgenstern, W. D. Schneider, and R. Berndt. Separation of a racemic mixture of two-dimensional molecular clusters by scanning tunneling microscopy. *Angewandte Chemie International Edition*, 38(6):821–823, 1999.

[70] A. Kühnle, T. R. Linderoth, B. Hammer, and F. Besenbacher. Chiral recognition in dimerization of adsorbed cysteine observed by scanning tunnelling microscopy. *Nature*, 415(6874):891–893, 2002.

[71] M.O. Lorenzo, C. J. Baddeley, C. Muryn, and R. Raval. Extended surface chirality from supramolecular assemblies of adsorbed chiral molecules. *Nature*, 404(6776):376–379, 2000.

[72] R.A. Sheldon. *Chirotechnology*. Dekker, New York / Basel, 1993.

[73] W. Graupner, F. Meghdadi, G. Leising, G. Lanzani, M. Nisoli, S. De Silvestri, W. Fischer, and F. Stelzer. Photoexcitations in para-hexaphenyl. *Physical Review B*, 56(16):10128, 1997.

[74] G. Grem, G. Leditzky, B. Ullrich, and G. Leising. Realization of a blue-light-emitting device using poly(p-phenylene). *Advanced Materials*, 4(1):36–37, 1992.

[75] D. J. Gundlach, Y. Y. Lin, T. N. Jackson, and D. G. Schlom. Oligophenyl-based organic thin film transistors. *Applied Physics Letters*, 71(26):3853–3855, 1997.

[76] R. Resel. Crystallographic studies on hexaphenyl thin films – a review. *Thin Solid Films*, 433(1-2):1–11, 2003.

[77] M. Era, T. Tsutsui, and S. Saito. Polarized electroluminescence from oriented p-sexiphenyl vacuum-deposited film. *Applied Physics Letters*, 67(17):2436–2438, 1995.

[78] G. Leising, S. Tasch, Ch. Brandstatter, F. Meghdadi, G. Froyer, and L. Athouel. Red-green-blue light emission from a thin film electroluminescence device based on parahexaphenyl. *Advanced Materials*, 9(1):33–36, 1997.

[79] H. Yanagi and S. Okamoto. Orientation-controlled organic electroluminescence of p-sexiphenyl films. *Applied Physics Letters*, 71(18):2563–2565, 1997.

[80] M. Oehzelt, L. Grill, S. Berkebile, G. Koller, F. P. Netzer, and M. G. Ramsey. The molecular orientation of para-sexiphenyl on cu(110) and cu(110) p(2×1)o. *ChemPhysChem*, 8(11):1707–1712, 2007.

[81] G. Koller, S. Berkebile, J.R. Krenn, G. Tzvetkov, G. Hlawacek, O. Lengyel, F.P. Netzer, C. Teichert, R. Resel, and M.G. Ramsey. Oriented sexiphenyl single crystal nanoneedles on tio2 (110). *Advanced Materials*, 16(23-24):2159–2162, 2004.

[82] Y. Hu, K. Maschek, L. D. Sun, M. Hohage, and P. Zeppenfeld. para-sexiphenyl thin film growth on cu(1 1 0) and cu(1 1 0)-(2×1)o surfaces. *Surface Science*, 600(3):762–769, 2006.

[83] W. P. Fehlhammer and M. Fritz. Emergence of a cnh and cyano complex based organometallic chemistry. *Chemical Reviews*, 93(3):1243–1280, 1993.

[84] T. Sleator and R. Tycko. Observation of individual organic molecules at a crystal surface with use of a scanning tunneling microscope. *Physical Review Letters*, 60(14):1418, 1988.

[85] N.A. Kato, M. Hara, Sasabe H., and W. Knoll. An interpretation for the stm imaging of an organic molecule, tetrathiafulvalene - tetracyanoquinodimethane (ttf - tcnq). *Nanotechnology*, 7(2):122, 1996.

[86] J.S. Miller. Organometallic- and organic-based magnets: New chemistry and new materials for the new millennium. *Inorganic Chemistry*, 39(20):4392–4408, 2000.

[87] J. S. Miller and A. J. Epstein. Tetracyanoethylene-based organic magnets. *Chemical Communications*, (13):1319–1325, 1998.

[88] F. Klappenberger, D. Kühne, W. Krenner, I. Silanes, A. Arnau, F. J. Garcia de Abajo, S. Klyatskaya, M. Ruben, and J. V. Barth. Dichotomous array of chiral quantum corrals by a self-assembled nanoporous kagomé network. *Nano Letters*, 9(10):3509–3514, 2009.

[89] D. Kühne, F. Klappenberger, R. Decker, U. Schlickum, H. Brune, S. Klyatskaya, M. Ruben, and J. V. Barth. High-quality 2d metal-organic coordination network providing giant cavities within mesoscale domains. *Journal of the American Chemical Society*, 131:3881–3883, 2009.

[90] U. Schlickum, F. Klappenberger, R. Decker, G. Zoppellaro, S. Klyatskaya, M. Ruben, K. Kern, H. Brune, and J. V. Barth. Surface-confined metal organic nanostructures from co-directed assembly of linear terphenyl-dicarbonitrile linkers on ag(111). *The Journal of Physical Chemistry C*, 114(37):15602–15606, 2010.

[91] I. Syozi. Statistics of kagomé lattice. *Progress of Theoretical Physics*, 6(3):306–308, 1951.

[92] F. Rosei, M. Schunack, Y. Naitoh, P. Jiang, A. Gourdon, E. Laegsgaard, I. Stensgaard, Ch. Joachim, and F. Besenbacher. Properties of large organic molecules on metal surfaces. *Progress in Surface Science*, 71(5-8):95–146, 2003.

[93] B. S. Swartzentruber, A. P. Smith, and H. Jónsson. Experimental and theoretical study of the rotation of si ad-dimers on the si(100) surface. *Physical Review Letters*, 77(12):2518, 1996.

[94] L. J. Lauhon and W. Ho. Single molecule thermal rotation and diffusion: Acetylene on cu(001). *The Journal of Chemical Physics*, 111(13):5633–5636, 1999.

[95] J. V. Barth. Fresh perspectives for surface coordination chemistry. *Surface Science*, 603(10-12):1533–1541, 2009.

[96] N. Richardson. Two-dimensional crystals: Through the looking glass. *Nature Mater*, 5(2):91–92, 2006.

[97] M. Volmer. The migration of adsorbed molecules on surfaces of solids. *Transactions of the Faraday Society*, 28:359–363, 1932.

[98] I. Langmoir. The adsorption of gases on plane surfaces of glass, mica and platinum. *Journal of the American Chemical Society*, 40(9):1361, 1918.

[99] G. Ehrlich and K. Stolt. Surface diffusion. *Annual Review of Physical Chemistry*, 31(1):603–637, 1980.

[100] T. T. Tsong. Quantitative investigations of atomic processes on metal surfaces at atomic resolution. *Progress in Surface Science*, 10(2):165–248, 1980.

[101] M.A. Moris, M. Bowker, and D.A. King. *Simple Processes at the Gas-Solid Interface*, volume 19. Elsevier, 1984.

[102] A. G. Naumovets and Yu S. Vedula. Surface diffusion of adsorbates. *Surface Science Reports*, 4(7-8):365–434, 1985.

[103] R. Gomer. Diffusion of adsorbates on metal surfaces. *Reports on Progress in Physics*, 53(7):917, 1990.

[104] T. Ala-Nissila, R. Ferrando, and S. C. Ying. Collective and single particle diffusion on surfaces. *Advances in Physics*, 51(3):949 – 1078, 2002.

[105] H.P. Bonzel. *Diffusion in Solid Metals and Alloys*. Springer, 1993.

[106] G. L. Kellogg. Field ion microscope studies of single-atom surface diffusion and cluster nucleation on metal surfaces. *Surface Science Reports*, 21(1-2):1–88, 1994.

[107] E. G. Seebauer and C. E. Allen. Estimating surface diffusion coefficients. *Progress in Surface Science*, 49(3):265–330, 1995.

[108] T. Ala-Nissila and S. C. Ying. Theory of classical surface diffusion. *Progress in Surface Science*, 39(3):227–323, 1992.

[109] S.J. Lombardo and A.T. Bell. A review of theoretical models of adsorption, diffusion, desorption, and reaction of gases on metal surfaces. *Surface Science Reports*, 13(1-2):3–72, 1991.

[110] A. Zangwill. *Physics at surfaces*. Cambridge University Press, Cambridge, 1988.

[111] S. Arrhenius. Über die reaktionsgeschwindigkeit bei der inversion von rohrzucker durch säuren. *Zeitschrift für Physikalische Chemie*, 4:226, 1889.

[112] J. C. Dunphy, M. Rose, S. Behler, D. F. Ogletree, M. Salmeron, and P. Sautet. Acetylene structure and dynamics on pd(111). *Physical Review B*, 57(20):R12705, 1998.

[113] J. Weckesser, J.V. Barth, and K. Kern. Direct observation of surface diffusion of large organic molecules at metal surfaces: Pvba on pd(110). *Journal of Chemical Physics*, 110(11):5351–5354, 1999.

[114] J. Weckesser, J. V. Barth, and K. Kern. Mobility and bonding transition of c_{60} on pd(110). *Physical Review B*, 64(16):161403, 2001.

[115] M. Schunack, E. Lægsgaard, I. Stensgaard, and F. Besenbacher. Bonding and ordering of decacyclene molecules on cu(110) studied by scanning tunneling microscopy. *The Journal of Chemical Physics*, 117(18):8493–8498, 2002.

[116] M. Schunack, T. R. Linderoth, F. Rosei, E. Laegsgaard, I. Stensgaard, and F. Besenbacher. Long jumps in the surface diffusion of large molecules. *Physical Review Letters*, 88(15):156102, 2002.

[117] Y. Shirai, A. J. Osgood, Y. Zhao, K. F. Kelly, and J. M. Tour. Directional control in thermally driven single-molecule nanocars. *Nano Letters*, 5(11):2330–2334, 2005.

[118] J. F. Morin, Y. Shirai, and J. M. Tour. En route to a motorized nanocar. *Organic Letters*, 8(8):1713–1716, 2006.

[119] G. Vives and J. M. Tour. Synthesis of single-molecule nanocars. *Accounts of Chemical Research*, 42(3):473–487, 2009.

[120] T. Sasaki, J. M. Guerrero, and J. M. Tour. The assembly line: self-assembling nanocars. *Tetrahedron*, 64(36):8522–8529, 2008.

[121] Ivar Giaever. Energy gap in superconductors measured by electron tunneling. *Physical Review Letters*, 5(4):147–148, 1960.

[122] J. Bardeen. Tunnelling from a many-particle point of view. *Physical Review Letters*, 6(2):57–59, 1961.

[123] L. Kipp. *http://www.ieap.uni-kiel.de/surface/ag-kipp/stm/stm.htm*.

[124] J. Tersoff and D. R. Hamann. Theory and application for the scanning tunneling microscope. *Physical Review Letters*, 50(25):1998–2001, 1983.

[125] J. Tersoff and D. R. Hamann. Theory of the scanning tunneling microscope. *Physical Review B*, 31(2):805–813, 1985.

[126] G. Binnig, H. Rohrer, C. Gerber, and E. Weibel. (7x7) reconstruction on si(111) resolved in real space. *Physical Review Letters*, 50(2):120–123, 1983.

[127] J. Wintterlin, J. Wiechers, H. Brune, T. Gritsch, H. Hofer, and R. J. Behm. Atomic-resolution imaging of close-packed metal-surfaces by scanning tunneling microscopy. *Physical Review Letters*, 62(1):59–62, 1989.

[128] C. J. Chen. Microscopic view of scanning tunneling microscopy. *Journal of Vacuum Science & Technology A-Vacuum Surfaces and Films*, 9(1):44–50, 1991.

[129] W. A. Hofer, A. S. Foster, and A. L. Shluger. Theories of scanning probe microscopes at the atomic scale. *Reviews of Modern Physics*, 75(4):1287–1331, 2003.

[130] T. Zambelli, J. V. Barth, J. Wintterlin, and G. Ertl. Complex pathways in dissociative adsorption of oxygen on platinum. *Nature*, 390(6659):495–497, 1997.

[131] M. Ø. Pedersen, L. Österlund, J. J. Mortensen, M. Mavrikakis, L. B. Hansen, I. Stensgaard, E. Lægsgaard, J. K. Nørskov, and F. Besenbacher. Diffusion of n adatoms on the fe(100) surface. *Physical Review Letters*, 84(21):4898, 2000.

[132] L. Bartels, G. Meyer, and K. H. Rieder. The evolution of co adsorption on cu(111) as studied with bare and co-functionalized scanning tunneling tips. *Surface Science*, 432(3):L621–L626, 1999.

[133] M. L. Bocquet and P. Sautet. Stm and chemistry: a qualitative molecular orbital understanding of the image of co on a pt surface. *Surface Science*, 360(1-3):128–136, 1996.

[134] B. I. Lundqvist, O. Gunnarsson, H. Hjelmberg, and J. K. Nørskov. Theoretical description of molecule-metal interaction and surface reactions. *Surface Science*, 89(1-3):196–225, 1979.

[135] B. Hammer, J. K. Nørskov, B.C. Gates, and H. Knozinger. Theoretical surface science and catalysis - calculations and concepts. *Academic Press*, Volume 45:71–129, 2000.

[136] D. M. Newns. Self-consistent model of hydrogen chemisorption. *Physical Review*, 178(3):1123, 1969.

[137] P. W. Anderson. Localized magnetic states in metals. *Physical Review*, 124(1):41, 1961.

[138] N. D. Lang. Vacuum tunneling current from an adsorbed atom. *Physical Review Letters*, 55(2):230, 1985.

[139] N. D. Lang. Theory of single-atom imaging in the scanning tunneling microscope. *Physical Review Letters*, 56(11):1164, 1986.

[140] A. Weber-Bargioni, W. Auwärter, F. Klappenberger, J. Reichert, S. Lefrançois, T. Strunskus, Ch. Wöll, A. Schiffrin, Y. Pennec, and J. V. Barth. Visualizing the frontier orbitals of a conformationally adapted metalloporphyrin. *ChemPhysChem*, 9(1):89–94, 2008.

[141] A. Weber-Bargioni, J. Reichert, A. P. Seitsonen, W. Auwärter, A. Schiffrin, and J. V. Barth. Interaction of cerium atoms with surface-anchored porphyrin molecules. *Journal of Physical Chemistry C*, 112(10):3453–3455, 2008.

[142] R. Berndt, J. K. Gimzewski, and R. R. Schlittler. Bias-dependent stm images of oxygen-induced structures on ti(0001) facets. *Surface Science*, 310(1-3):85–88, 1994.

[143] C. Julian Chen. Corrugation reversal in scanning tunneling microscopy. *The 1993 international conference on scanning tunneling microscopy*, 12:2193–2199, 1994.

[144] P. Sautet. Atomic adsorbate identification with the stm: a theoretical approach. *Surface Science*, 374(1-3):406–417, 1997.

[145] I. S. Tilinin, M. K. Rose, J. C. Dunphy, M. Salmeron, and M. A. Van Hove. Identification of adatoms on metal surfaces by stm: experiment and theory. *Surface Science*, 418(3):511–520, 1998.

[146] R Temirov, S Soubatch, O Neucheva, A C Lassise, and F S Tautz. A novel method achieving ultra-high geometrical resolution in scanning tunnelling microscopy. *New Journal of Physics*, 10(5):053012, 2008.

[147] E. K. Vestergaard. *Scanning Tunneling Microscopy Studies of Model Systems Relevant to Catalysis*. PhD thesis, University of Aarhus, 2004.

[148] J. P. Ibe, P. P. Bey, S. L. Brandow, R. A. Brizzolara, N. A. Burnham, D. P. Dilella, K. P. Lee, C. R. K. Marrian, and R. J. Colton. On the electrochemical etching of tips for scanning tunneling microscopy. *Journal of Vacuum Science & Technology A-Vacuum Surfaces and Films*, 8(4):3570–3575, 1990.

[149] G. Meyer. A simple low-temperature ultrahigh-vacuum scanning tunneling microscope capable of atomic manipulation. *Review of Scientific Instruments*, 67(8):2960–2965, 1996.

[150] K. Besocke. An easily operable scanning tunneling microscope. *Surface Science*, 181(1-2):145–153, 1987.

[151] K.F. Braun. *Manipulation mit einem Rastertunnelmikroskop bei tiefen Temperaturen*. PhD thesis, Freie Universität Berlin, 2000.

[152] CreaTec Fischer & Co. GmbH. *http://www.createc.de*.

[153] A. Schiffrin. *Self-assembly of Amino Acids on Noble Metal surfaces: Morphological, Chemical and Electronic Control of Matter at the Nanoscale*. PhD thesis, University of British Columbia, 2007.

[154] M. P. Seah and W. A. Dench. Quantitative electron spectroscopy of surfaces: A standard data base for electron inelastic mean free paths in solids. *Surface and Interface Analysis*, 1(1):2–11, 1979.

[155] S Hüfner. *Photoelectron Spectroscopy: Principles and Applications*. Springer-Verlag, Berlin, 1996.

[156] J. Stöhr. *NEXAFS Spectroscopy*. Springer-Verlag, Berlin, 1992.

[157] M. E. Cañas-Ventura, F. Klappenberger, S. Clair, S. Pons, K. Kern, H. Brune, T. Strunskus, Ch Wöll, R. Fasel, and J. V. Barth. Coexistence of one- and two-dimensional supramolecular assemblies of terephthalic acid on pd(111) due to self-limiting deprotonation. *The Journal of Chemical Physics*, 125(18):184710–8, 2006.

[158] J. Elemans, S. Lei, and S. De Feyter. Molecular and supramolecular networks on surfaces: From two-dimensional crystal engineering to reactivity. *Angewandte Chemie International Edition*, 48(40):7298–7332, 2009.

[159] N. Lin, S. Stepanow, M. Ruben, and J. V. Barth. Surface-confined supramolecular coordination chemistry. *Top. Curr. Chem.*, 287:1–44, 2009.

[160] M. Böhringer, K. Morgenstern, W. D. Schneider, R. Berndt, F. Mauri, A. De Vita, and R. Car. Two-dimensional self-assembly of supramolecular clusters and chains. *Physical Review Letters*, 83(2):324, 1999.

[161] M. Ch. Blüm, E. Cavar, M. Pivetta, F. Patthey, and W.D. Schneider. Conservation of chirality in a hierarchical supramolecular self-assembled structure with pentagonal symmetry. *Angewandte Chemie International Edition*, 44(33):5334–5337, 2005.

[162] M. Treier, P. Ruffieux, P. Groning, S. Xiao, C. Nuckolls, and R. Fasel. An aromatic coupling motif for two-dimensional supramolecular architectures. *Chemical Communications*, (38):4555–4557, 2008.

[163] S. Griessl, M. Lackinger, M. Edelwirth, M. Hietschold, and W. M. Heckl. Self-assembled two-dimensional molecular host-guest architectures from trimesic acid. *Single Molecules*, 3(1):25–31, 2002.

[164] A. Dmitriev, N. Lin, J. Weckesser, J. V. Barth, and K. Kern. Supramolecular assemblies of trimesic acid on a cu(100) surface. *The Journal of Physical Chemistry B*, 106(27):6907–6912, 2002.

[165] A. Otero, J. Fernandez-Baeza, A. Lara-Sanchez, C. Alonso-Moreno, I. Marquez-Segovia, L. F. Sanchez-Barba, and A. M. Rodriguez. Ring-opening polymerization of cyclic esters by an enantiopure heteroscorpionate rare earth initiator. *Angewandte Chemie International Edition*, 48(12):2176–9, 2009.

[166] M. E. Cañas-Ventura, W. Xiao, D. Wasserfallen, K. Müllen, H. Brune, J.V. Barth, and Roman Fasel. Self-assembly of periodic bicomponent wires and ribbons. *Angewandte Chemie International Edition*, 46(11):1814–1818, 2007.

[167] A. Schiffrin, A. Riemann, W. Auwärter, Y. Pennec, A. Weber-Bargioni, D. Cvetko, A. Cossaro, A. Morgante, and J. V. Barth. Zwitterionic self-assembly of l-methionine nanogratings on the ag(111) surface. *Proceedings of the National Academy of Sciences*, 104(13):5279–5284, 2007.

[168] M. Lackinger and W. M. Heckl. Carboxylic acids: Versatile building blocks and mediators for two-dimensional supramolecular self-assembly. *Langmuir*, 25(19):11307–11321, 2009.

[169] A. Dmitriev, H. Spillmann, N. Lin, J. V. Barth, and K. Kern. Modular assembly of two-dimensional metal-organic coordination networks at a metal surface. *Angewandte Chemie International Edition*, 42(23):2670–2673, 2003.

[170] S. Stepanow, N. Lin, and J. V. Barth. Modular assembly of low-dimensional coordination architectures on metal surfaces. *Journal of Physics: Condensed Matter*, 20:184002, 2008.

[171] A. Breitruck, H. E. Hoster, and R. J. Behm. Short-range order in a metal-organic network. *The Journal of Physical Chemistry C*, 113(51):21265–21268, 2009.

[172] N. Wintjes, J. Hornung, J. Lobo-Checa, T. Voigt, T. Samuely, C. Thilgen, M. Stöhr, F. Diederich, and . A. Jung. Supramolecular synthons on surfaces: Controlling dimensionality and periodicity of tetraarylporphyrin assemblies

by the interplay of cyano and alkoxy substituents. *Chemistry A European Journal*, 14(19):5794–5802, 2008.

[173] M. Marschall, J. Reichert, A. Weber-Bargioni, K. Seufert, W. Auwärter, S. Klyatskaya, G. Zoppellaro, M. Ruben, and J. V. Barth. Random two-dimensional string networks based on divergent coordination assembly. *Nat Chem*, 2(2):131–137, 2010.

[174] S. M. Barlow and R. Raval. Complex organic molecules at metal surfaces: bonding, organisation and chirality. *Surface Science Reports*, 50(6-8):201–341, 2003.

[175] S. Stepanow, N. Lin, F. Vidal, A. Landa, M. Ruben, J. V. Barth, and K. Kern. Programming supramolecular assembly and chirality in two-dimensional dicarboxylate networks on a cu(100) surface. *Nano Letters*, 5(5):901–4, 2005.

[176] F. Vidal, E. Delvigne, S. Stepanow, N. Lin, J. V. Barth, and K. Kern. Chiral phase transition in two-dimensional supramolecular assemblies of prochiral molecules. *Journal of the American Chemical Society*, 127(28):10101–6, 2005.

[177] A. Dmitriev, H. Spillmann, S. Stepanow, T. Strunskus, Ch. Wöll, A. P. Seitsonen, M. Lingenfelder, N. Lin, J. V. Barth, and K. Kern. Asymmetry induction by cooperative intermolecular hydrogen bonds in surface-anchored layers of achiral molecules. *ChemPhysChem*, 7(10):2197–2204, 2006.

[178] R. Fasel, A. Cossy, K. H. Ernst, F. Baumberger, T. Greber, and J. Osterwalder. Orientation of chiral heptahelicene $c_{30}h_{18}$ on copper surfaces: An x-ray photoelectron diffraction study. *The Journal of Chemical Physics*, 115(2):1020–1027, 2001.

[179] R. Fasel, M. Parschau, and K. H. Ernst. Chirality transfer from single molecules into self-assembled monolayers. *Angewandte Chemie International Edition*, 42(42):5178–5181, 2003.

[180] J. V. Barth, J. Weckesser, G. Trimarchi, M. Vladimirova, A. De Vita, C. Cai, H. Brune, P. Gunter, and K. Kern. Stereochemical effects in supramolecular self-assembly at surfaces: 1-d versus 2-d enantiomorphic ordering for pvba and peba on ag(111). *Journal of the American Chemical Society*, 124(27):7991–8000, 2002.

[181] S. Weigelt, C. Busse, L. Petersen, E. Rauls, B. Hammer, K. V. Gothelf, F. Besenbacher, and T. R. Linderoth. Chiral switching by spontaneous conformational change in adsorbed organic molecules. *Nature Materials*, 5(2):112–117, 2006.

[182] P. Bordat and R. Brown. A molecular model of p-terphenyl and its disorder-order transition. *Chemical Physics*, 246(1-3):323–334, 1999.

[183] W. von der Saal, R. A. Engh, A. Eichinger, B. Gabriel, R. Kucznierz, and J. Sauer. Syntheses and selective inhibitory activities of terphenyl-bisamidines for serine proteases. *Archiv der Pharmazie*, 329(2):73–82, 1996.

[184] W. Auwärter, A. Schiffrin, A. Weber-Bargioni, Y. Pennec, A. Riemann, and J. V. Barth. Molecular nanoscience and engineering on surfaces. *International Journal of Nanotechnology*, 5:1171–1193, 2008.

[185] I. Horcas, R. Fernandez, J. M. Gomez-Rodriguez, J. Colchero, J. Gomez-Herrero, and A. M. Baro. Wsxm: A software for scanning probe microscopy and a tool for nanotechnology. *Review of Scientific Instruments*, 78(1):013705–8, 2007.

[186] P. Feulner, T. Niedermayer, K. Eberle, R. Schneider, D. Menzel, A. Baumer, E. Schmich, A. Shaporenko, Y. Tai, and M. Zharnikov. Strong temperature dependence of irradiation effects in organic layers. *Physical Review Letters*, 93(17):178302, 2004.

[187] Y. Okuno, T. Yokoyama, S. Yokoyama, T. Kamikado, and S. Mashiko. Theoretical study of benzonitrile clusters in the gas phase and their adsorption onto a au(111) surface. *Journal of the American Chemical Society*, 124(24):7218–7225, 2002.

[188] J. Frommer. Scanning tunneling microscopy and atomic force microscopy in organic chemistry. *Angewandte Chemie International Edition*, 31(10):1298–1328, 1992.

[189] M. Itoh, M. Takamatsu, N. Kizu, and Y. Fujiwara. Van der waals cluster and excimer formations of 1-cyanonaphthalene and methyl-substituted 1-cyanonaphthalenes in supersonic expansion. *The Journal of Physical Chemistry*, 95(24):9682–9687, 1991.

[190] T. Michinobu, C. Boudon, J. P. Gisselbrecht, P. Seiler, B. Frank, N. N. P. Moonen, M. Gross, and F. Diederich. Donor-substituted 1,1,4,4-tetracyanobutadienes (tcbds): New chromophores with efficient intramolecular charge-transfer interactions by atom-economic synthesis. *Chemistry A European Journal*, 12(7):1889–1905, 2006.

[191] D. Duflot, J. P. Flament, J. Heinesch, and M. J. Hubin-Franskin. Re-analysis of the k-shell spectrum of benzene. *Journal of Electron Spectroscopy and Related Phenomena*, 113(1):79–90, 2000.

[192] S. Carniato, V. Ilakovac, J. J. Gallet, E. Kukk, and Y. Luo. Hybrid density-functional theory calculations of near-edge x-ray absorption fine-structure spectra: Applications on benzonitrile in gas phase. *Physical Review A*, 71(2):022511, 2005.

[193] J.-L. Baudour, Y. Delugeard, and P. Rivet. Structural phase transition in polyphenyls. vi. crystal structure of the low-temperature ordered phase of p-quaterphenyl at 110 k. *Acta Crystallographica Section B*, 34(2):625–628, 1978.

[194] J. V. Barth, J. Weckesser, Ch. Cai, P. Günter, L. Bürgi, O. Jeandupeux, and K. Kern. Building supramolecular nanostructures at surfaces by hydrogen bonding. *Angewandte Chemie International Edition*, 39(7):1230–1234, 2000.

[195] F. Klappenberger, M. E. Cañas-Ventura, S. Clair, S. Pons, U. Schlickum, Z. R. Qu, T. Strunskus, A. Comisso, Ch. Wöll, H. Brune, K. Kern, A. De Vita, M. Ruben, and J. V. Barth. Does the surface matter? hydrogen-bonded chain formation of an oxalic amide derivative in a two- and three-dimensional environment. *ChemPhysChem*, 9(17):2522–2530, 2008.

[196] C. A. Angell. Formation of glasses from liquids and biopolymers. *Science*, 267:1924–1935, 1995.

[197] P. G. Debendetti and F. H. Stillinger. Supercooled liquids and the glass transition. *Nature*, 410:259–267, 2001.

[198] R. Zallen. *The Physics of Amorphous Solids*. Wiley, NewYork, 1983.

[199] D. Chandler. Liquids: Condensed, disordered, and sometimes complex. *Proc. Natl Acad. Sci. USA*, 106:15111–15112, 2009.

[200] R. Otero, M. Lukas, R. E. A. Kelly, W. Xu, E. Laegsgaard, I. Stensgaard, L. N. Kantorovich, and F. Besenbacher. Elementary structural motifs in a random

network of cytosine adsorbed on a gold(111) surface. *Science*, 319(5861):312–315, 2008.

[201] M. O. Blunt, J. C. Russell, M. d. C. Giménez-Lopez, J. P. Garrahan, X. Lin, M. Schröder, N. R. Champness, and P. H. Beton. Random tiling and topological defects in a two-dimensional molecular network. *Science*, 322:1077–1081, 2008.

[202] H. Zhou, H. Dang, J. H. Yi, A. Nanci, A.and Rochefort, and J. D. Wuest. Frustrated 2d molecular crystallization. *Journal of the American Chemical Society*, 129:13774–13775, 2007.

[203] J. P. Garrahan, A. Stannard, M. O. Blunt, and P. H. Beton. Molecular random tilings as glasses. *Proc. Natl Acad. Sci. USA*, 106:15209–15213, 2009.

[204] M. P. Johansson and J. Olsen. Torsional barriers and equilibrium angle of biphenyl: Reconciling theory with experiment. *Journal of Chemical Theory and Computation*, 4(9):1460–1471, 2008.

[205] S. Weigelt, C. Busse, Ch. Bombis, M. M. Knudsen, K. V. Gothelf, E. Lægsgaard, F. Besenbacher, and T. R. Linderoth. Surface synthesis of 2d branched polymer nanostructures. *Angewandte Chemie International Edition*, 47(23):4406–4410, 2008.

[206] N. A. A. Zwaneveld, R. Pawlak, M. Abel, D. Catalin, D. Gigmes, D. Bertin, and L. Porte. Organized formation of 2d extended covalent organic frameworks at surfaces. *Journal of the American Chemical Society*, 130(21):6678–6679, 2008.

[207] S. Clair, S. Pons, S. Fabris, S. Baroni, H. Brune, K. Kern, and J. V. Barth. Monitoring two-dimensional coordination reactions: Directed assembly of coterephthalate nanosystems on au(111). *The Journal of Physical Chemistry B*, 110(11):5627–5632, 2006.

[208] P. Messina, A. Dmitriev, N. Lin, H. Spillmann, M. Abel, J. V. Barth, and K. Kern. Direct observation of chiral metal-organic complexes assembled on a cu100 surface. *J Am Chem Soc*, 124(47):14000–1, 2002.

[209] N. Lin, S. Stepanow, F. Vidal, J. V. Barth, and K. Kern. Manipulating surface-supported di-iron units via ligand control. *Chemical Communications*, pages 1681–1683, 2005.

[210] S. Stepanow, N. Lin, D. Payer, U. Schlickum, F. Klappenberger, G. Zoppellaro, M. Ruben, H. Brune, J. V. Barth, and K. Kern. Surface-assisted assembly of 2d metal-organic networks that exhibit unusual threefold coordination symmetry. *Angewandte Chemie International Edition*, 46:710–713, 2007.

[211] P. Przychodzen, T. Korzeniak, R. Podgajny, and B. Sieklucka. Supramolecular coordination networks based on octacyanometalates: from structure to function. *Coordination Chemistry Review*, 250:2234–2260, 2006.

[212] P. Gambardella, S. Stepanow, A. Dmitriev, J. Honolka, F. M. de Groot, M. Lingenfelder, S. Sen Gupta, D. D. Sarma, P. Bencok, S. Stanescu, S. Clair, S. Pons, N. Lin, A. P. Seitsonen, H. Brune, J. V. Barth, and K. Kern. Supramolecular control of the magnetic anisotropy in two-dimensional high-spin fe arrays at a metal interface. *Nat Mater*, 8(3):189–93, 2009.

[213] M. Pivetta, M. C. Blüm, F. Patthey, and W. D. Schneider. Two-dimensional tiling by rubrene molecules self-assembled in supramolecular pentagons, hexagons, and heptagons on a au(111) surface. *Angewandte Chemie International Edition*, 47:1076, 2008.

[214] T. Bauert, L. Merz, D. Bandera, M. Parschau, J. S. Siegel, and K. H. Ernst. Building 2d crystals from 5-fold-symmetric molecules. *Journal of the American Chemical Society*, 131:3460–3462, 2009.

[215] C. W. Tang and S. A. VanSlyke. Organic electroluminescent diodes. *Applied Physics Letters*, 51(12):913–915, 1987.

[216] J. Blochwitz, M. Pfeiffer, T. Fritz, and K. Leo. Low voltage organic light emitting diodes featuring doped phthalocyanine as hole transport material. *Applied Physics Letters*, 73(6):729–731, 1998.

[217] C. D. Sheraw, L. Zhou, J. R. Huang, D. J. Gundlach, T. N. Jackson, M. G. Kane, I. G. Hill, M. S. Hammond, J. Campi, B. K. Greening, J. Francl, and J. West. Organic thin-film transistor-driven polymer-dispersed liquid crystal displays on flexible polymeric substrates. *Applied Physics Letters*, 80(6):1088–1090, 2002.

[218] J. H. Burroughes, D. D. C. Bradley, A. R. Brown, R. N. Marks, K. Mackay, R. H. Friend, P. L. Burns, and A. B. Holmes. Light-emitting diodes based on conjugated polymers. *Nature*, 347(6293):539–541, 1990.

[219] L.L. Chua, J. Zaumseil, J. F. Chang, E. C. W. Ou, P. K. H. Ho, H. Sirringhaus, and R. H. Friend. General observation of n-type field-effect behaviour in organic semiconductors. *Nature*, 434(7030):194–199, 2005.

[220] A. R. Brown, C. P. Jarrett, D. M. de Leeuw, and M. Matters. Field-effect transistors made from solution-processed organic semiconductors. *Synthetic Metals*, 88(1):37–55, 1997.

[221] F. Garnier, A. Yassar, R. Hajlaoui, G. Horowitz, F. Deloffre, B. Servet, S. Ries, and P. Alnot. Molecular engineering of organic semiconductors: design of self-assembly properties in conjugated thiophene oligomers. *Journal of the American Chemical Society*, 115(19):8716–8721, 1993.

[222] C. W. Tang. Two-layer organic photovoltaic cell. *Applied Physics Letters*, 48(2):183–185, 1986.

[223] H.S. Nalwa and J.S. Shirk. *Phthalocyanines: Properties and Applications*, volume 4. VCH, New York, 1996.

[224] J. L. Brédas, D. Beljonne, V. Coropceanu, and J. Cornil. Charge-transfer and energy-transfer processes in π-conjugated oligomers and polymers: A molecular picture. *Chemical Reviews*, 104(11):4971–5004, 2004.

[225] M. Shtein, J. Mapel, J. B. Benziger, and S. R. Forrest. Effects of film morphology and gate dielectric surface preparation on the electrical characteristics of organic-vapor-phase-deposited pentacene thin-film transistors. *Applied Physics Letters*, 81(2):268–270, 2002.

[226] J. L. Brèdas, J. P. Calbert, D. A. da Silva Filho, and J. Cornil. Organic semiconductors: A theoretical characterization of the basic parameters governing charge transport. *Proceedings of the National Academy of Sciences of the United States of America*, 99(9):5804–5809, 2002.

[227] M. Marschall, J. Reichert, K. Seufert, W. Auwärter, F. Klappenberger, A. Weber-Bargioni, S. Klyatskaya, G. Zoppellaro, A. Nefedov, T. Strunskus, C. Woll, M. Ruben, and J. V. Barth. Supramolecular organization and chiral resolution of p-terphenyl-m-dicarbonitrile on the ag(111) metal surface. *Chemphyschem*, 11(7):1446–51, 2010.

[228] N. Stepanow, S. Lin and J.V. Barth. Modular assembly of low-dimensional coordination architectures on metal surfaces. *Journal of Physics: Condensed Matter*, 20(18):184002, 2008.

[229] G. Pawin, K. Wong, D. Kim, D. Sun, L. Bartels, S. Hong, T. Rahman, R. Carp, and M. Marsella. A surface coordination network based on substrate-derived metal adatoms with local charge excess. *Angewandte Chemie International Edition*, 47:8442–8445, 2008.

[230] K. Young Kwon, X. Lin, G. Pawin, K. Wong, and L. Bartels. Oxadiazole-metal interface: from isolated molecules to π-stacking. *Langmuir*, 22(3):857–859, 2005.

[231] S. Müllegger, K. Hänel, T. Strunskus, Ch. Wöll, and A. Winkler. Organic molecular beam deposition of oligophenyls on au(111): A study by x-ray absorption spectroscopy. *ChemPhysChem*, 7(12):2552–2558, 2006.

[232] S. Reiss, H. Krumm, A. Niklewski, V. Staemmler, and Ch. Wöll. The adsorption of acenes on rutile $tio_2(110)$: A multi-technique investigation. *The Journal of Chemical Physics*, 116(17):7704–7713, 2002.

[233] R. Püttner, C. Kolczewski, M. Martins, A. S. Schlachter, G. Snell, M. Sant'Anna, J. Viefhaus, K. Hermann, and G. Kaindl. The c 1s nexafs spectrum of benzene below threshold: Rydberg or valence character of the unoccupied σ-type orbitals. *Chemical Physics Letters*, 393(4-6):361–366, 2004.

[234] F. Klappenberger, D. Kühne, M. Marschall, S. Neppl, W. Krenner, A. Nefedov, T. Strunskus, K. Fink, Ch. Wöll, S. Klyatskaya, O. Fuhr, M. Ruben, and J. V. Barth. Uniform π-system alignment in thin films of template-grown dicarbonitrile-oligophenyls. *Advanced Functional Materials*, 21(9):1631–1642, 2011.

[235] S. Rangan, J. J. Gallet, F. Bournel, S. Kubsky, K. Le Guen, G. Dufour, F. Rochet, F. Sirotti, S. Carniato, and V. Ilakovac. Adsorption of benzonitrile on $si(001) - 2 \times 1$ at 300 k. *Physical Review B*, 71(16):165318, 2005.

[236] M. Piantek, J. Miguel, A. Krüger, C. Navio, M. Bernien, D. K. Ball, K. Hermann, and W. Kuch. Temperature, surface, and coverage-induced conformational changes of azobenzene derivatives on cu(001). *The Journal of Physical Chemistry C*, 113(47):20307–20315, 2009.

[237] E. E. Rennie, B. Kempgens, H. M. Koppe, U. Hergenhahn, J. Feldhaus, B. S. Itchkawitz, A. L. D. Kilcoyne, A. Kivimaki, K. Maier, M. N. Piancastelli, M. Polcik, A. Rudel, and A. M. Bradshaw. A comprehensive photoabsorption, photoionization, and shake-up excitation study of the c 1s cross section of benzene. *The Journal of Chemical Physics*, 113(17):7362–7375, 2000.

[238] K. F. Braun and Saw-Wai Hla. Probing the conformation of physisorbed molecules at the atomic scale using stm manipulation. *Nano Letters*, 5(1):73–76, 2004.

[239] M. Karimi, T. Tomkowski, G. Vidali, and O. Biham. Diffusion of cu on cu surfaces. *Phys Rev B Condens Matter*, 52(7):5364–5374, 1995.

[240] C. C. Perry, S. Haq, B. G. Frederick, and N. V. Richardson. Face specificity and the role of metal adatoms in molecular reorientation at surfaces. *Surface Science*, 409(3):512–520, 1998.

[241] M. Eichberger, M. Marschall, J. Reichert, A. Weber-Bargioni, W. Auwärter, R. L. Wang, H. J. Kreuzer, Y. Pennec, A. Schiffrin, and J. V. Barth. Dimerization boosts one-dimensional mobility of conformationally adapted porphyrins on a hexagonal surface atomic lattice. *Nano Lett*, 8(12):4608–13, 2008.

[242] J. L. Solomon, R. J. Madix, and J. Stöhr. Orientation and absolute coverage of benzene, aniline, and phenol on ag(110) determined by nexafs and xps. *Surface Science*, 255(1-2):12–30, 1991.

[243] A. F. Lee, R. M. Lambert, A. Goldoni, Al. Baraldi, and G. Paolucci. On the coverage-dependent adsorption geometry of benzene adsorbed on pd111: A study by fast xps and nexafs. *The Journal of Physical Chemistry B*, 104(49):11729–11733, 2000.

[244] W. Azzam, B. I. Wehner, R. A. Fischer, A. Terfort, and Ch. Wöll. Bonding and orientation in self-assembled monolayers of oligophenyldithiols on au substrates. *Langmuir*, 18(21):7766–7769, 2002.

[245] A. Crispin, X. Crispin, M. Fahlman, D. A. dos Santos, J. Cornil, N. Johansson, J. Bauer, F. Weissortel, J. Salbeck, J. L. Bredas, and W. R. Salaneck. Influence of dopant on the electronic structure of spiro-oligophenyl-based disordered organic semiconductors. *The Journal of Chemical Physics*, 116(18):8159–8167, 2002.

[246] S. Bedwani, D. Wegner, M.F. Crommie, and A. Rochefort. Strongly reshaped organic-metal interfaces: Tetracyanoethylene on cu(100). *Physical Review Letters*, 101(21):216105, 2008.

[247] X. Gonze, G.M. Rignanese, M. Verstraete, J.M. Beuken, Y. Pouillon, R. Caracas, F. Jollet, M. Torrent, G. Zerah, M. Mikami, Ph. Ghosez, M. Veithen, J.Y. Raty, V. Olevano, F. Bruneval, L. Reining, R. Godby, G. Onida, D.R.

Hamann, D.C. Allan, G. Zerah, F. Jollet, M. Torrent, A. Roy, M. Mikami, Ph. Ghosez, J.Y. Raty, and D.C. Allan. A brief introduction to the abinit software package. *Zeit. Kristallogr.*, 220:558–562, 2005.

[248] M. Torrent, F. Jollet, F. Bottin, G. Zerah, and X. Gonze. Implementation of the projector augmented-wave method in the abinit code. application to the study of iron under pressure. *Comput. Mat. Science*, 42:337–351, 2008.

[249] F. Klappenberger, M. E. Cañas-Ventura, S. Clair, S. Pons, U. Schlickum, Z. R. Qu, H. Brune, K. Kern, T. Strunskus, Ch. Wöll, A. Comisso, A. De Vita, M. Ruben, and J. V. Barth. Conformational adaptation in supramolecular assembly on surfaces. *ChemPhysChem*, 8(12):1782–1786, 2007.

[250] M. I. Page and W. P. Jencks. Entropic contributions to rate accelerations in enzymic and intramolecular reactions and the chelate effect. *Proceedings of the National Academy of Sciences*, 68(8):1678–1683, 1971.

[251] R. Otero, F. Hummelink, F. Sato, S. B. Legoas, P. Thostrup, E. Laegsgaard, I. Stensgaard, D. S. Galvao, and F. Besenbacher. Lock-and-key effect in the surface diffusion of large organic molecules probed by stm. *Nat. Mater.*, 3(11):779–782, 2004.

[252] W. Auwärter, F. Klappenberger, A. Weber-Bargioni, A. Schiffrin, T. Strunskus, Ch. Wöll, Y. Pennec, A. Riemann, and J. V. Barth. Conformational adaptation and selective adatom capturing of tetrapyridyl-porphyrin molecules on a copper (111) surface. *Journal of the American Chemical Society*, 129(36):11279–11285, 2007.

[253] C. M. Drain. Self-organization of self-assembled photonic materials into functional devices: Photo-switched conductors. *Proceedings of the National Academy of Sciences of the United States of America*, 99(8):5178–5182, 2002.

[254] W. Auwärter, A. Weber-Bargioni, A. Riemann, A. Schiffrin, O. Groning, R. Fasel, and J. V. Barth. Self-assembly and conformation of tetrapyridyl-porphyrin molecules on ag(111). *The Journal of Chemical Physics*, 124(19):194708–6, 2006.

[255] S. L. Tait, A. Langner, N. Lin, S. Stepanow, Ch. Rajadurai, M. Ruben, and K. Kern. One-dimensional self-assembled molecular chains on cu(100): interplay between surface-assisted coordination chemistry and substrate commensurability. *Journal of Physical Chemistry C*, 111:10982–10987, 2007.

[256] W. Auwärter, A. Weber-Bargioni, S. Brink, A. Riemann, A. Schiffrin, M. Ruben, and J. V. Barth. Controlled metalation of self-assembled porphyrin nanoarrays in two dimensions. *Chemphyschem*, 8(2):250–254, 2007.

[257] U. Wang, S. C. Kürpick and G. Ehrlich. Surface diffusion of compact and other clusters: ir_x on ir(111). *Physical Review Letters*, 81(22):4923, 1998.

[258] B. G. Briner, M. Doering, H.-P. Rust, and A. M. Bradshaw. Microscopic molecular diffusion enhanced by adsorbate interactions. *Science*, 278(5336):257–260, 1997.

[259] M. Labayen, C. Ramirez, W. Schattke, and O. M. Magnussen. Quasi-collective motion of nanoscale metal strings in metal surfaces. *Nat Mater*, 2(12):783–787, 2003.

[260] F. Klappenberger, A. Weber-Bargioni, W. Auwarter, M. Marschall, A. Schiffrin, and J. V. Barth. Temperature dependence of conformation, chemical state, and metal-directed assembly of tetrapyridyl-porphyrin on cu(111). *Journal of Chemical Physics*, 129(21):214702, 2008.

[261] N. Lin, A. Dmitriev, J. Weckesser, J. V. Barth, and K. Kern. Real-time single-molecule imaging of the formation and dynamics of coordination compounds. *Angewandte Chemie International Edition*, 41(24):4779–4783, 2002.

[262] T. Classen, G. Fratesi, G. Costantini, S. Fabris, F. L. Stadler, C. Kim, S. de Gironcoli, S. Baroni, and K. Kern. Templated growth of metal-organic coordination chains at surfaces. *Angewandte Chemie International Edition*, 44(38):6142–5, 2005.

[263] K. Morgenstern, S. Hla, and K. Rieder. Coexisting superstructures of iodobenzene on cu(111) near saturation coverage. *Surface Science*, 523:141–150, 2003.

[264] D. Heim, K. Seufert, W. Auwärter, C. Aurisicchio, Ch Fabbro, D. Bonifazi, and J. V. Barth. Surface-assisted assembly of discrete porphyrin-based cyclic supramolecules. *Nano Letters*, 10(1):122–128, 2009.

[265] D. Heim, D. Ecija, K. Seufert, W. Auwärter, C. Aurisicchio, Ch. Fabbro, D. Bonifazi, and J. V. Barth. Self-assembly of flexible one-dimensional coordination polymers on metal surfaces. *Journal of the American Chemical Society*, 132(19):6783–6790, 2010.

[266] Everly B. Fleischer and Allen L. Stone. The molecular structure of the diacid species of $\alpha\beta\gamma\delta$-tetra-4-pyridylporphine and $\alpha\beta\gamma\delta$-tetraphenylporphine. *Chemical Communications (London)*, (7):332–333, 1967.

[267] D. Ecija, M. Trelka, Ch. Urban, P. de Mendoza, E. Mateo-Marti, C. Rogero, J. A. Martin-Gago, A. M. Echavarren, R. Otero, J. M. Gallego, and R. Miranda. Molecular conformation, organizational chirality, and iron metalation of meso-tetramesitylporphyrins on copper(100). *The Journal of Physical Chemistry C*, 112(24):8988–8994, 2008.

[268] D. Ecija, K. Seufert, D. Heim, W. Auwärter, C. Aurisicchio, Ch. Fabbro, D. Bonifazi, and J. V. Barth. Hierarchic self-assembly of nanoporous chiral networks with conformationally flexible porphyrins. *ACS Nano*, 4(8):4936–4942, 2010.

[269] T. A. Jung, R. R. Schlittler, and J. K. Gimzewski. Conformational identification of individual adsorbed molecules with the stm. *Nature*, 386(6626):696–698, 1997.

[270] S. Clair, W. Pons, H. Brune, K. Kern, and J. V. Barth. Mesoscopic metallosupramolecular texturing by hierarchic assembly. *Angewandte Chemie International Edition*, 44:7294–7297, 2005.